Forward J/ψ in Ultraperipheral Collisions with the ALICE detector during LHC Run 2

Simone Ragoni

A thesis presented for the degree of

Doctor of Philosophy



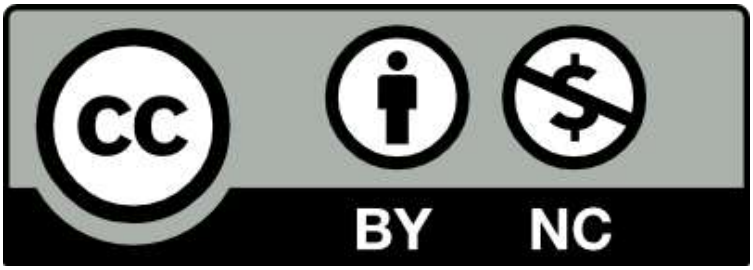
School of Physics and Astronomy

University of Birmingham

Birmingham, B15 2TT, UK

UNIVERSITY OF BIRMINGHAM

University of Birmingham Research Archive
e-theses repository



This unpublished thesis/dissertation is under a Creative Commons Attribution-NonCommercial 4.0 International (CC BY-NC 4.0) licence.

You are free to:

Share — copy and redistribute the material in any medium or format

Adapt — remix, transform, and build upon the material

The licensor cannot revoke these freedoms as long as you follow the license terms.

Under the following terms:



Attribution — You must give appropriate credit, provide a link to the license, and indicate if changes were made. You may do so in any reasonable manner, but not in any way that suggests the licensor endorses you or your use.



NonCommercial — You may not use the material for commercial purposes.

No additional restrictions — You may not apply legal terms or technological measures that legally restrict others from doing anything the license permits.

Notices:

You do not have to comply with the license for elements of the material in the public domain or where your use is permitted by an applicable exception or limitation.

No warranties are given. The license may not give you all of the permissions necessary for your intended use. For example, other rights such as publicity, privacy, or moral rights may limit how you use the material.

Unless otherwise stated, any material in this thesis/dissertation that is cited to a third-party source is not included in the terms of this licence. Please refer to the original source(s) for licencing conditions of any quotes, images or other material cited to a third party.

Forward J/ψ in Ultraperipheral Collisions with the ALICE detector during LHC Run 2

Simone Ragoni

Abstract

The ALICE Collaboration has studied coherent J/ψ photoproduction in Pb–Pb ultraperipheral collisions (UPC) since Run 1. The data sample collected during the LHC Run 2 at forward rapidity, i.e. $-4 < y < -2.5$, has opened new possibilities. New differential measurements are feasible, and it is then possible to study the properties of coherent J/ψ. A symmetric collision system such as Pb–Pb has an inherent ambiguity on the sign of the rapidity of the J/ψ with respect to the ion which is emitting the photon. The analysis of coherent J/ψ photoproduction in conjuction with neutron emission provides a viable new route to solve this ambiguity, and to probe for nuclear shadowing effects down to a Bjorken-x of about 10^{-5}. The two solutions with the forward rapidity acceptance of the ALICE detector are then sensitive to nuclear shadowing at Bjorken-$x \simeq 10^{-2}$ and 10^{-5}. In addition, the dataset also allows for the study of the angular distributions of the decay muons of the J/ψ, thus providing a tool to assess the polarisation of coherently photoproduced J/ψ. It is found that coherent J/ψ polarisation is measured to be consistent with transverse polarisation.

DECLARATION

I declare that this thesis has been solely written by myself. The studies here presented have been solely carried out for this dissertation. This is original work by the author.

Acknowledgement

First and foremost I would like to express my deepest gratitude to my supervisors, Prof. David Evans and Dr. Orlando Villalobos Baillie. I owe them far more than mere words on paper could possibly convey. My path ahead as a physicist will be built upon the foundation these years as a doctoral student have established. The discussions with both my supervisors have helped in increasing the overall quality of the analyses and ultimately deepening the physics message these entail.

I am also extremely grateful to Prof. Daniel Tapia Takaki and Dr. Roman Lietava, with whom I have shared quite a long step of this journey for the analysis of coherent J/ψ polarisation. Prof. Jesus Guillermo Contreras is also an important figure in this path of mine. His help was significant for both the neutron emission analysis and the analyses with the 2016 p–Pb sample. I have to extend my thanks to Tomáŝ Herman, fellow PhD researcher with whom I have shared the neutron emission analysis, and to Aude Glaenzer and her supervisor Dr. Michael Andreas Winn, with whom I have shared the 2016 p–Pb analysis. In addition, thanks to Dr. Spencer Klein and Prof. Joakim Nystrand for the useful discussions.

I would also like to thank all the ALICE Birmingham colleagues for their support for firmware development and hands-on related tasks: Marian Krivda, Anton Jusko, Jakub Kvapil.

Finally, this journey would not have been possible without the financial support of both the School of Physics and Astronomy of the University of Birmingham and the UKRI.

Contents

1 Using LHC to shine photons on nuclei **5**

1.1 Ultraperipheral collisions 6

1.1.1 Review of UPC results 7

1.1.2 Coherent J/ψ in Run 2 12

1.1.3 Disentangling low and high Bjorken-x 17

1.1.4 Exclusive J/ψ in p–Pb 24

1.1.5 Polarisation of the exclusive vector mesons 26

1.2 Overview of the formalism for polarisation measurements 26

2 ALICE detector at the LHC: an overview **29**

2.1 ALICE: A Large Ion Collider Experiment 31

2.2 The structure of the ALICE detector 31

2.2.1 Central barrel 32

2.2.2 Muon spectrometer 35

2.2.3 Forward detectors 38

2.3 The ALICE Trigger and DAQ System 41

3 Central Trigger System for LHC Run 3 **43**

3.1 TTCit: TTC Interface Test board 46

3.1.1 Dedicated hardware 46

3.1.2 A brief description of the firmware 50

3.1.3 TTCit: validation tools 54

3.2 CTP readout: State Machine . . . 58
3.2.1 Protocol . . . 58
3.2.2 The core scheme . . . 59
3.2.3 Data format sent via GBT . . . 62

4 Coherent J/ψ photoproduction and neutron emission **71**
4.1 A brief introduction to the analysis strategy . . . 71
4.2 Event and track selections . . . 72
4.2.1 Classifying neutron emission . . . 74
4.2.2 Control plots . . . 77
4.3 Fitting the invariant mass distributions . . . 83
4.4 p_{T} distributions and incoherent fractions . . . 86
4.5 Efficiency . . . 98
4.6 Feed-down f_{D} . . . 101
4.7 ZDC migration . . . 103
4.7.1 Propagation of the pile up and efficiency uncertainties . . . 106
4.8 Luminosity . . . 106
4.9 Correction for events lost due to V0A veto . . . 107
4.10 Cross sections . . . 109
4.11 Systematics . . . 111
4.12 Extracting $\sigma(\gamma\mathrm{Pb})$ . . . 112

5 Coherent J/ψ polarisation **119**
5.1 Physical considerations . . . 119
5.2 A brief introduction to the analysis strategy . . . 120
5.3 Polarisation formalism . . . 122
5.4 Event and track selections . . . 123
5.5 Fitting the invariant mass distributions . . . 124
5.6 Resolution in $\cos\theta$ and φ . . . 125

5.7 Raw yields . . . 125
5.8 Unfolding procedure . . . 129
5.8.1 Fitting the corrected distributions . . . 130
5.9 Closure tests . . . 131
5.9.1 Closure for the λ parameters . . . 132
5.9.2 Modulations in λ_φ . . . 137
5.9.3 Scan as a function of λ_φ . . . 144
5.10 Results in the helicity frame for ALICE data . . . 145
5.10.1 Correlations between the angular parameters . . . 146
5.11 Systematic uncertainties . . . 148
5.11.1 Variations to the $\cos\theta$ interval while fitting . . . 149
5.11.2 Signal Extraction . . . 150
5.11.3 Unfolding . . . 150
5.11.4 Response matrices . . . 150
5.11.5 Trigger and tracking . . . 151
5.12 Final results . . . 153
5.12.1 Comparison with past results . . . 154
5.13 Conclusions . . . 155

6 Conclusions **157**

A Relating rapidity of the vector meson to the Bjorken-x **159**

B Meaning of the bits assigned to the SSM **163**

C Fits to reconstructed STARlight distributions for the neutron emission analysis **165**

D Renormalising the fit function for the polarisation measurement **169**

E Conversion slice number to $\cos\theta$ interval for the coherent J/ψ polarisation measurement **171**

List of Figures

Figure 1.1: Schematics of ultraperipheral collisions shown in Fig. 1.1(a), while Fig. 1.1(b) shows the main diagram of a UPC event. W denotes the centre-of-mass energy of the γp system and the Mandelstam variable t is the four-momentum transfer between the incoming and the outgoing protons. 7

Figure 1.2: Event display of an ultraperipheral collision with forward J/ψ production during Run 1, captured by the ALICE detector. The clean topology of the process is a remarkable feature of UPC events, as only two decay muons can be found in an otherwise empty detector. 8

Figure 1.3: Coherent J/ψ in Pb–Pb during Run 1 at forward rapidity [1]. Fig. 1.3(a) shows the invariant mass distribution of the opposite sign muon pairs, with a clear J/ψ signal. Fig. 1.3(b) shows the p_{T} distribution for dimuon candidates in the J/ψ mass peak region instead. A clear low p_{T} coherent J/ψ excess can be appreciated. The plotted curves are obtained from reconstructed STARlight samples. 9

Figure 1.4: Forward and midrapidity cross sections for coherent J/ψ in Run 1 [2]. Despite the large uncertainties on either measurements, as theoretical models display the largest differences at midrapidity, the ALICE data point for the corresponding measurement succeeds in disfavouring more extreme models in terms of degree of involved nuclear shadowing. 10

Figure 1.5: Midrapidity cross section for incoherent J/ψ in Run 1 [2]. No model successfully describes the ALICE measurement. 11

Figure 1.6: Coherent ψ' in Pb–Pb during Run 1 at midrapidity [3]. Fig. 1.6(a) shows the cross sections measured for the three decay channels under investigation. Fig. 1.6(b) shows the averaged cross section as a function of rapidity. 12

Figure 1.7: Midrapidity cross section for coherent ρ^0 in Run 1 [4]. 13

Figure 1.8: Growth of the total cross sections for coherent and exclusive ρ^0 [4]. Both STAR and ALICE measurements are shown. 13

Figure 1.9: Coherent J/ψ in Pb–Pb during Run 2 at forward rapidity [5]. Fig. 1.9(a) shows the invariant mass distribution of opposite sign muons. J/ψ and ψ' peaks can both be seen. Fig. 1.9(b) shows the p_{T} distribution of the dimuons in the J/ψ mass region. The low p_{T} excess characteristic of coherent J/ψ photoproduction can be seen. 14

Figure 1.10: Coherent J/ψ cross sections as measured with the Run 2 data set [5]. Both forward and midrapidity measurements are provided. No model succeeds in properly reconstructing the complete trend of the data points. 16

Figure 1.11: Dimuon invariant mass distribution in the ultraperipheral sample as analysed by the LHCb Collaboration with Pb–Pb Run 2 data [6]. Abundant J/ψ production is seen, as well as a sizeable amount of ψ'. 16

Figure 1.12: Coherent J/ψ photoproduction cross sections as measured by the LHCb Collaboration [7, 6, 8]. The coverage provided by the LHCb analysis overlaps the rapidity acceptance of the ALICE measurement at forward rapidity [6]. The LHCb data points are reproduced by `EPS09`. 17

Figure 1.13: Nuclear suppression factor as a function of the Bjorken-x in Fig. 1.13(a), and comparison between ALICE and LHCb measurements in Fig. 1.13(b) [9]. 17

Figure 1.14: Possible vector meson photoproduction topology. Pb–Pb collisions hide an ambiguity, as either of the two nuclei may have originally emitted the photon, and thus, the vector meson may have either positive or negative absolute rapidity with respect to the photon emitter. 18

Figure 1.15: Impact parameter distributions for neutron emission classes with ρ^0 photoproduction, as computed by the $\mathbf{n^{O}_{O}n}$ generator [10]. . . . 20

Figure 1.16: Coherent ρ^0 cross sections in Pb–Pb during Run 2. Cross sections are also shown as a function of neutron emission classes [11]. . . . 21

Figure 1.17: Low p_{T} excess in the peripheral sample as observed by ALICE with Run 1 data [12]. 22

Figure 1.18: Coherent J/ψ photoproduction cross sections in the peripheral sample. Fig. 1.18(a) shows the cross section in the most peripheral centrality class, while Fig. 1.18(b) shows the coherent J/ψ photoproduction cross sections as a function of centrality [13]. 23

Figure 1.19: Exclusive J/ψ photoproduction cross sections as a function of the centre-of-mass energy of the γp system, $W_{\gamma\mathrm{p}}$ [14]. 24

Figure 1.20: Topology of a vector meson decaying to a lepton pair in the rest frame of the former. 27

Figure 2.1: Schematic view of the positioning of the four main LHC experiments. They are located underground at varying depths between 50 and 150 metres [15]. 30

Figure 2.2: The ALICE Run 2 detector is shown in all of its components and subdetectors. Human figures are also shown to give an idea of the size. 32

Figure 2.3: Schematic view of the ALICE Forward Muon Spectrometer. Picture taken from [16]. 37

Figure 2.4: Schematic view of the ZDC calorimeters positioned on the side of ALICE opposite the Muon Spectrometer. The neutron and proton ZDC are shown with the spatial separation due to the magnetic field protons are sensitive to. The ZEM is also shown. 40

Figure 2.5: ZDC energy spectra with midrapidity ρ^0 ALICE Pb–Pb UPC data. It is possible to distinguish clearly peaks due to neutrons being emitted on either side of the neutron ZDC. The energies clearly construct structures around the nominal energy carried by each nucleon i.e. 2.51 TeV. 41

Figure 3.1: Overview of the ALICE Central Trigger System, taken from [17]. The connections between CTP, LTUs, CRUs, FEEs are shown, along with the different types of connections available. 44

Figure 3.2: The ALICE Trigger Board prototype. The SFP cage is located on the right, the FMC channels are located on the left. 45

Figure 3.3: Fig. 3.3(a) and 3.3(b) show the front and back of the TTC-FMC card, respectively. The TTC-FMC card is then attached to the High Pin Count (HPC) connectors of both prototype boards. The important elements needed for the extrapolation of the signals and the data transmission can be singled out. In particular, the plug for the optical fibre is covered for protection, and the CDR chip is also quite visible (IC9 in fig. 3.3(a)). 47

Figure 3.4: Fig. 3.4(a) and 3.4(b) show the block diagram and scheme of the TTC-FMC card used in the TTCit development, respectively. The former shows which paths the signals have to travel on the TTC-FMC card up to the HPC connector, while the latter better displays the actual size of the card. 48

Figure 3.5: The fully assembled prototype board dedicated to the TTCit development. The LEDs and their meaning are also shown. 49

Figure 3.6: The block structure of TTCit. The signal is trasmitted by EMU TTC via optical fibre to the TTC-FMC card. Here the two channels A and B are separated. Ch A can be analysed by assessing the time duration of the signals seen by the firmware. Ch B has to be decoded separately, as the message is sent over via multiple words. All the decoded signals are then registered and sent to dedicated counters. 51

Figure 3.7: Working scheme of how TTCit is able to properly identify the signals over channel A. L0, L1, and calibration signals are 1-, 2-, 3-BC wide pulses. By assigning the Ch A signal to consecutive flip flops it is possible to assess the time duration as integer BC units by simply comparing the signals from the flip flops. As an example, only calibration signals can be high for three consecutive shifts, i.e. `qqq`, `qq` and `q` are all active. 52

Figure 3.8: The data format of LL1 messages as received by TTCit. The BRC messages contain eight bits of data and five bits of Hamming code, needed for checks over the transmission quality. The ADD messages are longer, needing fourteen bit strings to address single detectors, and contain sixteen bits of data and seven of Hamming code. 54

Figure 3.9: An example of the online capabilities of TTCit. The signals recorded by the SSM properly display the successful reception of a complete LL1 message. Each row refers to a different consecutive word recorded by the SSM. It is interesting to note that the S bit is raised as the same time as the F flag, as it should. Each row contains the F flag bit, the BC ID (twelve bits, three hexadecimal characters), the orbit ID (32 bits, eight hexadecimal characters), 32 bits of Trigger Types (the board is correctly receiving physics triggers, a decimal 2), Ch A-dedicated bits, strobes and bits related to transmission errors (the rightmost seventeen bits). 56

Figure 3.10: The second TTCit validation tool. Counters are useful to provide a fast tool for the health of the data transmission. 57

Figure 3.11: Flowchart describing the protocol the State Machine has to follow. It has to start a page (send SOP), send the raw data headers (RDH), and it is able to send data only when these steps have been completed. If a new orbit arrives, or if the maximum size of a page (8 KB) is reached, it has to signal the end of page (EOP), and restart the procedure. 60

Figure 3.12: Flowchart describing the chosen design of the CTP readout State Machine firmware. The packer receives as inputs the 64 bits for Trigger Classes, 12 bits of BC ID, and control bits for the orbit or the end of run. It arranges packets of 83 bits which are then sent to the FIFO. The FIFO redirects the first packet to a buffer when it is allowed to be read from the State Machine. This is due to the validation flag from the FIFO being delayed by one clock cycle with respect to its output. The State Machine handles the state decision, and the output to the GBT link. 63

Figure 3.13: Fig. 3.13(a) and 3.13(b) show the overall throughput of the GBT link with the data sent by the Trigger Class readout State Machine. The former shows the throughput with a pseudorandom number generator with high threshold, while the latter shows a much higher throughput caused by a very low threshold. 70

Figure 4.1: Fig. 4.1(a) and 4.1(b) show the invariant mass distribution and the p_{T} distribution for dimuons after selections. The invariant mass distribution has no p_{T} requirement applied to the dimuon p_{T}. The p_{T} distribution requires a dimuon invariant mass lying in the interval $2.85 < M_{\mu\mu} < 3.35$ GeV/c^2. 76

Figure 4.2: Fig. 4.2(a) and 4.2(b) show in red the neutron ZDC energy spectra before the timing selection is applied, and in blue the removal of the pedestal effected by the timing selection. The former shows the spectra for the neutron ZDC spectra on the A side, while the latter for the C side. Fig. 4.2(c) and 4.2(d) show the fit to the respective distributions after timing selection is requested. The fit is performed as a sum of Gaussian distributions. The peaks due to one, two and three neutron emission can be singled out. 79

Figure 4.3: Distribution of the total number of tracklets. The events have to pass muon quality requirements and exclusivity conditions. In addition, they have to be lying in a restricted dimuon invariant mass region around the J/ψ mass, i.e. $2.9 < M_{\mu\mu} < 3.3$ GeV/c^2. Fig. 4.3(a), 4.3(b), 4.3(c), and 4.3(d) show the distribution of the total number of tracklets for 0N0N, 0NXN, XN0N, and XNXN, respectively. 80

Figure 4.4: Distribution of the total number of activated V0C cells. The events have to pass both the muon quality requirements and the exclusivity conditions (apart from the veto on higher V0C cell activities). In addition, a dimuon invariant mass cut around the J/ψ peak region is required i.e. $2.9 < M_{\mu\mu} < 3.3$ GeV/c^2. Fig. 4.4(a), 4.4(b), 4.4(c), 4.4(d), and 4.4(e) show the distribution of the total number of activated V0C cells for 0N0N+0NXN+XN0N+XNXN, 0N0N, 0NXN, XN0N, and XNXN, respectively. 82

Figure 4.5: Raw yield extraction for the four neutron emission classes in the rapidity interval $-4.0 < y < -2.5$. Fig. 4.5(a), 4.5(b), 4.5(c), and 4.5(d) show the invariant mass distributions for 0N0N, 0NXN, XN0N, and XNXN, respectively. 86

Figure 4.6: Yield extraction for the 0N0N class, in three rapidity intervals. Fig. 4.6(a), 4.6(b), and 4.6(c) show the invariant mass distributions for the rapidity intervals $-4.0 < y < -3.5$, $-3.5 < y < -3.0$, and $-3.0 < y < -2.5$, respectively. 87

Figure 4.7: Yield extraction for the 0NXN class, in three rapidity intervals. Fig. 4.7(a), 4.7(b), and 4.7(c) show the invariant mass distributions for the rapidity intervals $-4.0 < y < -3.5$, $-3.5 < y < -3.0$, and $-3.0 < y < -2.5$, respectively. 88

Figure 4.8: Yield extraction for the XN0N class, in three rapidity intervals. Fig. 4.8(a), 4.8(b), and 4.8(c) show the invariant mass distributions for the rapidity intervals $-4.0 < y < -3.5$, $-3.5 < y < -3.0$, and $-3.0 < y < -2.5$, respectively. 89

Figure 4.9: Yield extraction for the XNXN class, in three rapidity intervals. Fig. 4.9(a), 4.9(b), and 4.9(c) show the invariant mass distributions for the rapidity intervals $-4.0 < y < -3.5$, $-3.5 < y < -3.0$, and $-3.0 < y < -2.5$, respectively. 90

Figure 4.10: Transverse momentum distributions in the four neutron emission classes for dimuon rapidity $-4 < y < -2.5$. In red, the actual p_{T} distribution used in the analysis, in green, the proper subsets of the corresponding events which would be rejected by an offline requirement of the emptiness in ADA. In blue, the analogous distributions if ADC is requested to be empty instead. Finally, in yellow, the proper subset of all the above, namely those events that would be rejected by asking the ADA decision being not empty AND the ADC decision being not empty. Fig. 4.10(a), 4.10(b), 4.10(c), and 4.10(d) show the distributions for 0N0N, 0NXN, XN0N, and XNXN, respectively. 91

Figure 4.11: $A \times \epsilon$ for p_{T} distributions, as obtained from the corresponding incoherent J/ψ reconstructed STARlight events. The flat trend of the $A \times \epsilon$ up to high p_{T} (limited by statistics, as the generation stops at around 1.8 GeV/c), implies that the p_{T} distributions can directly be fitted without firstly applying $A \times \epsilon$ corrections. 92

Figure 4.12: Transverse momentum distributions for the four neutron emission classes for the whole ALICE rapidity acceptance. Upper left: 0N0N. Upper right: 0NXN. Lower left: XN0N. Lower right: XNXN. 94

Figure 4.13: Transverse momentum distributions for the 0N0N class. Upper left: $-4.0 < y < -3.5$. Upper right: $-3.5 < y < -3.0$. Lower centre: $-3.0 < y < -2.5$. 96

Figure 4.14: Transverse momentum distributions for the 0NXN class. Upper left: $-4.0 < y < -3.5$. Upper right: $-3.5 < y < -3.0$. Lower centre: $-3.0 < y < -2.5$. 98

Figure 4.15: Transverse momentum distributions for the XN0N class. Upper left: $-4.0 < y < -3.5$. Upper right: $-3.5 < y < -3.0$. Lower centre: $-3.0 < y < -2.5$. 99

Figure 4.16: Transverse momentum distributions for the XNXN class. Upper left: $-4.0 < y < -3.5$. Upper right: $-3.5 < y < -3.0$. Lower centre: $-3.0 < y < -2.5$. 100

Figure 4.17: Luminosity of the sample used for the neutron emission measurement. 108

Figure 4.18: Coherent J/ψ photoproduction cross sections in neutron emission classes. Fig. 4.18(a) shows the cross sections measured at forward rapidity for all classes, along with the LTA predictions for the entire span of rapidity [18]. Fig. 4.18(b), 4.18(c), 4.18(d) and 4.18(e) show instead the 0N0N, 0NXN, XN0N, and XNXN classes, respectively. Systematic uncertainties are shown as boxes. 116

Figure 4.19: Solutions for photonuclear cross sections obtained by the simultaneous measurement of the 0N0N, 0NXN, XN0N and XNXN neutron emission classes, as reported in Sec. 4.10. The photonuclear cross sections show a growth as $W_{\gamma\mathrm{Pb}}$ increases, or, equivalently, if x decreases. The cross sections are fitted with a power-law function of the form $N \cdot (W_{\gamma\mathrm{Pb}}/W_0)^{\delta}$, and the fit parameters are also shown. The predictions from STARlight and the Impulse Approximation are also shown. 117

Figure 4.20: Suppression factors as a function of $W_{\gamma\mathrm{Pb}}$ and Bjorken-x for photonuclear cross sections obtained by the simultaneous measurement of the 0N0N, 0NXN, XN0N and XNXN neutron emission classes, as reported in Sec. 4.10. The measured suppression factors for $x \sim 10^{-2}$ are in agreement with the value reported in [5]. The suppression factors for $10^{-4} \lesssim x \lesssim 10^{-5}$ are in agreement with the reweighting carried out in [9]. 118

Figure 5.1: The procedure used for this measurement. Both real data and Monte Carlo simulations are analysed. The latter are used to create templates needed for the signal extraction of the former. In addition, Monte Carlo simulations are used to create the response matrices, needed to effect the unfolding of the raw distributions. Finally, the unfolded distributions are fitted to extract the λ parameters. 121

Figure 5.2: Resolutions in $\cos\theta$ and φ. The resolution in $\cos\theta$ is quite good. The resolution in φ necessitates unfolding to properly resolve a potential structure in the distribution. 126

Figure 5.3: Distribution of reconstructed $\cos\theta$, obtained from STARlight Monte Carlo events. The distribution shows a range of accessible $\cos\theta$ up to $|\cos\theta| < 0.6$. 127

Figure 5.4: Raw yield distribution in the helicity frame for coherent J/ψ polarisation. The events are focused in the region $|\cos\theta| < 0.3$. . . . 128

Figure 5.5: Physically allowed regions for λ_θ, λ_φ, $\lambda_{\theta\varphi}$. Fig. 5.5(a) shows the allowed region for λ_θ against λ_φ. Fig. 5.5(b) shows the allowed region for $\lambda_{\theta\varphi}$ against λ_θ, with the choice of λ_φ set to $\lambda_\varphi = 0$. . . 130

Figure 5.6: Fig. 5.6(a) shows the relative difference of the unfolded reconstructed–level and the generated–level STARlight events after one iteration of the unfolding procedure. Fig. 5.6(b) shows the same distribution after five iterations instead. The agreement is at the level of 10^{-15} for both distributions, since the same sample is used to generate both the response matrices, and the reconstructed–level distributions. 133

Figure 5.7: Fig. 5.7(a) shows the relative difference of the refolded unfolded and reconstructed–level STARlight events after one iteration of the unfolding procedure. Fig. 5.7(b) shows the same distribution after five iterations instead. The same sample is used to generate both the response matrices, and the reconstructed–level distributions. . 134

Figure 5.8: Fig. 5.8(a) shows the unfolded reconstructed–level distribution in intervals of $\cos\theta$ and φ after five iterations of bayesian unfolding. Fig. 5.8(b) shows instead the generated–level distribution. 136

Figure 5.9: Fig. 5.9(a) shows the generated–level distribution in intervals of $\cos\theta$ and φ, with the input of $(\lambda_\theta, \lambda_\varphi, \lambda_{\theta\varphi}) = (0, 1, 0)$. Fig. 5.9(b) shows the same generated–level distribution, but in a bidimensional view. 140

Figure 5.10: The same generated–level distribution as shown in Fig. 5.9(b), but with same binning applied to real data. 141

Figure 5.11: Scan of the average correlation coefficient as a function of the number of iterations when a modulation in φ is provided as input data matrix. A minimum is found at around fifteen iterations. 141

Figure 5.12: Fig. 5.12(a) and 5.12(b) show the relative difference of the refolded distributions to the reconstructed–level distributions, for all bins, with increasing bin numbers, with STARlight and reweighted STARlight matrices, respectively. 142

Figure 5.13: Unfolded reconstructed–level distribution with generated $\lambda_\varphi = 1$, with the same binning as real data. Large modulations are also returned by the unfolding procedure. 143

Figure 5.14: Fit to the scan in possible modulations in φ. This unfolding technique recovers consistently the input modulation. 144

Figure 5.15: Scan of the average correlation coefficient as a function of the number of iterations when the yields from real ALICE data are used as input data matrix. A minimum is found at around fifteen iterations. 145

Figure 5.16: Fig. 5.16(a) shows the relative difference of the refolded to reconstructed–level distribution in the case of real ALICE data. Fig. 5.16(b) shows instead the fit to the unfolded distribution, along with the results. 147

Figure 5.17: The correlations of the three lambda parameters are shown as one, two and three sigma contours in red, blue, and black, respectively, along with the central value shown as a black dot. 148

Figure 5.18: Detail taken from `starlight/src/gammaavm.cpp`. It is shown how STARlight models the decay in the helicity frame of the J/ψ. The J/ψ is purely transverse. 151

Figure 5.19: Trigger systematic uncertainties for λ_θ, λ_φ and $\lambda_{\theta\varphi}$ in Fig. 5.19(a), 5.19(b) and 5.19(c), respectively. 152

Figure 5.20: ALICE results for coherent J/ψ polarisation are shown translated to spin-density matrix elements. This allows for the direct comparison with the results achieved by H1 and ZEUS collaborations. ALICE results display better agreement with the measurement performed by H1, as expected considering that both are probing the photoproduction regime. 156

Figure A.1: Possible vector meson photoproduction topology. The photon from the emitter interacts with a Pomeron from the target. A vector meson is produced in the final state. 159

Figure C.1: Fit to reconstructed STARlight distributions for J/ψ. Fig. C.1(a), C.1(b), C.1(c), and C.1(d) show the fits to the J/ψ distributions with dimuon rapidity lying in the interval $-4 < y < -2.5$, $-4 < y < -3.5$, $-3.5 < y < -3$, and $-3 < y < -2.5$, respectively. 166

Figure C.2: Fit to reconstructed STARlight distributions for ψ'. Fig. C.2(a), C.2(b), C.2(c), and C.2(d) instead show the fits to the ψ' distributions with dimuon rapidity lying in the interval $-4 < y < -2.5$, $-4 < y < -3.5$, $-3.5 < y < -3$, and $-3 < y < -2.5$, respectively. . 167

Figure C.3: Fit to reconstructed STARlight distributions for the $\gamma\gamma$ background. Finally, Fig. C.3(a), C.3(b), C.3(c), and C.3(d) show the fits to the background distributions with dimuon rapidity lying in the interval $-4 < y < -2.5$, $-4 < y < -3.5$, $-3.5 < y < -3$, and $-3 < y < -2.5$, respectively. 168

List of Tables

3.1 Example page sent by the CTP readout via GBT to the CRU using the hexadecimal system. The full progression of the readout chain can be visually inspected. 64

3.2 Example of a dump to file of the State Machine's simulation, where all the entries are using the hexadecimal system. A constant payload is used (`32BF8`). The quick succession of RDH can also be visually inspected. . . . 66

3.3 Output of the State Machine on the GBT link in the hexadecimal system. The typical format of the Trigger Classes readout is seen as an oblique structure. Two freely running counters are used, one for payload, and the other being the BC ID. 68

4.1 Available events, with the correct online trigger, and two opposite-sign muons satisfying the quality requirements for muon tracks. Total events and partials per run period are also shown. 73

4.2 Number of events which would be rejected by applying the corresponding condition. Numbers are shown both for the total dataset and the single run periods. The final row shows the events rejected by all the exclusivity selections. 74

4.3 Events passing all selections, and also the coherent dimuon p_{T} requirement. Numbers are also shown for rapidity intervals. No neutron emission class is applied. 75

4.4 Events passing all selections, and also the coherent dimuon p_{T} requirement. Numbers are also shown for rapidity intervals. The 0N0N class selection is applied. 77

4.5 Events passing all selections, and also the coherent dimuon p_{T} requirement. Numbers are also shown for rapidity intervals. The 0NXN class selection is applied. 78

4.6 Events passing all selections, and also the coherent dimuon p_{T} requirement. Numbers are also shown for rapidity intervals. The XN0N class selection is applied. 78

4.7 Events passing all selections, and also the coherent dimuon p_{T} requirement. Numbers are also shown for rapidity intervals. The XNXN class selection is applied. 78

4.8 Summary table with the incoherent fractions. The values are obtained with both methods in neutron emission classes as a function of rapidity. A comparison with the corresponding value of the feed-down, f_{D}, is also provided. 97

4.9 $A \times \epsilon$ values for coherent J/ψ. The values are differential only in rapidity intervals. No simulation is available for neutron emission classes. 101

4.10 Branching ratio values taken from the PDG. Both central values and systematic uncertainties are presented. 102

4.11 Pile up probabilities and neutron ZDC detection efficiencies. The values are obtained with a separate study internal to the ALICE Collaboration. . 105

4.12 ZDC migration correction matrix after inversion. These values are directly applied to compute the corrected cross sections. 106

4.13 Systematic effect due to the variation of one sigma of pile up and neutron detection efficiency. The numbers shown represent half the discrepancy between the effects of an upward and a downward variation of one sigma of the corresponding parameters. 107

4.14 Summary table with coherent J/ψ photoproduction cross sections in neutron emission classes as a function of rapidity. Statistical and systematic uncertainty are also shown. 110
4.15 Systematic uncertainties for the neutron emission analysis. 113
4.16 Photonuclear cross sections obtained from the analysis of the neutron emission classes, compared to the predictions for the Impulse Approximation model from STARlight in the same $W_{\gamma \mathrm{Pb}}$ interval. The suppression factors are also presented. 115

5.1 Correlation coefficients among the fit parameters for real data. The correlations between the λ parameters and the normalisation from the fit, I, are also given. 149
5.2 Table summarising the absolute systematic uncertainties for the measurement of coherent J/ψ polarisation. The main systematic uncertainties considered are due to variations on the fitted $\cos\theta$ interval, the impact of different descriptions of the J/ψ line shape, the unfolding, the input Monte Carlo shape used for the response matrices, and the trigger effects on the single muons comprising the J/ψ. 153
5.3 Final results for the measurement of coherent J/ψ polarisation in the helicity frame. 153

Acronyms

ACORDE *ALICE COsmic Ray DEtector*.

AD *ALICE Diffractive Detector*.

ADA *ALICE Diffractive Detector*-A.

ADC *ALICE Diffractive Detector*-C.

ADC Analog-to-Digital Converter.

ADD *individually addressed commands*.

ALICE A Large Ion Collider Experiment.

BC bunch crossing.

BC ID Bunch Crossing IDentifier.

BRC *broadcast commands*.

CDR *Clock Data Recovery*.

CERN *European Organization for Nuclear Research*.

CPV Charged Particle Veto.

CRU Common Readout Unit.

CTP Central Trigger Processor.

CTS Central Trigger System.

D-RORC DAQ Readout Receiver Cards.

DDL Detector Data Links.

EMCAL *ElectroMagnetic CALorimeter*.

EOP *End of Page*.

EOx *End of Run*.

FEE Front End Electronics.

FMC FPGA Mezzanine Card.

FMD *Forward Multiplicity Detector*.

GBT GigaBit Transceivers.

GDC Global Data Collectors.

HB *Heartbeat*.

HMPID *High-Momentum Particle Identification Detector*.

HPC High Pin Count.

ITS *Inner Tracking System*.

LDC Local Data Concentrators.

LEIR Low Energy Ion Ring.

LFSR *Linear Feedback Shift Register*.

LHC *Large Hadron Collider*.

LHCb Large Hadron Collider beauty.

LL1 *Long L1 messages*.

LOL *loss of lock*.

LOS *loss of signal*.

LTA Leading Twist Approximation.

LTU Local Trigger Unit.

LUT Look-Up Tables.

MIP Minimum Ionising Particle.

MRPC Multigap Resistive Plate Chambers.

MWPC multi-wire proportional chambers.

OLT Optical Line Terminal.

ONU Optical Network Unit.

PAG-UPC Physics Analysis Group Ultraperipheral Collisions.

PDF parton distribution function.

PHOS *PHOton Spectrometer*.

PMD *Photon Multiplicity Detector*.

PON Passive Optical Network.

PS Proton Synchrotron.

PSB Proton Synchrotron Booster.

PWG-LF Physics Working Group Light Flavour.

PWG-UD Physics Working Group Ultraperipheral and Diffractive.

RDH *Raw Data Header*.

RPC Resistive Plate Chambers.

SCHC *s-channel helicity conservation*.

SDD Silicon Drift Detector.

SFP+ Small Form-factor Pluggable transceiver.

SOP *Start of Page*.

SPD Silicon Pixel Detector.

SPS Super Proton Synchrotron.

SSD Silicon Strip Detector.

SSM *snapshot memory*.

STAR Solenoidal Tracker at RHIC.

SWT *Single Word Transaction*.

TDS Transient Data Storage.

TOF *Time-Of-Flight*.

TPC Time Projection Chamber.

TRD *Transition Radiation Detector*.

TTC Trigger and Timing Control.

TTCit TTC Interface Test board.

UPC Ultraperipheral Collisions.

VDM Vector Dominance model.

ZDC *Zero Degree Calorimeter*.

ZNC C-side neutron ZDC.

Author's contribution

The author has been a part of the ALICE Collaboration since his master thesis. Originally involved in the so called Physics Working Group Light Flavour (PWG-LF), with measurements of hadron spectra in Xe–Xe collisions, he moved to the Physics Working Group Ultraperipheral and Diffractive (PWG-UD) since he started his doctoral studies. In particular, he has been a member of the Physics Analysis Group Ultraperipheral Collisions (PAG-UPC), for almost four years by the time this thesis was written.

His contributions to the group have been numerous, under the supervision of the Birmingham ALICE Team. He was the sole analyser for the first measurement of coherent J/ψ polarisation in Pb–Pb Ultraperipheral Collisions (UPC) at $\sqrt{s_{\mathrm{NN}}} = 5.02$ TeV, he greatly contributed to the measurement of coherent J/ψ production in neutron emission classes (focusing on the forward measurement). He also greatly contributed to the measurement of exclusive J/ψ production in p–Pb UPC at $\sqrt{s_{\mathrm{NN}}} = 8.16$ TeV, the first measurement of dissociative J/ψ production and exclusive dimuon production in p–Pb UPC at $\sqrt{s_{\mathrm{NN}}} = 8.16$ TeV. He has also marginally contributed to the measurement of coherent J/ψ production in Pb–Pb UPC at $\sqrt{s_{\mathrm{NN}}} = 5.02$ TeV, where his contribution was to provide a cross-check of the results that were about to be published at the time. This latter and the p–Pb measurements have not been integrated to this document.

Concerning technical tasks, he has tested all the Central Trigger Processor (CTP) and Local Trigger Unit (LTU) boards for Run 3 during the months from February to August

2020. He has developed the TTC Interface Test board (TTCit) firmware for the Birmingham CTP team, and has also been tasked with the design of the CTP readout firmware. Both firmware projects will be extensively used during LHC Run 3.

Regarding contributions to national and international conferences, his contributions may be broadly divided in three groups: posters, talks and conference proceedings.

Poster contributions:

- **INPC 2019**, Glasgow: *Recent results for forward* J/ψ *production in Pb–Pb Ultra-Peripheral Collisions at* $\sqrt{s_{\mathrm{NN}}} = 5.02$ *TeV with the ALICE Detector*, which is available at the following link: https://cdn.eventsforce.net/files/ef-q5vmtsq56tk6/website/1303/simone_ragoni.pdf;
- **LHCP 2020**, Paris, but online: *UPC: a powerful tool for* J/ψ *photoproduction analysis in ALICE*, which is available at the following link: https://indico.cern.ch/event/856696/contributions/3853629/.

Talk contributions:

- **ALICE Physics Week 2019**, Prague, August 2019: talk to the Collaboration about the progress of the measurements presented in this document;
- **ALICE Juniors Day 2020**, CERN, but online, March 2020: talk to the Junior Community of the Collaboration, overview of the recent results on J/ψ photoproduction in UPC;
- **UK Lockdown Seminars 2020**, online, September 2020: talk to the UK Nuclear Community, with title *UPC in ALICE: a powerful microscope for gluon pdf*;
- **ALICE Physics Week 2020**, CERN, September 2020: talk to the Collaboration about the progress of the polarisation measurement presented in this document (the

paper draft was being written at the time);

- **Joint IOP**, online, April 2021: J/ψ *photoproduction in Pb–Pb UPC: from* $x \sim 10^{-2}$ *to* 10^{-5}, available at the following link: https://indico.cern.ch/event/1013634/contributions/4313655/;
- **LHCP 2021**, Paris, but online: *New measurements on diffractive vector mesons*, joint ALICE and LHCb talk, which is available at the following link: https://indico.cern.ch/event/905399/contributions/4291683/;
- **ALICE Physics Week 2021**, CERN, September 2021: talk to the Collaboration about the progress of the polarisation measurement presented in this document (the Editorial Board review was ongoing, and about to move to Collaboration Rounds), and the neutron emission measurement;
- **Low-x 2021**, Elba, first in-person workshop after the pandemic: *Recent ALICE results on vector meson photoproduction*, which is available at the following link: https://indico.cern.ch/event/1003281/contributions/4479105/.

Proceedings contributions:

- **INPC 2019**, Glasgow: *Recent results for forward* J/ψ *production in Pb–Pb Ultra-Peripheral Collisions at* $\sqrt{s_{\mathrm{NN}}} = 5.02$ *TeV with the ALICE Detector* [19];
- **LHCP 2020**, Paris, but online: *UPC: a powerful tool for* J/ψ *photoproduction analysis in ALICE* [20];
- **LHCP 2021**, Paris, but online: *New measurements on diffractive vector mesons* [21];
- **Low-x 2021**, Elba: *Recent ALICE results on vector meson photoproduction*, to be published.

Chapter 1

Using LHC to shine photons on nuclei

A description of most subatomic interactions and phenomena is provided by the Standard Model of Particle Physics. The current Standard Model is formed essentially by two types of particles, *fermions* and *bosons*. The former make up all observable matter, while the latter are the mediators of the interactions. Fermions are divided into *quarks* and *leptons*, where the former combine to form hadrons, and the latter are not affected by the strong interaction. Both quarks and leptons are divided into three generations, each coming in pairs. Hence, there are six quarks, u, d, c, s, t, and b (up, down, charm, strange, top, bottom/beauty), and six leptons, e, ν_{e}, μ, ν_{μ}, τ and ν_{τ} (electron, electron neutrino, muon, muon neutrino, tau, tau neutrino). In the current state of the Standard Model, both quarks and leptons are fundamental constituents. The remaining particles are the bosons, γ, $W^{\pm}/Z$, g, responsible for the electromagnetic, weak, and strong interactions, respectively, and the Higgs boson.

Historically, the J/ψ meson constitutes the first observation of the fourth quark, the *charm* quark, since it is a bound state $c\bar{c}$, with a mass of about 3.1 GeV/c^2 [22]. This was the first example of a quark q being discovered by means of its bound state with its antiquark, $q\bar{q}$, during the so called *November Revolution*, in 1974.

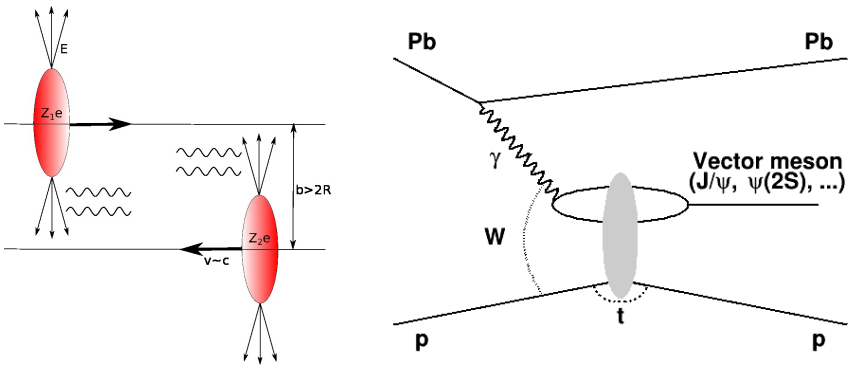
Special emphasis is given to the J/ψ meson in the rest of the chapter, since the later parts of this thesis will be focusing on differential measurements of J/ψ photoproduction in ultraperipheral collisions, with the data collected by the A Large Ion Collider Experiment (ALICE) Collaboration. An overview of ultraperipheral collisions and of the research programme that is being carried out inside the ALICE Collaboration, is given in the following.

1.1 Ultraperipheral collisions

Exclusive vector meson production i.e. the process A + A $\longrightarrow$ A + A + VM, where VM denotes the vector meson and A = p, Xe, Au, Pb, ... , can take place in ultraperipheral collisions - UPC. These events are characterised by large impact parameters, larger than the sum of the nuclear radii i.e. impact parameters $b > R_1 + R_2$, where the subscripts 1 and 2 denote the two nuclei. This is shown in Fig. 1.1(a). As such, hadronic interactions are suppressed. One of the two nuclei acts as a photon source, and thus a photon from the emitter interacts with the gluons of the target, and gives a vector meson in the final state, as shown in Fig. 1.1(b).

It is interesting to note that an important feature of ultraperipheral collisions is that the diagram is factorisable. In fact, as can be observed in Fig. 1.1(b), the diagram can be treated as separable into a vertex where only the photon flux is involved, and the other where only the gluons enter. This will also be discussed again in Sec. 1.1.1.

The vector meson decays, and at the detector level the topology will be very clean: only their decay products will be found, in an otherwise empty detector. Fig. 1.2 shows an event display of a UPC event collected by the ALICE detector during Run 1. The event is compatible with J/ψ production at forward rapidity, with the J/ψ reconstructed through its decay to a muon pair. The nomenclature of ultraperipheral collisions changes in



(a) (b)

Figure 1.1: Schematics of ultraperipheral collisions shown in Fig. 1.1(a), while Fig. 1.1(b) shows the main diagram of a UPC event. W denotes the centre-of-mass energy of the γp system and the Mandelstam variable t is the four-momentum transfer between the incoming and the outgoing protons.

literature depending on the collision system. The following classification will be employed:

- **exclusive vector meson production**, when p–Pb or pp collisions are involved;
- **coherent vector meson production**, when Pb–Pb collisions are involved and the photon interacts coherently with the whole nucleus;
- **incoherent vector meson production**, when Pb–Pb collisions are involved and the photon interacts with a single nucleon of the target.

1.1.1 Review of UPC results

ALICE has been involved in ultraperipheral collisions since Run 1. Analyses at forward and central rapidity were both possible, and both were performed. Several different states can be studied with the ALICE detector. Generally speaking, ALICE is able to investigate mostly charmonium states at forward rapidity and midrapidity, and ρ^0 at midrapidity.

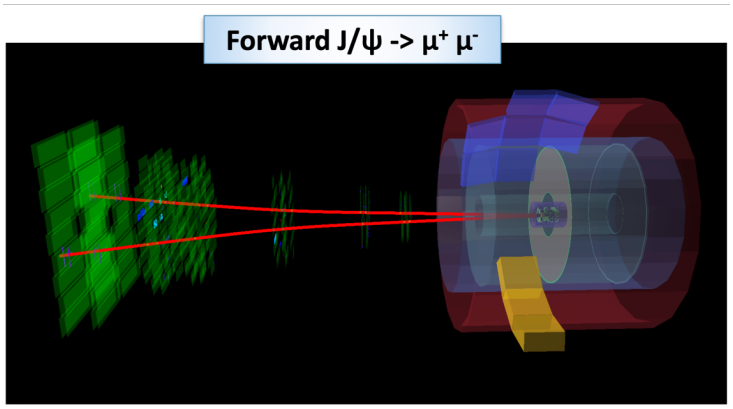


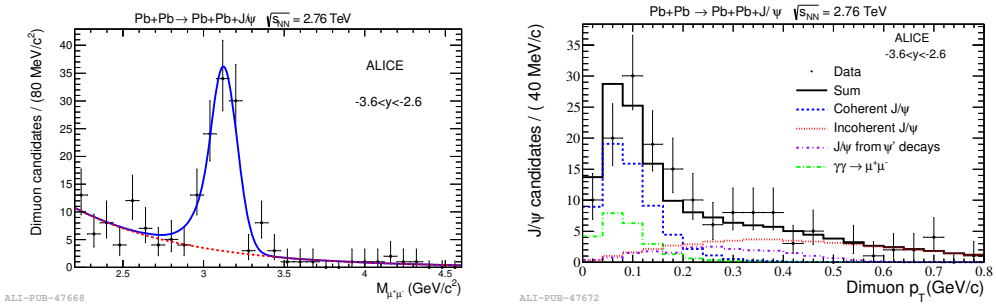
Figure 1.2: Event display of an ultraperipheral collision with forward J/ψ production during Run 1, captured by the ALICE detector. The clean topology of the process is a remarkable feature of UPC events, as only two decay muons can be found in an otherwise empty detector.

The ultimate goal of coherent J/ψ photoproduction in Pb–Pb interactions is to further the understanding on the phenomenon called *nuclear shadowing*, which is a decrease of the production cross section on the whole nucleus, compared to nucleons without nuclear effects involved.

The first ALICE measurement with ultraperipheral events was performed at forward rapidity [1] at $\sqrt{s_{\mathrm{NN}}} = 2.76$ TeV. The recorded luminosity was 55 $\mu\mathrm{b}^{-1}$, an order of magnitude lower than the Run 2 integrated luminosity. This first measurement at forward rapidity led to a total number of available coherent J/ψ candidates of about a hundred, see Fig. 1.3(a). The corresponding p_{T} distribution, Fig. 1.3(b) already shows a low p_{T} excess compatible with the expectations of coherent J/ψ photoproduction. Incoherent J/ψ photoproduction can also be visually inspected, featuring a much broader distribution. The resulting coherent J/ψ photoproduction cross section [1],

$$\frac{\mathrm{d}\sigma^{\mathrm{coh}}_{\mathrm{J}/\psi}}{\mathrm{d}y} = 1.00 \pm 0.18\ (\mathrm{stat.}) \pm^{+0.24}_{-0.26}\ (\mathrm{sys.})\ \mathrm{mb}, \tag{1.1}$$

did not reject any of the models available at the time, as shown in Fig. 1.4, since their predictions converge at the rapidity measured. Most of the models show agreement or fail to display a large disagreement with the only available forward rapidity point.



(a) (b)

Figure 1.3: Coherent J/ψ in Pb–Pb during Run 1 at forward rapidity [1]. Fig. 1.3(a) shows the invariant mass distribution of the opposite sign muon pairs, with a clear J/ψ signal. Fig. 1.3(b) shows the p_{T} distribution for dimuon candidates in the J/ψ mass peak region instead. A clear low p_{T} coherent J/ψ excess can be appreciated. The plotted curves are obtained from reconstructed STARlight samples.

The midrapidity measurement of coherent J/ψ during Run 1 proved more effective at distinguishing between models [2]. As shown again in Fig. 1.4, the single available midrapidity point is already not compatible with models with either no or very strong nuclear shadowing effects. As such, historically ALICE concludes that the data are in agreement with moderate nuclear shadowing. It is already interesting to attempt the extraction of the so called nuclear shadowing factor S_{Pb}, defined starting directly from the available data as shown in the following Eq. 1.2 [9]:

$$S_{\mathrm{Pb}} = \sqrt{\frac{\mathrm{d}\sigma_{\mathrm{data}}/\mathrm{d}y}{\mathrm{d}\sigma_{\mathrm{IA}}/\mathrm{d}y}}\ , \tag{1.2}$$

where $d\sigma_{\mathrm{data}}/dy$ is the cross section as measured by ALICE, and $d\sigma_{\mathrm{IA}}/dy$ is the cross section from the *Impulse Approximation* model, which considers the nucleus as a superposition of nucleons, all of which contribute to the interaction, but without nuclear effects. In Fig. 1.4, the Impulse Approximation is referred to as `AB-MSTW08`, but it will be referred to below as either `IA` or Impulse Approximation model. The measurement performed by the ALICE Collaboration is thus consistent with a nuclear shadowing factor $S_{\mathrm{Pb}} \sim 0.6$.

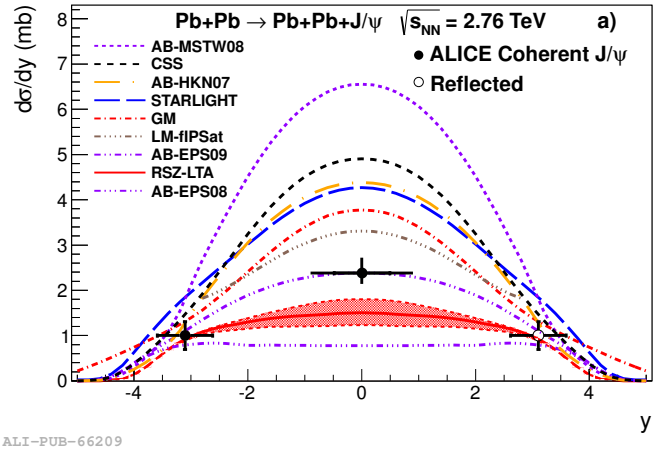


Figure 1.4: Forward and midrapidity cross sections for coherent J/ψ in Run 1 [2]. Despite the large uncertainties on either measurements, as theoretical models display the largest differences at midrapidity, the ALICE data point for the corresponding measurement succeeds in disfavouring more extreme models in terms of degree of involved nuclear shadowing.

The ALICE Collaboration has also measured the incoherent J/ψ photoproduction cross sections at midrapidity only, thus complementing the picture provided by the measurement of coherent J/ψ photoproduction[1], as shown in Fig. 1.5. No model manages to describe the trend of both coherent and incoherent J/ψ photoproduction. It is interesting to compute the ratio of the measurements for incoherent and coherent J/ψ production. As previously mentioned, the difference between the two lies in the way the photon couples with the target: with a single nucleon of the target for incoherent photoproduction, the whole nucleus for coherent photoproduction. As the photon flux is factorisable and shared between the two measurements, the ratio actually reflects the ratio of the photonuclear cross sections only. The ratio R, is then measured to be [2]:

$$R = \frac{\frac{\mathrm{d}\sigma^{\mathrm{incoh}}_{\mathrm{J}/\psi}}{\mathrm{d}y}}{\frac{\mathrm{d}\sigma^{\mathrm{coh}}_{\mathrm{J}/\psi}}{\mathrm{d}y}} = 0.41^{+0.10}_{-0.08}\ (\mathrm{stat.} + \mathrm{sys.})\ , \tag{1.3}$$

which is consistent with the value computed by STARlight for the ratio $R_{\mathrm{SL}} = 0.41$,

[1]Both measurements employ a p_{T} cut in the invariant mass distributions with no overlap in p_{T} coverage, thus complementing each other.

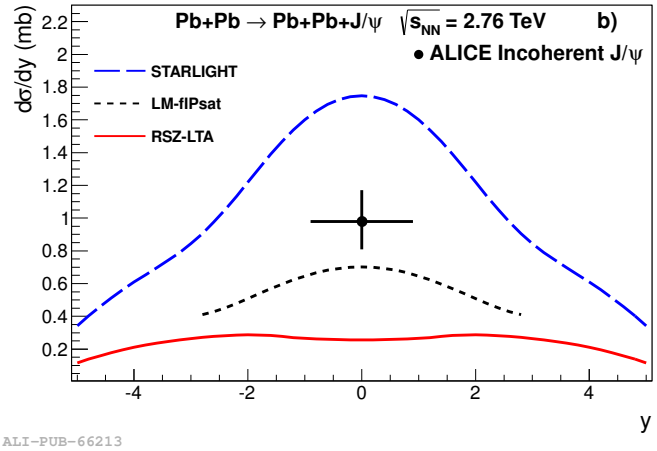


Figure 1.5: Midrapidity cross section for incoherent J/ψ in Run 1 [2]. No model successfully describes the ALICE measurement.

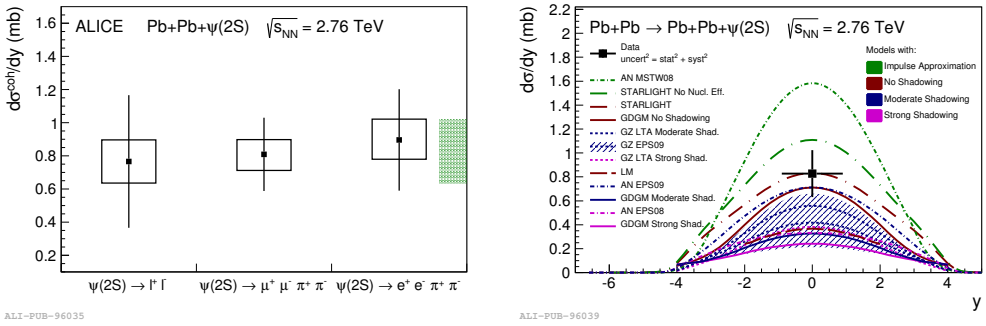
despite failing to describe the measured individual cross sections, for both coherent and incoherent photoproduction.

The ALICE Collaboration has also published results for coherent ψ' photoproduction at midrapidity with Run 1 data [3]. The measurement was performed in the channels $\psi' \longrightarrow ll$, $\mu\mu\pi\pi$, ee$\pi\pi$, where $l = \mathrm{e}, \mu$, and then combined by a weighted average, see Fig. 1.6(a). The combined cross section is plotted against models in Fig. 1.6(b). The ψ' shows a similar nuclear shadowing factor to the J/ψ. ALICE finds a ratio for the ψ' to J/ψ coherent photoproduction cross sections equal to:

$$R[\psi'/\mathrm{J}/\psi] = \frac{\frac{\mathrm{d}\sigma^{\mathrm{coh}}_{\psi'}}{\mathrm{d}y}}{\frac{\mathrm{d}\sigma^{\mathrm{coh}}_{\mathrm{J}/\psi}}{\mathrm{d}y}} = 0.34^{+0.08}_{-0.07}\ (\mathrm{stat.} + \mathrm{sys.})\ . \tag{1.4}$$

The result is compared with the Run 2 measurements in Sec. 1.1.2.

ALICE has also measured coherent ρ^0 photoproduction with Run 1 data [4]. Fig. 1.7 shows the data point obtained at midrapidity. The measured cross section is found to be consistent with STARlight. The single measurement by ALICE at midrapidity can be plotted together with the three measurements available with the Solenoidal Tracker



(a) (b)

Figure 1.6: Coherent ψ' in Pb–Pb during Run 1 at midrapidity [3]. Fig. 1.6(a) shows the cross sections measured for the three decay channels under investigation. Fig. 1.6(b) shows the averaged cross section as a function of rapidity.

at RHIC (STAR) data [23, 24, 25], in terms of total cross sections, where the integration over the entire rapidity domain from the corresponding $\mathrm{d}\sigma/\mathrm{d}y$ is carried out with models. The results are shown in Fig. 1.8. It can be seen that the growth of the cross section as a function of the centre-of-mass energy per nucleon pair, $\sqrt{s_{\mathrm{NN}}}$, is well described by STARlight.

1.1.2 Coherent J/ψ in Run 2

Run 2 was particularly successful in collecting data for ultraperipheral collisions with the ALICE detector. Improved trigger conditions helped in delivering an integrated luminosity of about 750 $\mu\mathrm{b}^{-1}$, with roughly 22000 coherent J/ψ candidates at forward rapidity. This in turn, enabled more differential measurements, such as, for example, the first measurement of coherent J/ψ polarisation in UPC, which is presented in Chapter 5.

The new trigger conditions for data taking at forward rapidity employed by the ALICE Collaboration for Run 2 firstly expanded the useful rapidity probed by the detector (from

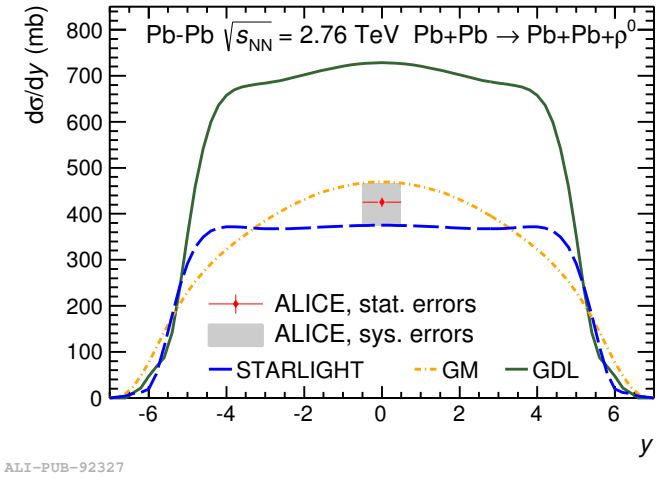


Figure 1.7: Midrapidity cross section for coherent ρ^0 in Run 1 [4].

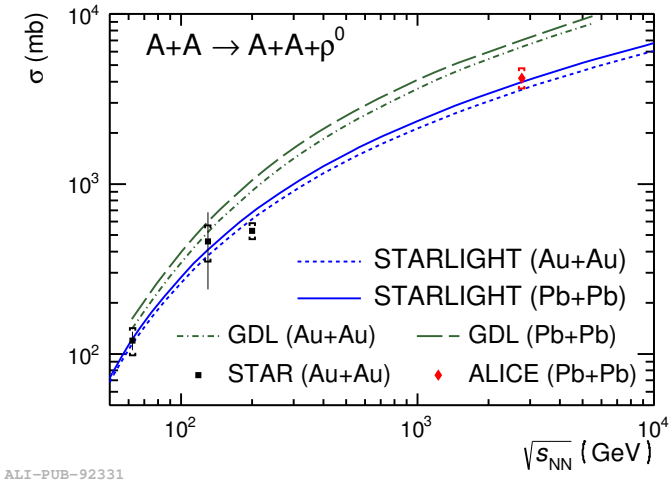
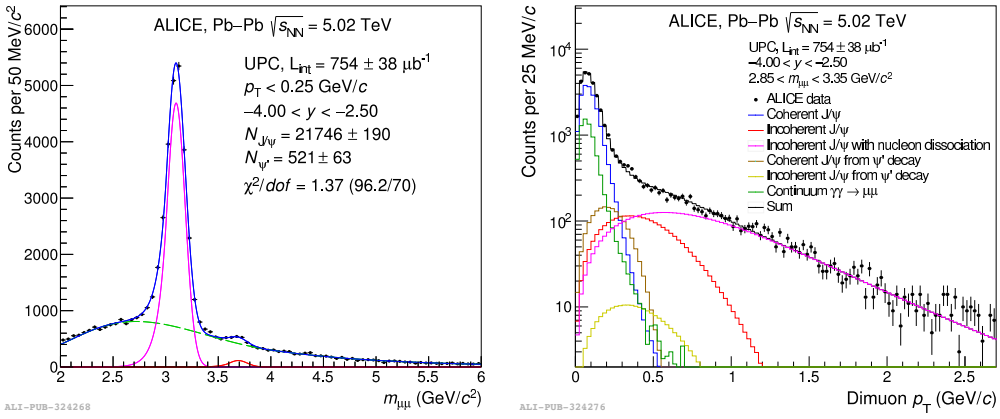


Figure 1.8: Growth of the total cross sections for coherent and exclusive ρ^0 [4]. Both STAR and ALICE measurements are shown.

the single unit of rapidity available in Run 1 i.e. $-3.6 < y < -2.6$, to the 1.5 units of rapidity characteristic of Run 2 i.e. $-4.0 < y < -2.5$). As shown in Fig. 1.9(a) [5], the data set features a very clean and clear J/ψ peak, containing about 22000 J/ψ candidates, now also displaying a bump due to the presence of ψ' candidates. Fig. 1.9(b) displays the p_{T} distribution of opposite sign muon pairs in the J/ψ mass region. This distribution also shows the potential of the Run 2 data set for future incoherent J/ψ measurements at forward rapidity. The fit shown in Fig. 1.9(a) provides information on the ratio ψ' to



(a) (b)

Figure 1.9: Coherent J/ψ in Pb–Pb during Run 2 at forward rapidity [5]. Fig. 1.9(a) shows the invariant mass distribution of opposite sign muons. J/ψ and ψ' peaks can both be seen. Fig. 1.9(b) shows the p_{T} distribution of the dimuons in the J/ψ mass region. The low p_{T} excess characteristic of coherent J/ψ photoproduction can be seen.

J/ψ. The forward ALICE measurement of the ratio $R[\psi'/\mathrm{J}/\psi]$ [5] finds:

$$R[\psi'/\mathrm{J}/\psi] = 0.150 \pm 0.018\ (\mathrm{stat.}) \pm 0.021\ (\mathrm{syst.}) \pm 0.007\ (\mathrm{BR}). \tag{1.5}$$

There is some tension between the result shown in Eq. 1.4 and the one shown in Eq. 1.5 above, probably due to the difficulties encountered in extracting the signal with the sample collected during Run 1.

The ALICE Collaboration reports the measurement of the coherent J/ψ photoproduction

cross sections at both forward and midrapidity with the Run 2 data set [5, 26]. The rapidity distribution is shown in Fig. 1.10.

The data points are compared with a few models. STARlight [27] is based on the Vector Dominance model (VDM) and is based on HERA data for exclusive J/ψ photoproduction off protons. The Impulse Approximation is taken from STARlight by neglecting nuclear effects [27]. Finally, the last model which is of interest for the remainder of this document is the Leading Twist Approximation (LTA), which implements the diffractive PDFs from HERA data [28].

No model manages to fully reproduce the cross sections at both forward and midrapidity, even though EPS09 delivers consistent midrapidity cross sections. It is also possible to carry out the exercise previously shown in Sec. 1.1.1 for the nuclear shadowing factor. It is then quite straightforward to confirm that ALICE data at midrapidity are consistent with a nuclear shadowing factor of $S_{\mathrm{Pb}} \sim 0.6$. The Large Hadron Collider beauty (LHCb) Collaboration has also performed a measurement of coherent J/ψ photoproduction at forward rapidity [7, 6, 8], and also finds a very clean and clear J/ψ peak and also a hint of a ψ' peak in their dimuon invariant mass distributions, as shown in Fig. 1.11. As a single-arm muon spectrometer, LHCb has a slightly wider rapidity acceptance compared to the ALICE detector, and succeeds in delivering a coverage of 2.5 units of rapidity at forward rapidity i.e. $2.0 < y < 4.5$, against the 1.5 units available in ALICE, perfectly overlapping the rapidity coverage offered by the ALICE measurement. It is quite interesting to observe how the LHCb data points are perfectly reproduced by EPS09, as shown in Fig. 1.12. Fig. 1.13(b) [9] shows the ALICE and LHCb points plotted together.

Fig. 1.13(b) [9] also shows a slight tension between ALICE forward and midrapidity points. The authors of the paper measure a nuclear shadowing factor of $S_{\mathrm{Pb}} \sim 0.6$ from fits to the available LHCb and ALICE data, as shown in Fig. 1.13(a), thus confirming what the simple exercise shown in Sec. 1.1.1 was able to provide.

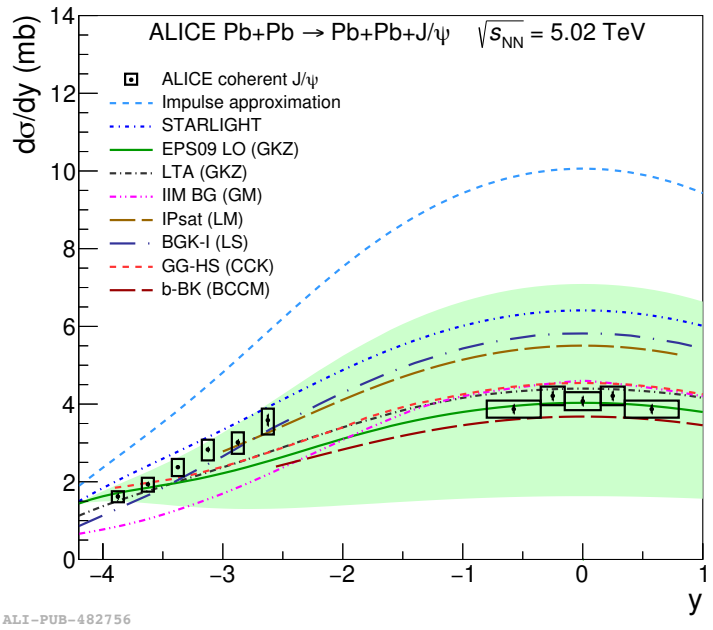


Figure 1.10: Coherent J/ψ cross sections as measured with the Run 2 data set [5]. Both forward and midrapidity measurements are provided. No model succeeds in properly reconstructing the complete trend of the data points.

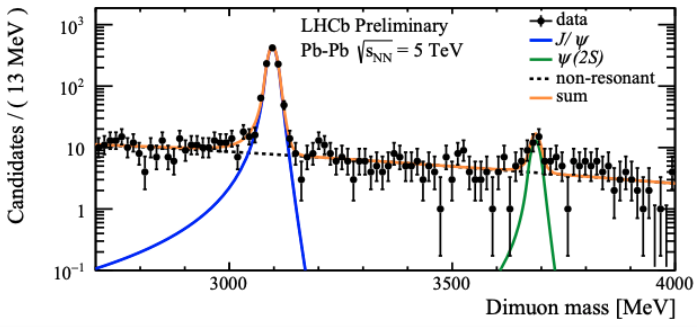


Figure 1.11: Dimuon invariant mass distribution in the ultraperipheral sample as analysed by the LHCb Collaboration with Pb–Pb Run 2 data [6]. Abundant J/ψ production is seen, as well as a sizeable amount of ψ'.

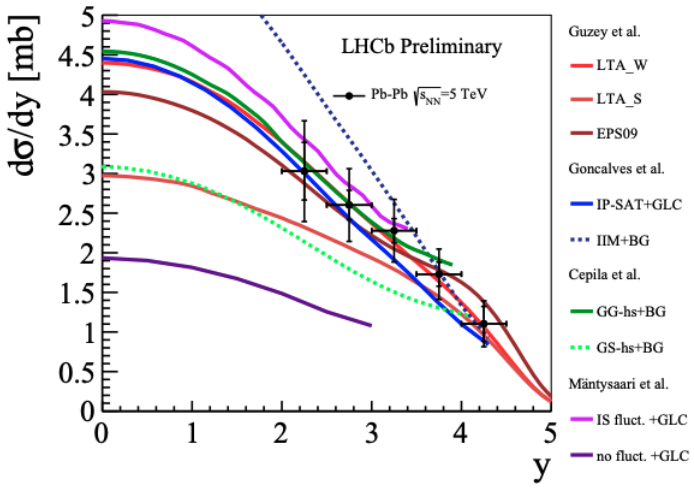
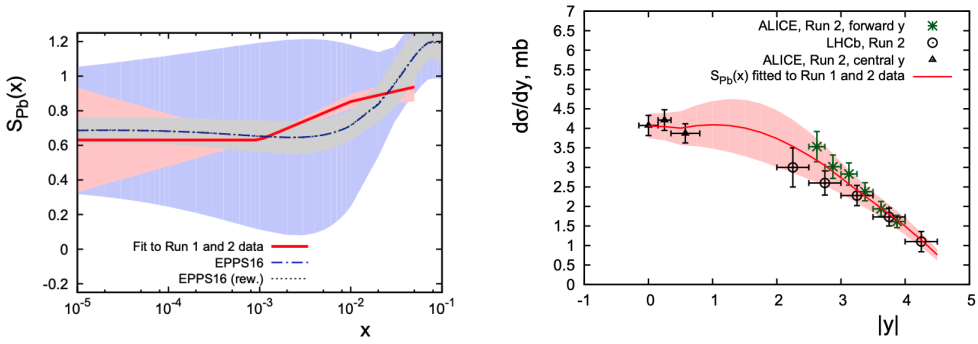


Figure 1.12: Coherent J/ψ photoproduction cross sections as measured by the LHCb Collaboration [7, 6, 8]. The coverage provided by the LHCb analysis overlaps the rapidity acceptance of the ALICE measurement at forward rapidity [6]. The LHCb data points are reproduced by EPS09.



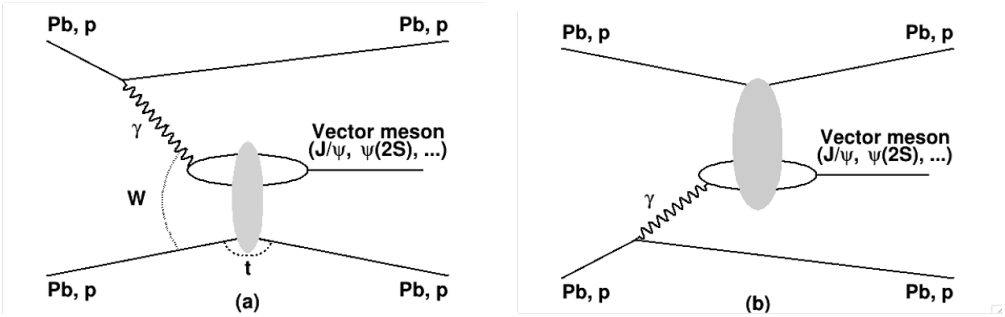
(a) (b)

Figure 1.13: Nuclear suppression factor as a function of the Bjorken-x in Fig. 1.13(a), and comparison between ALICE and LHCb measurements in Fig. 1.13(b) [9].

1.1.3 Disentangling low and high Bjorken-x

Until now, only Pb–Pb results have been considered. As this is a symmetrical system, either of the two interacting nuclei might have been the original photon emitter, as shown

in Fig. 1.14(a) and 1.14(b). As a consequence, the resulting photoproduced vector meson can have either negative or positive rapidity with respect to the photon emitter. This has



(a) (b)

Figure 1.14: Possible vector meson photoproduction topology. Pb–Pb collisions hide an ambiguity, as either of the two nuclei may have originally emitted the photon, and thus, the vector meson may have either positive or negative absolute rapidity with respect to the photon emitter.

quite tangible consequences. As it turns out, the relevant Bjorken-x of the process can be shown from kinematics to be expressed as a function of the vector meson rapidity[2], as presented in Eq. 1.6:

$$x = \frac{M_{\mathrm{J}/\psi}}{\sqrt{s_{\mathrm{NN}}}} \cdot \exp(\pm|y|) \ , \tag{1.6}$$

where $M_{\mathrm{J}/\psi}$ is the mass of the J/ψ, $\sqrt{s_{\mathrm{NN}}}$ is the centre-of-mass energy of the collision system, and y the rapidity of the vector meson with respect to the photon emitter. At midrapidity, $y \sim 0$, this is of little importance. At forward rapidity, instead, with ALICE Run 2 kinematics, this inherent ambiguity leads to a mixture of $x \sim 10^{-2}$ and 10^{-5} events.

One of the most interesting features of ultraperipheral collisions is that the diagram can be treated as factorisable. The basic process can be expressed in terms of the photon flux, n, and the photonuclear cross section $\sigma_{\gamma\mathrm{Pb}}$. The ambiguity appears then as the sum of

[2]Derived in Appendix A.

two components as shown in Eq. 1.7:

$$\frac{d\sigma_{\mathrm{PbPb}}}{dy} = n(+y) \cdot \sigma_{\gamma\mathrm{Pb}}(+y) + n(-y) \cdot \sigma_{\gamma\mathrm{Pb}}(-y) \ . \tag{1.7}$$

The unknown quantities are then the two photonuclear cross sections at either positive or negative rapidity. To resolve the ambiguity one must therefore separate the equation into a system of equations by using a well-known quantity. As there are two unknown quantities, it is necessary to have at least two equations. The photon flux is known from models, and it is the best quantity to base this study on. The most interesting strategy is to prepare equations for different impact parameters. Then the photon flux may be computed for the different impact parameters, thus finally removing the ambiguity.

At the moment, there are two possible ways to do this:

- *neutron emission*;
- *peripheral photoproduction*.

The first approach is the neutron emission principle. It was argued [29] that splitting the currently available ALICE UPC dataset based on neutron emission could help in selecting different impact parameters. These neutrons originate from additional photon exchanges between the two lead nuclei, and these two processes should be independent from each other and hence, factorisable. The $\mathbf{n^{O}_{O}n}$ generator [10] predicts the average impact parameter dependence for different neutron emission classes, as shown in Fig. 1.15. The available datasets can be separated into neutron emission classes by means of *zero degree calorimeters*. It is possible to have no neutrons on both sides of the detectors (which can be labelled as 0N0N), neutrons on one side only (which can be labelled as 0NXN), and neutrons on both sides (which can be labelled as XNXN). As Fig. 1.15 shows, these three classes display a hierarchy in terms of average impact parameter $\langle b \rangle$, which is clarified in the following Eq. 1.8:

$$\langle b_{\mathrm{XNXN}} \rangle < \langle b_{\mathrm{0NXN}} \rangle < \langle b_{\mathrm{0N0N}} \rangle \ . \tag{1.8}$$

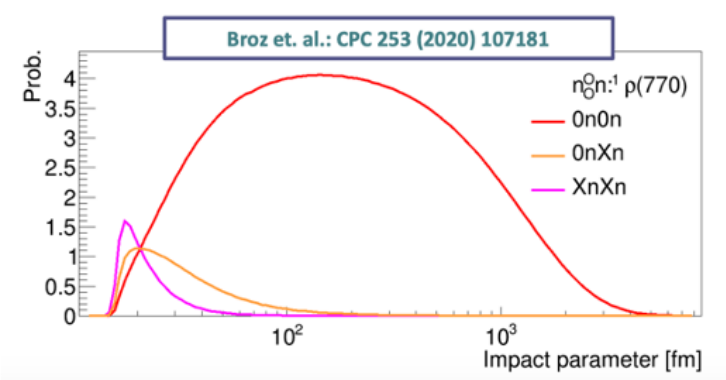


Figure 1.15: Impact parameter distributions for neutron emission classes with ρ^0 photoproduction, as computed by the $\mathbf{n^{O}_{O}n}$ generator [10].

This technique has firstly been successfully applied by the ALICE Collaboration at midrapidity for ρ^0 photoproduction in Pb–Pb [11], and the cross sections for the 0N0N+0NXN+XNXN, 0N0N, 0NXN, and XNXN classes are shown in Fig. 1.16(a), 1.16(b), 1.16(c), and 1.16(d), respectively. The generally good agreement with the available models implies that factorisation of the main photoproduction process and the additional photon exchanges holds. However, the data points still have sizeable uncertainties, so the measurement can be considered a good proof-of-principle for the future, while also waiting for the measurement of coherent J/ψ photoproduction in neutron emission classes, which is presented in Chapter 4. Ultimately, the system of equations will then be presented as in Eq. 1.9:

$$\begin{aligned}
\frac{\mathrm{d}\sigma^{0N0N}_{PbPb}}{\mathrm{d}y} &= n_{0N0N}(\gamma,+y)\cdot\sigma_{\gamma Pb}(+y) + n_{0N0N}(\gamma,-y)\cdot\sigma_{\gamma Pb}(-y)\ , \\
\frac{\mathrm{d}\sigma^{0NXN}_{PbPb}}{\mathrm{d}y} &= n_{0NXN}(\gamma,+y)\cdot\sigma_{\gamma Pb}(+y) + n_{0NXN}(\gamma,-y)\cdot\sigma_{\gamma Pb}(-y)\ , \\
\frac{\mathrm{d}\sigma^{XNXN}_{PbPb}}{\mathrm{d}y} &= n_{XNXN}(\gamma,+y)\cdot\sigma_{\gamma Pb}(+y) + n_{XNXN}(\gamma,-y)\cdot\sigma_{\gamma Pb}(-y)\ .
\end{aligned} \tag{1.9}$$

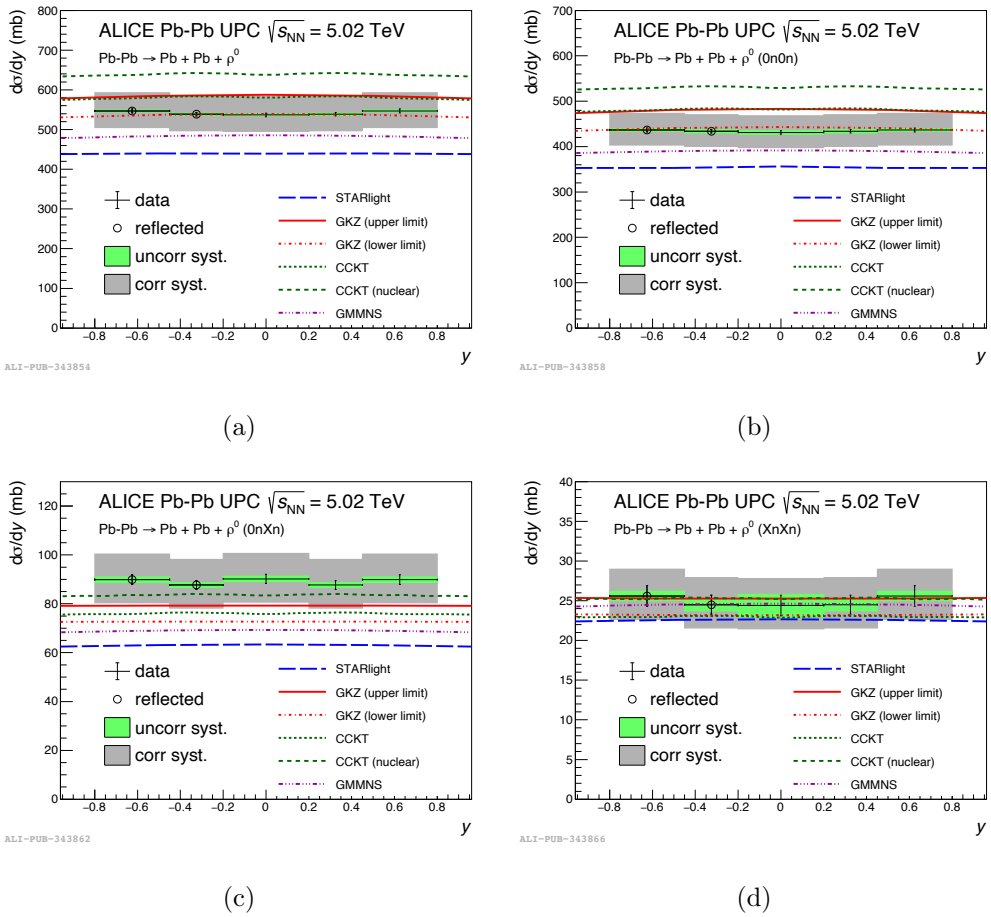


Figure 1.16: Coherent ρ^0 cross sections in Pb–Pb during Run 2. Cross sections are also shown as a function of neutron emission classes [11].

At midrapidity, Eq. 1.9 may be rewritten as shown in Eq. 1.10:

$$\begin{aligned}
\frac{\mathrm{d}\sigma^{0N0N}_{PbPb}}{\mathrm{d}y} &= 2 \cdot n_{0N0N}(\gamma, y \sim 0) \cdot \sigma_{\gamma Pb}(y \sim 0) \ , \\
\frac{\mathrm{d}\sigma^{0NXN}_{PbPb}}{\mathrm{d}y} &= 2 \cdot n_{0NXN}(\gamma, y \sim 0) \cdot \sigma_{\gamma Pb}(y \sim 0) \ , \\
\frac{\mathrm{d}\sigma^{XNXN}_{PbPb}}{\mathrm{d}y} &= 2 \cdot n_{XNXN}(\gamma, y \sim 0) \cdot \sigma_{\gamma Pb}(y \sim 0) \ .
\end{aligned} \tag{1.10}$$

Hence, factorisation of the main photoproduction process and the additional photon exchange implies that any neutron emission class cross section may be computed starting from any of the others, when scaled by the corresponding photon flux.

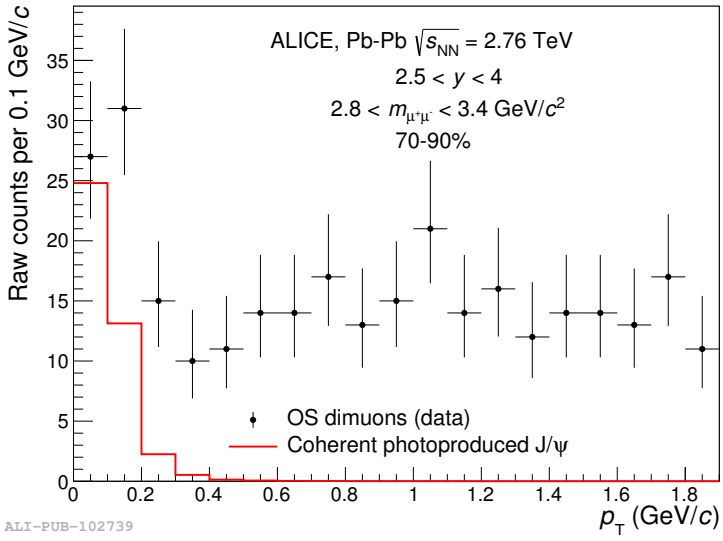


Figure 1.17: Low p_{T} excess in the peripheral sample as observed by ALICE with Run 1 data [12].

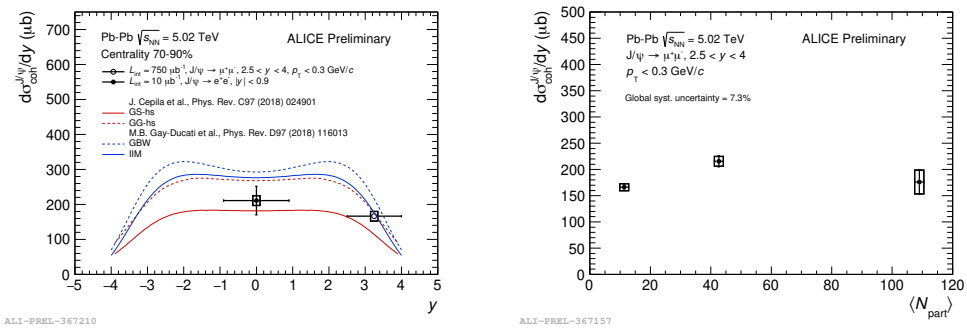
The other approach consists of interacting directly with the impact parameter. In ultra-peripheral collisions the impact parameter is larger than the sum of the nuclear radii i.e. $b > R_1 + R_2$, and no hadronic interactions should occur. By moving to the peripheral collisions instead, the impact parameter is now smaller than the sum of nuclear radii, hadronic interactions occur, and it is possible to consider whether photoproduction may still happen. If conclusive evidence that coherent J/ψ photoproduction happens even in peripheral collisions were to appear, it would be possible to write:

$$\begin{aligned} \frac{\mathrm{d}\sigma^{P}_{PbPb}}{\mathrm{d}y} &= n_P(\gamma,+y)\cdot\sigma_{\gamma Pb}(+y) + n_P(\gamma,-y)\cdot\sigma_{\gamma Pb}(-y)\ , \\ \frac{\mathrm{d}\sigma^{U}_{PbPb}}{\mathrm{d}y} &= n_U(\gamma,+y)\cdot\sigma_{\gamma Pb}(+y) + n_U(\gamma,-y)\cdot\sigma_{\gamma Pb}(-y)\ , \end{aligned} \tag{1.11}$$

where P and U refer to the peripheral and ultraperipheral results, respectively. This technique was proposed in [30].

The assumption is then that coherent J/ψ photoproduction occurs in peripheral events. The result comes from ALICE Collaboration Run 1 data [12], with the observation of a low p_{T} excess in the p_{T} distribution of opposite sign muon pairs at forward rapidity, as shown in Fig. 1.17. The observation has also been confirmed by the STAR [31] and

LHCb [32] collaborations. ALICE recently presented an updated study of coherent J/ψ photoproduction in the peripheral sample at forward rapidity [13]. Fig. 1.18(a) shows the cross section in the most peripheral centrality class studied, while Fig. 1.18(b) shows the coherent J/ψ photoproduction cross sections as a function of centrality (a lower value of average number of participants, $\langle N_{\text{part}} \rangle$, means a more peripheral class). The cross sections, being mostly independent from the centrality class under examination, are hence consistent with the picture of coherent photoproduction as the underlying production mechanism.



(a) (b)

Figure 1.18: Coherent J/ψ photoproduction cross sections in the peripheral sample. Fig. 1.18(a) shows the cross section in the most peripheral centrality class, while Fig. 1.18(b) shows the coherent J/ψ photoproduction cross sections as a function of centrality [13].

It is possible to specialise Eq. 1.11 to midrapidity, giving:

$$\frac{\mathrm{d}\sigma^{P}_{PbPb}}{\mathrm{d}y} = \frac{n_P(\gamma, y \sim 0)}{n_U(\gamma, y \sim 0)} \cdot \frac{\mathrm{d}\sigma^{U}_{PbPb}}{\mathrm{d}y} \ , \tag{1.12}$$

as described in [30].

Overall, it is then evident how the two approaches operate on a similar basis, by using the impact parameter and the fluxes, which are presumed to be calculable. The similarities are apparent once Eq. 1.9 and Eq. 1.11 are examined together, or equivalently, when

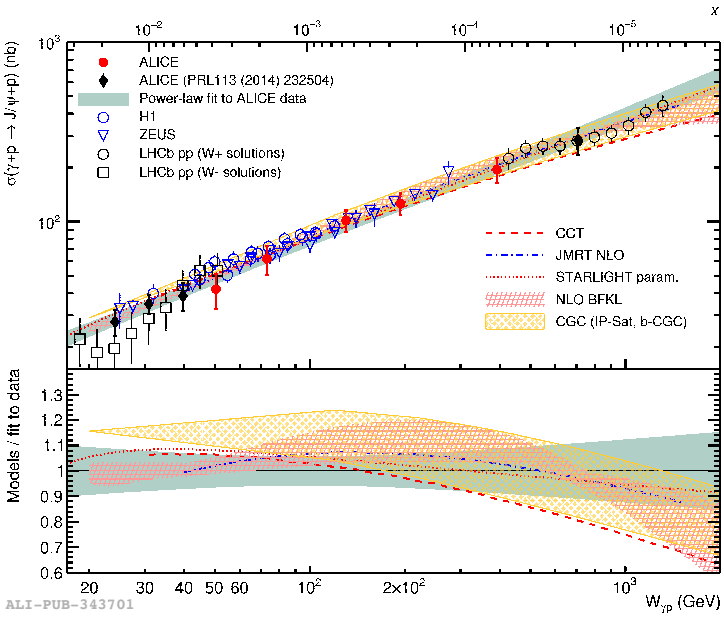


Figure 1.19: Exclusive J/ψ photoproduction cross sections as a function of the centre-of-mass energy of the γp system, $W_{\gamma p}$ [14].

the corresponding midrapidity specialisations from Eq. 1.10 and Eq. 1.12 are compared instead.

1.1.4 Exclusive J/ψ in p–Pb

Until now, only Pb–Pb UPC have been discussed. It is now clear how the ultimate goal of Pb–Pb UPC is to improve the understanding of nuclear shadowing. The ALICE Collaboration has also reported measurements with p–Pb UPC. The focus shifts to a different topic. These data are useful to study the growth of the gluon parton distribution functions at low momentum fraction x. The ultraperipheral cross section depends on the square of the gluon parton distribution functions (PDFs). It is thus a valuable tool to study the behaviour of the gluon PDFs. Exclusive J/ψ production i.e. the process $\gamma + \mathrm{p} \longrightarrow \mathrm{J}/\psi + \mathrm{p}$, has been studied extensively at HERA, both at H1 and ZEUS [33, 34]. The measurements by both H1 and ZEUS cover the range in centre-of-mass energy of the

γp system, $W_{\gamma p}$, between 20 and 305 GeV. Using the formula [35] shown in Eq. 1.13:

$$x = \frac{M_{J/\psi}^2}{W_{\gamma p}^2} \ , \tag{1.13}$$

it is straightforward to relate the pre-existing measurements to an interval of probed x. It is then found that the measurements from H1 and ZEUS could probe the range in $x \sim 10^{-2}$ down to 10^{-4}. Measurements from both LHCb and ALICE [36, 37, 38, 14, 39, 40] extended the probed range. In particular, LHCb has presented results obtained with pp events at the centre-of-mass energy $\sqrt{s}$ = 7 TeV, $\sqrt{s}$ = 8 TeV, and $\sqrt{s}$ = 13 TeV, extending the range down to $x \sim 2 \cdot 10^{-6}$. The ALICE Collaboration is able to analyse p–Pb UPC data. In this particular type of collision system, the photon flux is assumed to be emitted mainly by the Pb ion. It is then possible to assign unambiguously the correct type of UPC diagram, and hence, the sign of the vector meson rapidity. ALICE measurements have been performed with three types of configurations: forward rapidity, carried out with both p–Pb and Pb–p, midrapidity, and the semiforward configuration. At non-central rapidity, the sign of the rapidity of the vector meson changes when moving from one beam configuration to the other, and both muons from the J/ψ decay are identified in the Forward Muon Spectrometer. At midrapidity, both muons are measured in the central barrel. In the semiforward configuration instead, intermediate J/ψ rapidities are achieved by having one muon in the central barrel of the ALICE detector, and the other in the Forward Muon Spectrometer. The results for the analysis of ALICE exclusive J/ψ production are shown in Fig. 1.19. The ALICE data points are shown in black and red, for the forward and for the semiforward and central configurations, respectively. Fig. 1.19 shows that there is no change in the behaviour of the gluon PDFs going towards smaller x.

1.1.5 Polarisation of the exclusive vector mesons

Lastly, the *s-channel helicity conservation* (SCHC) hypothesis leads to the vector meson produced in the final state having the same polarisation as the photon of the initial state. H1 and ZEUS report measurements of the angular distributions of the muons from the decay of the J/ψ in [33, 34]. The results of both measurements are shown in Fig. 5.20. STAR has more recently measured the polarisation of exclusive ρ^0 in ultraperipheral collisions [25], and the results are consistent with the SCHC hypothesis. A measurement of J/ψ polarisation in UPC events would be of critical importance in closing the picture of SCHC for photoproduction processes, see Ch. 5.

1.2 Overview of the formalism for polarisation measurements

Sec. 1.1.5 briefly discusses previous measurements for the polarisation of exclusive vector mesons. Ch. 5 presents in fact the first polarisation measurement of coherent J/ψ polarisation in ultraperipheral collisions, with Pb–Pb data at $\sqrt{s_{\mathrm{NN}}} = 5.02$ TeV. It thus becomes necessary to briefly introduce polarisation, and the formalism needed to describe it. The polarisation of vector mesons is usually tackled both in theory and experiments by studying the angular distributions of the lepton pairs they decay to. This is characterised by a very clean process both from a theoretical and an experimental point of view, e.g. it is a back-to-back topology for theory computations.

One way to assess polarisation is to boost the system to the rest frame of the vector meson. This is what is shown in Fig. 1.20. This is done as it enables the use of polarisation axes and reference frames. The helicity frame is chosen as the reference frame for the measurement reported in Ch. 5, where the z-axis is taken to be the flight direction of the

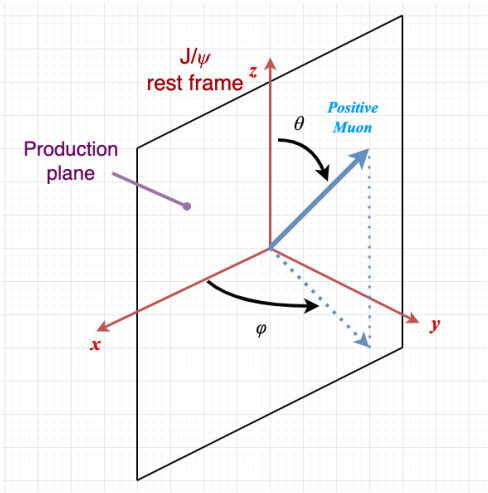


Figure 1.20: Topology of a vector meson decaying to a lepton pair in the rest frame of the former.

J/ψ in the overall centre-of-mass frame, the y-axis is perpendicular to the plane formed by the directions of the colliding particles and the direction of the J/ψ, and the x-axis is chosen to form a right-handed triplet [41]. The following definitions are then used for the unit vectors of the axes, namely $\hat{x}$, $\hat{y}$ and $\hat{z}$:

$$\begin{aligned} \hat{z} &= \frac{\vec{p}^{\,CM}_{\mathrm{J}/\psi}}{|\vec{p}^{\,CM}_{\mathrm{J}/\psi}|} \ , \\ \hat{y} &= \frac{\vec{p}^{\,rest}_{beam\ 1} \times \vec{p}^{\,rest}_{beam\ 2}}{|\vec{p}^{\,rest}_{beam\ 1} \times \vec{p}^{\,rest}_{beam\ 2}|} \ , \\ \hat{x} &= \frac{\hat{y} \times \hat{z}}{|\hat{y} \times \hat{z}|} \ , \end{aligned} \tag{1.14}$$

where $\vec{p}^{\,CM}_{\mathrm{J}/\psi}$ is the momentum vector of the J/ψ in the overall centre-of-mass frame, and $\vec{p}^{\,rest}_{beam\ 1}$ and $\vec{p}^{\,rest}_{beam\ 2}$ are the momentum vectors of either beams in the rest frame of the J/ψ.

The formalism here shown is described in [42], and was later adapted for use in ALICE's own measurements with inclusive data in [43] and later in [44].

For the J/ψ, the total angular momentum is equal to 1. This means that there are three possible angular momentum states if, in a reference frame, the projection of the angular

momentum on the z-axis is considered. A vector meson such as the J/ψ as shown in Fig. 1.20 decays to a lepton pair.

The angular distribution is shown to be [42, 43, 44]:

$$W(\cos\theta,\varphi) \propto \frac{1}{3+\lambda_\theta} \cdot [1 + \lambda_\theta \cdot \cos^2\theta + \lambda_\varphi \cdot \sin^2\theta \cdot \cos 2\varphi + \lambda_{\theta\varphi} \cdot \sin 2\theta \cos\varphi + \\ + \lambda_\varphi^\perp \cdot \sin^2\theta \cdot \sin 2\varphi + \lambda_{\theta\varphi}^\perp \cdot \sin 2\theta \cdot \sin\varphi] \ , \tag{1.15}$$

with respect to the reference frame of choice, with the angles as shown in Fig. 1.20.

The last two terms may be observed only when the production plane is available, but this is not possible in the inclusive sample [44] or in the photoproduction regime (γ-target reference frame is not readily available). The full distribution is then reduced to:

$$W(\cos\theta,\varphi) \propto \frac{1}{3+\lambda_\theta} \cdot \left[1 + \lambda_\theta \cdot \cos^2\theta + \lambda_\varphi \cdot \sin^2\theta \cdot \cos 2\varphi + \lambda_{\theta\varphi} \cdot \sin 2\theta \cos\varphi\right] \ . \tag{1.16}$$

Chapter 2

ALICE detector at the LHC: an overview

The state-of-the-art collider of the present day is the *Large Hadron Collider* (LHC), situated on the border between Switzerland and France, belonging to the *European Organization for Nuclear Research* (CERN). It is a 27 km circumference collider, with maximum foreseen energies in the centre-of-mass of 14 TeV when colliding protons, although at the moment the highest achieved centre-of-mass energy is 13.6 TeV. The LHC is also able to accelerate nuclei and there have been Pb–Pb, p–Pb, and Xe–Xe runs. Multiple collaborations operate at CERN, of varying size. The four biggest collaborations have built dedicated detectors at four points of the LHC, namely the ALICE, ATLAS, CMS, and LHCb detectors, from which the collaborations derive their names. Fig. 2.1 shows how the four giant experiments are positioned around the LHC. The Super Proton Synchrotron (SPS), which is the last step in the acceleration chain before the LHC, is also shown, hence giving a reference point using which it is possible to understand the orientation of the experiments. In particular, ATLAS is the only experiment on Swiss soil. The LHC is able to accelerate both protons and ions, with different strategies:

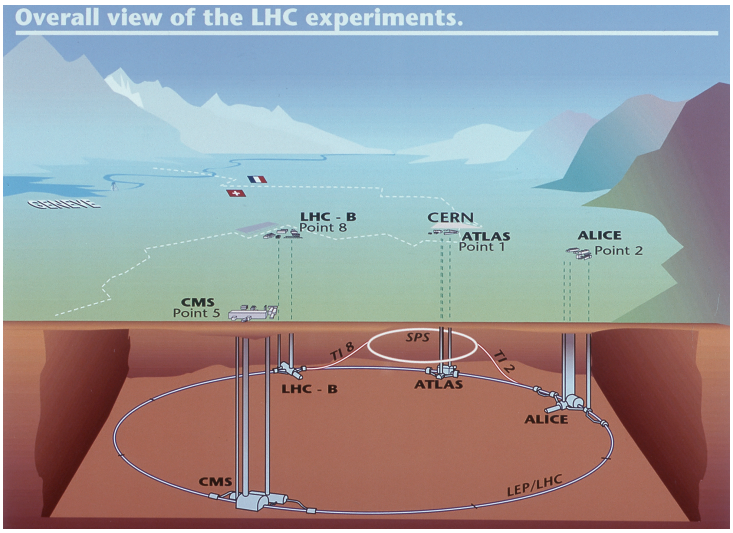


Figure 2.1: Schematic view of the positioning of the four main LHC experiments. They are located underground at varying depths between 50 and 150 metres [15].

- **protons**: they are accelerated by the Linac2 up to 50 MeV, before being sent to the Proton Synchrotron Booster (PSB) where they reach an energy of 1.4 GeV. They are then further accelerated up to 25 GeV by the Proton Synchrotron (PS), before being injected to the SPS where they reach 450 GeV. Finally, the LHC brings them to the target 6.5 GeV (for a centre-of-mass energy of $\sqrt{s} = 13$ TeV as it was in Run 2);

- **ions**: the ions are accelerated to an energy per nucleon of 4.2 MeV in the Linac3, and accumulated in the Low Energy Ion Ring (LEIR) which brings them up to 72 MeV per nucleon. The PS then further accelerates them to 5.9 GeV per nucleon, before being transferred to the SPS where they are accelerated up to 177 GeV per nucleon. Finally, the LHC accelerates them to an energy of 2.76 TeV per nucleon.

The filling scheme followed by the LHC is based on a gap of about 25 ns between two proton packets, also called *bunches*. Each bunch contains a minimum of 5×10^9 [45] to a maximum of 1.15×10^{11} [46] protons. The beams are organised as 39 batches, each with 72 bunches, thus a total of 2808 out of a total bunch structure of 3564 for proton

beams. In the case of Pb runs instead, each bunch contains a minimum of 1.07×10^8 to a maximum of 2.2×10^8 Pb nuclei [47]. The number of bunches is chosen to be 733 in the second half of the 2018 Pb runs when the LHC injectors allowed for a minimum spacing of 75 ns.

2.1 ALICE: A Large Ion Collider Experiment

The ALICE, ATLAS, CMS and LHCb were detectors built with very different purposes: while ATLAS and CMS are general purpose detectors specialising in high p_{T} tracks, LHCb was specially built as a single arm detector to study beauty flavoured hadrons, and finally, ALICE was designed with heavy ions as its main goal. However, the collaborations also embrace a wider physics program, e.g. ATLAS, CMS and LHCb can now probe heavy ion physics.

2.2 The structure of the ALICE detector

The ALICE detector is shown in Fig. 2.2. The detector built by the ALICE Collaboration is the only detector built specifically to study heavy ion collisions, with excellent particle identification capabilities. The peculiarity of heavy ion collisions lies in the extreme particle multiplicities that may be generated in central collisions[1]. Prior to LHC startup, particle multiplicities for central collisions per unit of rapidity, $\frac{dN}{d\eta}$, were estimated to range between 2000 and 8000 charged particles. The ALICE detector was designed to target a $\frac{dN}{d\eta} \sim 4000$ [48].

[1]Heavy ions are extended objects. As such, it is possible to define a degree of centrality of the collision. The more "head-on" the collision, the more central it is. In more central collisions all the nucleons take part to the event, while in peripheral collisions there are quite a few spectator nucleons i.e. nucleons that do not participate to the event and continue along with the beams.

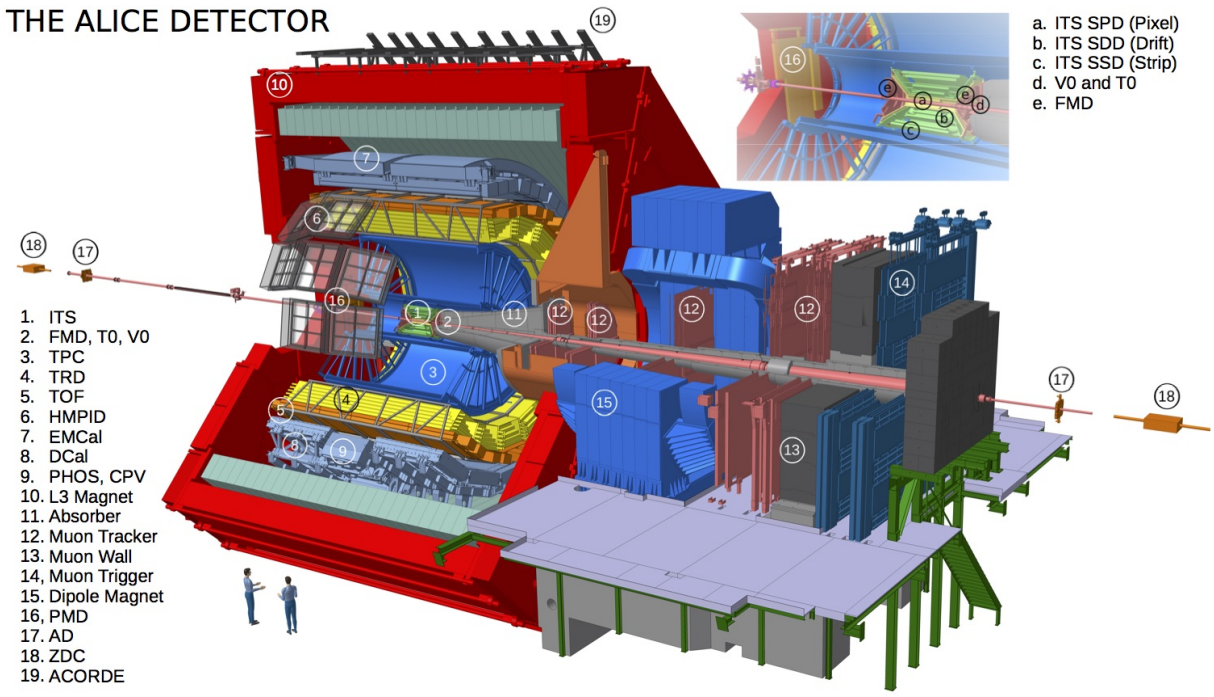


Figure 2.2: The ALICE Run 2 detector is shown in all of its components and subdetectors. Human figures are also shown to give an idea of the size.

The ALICE detector, a $16 \times 16 \times 26$ m^3 detector, is composed of eighteen subdetectors, most of which can run in either stand-alone mode or as a whole, together with the Central Trigger Processor (CTP), which acts as the brain of the whole detector and governs its operations. It is possible to classify the subdetectors as belonging to three different groups, namely the *central barrel*, *muon spectrometer*, and *forward* detectors.

2.2.1 Central barrel

The central barrel detectors give access to the pseudorapidity η region $-0.9 < \eta < 0.9$. It is possible to alternatively describe them as the detectors enclosed in the solenoid magnet, which is normally set to provide a 0.5 T magnetic field; the magnetic field has also been previously set to lower settings e.g. during the Xe–Xe data taking period at 0.2 T, thus providing an opportunity to explore lower p_{T} regions.

They can be listed:

- **ITS**, *Inner Tracking System*: the ITS is the closest detector to the beam pipe [49, 50]. It is made up of six layers, or three subdetectors, Silicon Pixel Detector (SPD), Silicon Drift Detector (SDD), and Silicon Strip Detector (SSD), each comprising two consecutive layers. It covers the pseudorapidity range $|\eta| < 0.9$. Its main tasks include the identification of primary and secondary vertices, caused by e.g. decays of B mesons, while also allowing for a certain degree of particle identification capability. It is crucial for particles with transverse momentum less than 100 MeV, since these particles would not be able to reach the subsequent detector, the Time Projection Chamber (TPC). The SPD is formed by the two layers closest to the beam pipe. It is made up of about 10^7 cells [51], needed to achieve the granularity needed to cope with a track density of about 90 cm^{-2}. Each cell measures 425 μm $\times$ 50 μm in size. The SDD and the SSD are instead finely segmented in one direction only. The former uses the drift time of the charge induced by the particles to determine the position in the coarsely segmented direction, taking advantage of the low rates of heavy-ion collisions. The SDD achieves spatial resolutions better than 50 μm. The latter, being at the outer edge of the ITS, has to cope with lower track densities of less than 1 cm^{-2}. It is a double sided detector, allowing for a two-dimensional assessment of the position of the track. Its main task is to allow for the correct propagation of the tracks from the ITS to the TPC;

- **TPC**, *Time Projection Chamber*: the TPC is perhaps the single most important detector of the ALICE detector [52]. Its tasks are to reconstruct the trajectory of charged particles and to measure their momentum, while also performing particle identification. It covers the pseudorapidity range $|\eta| < 0.9$ for tracks with full radial length[2], while also allowing for an acceptance up to $|\eta| < 1.5$ for reduced track length instead. It follows the ITS in radial development from the beam pipe. It is

[2]Tracks which were also reconstructed in ITS, TRD and TOF detectors

cylindrical in shape, with inner and outer radii of about 85 and 250 cm, respectively, with a length of about 5 m in the longitudinal direction. It is divided in two by its central cathode. Electrons produced by the ionisation of the charged particles are drifted for at most 2.5 m towards the closest end plate by a uniform electric field of 400 V/cm, where the central cathode provides a voltage of 100 kV, with a maximum drift time of about 90 μs. The end plates are divided into 18 sectors, each covered in multi-wire proportional chambers (MWPC) with cathode pad readout. The TPC manages to cover a wide range in p_{T} from about 0.1 GeV/c to about 100 GeV/c, and achieves a momentum resolution better than 1% for particles with transverse momenta in the range $0.2 < p_{\mathrm{T}} < 1$ GeV/c, and better than 5% for particles with transverse momenta less than 10 GeV/c;

- **TRD**, *Transition Radiation Detector*: its main task is to provide identification for electrons with momenta above a 1 GeV/c threshold. It also serves as a way to correct for distortions of charged particle tracks in the TPC (since Run 2) [53]. The TRD has full acceptance in the azimuthal angle, and it covers the pseudorapidity range $|\eta| < 0.84$. It is located at a radial distance of 2.90 m up to 3.68 m from the beam pipe. The detector is made up of 522 chambers, each composed of a radiator, a drift region of 3 cm filled with a Xe/CO_2 mixture, and a MWPC. The chambers are then arranged in eighteen sectors, each containing thirty chambers, further arranged in five stacks along the longitudinal direction and six layers in the radial coordinate, for an overall length along z of about 7.8 m. With the addition of the TRD, the overall transverse momentum resolution of charged particle tracks is measured to be better than 5% up to $p_{\mathrm{T}} \sim 100$ GeV/c;

- **TOF**, *Time-Of-Flight*: its main tasks are to provide particle identification capabilities for pions, kaons and protons in the momentum range from about 0.5 GeV/c up to about 2.5 GeV/c for π/K, and up to 4 GeV/c for protons [54, 55] by measuring their Time-Of-Flight with respect to the collision time (also provided by the

TOF system itself), and to provide a trigger for Cosmic Rays. It is a cylindrical array with internal radius of about 3.90 m from the beam pipe, and a coverage in pseudorapidity $|\eta| < 0.9$. It is made up of 1593 Multigap Resistive Plate Chambers (MRPC), each consisting of two stacks with five gaps. The MRPCs are arranged in eighteen sectors in azimuth. The timing resolution of the TOF during Run 2 was measured to be about 56 ps [56];

- **HMPID**, *High-Momentum Particle Identification Detector*: a single arm proximity focusing Ring Imaging Cherenkov (RICH) with a limited angular acceptance, which aims to expand the momentum range for π, K, and p identification;

- **PHOS**, *PHOton Spectrometer* and **EMCAL**, *ElectroMagnetic CALorimeter*: electromagnetic calorimeters, each with a limited acceptance of about 100° and 107° in azimuthal coverage, respectively. PHOS modules are made up of a Charged Particle Veto (CPV) and a calorimeter consisting of lead-tungstate crystals, while EMCAL modules are lead-scintillator sampling calorimeters. They are positioned opposite to each other, with EMCAL towards the upper part of ALICE, and PHOS at the bottom;

- **ACORDE**, *ALICE COsmic Ray DEtector*: an array of sixty plastic scintillator modules, serving as a cosmic ray detector, installed externally to the magnet.

2.2.2 Muon spectrometer

The ultimate goal of the Forward Muon Spectrometer is to provide sensitivity to vector mesons such as charmonium and bottomonium states via their decay to muons. It allows the study of quarkonia production in the pseudorapidity region $-4 < \eta < -2.5$ down to very low p_{T} [57, 58], as will be explained further in the analysis chapters in the following sections of this thesis. The main components of the Forward Muon Spectrometer are the

following:

- **Absorbers**, there are three: the *front absorber*, the *beam shield* and the *muon filter*. The front absorber is located at 90 cm from the interaction point to stop the remaining hadronic radiation at forward rapidity, while also stopping potential backscattering to the central barrel detectors. It has a length of 4 m, and is essentially divided into three parts, namely a central cone, an inner and an outer shield. The central cone is made of low atomic number materials such as carbon and concrete to limit multiple scattering for the part closest to the interaction point, while the part closest to the spectrometer is made of lead and tungsten to limit the backscattering and to avoid secondaries produced by the absorber itself. The inner and outer shields are also made of high atomic number materials. The materials that constitute the beam shield are again lead and tungsten, and steel. It surrounds the beam pipe, shielding the spectrometer from secondary particles and particles produced at very forward rapidity. Finally, the role of the muon filter (also called *iron wall*) is to shield the trigger chambers of the Forward Muon Spectrometer from any hadronic background. It is hence positioned at around 15 m from the interaction point, between the tracking and the trigger chambers;

- **Dipole**, needed to provide a way to measure the momenta of the single muons and to also assess their charge, it is a dipole with a magnetic field of 0.7 T, for an overall field integral of 3 T·m [59, 60];

- **Muon Tracker**, a system of five stations with two planes of MWPC each with cathode pad readout, for a total of ten detection planes. As shown in Fig. 2.3, the first two stations are located between the front absorber and the dipole, the middle station is positioned inside the dipole, and the remaining two are positioned after the dipole but before the muon filter;

- **Muon Trigger**, which selects those events which contain muons from decays[3]. It comprises two trigger stations, each with two layers of eighteen Resistive Plate Chambers (RPC) each. They have a time resolution better than 2 ns, enabling a fast trigger decision in less than 700 ns, which contributes to the generation of the L0 trigger.

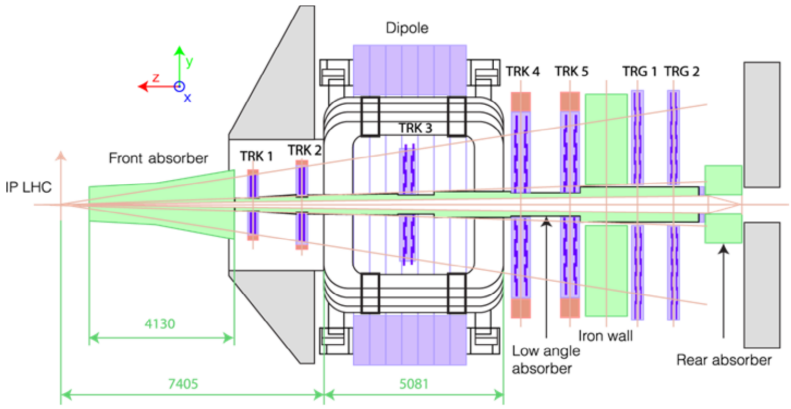


Figure 2.3: Schematic view of the ALICE Forward Muon Spectrometer. Picture taken from [16].

The trigger chambers are able to select an interesting event containing either a single muon or a dimuon above a p_{T} threshold, in less than 700 ns. For any single or double hit on the readout strips on the first trigger station, the readout collects the signals on a restricted region of the hypothetical track along the bending plane. A first condition for the track is then the presence of hits in the allowed region on at least three out of four of the trigger layers. Then, the retrieved topology is compared to Look-Up Tables (LUT), which are constructed with a simulation of the muon tracks with a realistic description of the Muon Spectrometer. Afterwards a final decision is made for five possible trigger inputs for the Central Trigger Processor, e.g. a single low p_{T} muon [61].

[3]The typical forward UPC trigger for ALICE consists of either a single muon input signal or the presence of a dimuon, along with vetoes from other detectors.

The default algorithm for offline track reconstruction with the Forward Muon Spectrometer is the Kalman Filter [58], with seed in the last station of the tracking chambers (radially from the nominal interation vertex). The algorithm starts by connecting clusters on the last two stations, before being then propagated back to the interaction point to provide a first estimate on the momenta. Only tracks with momenta above 3 GeV/c and below 3 TeV/c are accepted for a second step of the algorithm. In this second step the Kalman Filter procedure is applied to find and fit the track. Finally, in a third step, the tracks are propagated to the interaction point, and they can optionally be corrected for multiple scattering effects in the absorber.

The p_{T} resolution on the single muon tracks is estimated to be better than 3% in the range $2 \sim p_{\mathrm{T}} < 60$ GeV/c, the invariant mass resolution in the case of the J/ψ, by also correcting for multiple scattering of the single muons, is estimated to be better than 80 MeV/c^2 up to a transverse momentum of the J/ψ of about 3 GeV/c [62].

2.2.3 Forward detectors

Lastly, the forward detectors. These are smaller in size compared to the others, and the reason they are called *forward detectors* is that they are either very close to the beam pipe, or very forward pseudorapidity acceptances. They have the most disparate uses, and thus, their role has to be examined case by case. They are the following:

- **T0**, two arrays consisting of twelve Cherenkov counters each, which can provide an alternative collision time that can be used in conjuction with the TOF;
- **VZERO**: two arrays of scintillator counters V0A and V0C, positioned at 340 cm from the centre of ALICE on the A side and on the front face of the Muon Absorber on the C side (90 cm from the interaction point), respectively. Each of them is composed of 32 elements altogether, divided into four rings of eight elements each,

of varying size in order to have a uniform coverage in terms of pseudorapidity. The voltage of each element is chosen as to have 15 counts of the 12-bit Analog-to-Digital Converter (ADC) for a Minimum Ionising Particle (MIP) in pp collisions, which corresponds to 2 kV in pp, while it is set to 1.5 kV for Pb–Pb collisions owing to the much higher multiplicities [63]. V0A covers the range in pseudorapidity $2.8 < \eta < 5.1$ while V0C covers $-3.7 < \eta < -1.7$ instead. They are used to select Minimum Bias events by adjusting the timing window of the ADC counts to a beam-beam timing. Their use is specialised in UPCs, as V0A can and is used as a valid veto for online triggers, while V0C has a similar coverage as the Muon Spectrometer, and thus, it can complement the muon detection capabilities of the Spectrometer in actual analyses;

- **AD**, *ALICE Diffractive Detector* [64]: two arrays of four sectors each of scintillator pads, positioned on both sides of ALICE, with pseudorapidity acceptances $-6.9 < \eta < -4.9$ (ADC, located at about 19 m on the C side) and $4.7 < \eta < 6.3$ (ADA, located at about 17.5 m on the A side). They have a time resolution better than 0.5 ns [65]. Used extensively as vetoes for UPC data taking;

- **FMD**, *Forward Multiplicity Detector*: five rings of silicon strip detectors, which extend the measurement of charged particle multiplicity with the pseudorapidity ranges $-3.4 < \eta < -1.7$ (one ring) and $1.7 < \eta < 5$ (four rings);

- **PMD**, *Photon Multiplicity Detector*: two detection planes with twentyfour modules each. Each module is made up of 576 hexagonal proportional chambers [66], to measure photon multiplicity in the pseudorapidity range $2.3 < \eta < 3.7$;

- **ZDC**, *Zero Degree Calorimeter*: there are three sets of ZDC calorimeters in ALICE, two sets positioned symmetrically at either side of the detector at approximately 116 m, and the third only on the side opposite the Muon Spectrometer. Fig. 2.4 shows the schematic view of the A side of the ZDC calorimeters i.e. the side opposite

the Muon Spectrometer. The former two sets are the neutron and proton ZDC, respectively. The remaining set of calorimeters constitutes the ZEM detector, which is mainly used as an internal evaluation of the event centrality by the ZDC system.

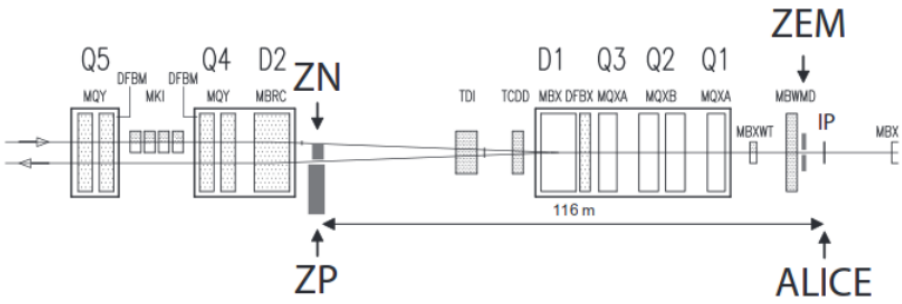


Figure 2.4: Schematic view of the ZDC calorimeters positioned on the side of ALICE opposite the Muon Spectrometer. The neutron and proton ZDC are shown with the spatial separation due to the magnetic field protons are sensitive to. The ZEM is also shown.

As can be appreciated from Fig. 2.4, the neutron and proton ZDCs are spatially separated as the design had to account for the deflection of protons by the magnets in the beam. Neutrons in particular manage to produce very clean signals in these detectors. The case can be further specialised to ultraperipheral collisions, where the very clean signals due to the minimal physical background give rise to peaks clearly due to one, two and three emitted neutrons. Fig. 2.5 shows the case for ρ^0 photoproduction in Pb–Pb UPC. The plot shows the neutron ZDC energy on the A side of ALICE, opposite the Muon Spectrometer, against the energy contained in the C side. The energies are grouped at multiples of half the nominal centre-of-mass energy per nucleon pair i.e. 2.51 TeV, which is the energy that each nucleon is expected to carry. As anticipated, peaks due to no, one, two and a hint of three emitted neutrons can be observed.

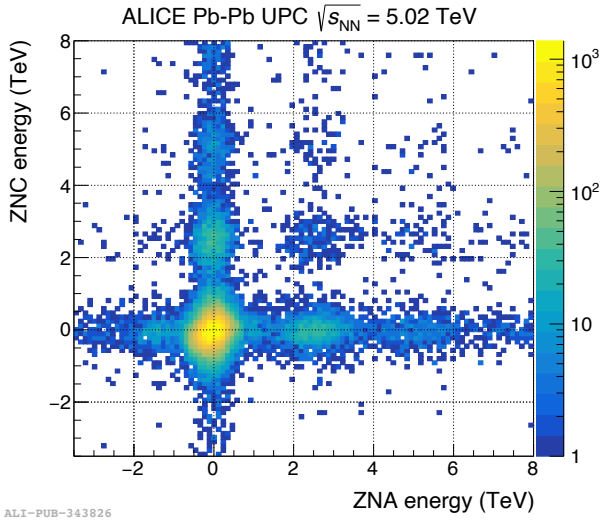


Figure 2.5: ZDC energy spectra with midrapidity ρ^0 ALICE Pb–Pb UPC data. It is possible to distinguish clearly peaks due to neutrons being emitted on either side of the neutron ZDC. The energies clearly construct structures around the nominal energy carried by each nucleon i.e. 2.51 TeV.

2.3 The ALICE Trigger and DAQ System

The ALICE Trigger System, operational during Run 1 and 2, aims to deliver both trigger and timing information to the subdetectors of the ALICE detector. It is made up of a single Central Trigger Processor (CTP), and 24 Local Trigger Units (LTU), one for each subdetector [67].

The CTP itself is made up of eleven 6U VME boards. It operates on a four trigger level logic during LHC Run 1 and 2. It distributes LM, L0, L1, and L2 signals to the detectors. The four trigger levels have different latencies: 650 ns for LM - a wake-up trigger sent only to the TRD -, 900 ns for L0, 6.5 μs for L1 , and 88 μs for L2 [67]. The L0 and L1 triggers are sent via Channel A of the Trigger and Timing Control (TTC) system [68], while additional L1 related bits are sent via Channel B of the TTC system. L2 triggers

are also sent via Channel B, with their delay of 88 μs driven by past-future protection of the TPC.

The connection of the CTP to the Front End Electronics (FEE) of the single detectors is effected by means of the LTUs, which can also emulate the behaviour of the CTP protocol, thus allowing for a stand-alone mode of the subdetectors, decoupled from the entire ALICE detector. While in global mode with the rest of the system, LTUs handle the signals from the CTP, and they also send the L0 triggers to the subdetectors via LVDS cables, and L1 and L2 triggers via the TTC system. The LTUs can also send L0 triggers via the TTC system.

The CTP logic identifies fifty *physics trigger classes* and six *clusters*. A class is formed by a logical AND of subsets of the trigger inputs, which can also be negated[4]. The classes are then passed to the corresponding clusters, which are groups of detectors which are triggered together and are then characterised by similar read out timing. Each class is associated to a single cluster, but a single cluster can be associated to multiple classes. There are also overlapping clusters, since a subdetector can be shared among multiple clusters.

After the FEEs receive the relevant triggers from the LTUs, they communicate via the Detector Data Links (DDL) with the DAQ Readout Receiver Cards (D-RORC), hosted by the Local Data Concentrators (LDC). A single LDC can host multiple D-RORC. The LDCs start to assemble the fragments of the event sent by the FEEs via the DDLs into a sub-event. The LDCs then send each sub-event to the Global Data Collectors (GDC), where the final assembly of the event is carried out. The event data are finally sent to the Transient Data Storage (TDS) [69].

[4]This is used to enforce a veto instead.

Chapter 3

Central Trigger System for LHC Run 3

The ALICE Central Trigger System (CTS) went through a major upgrade during Long Shutdown 2, in preparation for LHC Run 3. It is based on three trigger levels, LM - for the TRD only -, L0, and L1, which will be used for triggered data-taking mode, owing especially to those few detectors that did not undergo an upgrade of the readout system, i.e. CPV, PHOS, TRD, EMC, HMPID, whereas all the remaining detectors do not necessitate a trigger. It also enables a continuous data-taking mode. Thus, the main functionality of the CTS is not to provide selectivity for interesting events, but to distribute the time of each interaction. It will provide the LHC clock, which is about 40 MHz, with each bunch crossing being 25 ns apart from the next. It will provide *Heartbeat* (HB) triggers to detectors in continuous mode for synchronisation purposes, where each Heartbeat trigger corresponds to a time length of 3564 bunch crossings, which will also be called *orbit* in the following[1].

The new CTS is comprised of one Central Trigger Processor (CTP) board, distributing clocks and triggers, and eighteen Local Trigger Unit (LTU) boards. Similarly to Run

[1]The Heartbeat is an arbitrary measure which can be set to a programmable multiple of the orbit. At present, and to the best of the knowledge of the author, Heartbeat is equal to orbit.

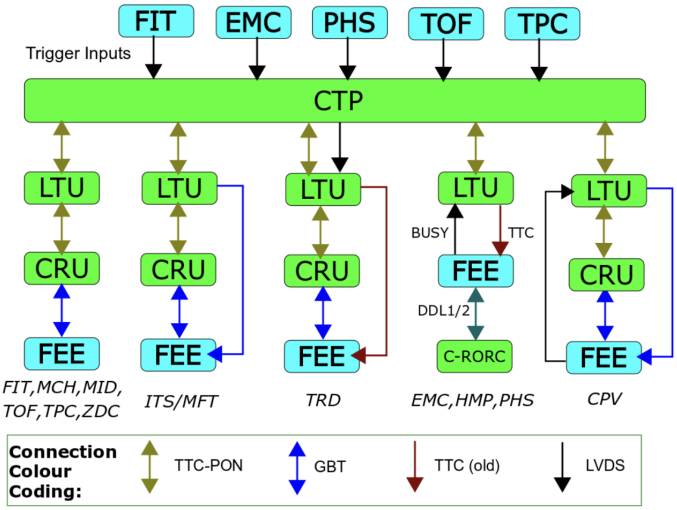


Figure 3.1: Overview of the ALICE Central Trigger System, taken from [17]. The connections between CTP, LTUs, CRUs, FEEs are shown, along with the different types of connections available.

1 and 2, LTUs can be decoupled from the CTP and operate in stand-alone mode, and the LTUs can then function as a CTP since they implement a CTP emulator. The connection between LTUs and detectors that are upgrading their Front End Electronics (FEE) is effected by means of a Common Readout Unit (CRU) card, via a Passive Optical Network (PON). The latter is implemented using a Optical Line Terminal (OLT) acting as a transmitter, and a Optical Network Unit (ONU) acting as a receiver, allowing for up to 9.6 Gbps of data transmission. OLTs and ONUs can act as both transmitters and receivers, but the communication in the opposite way (upstream) is limited to 2.4 Gbps. Finally, the FEEs are connected to the CRUs via GigaBit Transceivers (GBT), which allow bidirectional transmission of data. An overview of the CTS during Run 3 is shown in Fig. 3.1. The CTP board also has a direct connection to a CRU via GBTs, where trigger classes and trigger inputs are sent for bookkeeping.

The design of the ALICE Trigger Boards that will be used throughout Run 3 and 4 is shown in Fig. 3.2. The boards are 6U VME boards, using the VME backplane only as a

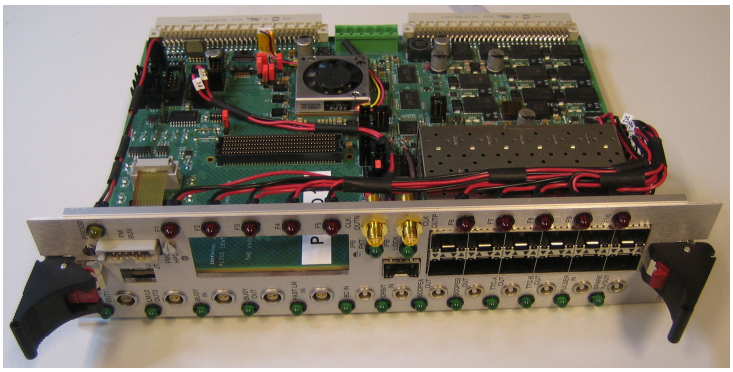


Figure 3.2: The ALICE Trigger Board prototype. The SFP cage is located on the right, the FMC channels are located on the left.

power supply. They are equipped with FPGA Ultrascale Kintex, with a slight difference in models between CTP and LTU boards due to the different demands in project sizes (CTP logic has to handle more operations than the LTU's), the former using XCKU060-2FFVA1156E, and the latter XCKU040-2FFVA1156E. They are also equipped with two 1 GB DDR4 memories, used for monitoring purposes. The boards themselves otherwise show no apparent difference between CTP and LTU versions: both feature a two-fold Small Form-factor Pluggable transceiver (SFP+) cage (on the right of Fig. 3.2), a single-fold SFP (in the centre of Fig. 3.2), and the FPGA Mezzanine Card (FMC) port which grants the boards the concept of *universality/versatility* [17, 70]. A module may in fact be plugged onto the FMC port, thus effectively repurposing the board itself: the CTP board may be equipped with a FMC-CTP card - the running condition for data-taking purposes - or equipped with a FMC-S18 card, which grants it an additional eight SFP channels. The boards can then deal with either 12 or 20 SFP channels, depending on whether the FMC-S18 card is used or not. A single cage of SFP is however always dedicated to the IPbus, thus allowing for both monitoring and configuration of the boards. Alternatively, a LTU board may be equipped with e.g. a FMC-TTC card, as shown in Sec. 3.1.

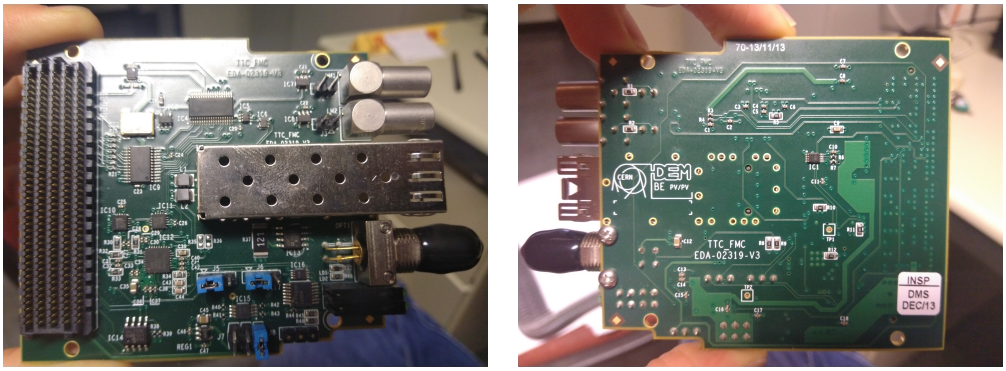
3.1 TTCit: TTC Interface Test board

The TTCit - TTC Interface Test board - monitors the data traffic sent from the CTP (situated in the ALICE pit) to the LTUs for the detectors, through optical fibres. In particular, TTCit follows the transit of the L0, L1, and *Long L1 messages* (LL1) to the ALICE subdetectors which have not undergone an upgrade process in the passage from Run 2 [71] to Run 3 i.e. TOF, HMPID, PHOS, CPV, and TRD. The way it works is that TTCit effectively emulates a subdetector LTU, and it is likewise connected via optical fibres, as will be shown in the following. TTCit reimplements the original TTCrx [72, 73] protocol in FPGA. The author was tasked with the integration of the hardware developed by CERN with the ALICE CTS system, and the development of the dedicated firmware, starting from a core implementing the TTCrx protocol, which is provided to all collaborations using this hardware.

3.1.1 Dedicated hardware

Two boards are dedicated to the development of the related firmware, `ATBP_7` and `ATBP_8` in ALICE nomenclature, so as to say the *ALICE trigger boards prototypes* number 7 and 8, respectively. They have a Kintex Ultrascale XCKU040-1FFVA1156C, the lowest grade of boards the CTP team has at its disposal, due to the very small size of this project. The peculiarity of the trigger boards ALICE is about to use in the Run 3, is their *universality*, as already stressed in this document. This is all due to the HPC connector that accompanies each LTU or CTP board, as each board may be repurposed simply by swapping the additional module which is connected to the HPC connector. This choice was crucial even for the TTCit project, as it turns out that optical fibres can be connected to the TTC-FMC card designed by the CERN Engineering Department [74], which receives the optical signal and does preliminary analysis of the raw signal before it

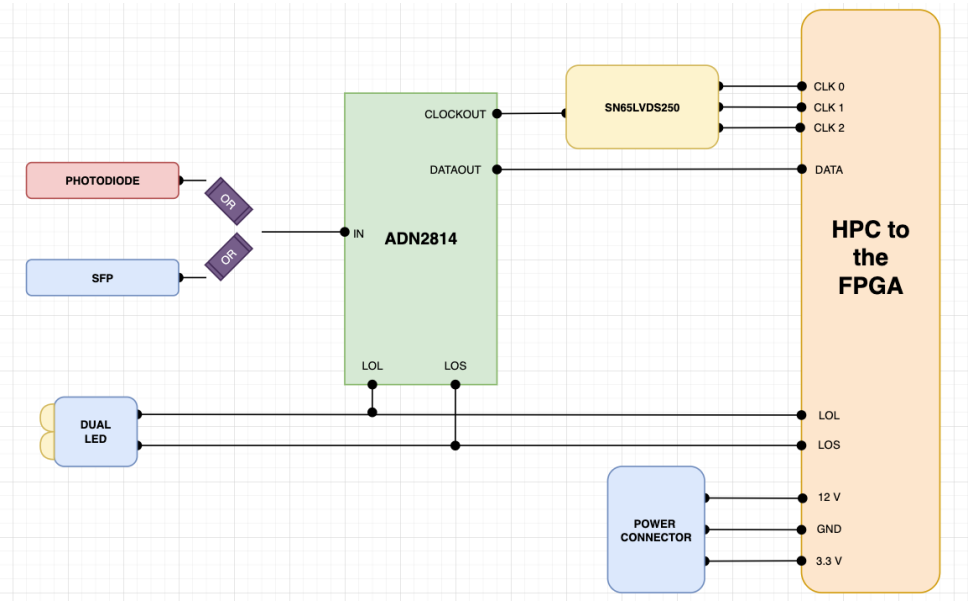
is sent to the FPGA for further processing and decoding. Fig. 3.3(a) and 3.3(b) show the front and the back of the TTC-FMC card, respectively.



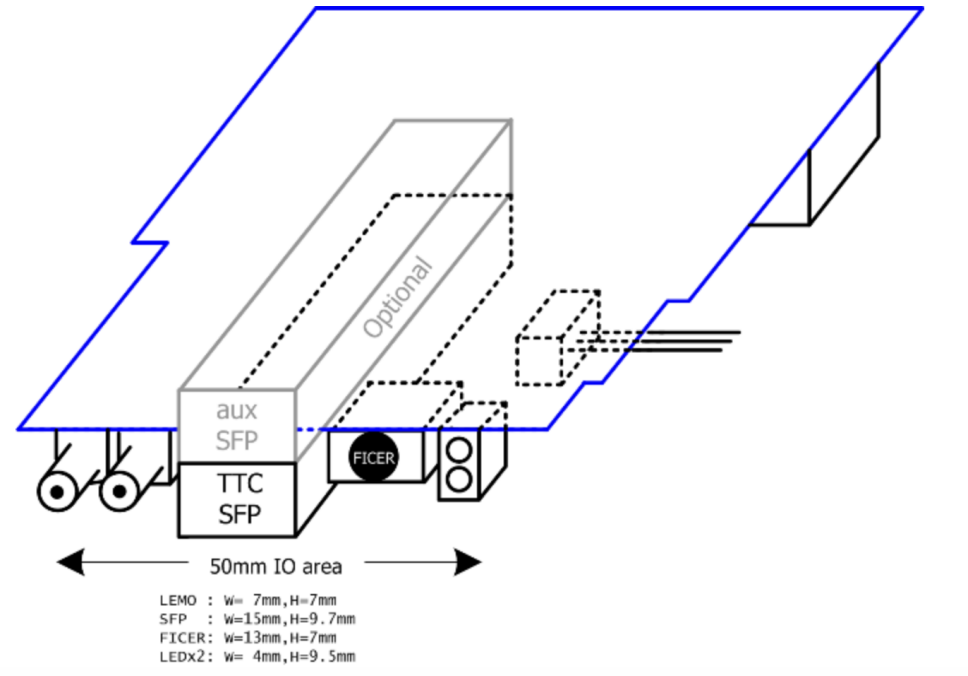
(a) (b)

Figure 3.3: Fig. 3.3(a) and 3.3(b) show the front and back of the TTC-FMC card, respectively. The TTC-FMC card is then attached to the HPC connectors of both prototype boards. The important elements needed for the extrapolation of the signals and the data transmission can be singled out. In particular, the plug for the optical fibre is covered for protection, and the CDR chip is also quite visible (IC9 in fig. 3.3(a)).

The main components for input and output of signals from the TTC-FMC card can be seen in Fig. 3.4(a) and 3.4(b), and also the first signal processing components. In particular, Fig. 3.4(a) shows how the sole photodiode (optical fibres connected) can drive the entire logic. The element `ADN2814` [75] makes a first decomposition of the signal (*CDR*, *Clock Data Recovery*), singling out the clocks and the data to be sent to the FPGA. The choice of the clock to be sent to the FPGA is made by choosing the output of the cross switch `SN65LVDS250` [76] by means of a logical multiplexer.



(a)



(b)

Figure 3.4: Fig. 3.4(a) and 3.4(b) show the block diagram and scheme of the TTC-FMC card used in the TTCit development, respectively. The former shows which paths the signals have to travel on the TTC-FMC card up to the HPC connector, while the latter better displays the actual size of the card.

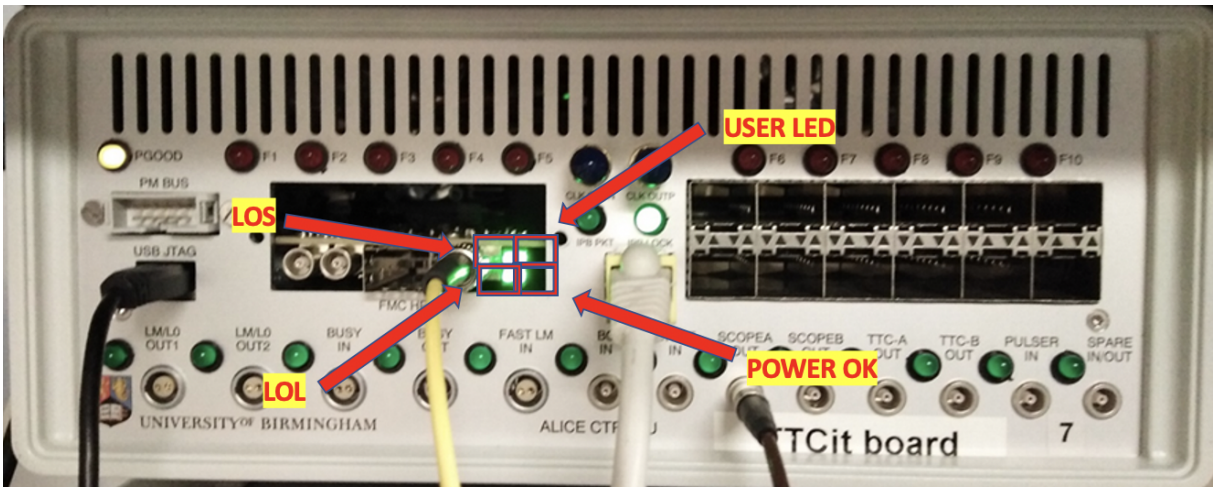


Figure 3.5: The fully assembled prototype board dedicated to the TTCit development. The LEDs and their meaning are also shown.

Once all the connections have been verified and the output of each component of the card was properly understood and set e.g. crosspoint switch, the TTC-FMC cards could be mounted to the respective boards before the final assembly of the front panels. The final result for `ATBP_7`, is shown in Fig. 3.5. It is mounted inside a standalone box. This way the board can easily be deployed to other setups, as it would come shipped with its own power supply. The great advantage of having a TTCit system is that firmware development happens concurrently together with the development for other detector subsystems. These subsystems depend, to a certain degree, on the CTP firmware. If a malfunction or unexpected feature is discovered, it could either be a bug on the subsystem's side or, on the CTP side. If the TTCit manages to see the right signals in the CTP setup, while it fails to detect intelligible signals on other setups, it would provide a guideline for firmware fixes and further developments. The TTCit also serves as a validation tool for the trigger sequences of both CTP and LTU boards, depending on whether global or standalone modes are tested.

The TTCit is equipped with a set of LEDs to help the user in understanding when the behaviour caught by the firmware is reflecting the real signals seen by the firmware. Fig. 3.5

shows the meaning of the LEDs attached to the TTC-FMC card. In fact, Fig. 3.4(a) already provided the hint of the existence of four LEDs. Two of them indicate the *loss of signal* (LOS) and a *loss of lock* (LOL), which are derived signals from the CDR chip, one is related to the power delivery system of the TTC-FMC card, and hence, of the board itself. The last LED is user defined. The meaning that the group has agreed upon is that the LED is turned on to indicate that TTCit is able to take the signal via optical fibre.

3.1.2 A brief description of the firmware

The author was involved in two firmware development projects. The first of the firmware tasks undertaken by the author was to develop the TTCit firmware. The main tasks of TTCit are to interpret L0, L1 and LL1 messages (LM, L0, and calibration signals in case TRD mode is invoked, where LM and L0 signals have the same structure). To do so, the block structure shown in Fig. 3.6 was implemented. The CTP emulator is sending L0s, L1s and LL1 messages via optical fibre to TTCit. The FPGA interprets the received signal: if it detects a L0, a L1, or a calibration signal, it starts the *Ch A* (channel A) procedure, *Ch B* (channel B) otherwise. The way it interprets the Ch A signals, is that it counts how many consecutive bunch crossing (BC) pulses wide the signal is. In fact, L0, L1, calibration signals correspond to 1-, 2-, 3-BC wide pulses. As shown in Fig. 3.7, the procedure TTCit uses to identify the proper L0, L1 and calibration signals, is by assigning the Ch A signal to flip flops (which will be referred to below as `q`, `qq` and `qqq`) in the VHDL meaning of it. This operatively means that the signal in Ch A is delayed by one, two and three clock cycles, and assigned to the corresponding signal, namely `q`, `qq` and `qqq`. By direct comparison with the schematics shown in Fig. 3.7, it is then quite straightforward to raise a calibration signal, when, at any instance of the clock of the firmware, `qqq`, `qq` and `q` are all active (calibration signal is a 3-BC wide pulse), L1 if `qq` and `q` are both high (L1 and calibration signals are mutually exclusive i.e. if the firmware is running in calibration mode

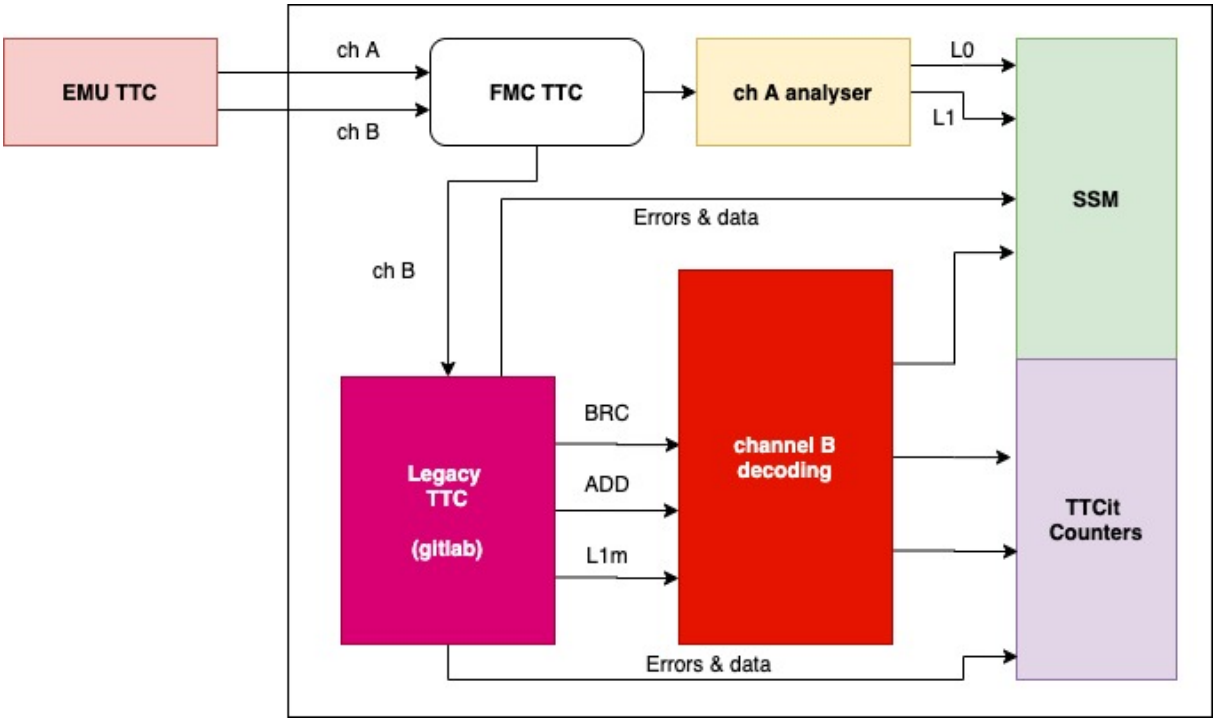


Figure 3.6: The block structure of TTCit. The signal is trasmitted by EMU TTC via optical fibre to the TTC-FMC card. Here the two channels A and B are separated. Ch A can be analysed by assessing the time duration of the signals seen by the firmware. Ch B has to be decoded separately, as the message is sent over via multiple words. All the decoded signals are then registered and sent to dedicated counters.

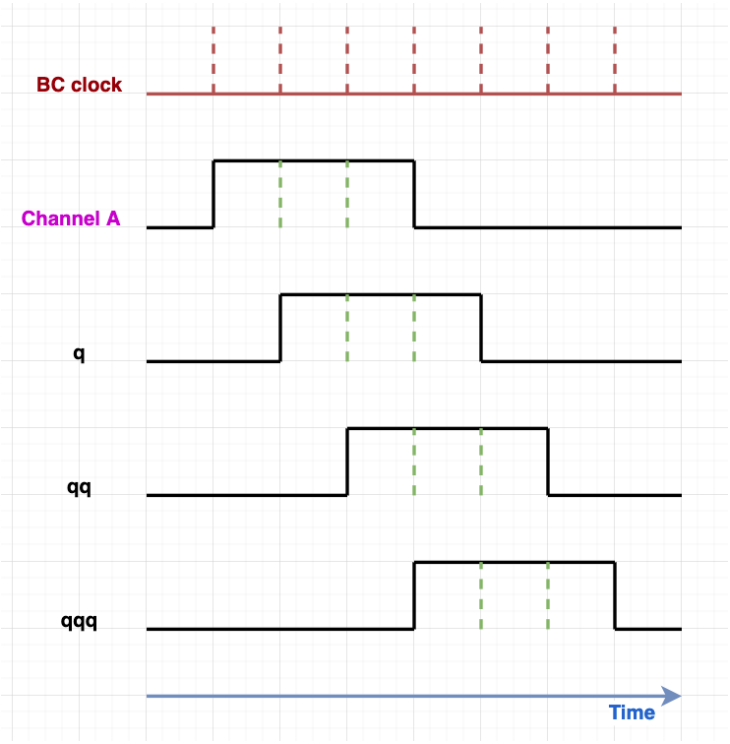


Figure 3.7: Working scheme of how TTCit is able to properly identify the signals over channel A. L0, L1, and calibration signals are 1-, 2-, 3-BC wide pulses. By assigning the Ch A signal to consecutive flip flops it is possible to assess the time duration as integer BC units by simply comparing the signals from the flip flops. As an example, only calibration signals can be high for three consecutive shifts, i.e. `qqq`, `qq` and `q` are all active.

no L1 trigger is sent and viceversa), L0 otherwise. The LL1 messages are sent instead to a piece of dedicated firmware, *Legacy TTC*, which further arranges the LL1 strings before being interpreted by the decoding procedure[2]. The different types of LL1 messages are shown in Fig. 3.8. The two types are: *broadcast commands* (BRC), which have a `00` header to differentiate them from *individually addressed commands* (ADD), which have a `01` header instead. BRC messages are the shorter of the two types, containing essentially only eight bits, with five additionally bits to account for transmission errors and parity checks (a Hamming code, called CHCK in Fig. 3.8). The ADD messages instead, have to be able to address individual subdetectors. They require a fourteen-bit long string for the address, which is followed by a fixed mid-header, `E1`, sixteen bits for data and seven to account for errors (Hamming code). The meaning of the eight bits of data carried by a BRC message is the following: the first two are the resets for the bunch counter and the event counter, then *heart beat*, *heart beat reject*, *time frame*, *prepulse*, and finally, two dedicated user message bits, which are currently unassigned.

The LL1 messages come in seven consecutive words of ADD messages, and are asynchronous with BRC messages. It is then imperative to keep track of how many have been received by TTCit to be able to decode their meaning properly. They carry, 32 bits of *Trigger Types*, 32 bits of orbit identifier, twelve bits of bunch crossing identifier, to be able to properly match them to a previously sent L1 trigger. The TTCit is able to recognise the first of the seven words because it carries a `0001` header, while all the others have a `0010` instead.

[2]The Legacy TTC is a piece of firmware provided centrally by the CERN Engineering department to ease the deployment of its own TTC-FMC cards among the experiments. It emulates the behaviour of the TTCrx chip. It decodes Ch B before any interpretation of the signal is provided according to the requirements of each development team.

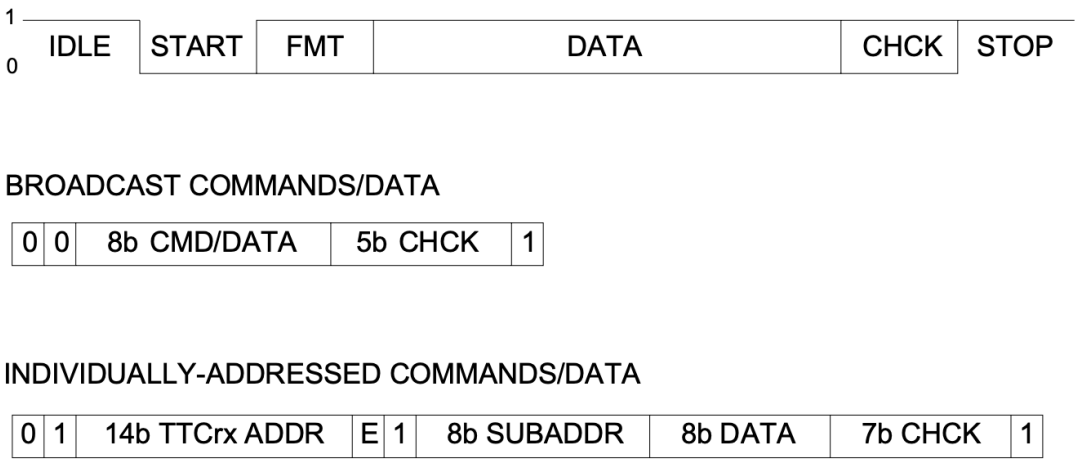


Figure 3.8: The data format of LL1 messages as received by TTCit. The BRC messages contain eight bits of data and five bits of Hamming code, needed for checks over the transmission quality. The ADD messages are longer, needing fourteen bit strings to address single detectors, and contain sixteen bits of data and seven of Hamming code.

3.1.3 TTCit: validation tools

The system has a variety of user friendly tools to cross check the quality of the incoming data and for debugging of TTCit itself. They are obviously very useful in also checking the health of the transmission, and the status of all detectors.

Fig. 3.9 shows one of the functions of the TTCit. This makes use of the first of the two main tools, the *snapshot memory* (SSM). It records the signals TTCit receives in a given amount of time. Usually the SSM is asked to record either one second, or 100 ms, and the maximum length of time it can record is 67108864 BCs (about 1.67 s). This is useful as it is possible to relate the output directly to the settings of the board that is sending the data over the optical fibres. As a working example, it is possible to ask a temporal separation between a L1 and a successive L0 signal to protect the event that is in the pipeline. If so, then the SSM should show this separation between the signals. The way it

works then is to read a certain amount of words the SSM had recorded. The CTP team has decided on a certain format to make full use of the 128 bits SSM is composed of.

Fig. 3.9 shows an example of this. The first bit is the so called *SSM Flag*, *F*, which is high only when a full LL1 message has been recorded and interpreted. The following twelve bits account for the bunch crossing identifier, then 32 bits for orbit identifier. The following 32 display the Trigger Types. The configuration shown in Fig. 3.9 represents a working example. The labels A and 1 correspond to L1 and Ch A signals, respectively. To complement the flag *F*, the *S* bit is also raised upon each successful reception of a LL1 message word. The meaning of each bit assigned to the SSM is also shown in Appendix B.

The second set of tools available in TTCit is the raw counters. They can be seen in Fig. 3.10. The basic idea is the same. TTCit records data for a set amount of time. The counters then count the occurrence of the requested signals in firmware. This observable is then directly related to the rates of the signals and the triggers. A total of 135 counters are available for the specific TTCit task domain. The last twelve bits (counter 134 down to 123, where the numbers are counted starting from 0) are dedicated to the bunch crossing identifier. However, each counter counts only the corresponding bit. In the case of the BC ID, this means that each counter would integrate in time only the signal in the corresponding bit. As such, it is to be expected that these counters would feature on average approximately the same quantity, as they have to toggle at each bunch crossing. They can be used as an additional diagnostic tool - if they are on average very different from each other would imply that either the decoding was not successful, or the presence of a bug in the firmware of the board that is sending over data. The following 32 bits are dedicated to the orbit identifier. Then, counters 90 down to 59 show the Trigger Types. It is interesting to see, in fact, only counter number 63 active. This is reflecting the well controlled behaviour of both the TTCit and the LTU firmwares. This counter is dedicated to physics triggers, and it has to be cross checked with the response from Ch

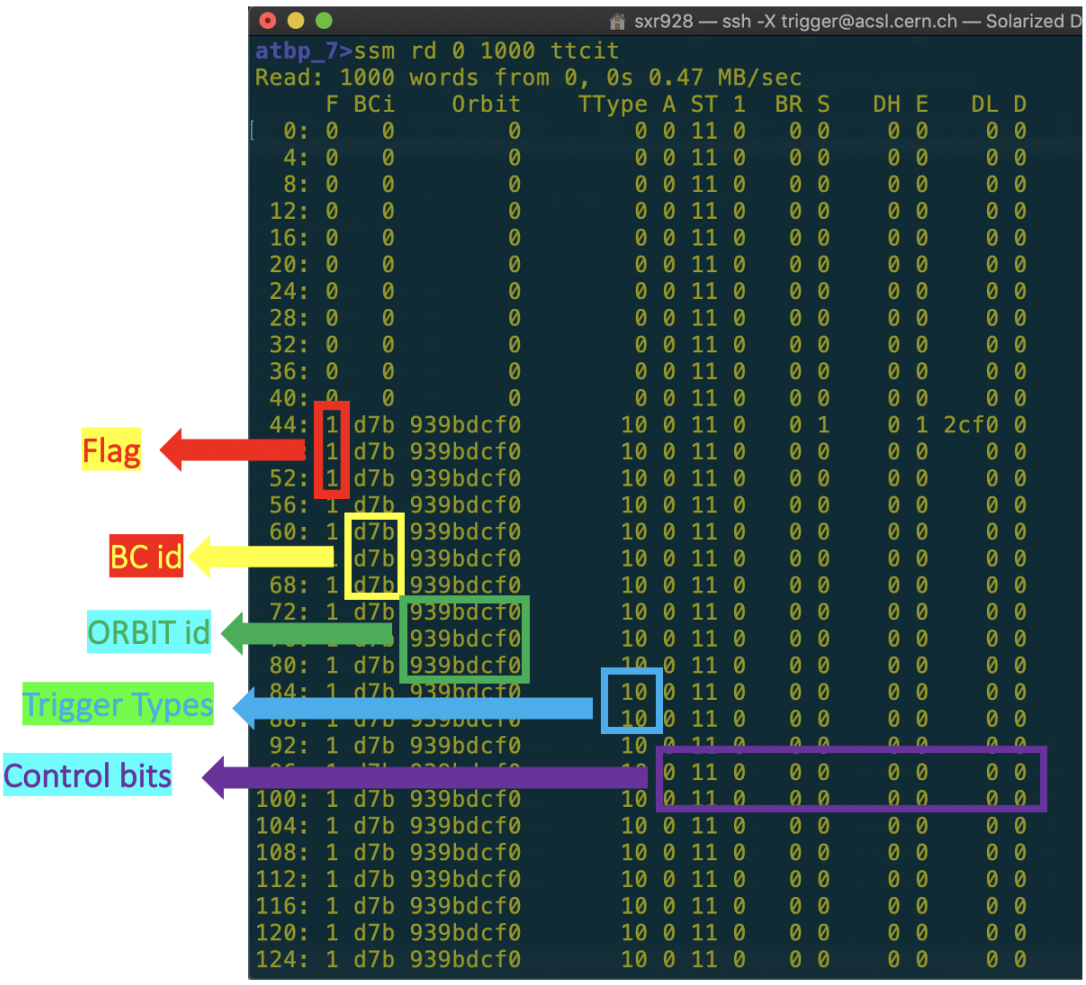


Figure 3.9: An example of the online capabilities of TTCit. The signals recorded by the SSM properly display the successful reception of a complete LL1 message. Each row refers to a different consecutive word recorded by the SSM. It is interesting to note that the S bit is raised as the same time as the F flag, as it should. Each row contains the F flag bit, the BC ID (twelve bits, three hexadecimal characters), the orbit ID (32 bits, eight hexadecimal characters), 32 bits of Trigger Types (the board is correctly receiving physics triggers, a decimal 2), Ch A-dedicated bits, strobes and bits related to transmission errors (the rightmost seventeen bits).

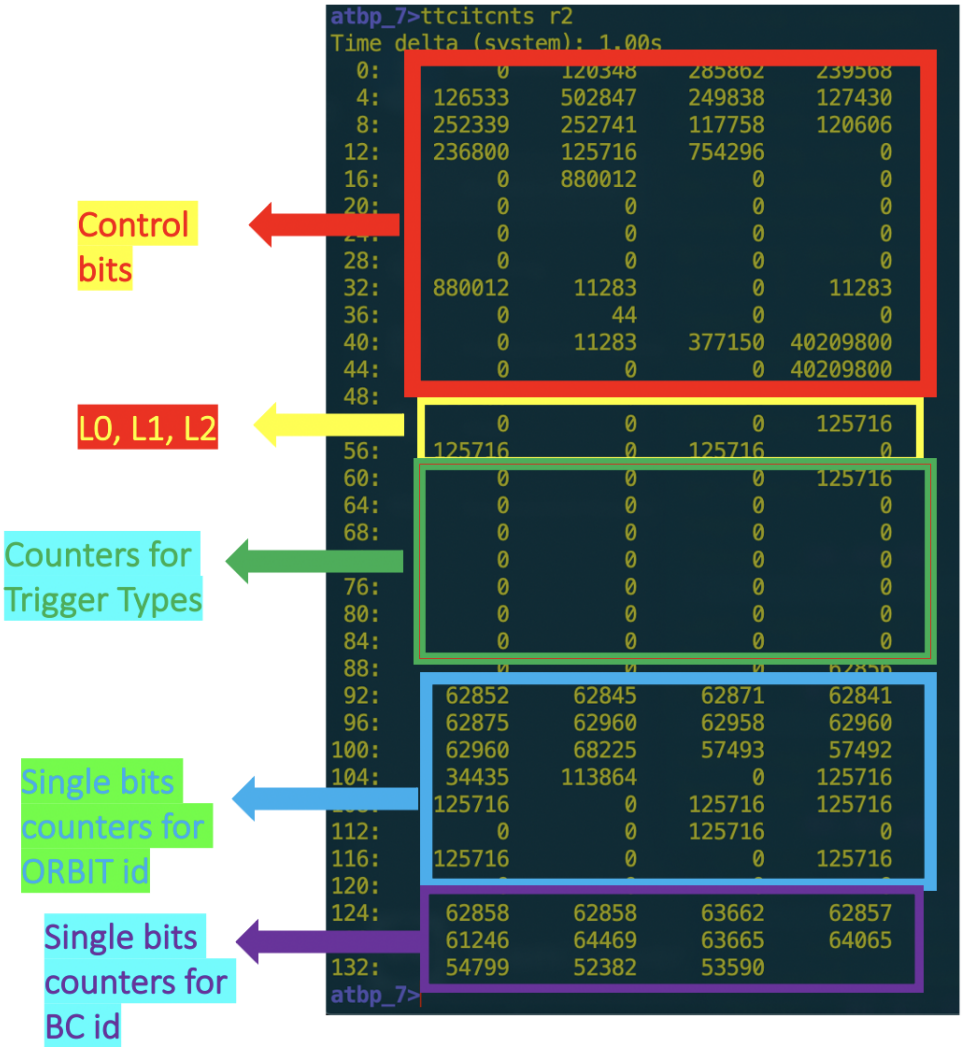


Figure 3.10: The second TTCit validation tool. Counters are useful to provide a fast tool for the health of the data transmission.

A. This is carried out by looking at counters number 55, 56, 58, which represent L0, L1, and the SSM flag, respectively. The fact that L0 and L1 are the same means that TTCit successfully assigned a L1 trigger to each L0. This number being equal to SSM flag's implies that each L1 trigger managed to be coupled to its corresponding LL1 message (wholly). This is not a trivial condition, as LL1 and L1 are in theory decoupled from each other, and totally asynchronous. If the number of physics triggers is the same as the number representing SSM flag both pieces of firmware are working properly.

The TTCit board, and the tools here presented, have been extensively used during the development of the firmware for both CTP and LTU boards, and will also be used for the data taking during LHC Run 3.

3.2 CTP readout: State Machine

The second of the author's tasks concerned the firmware for the CTP readout. The CTP boards have to be able to communicate with the CRU modules on different levels. They have to be able to send the Trigger Types and the Trigger Classes. As a second project, the author was tasked with the design of the State Machine firmware to send the Trigger Classes to the CRU via the GBT link.

3.2.1 Protocol

The State machine has a centrally decided protocol, which is shown in Fig. 3.11.

1. it has to start from an *idle* state, while waiting for the CRU to be ready to accept data via GBT link;
2. at the *Start of Run* it sends a *Start of Page* (SOP) message;
3. the protocol is thus initiated, and it sends four *Raw Data Header* (RDH) words consecutively;
4. it is now ready to send data i.e. if data are available, it *sends* them, otherwise it *waits* for the incoming data;
5. if, at any time, it receives either a HeartBeat trigger or an *End of Run* (EOx) trigger, or the size cap of the package is reached, it sends an *End of Page* (EOP) message, which is followed by a *new* RDH message;

6. at this point the State Machine starts its cycle again with a SOP message.

3.2.2 The core scheme

This State Machine has to satisfy a few requirements:

- it has to send 76 bits (64 bits with Trigger Classes, plus the annexed identifier for the Bunch Crossing they refer to, i.e. 12 bits of BC ID) over the GBT link, which is instead able to cope with 80 bits only;
- it has to be able to avoid sending over empty Trigger Classes i.e. it has to operate *zero suppression*, so as not to consume bandwidth to send over empty Trigger Classes;
- it has to be as optimized as possible, to use as little bandwidth as possible.

Thus, it is clear that:

1. the input data have to be sent to a packer so as to organise them in a format that the GBT can interpret in later stages (the GBT is only able to cope with 80 bits at a time);
2. the packer has to avoid sending any bits if no trigger classes are being sent (zero suppression) to conserve bandwidth;
3. the data from the packer have to be sent to a buffer, as the State Machine requires a slight delay from the time it is able to send data i.e. it has to adhere its ordered protocol;
4. the entire logic has to be governed by the State Machine;

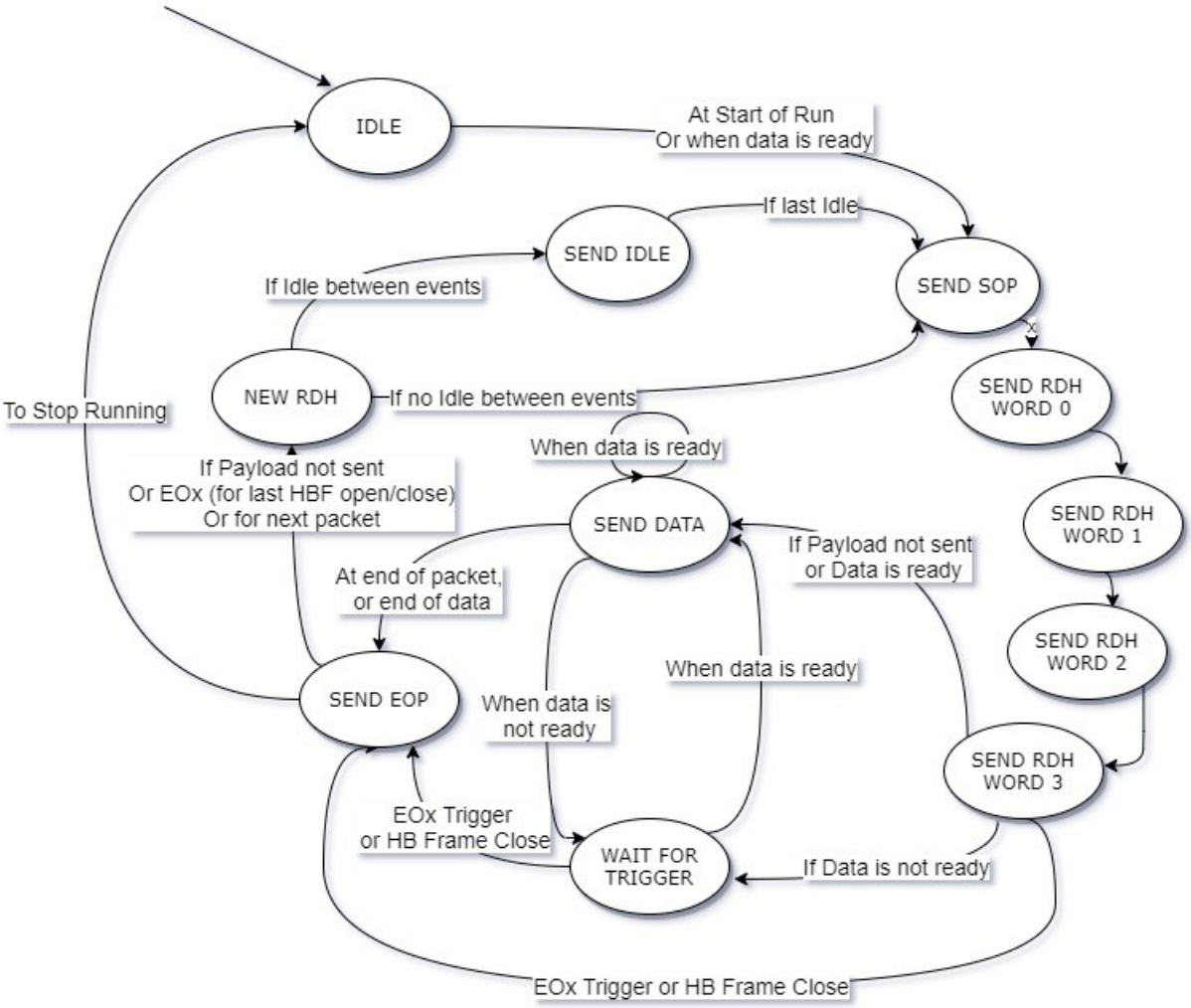


Figure 3.11: Flowchart describing the protocol the State Machine has to follow. It has to start a page (send SOP), send the raw data headers (RDH), and it is able to send data only when these steps have been completed. If a new orbit arrives, or if the maximum size of a page (8 KB) is reached, it has to signal the end of page (EOP), and restart the procedure.

5. it is meaningful to send data from the packer only when there are more than 80 bits available;

6. if the number of bits inside the packer is less than 80 they are kept until 76 new bits (64 Trigger Classes and 12 BC ID bits) arrive.

The last item in particular has a few important implications:

1. the packer has to release the remaining bits once a new HeartBeat (HB) trigger is sent, while also saving the 76 bits (64 Trigger Classes, 12 BC ID bits) which are sent at the same time;

2. the State Machine would have no way of knowing when to initiate its protocol if no flag is present in the sent data, i.e. it has to know when to generate a new package for an incoming new ORBIT.

To meet these requirements, the design of the firmware follows the structure shown in Fig. 3.12. The CTP logic firmware to which it is integrated, generates the 64 bits of Trigger Classes, the 12 bits needed for the Bunch Crossing IDentifier (BC ID), and it generates the Trigger Types, which contain the HB trigger and the EOx triggers to stop the run. These three bit ensembles are then sent to the packer, which operates on 80 bits logic plus an additional three bits representing the HB, and the two EOx triggers, needed to regulate the protocol of the State Machine. This gives a total of 83 bits that are used to both send data to and to regulate the State Machine itself.

The packer properly effects the transition to 83 bits before sending them to a FIFO for bookkeeping. The FIFO is an intellectual property of Xilinx, and version `13.2`. This creates another unnecessary complication. Its readout is subjected to the condition that the data are validated by a flag sent from the FIFO, which is however made available one

clock cycle *after* the data are sent. This made it necessary to have an additional simple user-defined buffer to store the data before finally sending them to the State Machine.

Finally, the State Machine reads the 83 bits, isolates the last three bits to interpret them as state-decision flags, while sending over 80 bits to the GBT.

As an additional note, it is important to mention that the procedure explained in this document, which passes through the HB trigger bit as part of the 83 bits which are sent to the State Machine, actually would have one weak point, and that is the loss of the correspondence of orbit and bunch crossing time of the project with respect to the central CTP time. In order to avoid this, each time the protocol starts sending a new page due to the reception of the HB trigger, the central CTP orbit number is checked, together with the central bunch crossing time, and reset accordingly. This is only done once per HB trigger, to synchronise the two firmwares before sending data to CRU.

3.2.3 Data format sent via GBT

The format sent by the State Machine via GBT is shown in Table 3.1, using the hexadecimal system. The table shows an example where only two 80 bit words of data are sent before the system detects a HB trigger. As such, the first data word is made of 76 bits from the first class, plus an additional four bits from the following. Then, if the HB trigger is sent, only 72 meaningful bits are sent over, together with eight zero bits.

In a first step, the firmware is passed through a simulation, and the output of the State Machine is sent to file to make sure of the actual format that would have been otherwise transmitted to GBT. The behaviour of the input signals is simulated from inside the program used to generate the firmware (VIVADO, since the ALICE Birmingham team is using Xilinx Ultrascale FPGAs), without any actual physical connection of the boards themselves. An example of such a dump is shown in Table 3.2. For simplicity, this

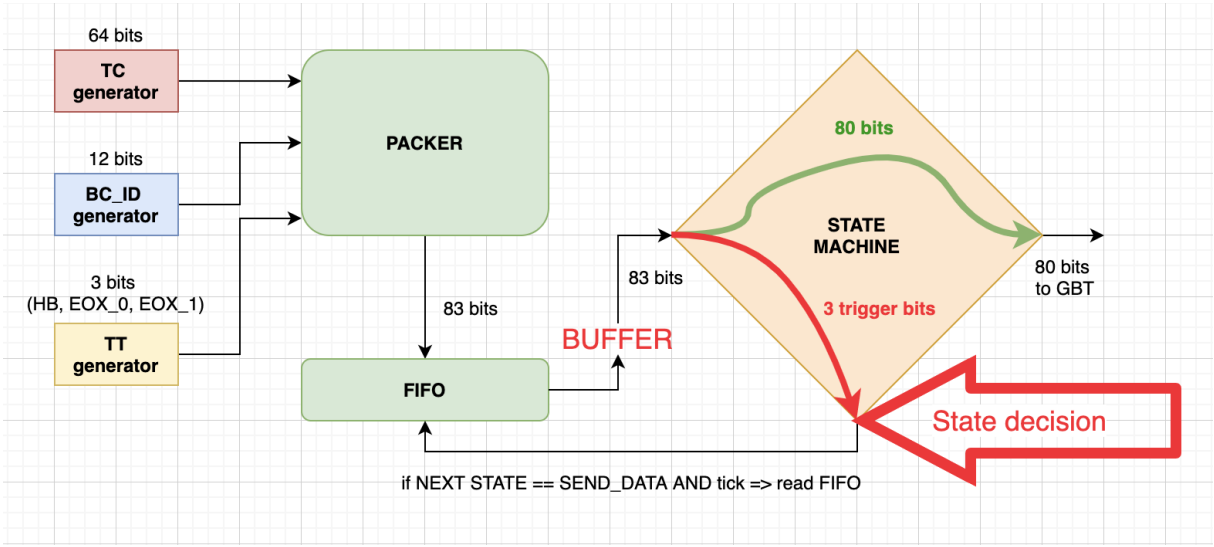


Figure 3.12: Flowchart describing the chosen design of the CTP readout State Machine firmware. The packer receives as inputs the 64 bits for Trigger Classes, 12 bits of BC ID, and control bits for the orbit or the end of run. It arranges packets of 83 bits which are then sent to the FIFO. The FIFO redirects the first packet to a buffer when it is allowed to be read from the State Machine. This is due to the validation flag from the FIFO being delayed by one clock cycle with respect to its output. The State Machine handles the state decision, and the output to the GBT link.

Table 3.1: Example page sent by the CTP readout via GBT to the CRU using the hexadecimal system. The full progression of the readout chain can be visually inspected.

STATE	**bits sent via GBT**																			
SOP	1	0	0	0	0	0	0	0	0	0	0	0	0	0	0	0	0	0	0	0
RDH 0	0	0	0	0	0	0	0	0	SOURCE		0	0	FEE_ID				40		06	
RDH 1	0	0	0	0	ORBIT								0	0	0	0	0	BC_ID		
RDH 2	0	0	0	0	0	0	0	STOP	PAGE_COUNTER				TRIGGER_TYPES							
RDH 3	0	0	0	0	0	0	0	0	0	0	0	0	RUN_PATTERN							
DATA	BC	TRIGGER_CLASSES																BC_ID		
DATA	0	0	TRIGGER_CLASSES																BC_ID	
EOP	2	0	0	0	0	0	0	0	0	0	0	0	0	0	0	0	0	0	0	0
IDLE	0	0	0	0	0	0	0	0	0	0	0	0	0	0	0	0	0	0	0	0
NEW RDH	0	0	0	0	0	0	0	0	0	0	0	0	0	0	0	0	0	0	0	0
WAIT	0	0	0	0	0	0	0	0	0	0	0	0	0	0	0	0	0	0	0	0
SEND IDLE	0	0	0	0	0	0	0	0	0	0	0	0	0	0	0	0	0	0	0	0

simulation was carried out with a constant payload and with a redefinition of the length of an ORBIT (12 bunch crossings instead of 3563) to emphasize the spread in terms of orbits. The simulation clearly shows the `32BF8` constant payload (the 64 Trigger Classes are all zeroes and `32BF8`), followed by the BC ID. The characteristic feature of the format is that the payload is shifted by one hexadecimal character in the output. This is quite noticeable whenever the payload is known and easy to interpret (for example when the payload is fixed or a simple counter). This is also seen in Table 3.2. The sequence starts with the State Machine sending the start of page, as shown in Fig. 3.11. The SOP message is empty apart from the hexadecimal `1` at the front of the message. It is then followed by four words of RDH, which contain features which will become clearer when compared to the real data output. The State Machine sends the end of page once it gets the HB trigger, and the protocol can start again.

In a second step, the firmware is loaded to the boards, the physical connections are then established, and the State Machine manages to send data over the GBT link. The output can be read, and Table 3.3 shows its appearance for a random set of fourteen words. It is interesting to appreciate the shift in the data being sent caused by the unique format of the State Machine, which aims to make full use of the 80 bits wide payload of the GBT message, despite having to send 76 bits instead. The State Machine requires a specific word to be able to start sending any data. This is because the receiving end has to first acknowledge or assert its availability. The *Single Word Transaction* (SWT) is sent [77] and it contains the string `deadbeef`. The stop word is `beefdead`. The State Machine is equipped with a counter to check whether it has received a SWT word to start the data transmission. It also serves as a quick check for the health of the link.

It is then possible to analyse the output of the State Machine from Table 3.3. The CRU ignores part of the output from the State Machine. The protocol dictates that it is insensitive to SOP, EOP, IDLE, NEW RDH, and WAIT FOR TRIGGERS messages. Hence, the first message that has to be seen in the output is the RDH 0 (words `1` to `14`

Table 3.2: Example of a dump to file of the State Machine's simulation, where all the entries are using the hexadecimal system. A constant payload is used (32BF8). The quick succession of RDH can also be visually inspected.

Word	STATE	bits sent via GBT
0	**SOP**	1 0 0 0 0 0 0 0 0 0 0 0 0 0 0 0 0 0 0 0
1	**RDH 0**	2000 0 0 0 0 11 0 0 013F 40 06
2	**RDH 1**	0 0 0 0 00000000 0 0 0 0 0 000
3	**RDH 2**	0 0 0 0 0 0 0 0 0000 CAFECAFE
4	**RDH 3**	0 0 0 0 0 0 0 0 0 0 0 0 12345678
5	**DATA**	1 000000000032BF80 000
6	**DATA**	02 000000000032BF80 00
7	**DATA**	003 000000000032BF80 0
8	**DATA**	0 004 000000000032BF80
9	**DATA**	80 005 000000000032BF8
10	**DATA**	F80 006 000000000032BF
11	**DATA**	BF80 007 000000000032B
12	**DATA**	2BF80 008 000000000032
13	**DATA**	32BF80 009 00000000003
14	**DATA**	032BF80 00A 0000000000
15	**DATA**	0032BF80 00B 000000000
16	**DATA**	0 0 0 0 0 0 0 0 0 0 0 0 00000000
17	**EOP**	2 0 0 0 0 0 0 0 0 0 0 0 0 0 0 0 0 0 0 0
18	**NEW RDH**	0 0 0 0 0 0 0 0 0 0 0 0 0 0 0 0 0 0 0 0

in Table 3.2 can be compared with words 1 to 14 in Table 3.3, whereas word 0 in Table 3.2 is not propagated to the output from the GBT). The characters appearing in Fig. 3.3 are all hexadecimal characters. The State Machine sends only 80 bits at a time, but 128 bits can be counted. The firmware on the receiving end of the GBT link automatically attaches an additional 48 bits to the message (they are important only for RDH, while they are zeroes whenever payloads are sent).

The first line shows RDH 0: the first 32 bits show the page number as seen by the receiving end of the GBT - a 6 -, the link ID - a 1, the link to which the GBT has to be physically plugged to -, the actual size of the page twice -a hexadecimal 2000, which correctly corresponds to 8192 bits as dictated by protocol -, and then what the State Machine is actually sending: the source ID, which is the CTP system, identified by a hexadecimal 11, 17 in decimal, and the format of the remaining 32 bits is hexadecimal 0 - blank in the output -, hexadecimal 1 for link ID, the hexadecimal serial number of the board that is being used - 3F, which corresponds to 63, which is the board used for this output. Finally, the header size and version, 40 and 06, respectively.

The second line shows RDH 1: the first and second 32 bits words are empty, the third shows the orbit ID as sent from the CTP, and the last word the BC ID. The BC ID is 0 when the HB trigger is sent (or, equivalently, when the orbit ID changes).

The third line shows the RDH 2: the first and second 32 bits words are empty, the third shows the page ID, which is 0 for the first page when the orbit ID changes, and the last word the Trigger Types, which are also sent together with the Trigger Classes, but only in the RDH.

The fourth line shows RDH 3: it is empty apart from the last word, the *run pattern*, which indicates which detectors are active during the data taking.

Starting from the fifth row payloads are sent over. The output is showing a counter as

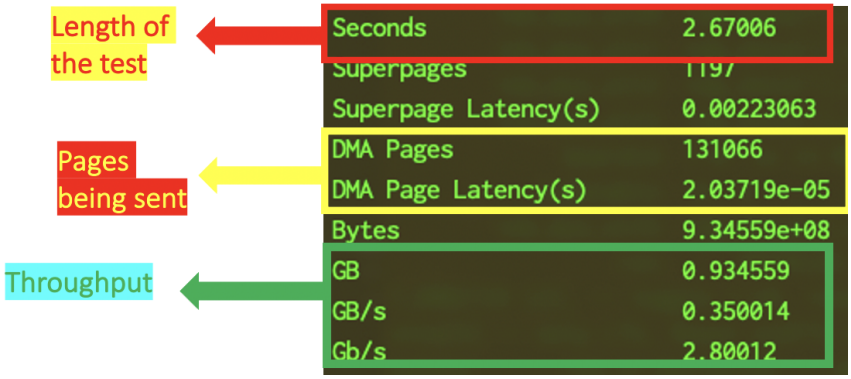
Table 3.3: Output of the State Machine on the GBT link in the hexadecimal system. The typical format of the Trigger Classes readout is seen as an oblique structure. Two freely running counters are used, one for payload, and the other being the BC ID.

Word	output from the CRU																															
1	0	0	0	0	0	601			2000				2000				0	0	0	0	11		0	0	013F			40		06		
2	0	0	0	0	0	0	0	0	0	0	0	0	0	0	0	0	27A483A4								0	0	0	0	0	000		
3	0	0	0	0	0	0	0	0	0	0	0	0	0	0	0	0	0	0	0	0	0000				00006803							
4	0	0	0	0	0	0	0	0	0	0	0	0	0	0	0	0	0	0	0	0	0	0	0	0	00000003							
5	0	0	0	0	0	0	0	0	0	0	0	0	1	000000000000050D																000		
6	0	0	0	0	0	0	0	0	0	0	0	0	02	000000000000050E																	00	
7	0	0	0	0	0	0	0	0	0	0	0	0	003	000000000000050F																		0
8	0	0	0	0	0	0	0	0	0	0	0	0	1	004			0000000000000510															
9	0	0	0	0	0	0	0	0	0	0	0	0	11	005			000000000000051															
10	0	0	0	0	0	0	0	0	0	0	0	0	512	006			00000000000005															
11	0	0	0	0	0	0	0	0	0	0	0	0	0513	007			0000000000000															
12	0	0	0	0	0	0	0	0	0	0	0	0	00514	008			000000000000															
13	0	0	0	0	0	0	0	0	0	0	0	0	000515	009			00000000000															
14	0	0	0	0	0	0	0	0	0	0	0	0	0000516	00A			0000000000															

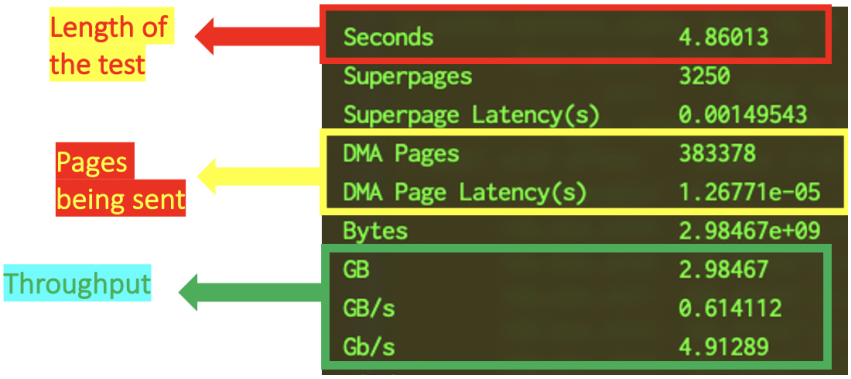
payload. For the first payload that is sent (in this output every BC ID is accompanied by the payload) BC ID has to be `0`. BC ID is twelve bits long, so the first three hexadecimal characters from the right have to be `000`. Then the counter, which should be 64 bits long, but for simplicity, only a twelve bits large counter is used, which can count from hexadecimal `000` to `FFF`. The remaining bits are all zeroes. This makes the typical shift format of the Trigger Classes output quite noticeable, as from Table 3.3 the oblique structure is well reproduced. The choice of a counter is also quite noticeable, as the output would then display two freely running counters. As the format is sending 80 bits instead of 76 bits, the first four bits of the next payload should appear in the first row of sent data. Considering that the first twelve bits correspond to BC ID, and the BC ID for the first page starts from `000`, a hexadecimal `1` appears at the leftmost character in the first row of payload. Similar arguments hold for the following rows of data.

The firmware is able to freely shift between two types of input data: the counter and a pseudorandom number generator. This is carried out by writing to a register the `tcr_input_data_sel`, which is the name of the Trigger Classes input data selection bit. This is done as a test for the future, when the firmware will be used for LHC Run 3 data taking. Using a pseudorandom number generator, a *Linear Feedback Shift Register* (LFSR) [78], the payload will be closer in looks to what will be effectively sent by the CTP via the GBT link. In the firmware there is also the possibility of using a user defined threshold to limit the amount of actual data being sent (which can also be changed at run time by writing to a register). This is also done by writing to the corresponding register. The firmware will then send data only if the output is greater than the threshold. This is shown in Fig. 3.13(a) and 3.13(b). In the former, a somewhat high threshold is used, which lowers the output to around 2.8 Gbps, while in the latter a very low threshold is used, which brings the output to around 4.9 Gbps, close to the absolute limit for the State Machine[3].

[3]The GBT copes with 128 bits every 25 ns, this means around 5.1 Gbps. This small computation refers to the thoughput to the GBT, which is what Fig. 3.13(a) and 3.13(b) are actually showing.



(a)



(b)

Figure 3.13: Fig. 3.13(a) and 3.13(b) show the overall throughput of the GBT link with the data sent by the Trigger Class readout State Machine. The former shows the throughput with a pseudorandom number generator with high threshold, while the latter shows a much higher throughput caused by a very low threshold.

Chapter 4

Coherent J/ψ photoproduction and neutron emission

Neutron emission classes are particularly useful to try and separate the low Bjorken-x component $\sim 10^{-5}$ from the higher $x \sim 10^{-2}$. Forward data provide this unique possibility of accessing nuclear pdfs in this unprecedented x-domain.

4.1 A brief introduction to the analysis strategy

The strategy for the analysis is quite straightforward. Firstly, the data have to be properly split into neutron emission classes. Then, the invariant mass distributions are fitted so as to extract the raw yields. In a third step, the correction factors are measured or computed, to correct for the coherent component of the signal, before finally computing the central values of the cross sections.

4.2 Event and track selections

This analysis aims to measure vector meson photoproduction accompanied by neutron emission. Since the neutrons are due to additional photon exchanges compared to the sole $\gamma\mathbb{P}$, where $\mathbb{P}$ indicates the Pomeron, interesting events could be vetoed by an online trigger. As a consequence, a more open trigger is required, and only the 2018 Pb–Pb UPC data sample can be used. This limits the integrated luminosity $\mathcal{L}$ to $\mathcal{L} \sim 530\ \mu\text{b}^{-1}$. The online trigger required a dimuon in the Forward Muon Spectrometer and a veto in the V0A.

Further vetoes and selections are requested offline. They can be separated into two categories, namely those relating to the quality of the muon tracks, and those related to the exclusivity of each event. The former are the following:

- each of the muon tracks has to be within the angular coverage of the hadronic absorber i.e. 17.5 cm $< R_{\text{absorber}} <$ 89.5 cm. This refers to the radial opening of the absorber cone at the extremity closest to the Forward Muon Spectrometer;

- an additional $p \times DCA$ requirement, where the *Distance of Closest Approach*, DCA, refers to the distance of the track from the nominal interaction vertex, which is taken to be the centre of the apparatus inside the beam cavity. The product $p \times DCA$ is approximately independent of the momentum of the muons;

- each of the two muons of the dimuon candidate has to be within the pseudorapidity acceptance of the Forward Muon Spectrometer i.e. the pseudorapidity of each muon η_μ has to be $-4.0 < \eta_\mu < -2.5$.

Those related to the exclusivity of each event are instead:

Table 4.1: Available events, with the correct online trigger, and two opposite-sign muons satisfying the quality requirements for muon tracks. Total events and partials per run period are also shown.

	LHC18q	LHC18r	Total
Available events	36302800	55803700	92106500
Online trigger	19615900	33836700	53452600
Two good muons	48776	54598	103374
Opposite-sign dimuon	39644	46148	85792
Like-sign dimuon	9132	8450	17582

- empty V0A decision[1];
- V0C decision either empty or in beam-beam timing[2];
- a maximum of two V0C cells crossed in the same event;
- the dimuon candidate has to satisfy the rapidity requirement $-4.0 < y < -2.5$.

The available dataset corresponds to the sum of two run periods, namely LHC18q and LHC18r. Table 4.1 shows the number of usable events before the exclusivity conditions are applied, i.e. it shows the number of events with the correct online trigger class, which also had two muons satisfying the requirements on the quality of the muon tracks.

The 85792 opposite-sign dimuon events with the correct online trigger (as shown in Table 4.1), are then filtered again. The exclusivity conditions are now applied, as shown in Table 4.2.

Table 4.3 shows the events, passing even the exclusivity requirements, which also satisfy

[1] V0A veto already required in the online trigger.

[2] Any number of muons between zero and two can cross the V0C if a dimuon has been produced in the event.

Table 4.2: Number of events which would be rejected by applying the corresponding condition. Numbers are shown both for the total dataset and the single run periods. The final row shows the events rejected by all the exclusivity selections.

	LHC18q	LHC18r	Total
Empty V0A decisions	13206	8163	21369
V0C empty or beam-beam timing	1423	939	2362
Maximum of two V0C cells	11301	7586	18887
All of the above	15065	10862	25927

the dimuon p_{T} selection for coherent events, i.e. the dimuon p_{T} is required to be less than 0.25 GeV/c. The numbers are also shown for rapidity intervals.

Fig. 4.1(a) and 4.1(b) show the invariant mass distribution for all the dimuons (with no requirement on p_{T}) and the p_{T} distribution underneath the J/ψ mass peak, i.e. the dimuon invariant mass is required to lie within the interval
$2.85 < M_{\mu\mu} < 3.35$ GeV/c^2, respectively. The former shows two clear peaks at invariant masses consistent with J/ψ and ψ' masses. The latter shows a clear coherent peak in the p_{T} distribution, at p_{T} smaller than 0.25 GeV/c.

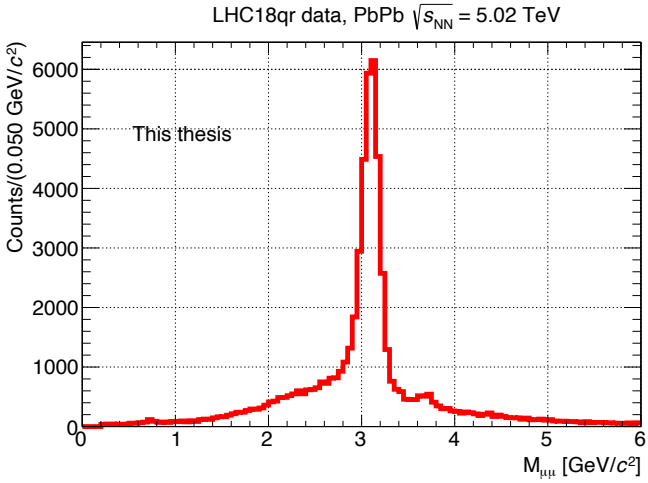
4.2.1 Classifying neutron emission

The first technical detail requiring attention in a neutron emission differential analysis is how to classify each event. One option, originally used in ALICE during Run 1, would be to separate the events based on energy thresholds on the neutron ZDC energy spectra. Fig. 2.5 shows the distribution of the C-side neutron ZDC (ZNC) when plotting the energy of the A side against the energy of the C side, obtained from the midrapidity Pb–Pb ρ^0 analysis published by ALICE [11]. It is clear that most of the events are characterised by no neutron being emitted on either side of the ALICE detector. Two bands can be

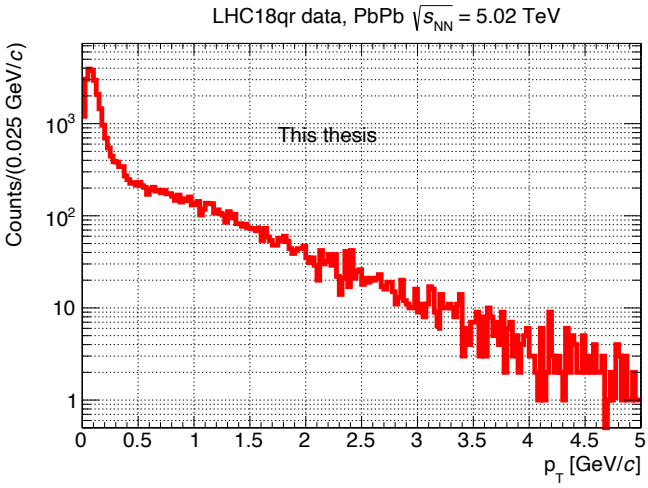
Table 4.3: Events passing all selections, and also the coherent dimuon p_{T} requirement. Numbers are also shown for rapidity intervals. No neutron emission class is applied.

Coherent p_{T} selection	LHC18q	LHC18r	Total
$-4 < y < -2.5$	17148	24813	41961
$-4 < y < -3.75$	746	1072	1818
$-3.75 < y < -3.5$	2533	3725	6258
$-3.5 < y < -3.25$	4599	6611	11210
$-3.25 < y < -3$	5048	7252	12300
$-3 < y < -2.75$	3329	4883	8212
$-2.75 < y < -2.5$	893	1270	2163

identified as one-sided emission, and a few events can be classified as events with neutrons being emitted in both directions (forward and backward). It is remarkable to see how the centroids of each data grouping can be identified as multiples of the energy of one nucleon in the Pb beam, which indicates that the neutrons are moving together with the beam. A newer approach is instead to focus on the timing of the particles seen in either of the neutron ZDC. This effectively means asking for a signal in a timing window around the event time. A quite permissive timing window is $|\Delta t| < 2$ ns, with respect to the time of the recorded event. The effect of moving in the direction of the timing selection is shown in Fig. 4.2(a) and 4.2(b), which show the energy spectra of the neutron ZDC on the A side and C side, respectively. The red curves show all the data, while the blue curves show the data after the timing selection has been applied. The timing selection effectively results in the suppression of the so-called *pedestal* peak, the peak corresponding to no neutrons being emitted, as this peak is all due to electronic noise in the calorimeters. Using timing (and thus, pedestal removal) instead of a simpler, and more intuitive, energy threshold technique, means that the final cross sections do not have to be corrected for the residual contributions, i.e. the residual contribution of pedestal



(a)



(b)

Figure 4.1: Fig. 4.1(a) and 4.1(b) show the invariant mass distribution and the p_{T} distribution for dimuons after selections. The invariant mass distribution has no p_{T} requirement applied to the dimuon p_{T}. The p_{T} distribution requires a dimuon invariant mass lying in the interval $2.85 < M_{\mu\mu} < 3.35$ GeV/c^2.

background and 1-neutron peak which would have had to otherwise be taken into account

Table 4.4: Events passing all selections, and also the coherent dimuon p_{T} requirement. Numbers are also shown for rapidity intervals. The 0N0N class selection is applied.

Coherent p_{T} selection, 0N0N	LHC18q	LHC18r	Total
$-4 < y < -2.5$	13697	19936	33633
$-4 < y < -3.5$	2664	3950	6614
$-3.5 < y < -3$	7721	11176	18897
$-3 < y < -2.5$	3312	4810	8122

with an energy threshold[3]. The data after timing selection can be described as a simple sum of Gaussian distributions accounting for one, two and three neutrons being emitted, as shown in Fig. 4.2(c) and 4.2(d). It is now possible to classify the events based on the topology of the neutron emission. In the following, four classes will be considered: 0N0N (no neutrons being emitted on either side of the ALICE detector), 0NXN (neutrons only in the C side), XN0N (neutrons only in the A side), and XNXN (neutrons on both sides). It is also possible to perform a rapidity differential analysis with the available data.

Table 4.4, 4.5, 4.6, and 4.7 show the number of events passing the coherent p_{T} selection, when the neutron emission selections are applied, for the 0N0N, 0NXN, XN0N, and XNXN classes, respectively. Numbers are also shown for rapidity bins. Note that most of the events fall under the 0N0N class, while only a few hundred events are available for the XNXN class.

4.2.2 Control plots

A few control plots are used to monitor the quality of the available datasets. Fig. 4.3(a), 4.3(b), 4.3(c), and 4.3(d) show the distribution of the total number of tracklets for 0N0N,

[3]Approximately 1.6% of the 1-neutron peak would be excluded by a selection of neutron energies above 1.5 TeV.

Table 4.5: Events passing all selections, and also the coherent dimuon p_{T} requirement. Numbers are also shown for rapidity intervals. The 0NXN class selection is applied.

Coherent p_{T} selection, 0NXN	LHC18q	LHC18r	Total
$-4 < y < -2.5$	1562	2329	3891
$-4 < y < -3.5$	291	437	728
$-3.5 < y < -3$	873	1288	2161
$-3 < y < -2.5$	398	604	1002

Table 4.6: Events passing all selections, and also the coherent dimuon p_{T} requirement. Numbers are also shown for rapidity intervals. The XN0N class selection is applied.

Coherent p_{T} selection, XN0N	LHC18q	LHC18r	Total
$-4 < y < -2.5$	1201	1607	2808
$-4 < y < -3.5$	215	285	500
$-3.5 < y < -3$	664	853	1517
$-3 < y < -2.5$	322	469	791

Table 4.7: Events passing all selections, and also the coherent dimuon p_{T} requirement. Numbers are also shown for rapidity intervals. The XNXN class selection is applied.

Coherent p_{T} selection, XNXN	LHC18q	LHC18r	Total
$-4 < y < -2.5$	688	941	1629
$-4 < y < -3.5$	109	125	234
$-3.5 < y < -3$	389	546	935
$-3 < y < -2.5$	190	270	460

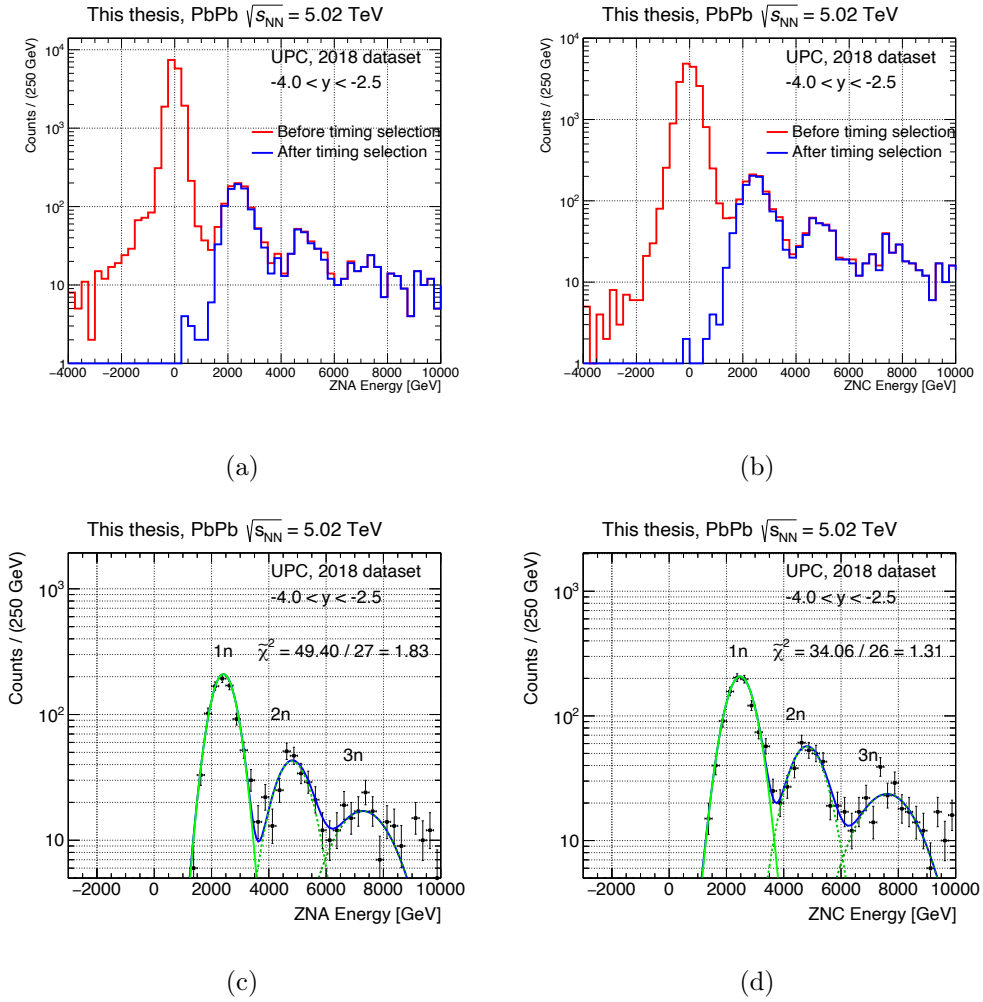


Figure 4.2: Fig. 4.2(a) and 4.2(b) show in red the neutron ZDC energy spectra before the timing selection is applied, and in blue the removal of the pedestal effected by the timing selection. The former shows the spectra for the neutron ZDC spectra on the A side, while the latter for the C side. Fig. 4.2(c) and 4.2(d) show the fit to the respective distributions after timing selection is requested. The fit is performed as a sum of Gaussian distributions. The peaks due to one, two and three neutron emission can be singled out.

0NXN, XN0N, and XNXN, respectively, i.e. the total number of track segments recorded by the ITS in the selected event. A UPC event at forward rapidity is characterised by a very low number of tracklets seen in the ITS. The distribution is thus supposed to fall

rapidly as a function of increasing amounts of tracklets.

In particular, Fig. 4.3(a), 4.3(b), 4.3(c), and 4.3(d) show these distributions for events passing muon track quality requirements, exclusivity conditions, for all dimuons and the proper subset with dimuon invariant masses lying in a restricted region around the J/ψ mass, which, for the purpose of this visual inspection only, was chosen to be $2.9 < M_{\mu\mu} < 3.3$ GeV/c^2.

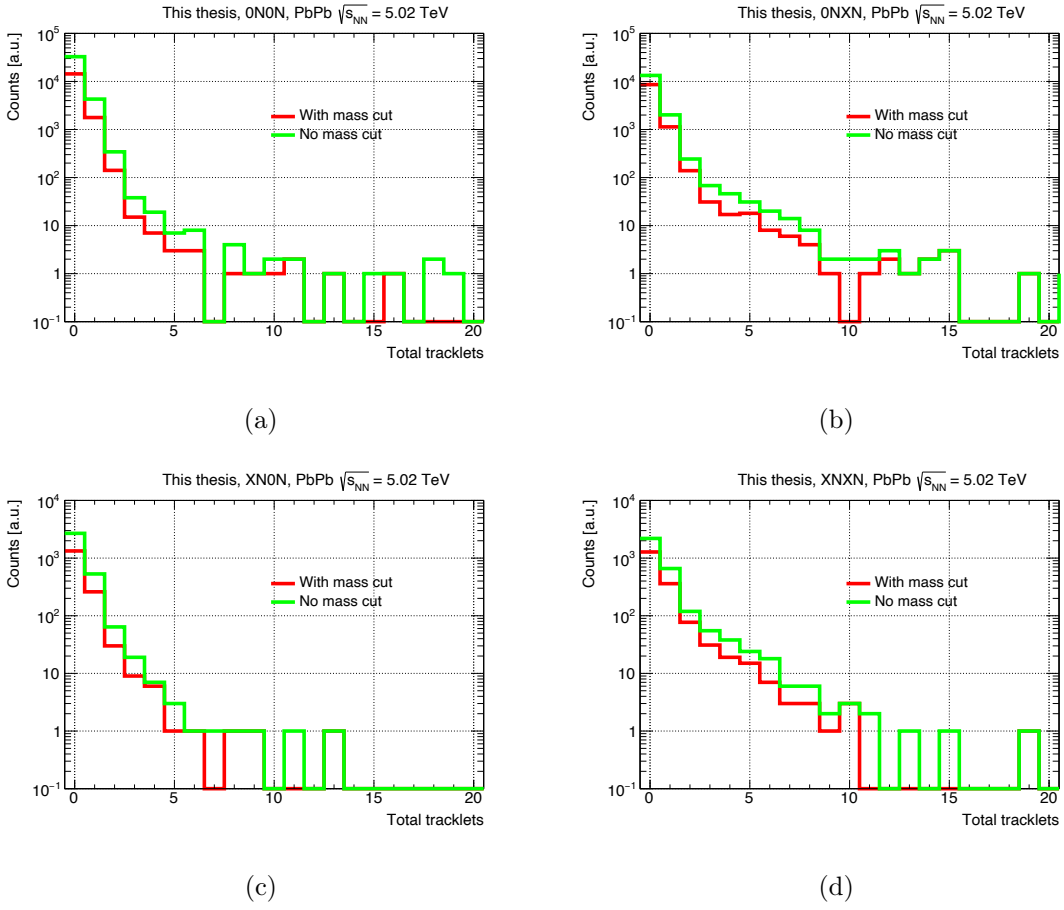


Figure 4.3: Distribution of the total number of tracklets. The events have to pass muon quality requirements and exclusivity conditions. In addition, they have to be lying in a restricted dimuon invariant mass region around the J/ψ mass, i.e. $2.9 < M_{\mu\mu} < 3.3$ GeV/c^2. Fig. 4.3(a), 4.3(b), 4.3(c), and 4.3(d) show the distribution of the total number of tracklets for 0N0N, 0NXN, XN0N, and XNXN, respectively.

It is interesting to compare the plots with and without the invariant mass requirement. This is because outside the J/ψ mass region, the background is supposed to be dominated by a completely different process, exclusive dimuon production i.e. $\gamma\gamma \longrightarrow \mu\mu$. No change of behaviour can be seen in the tracklet distributions.

Fig. 4.4(a), 4.4(b), 4.4(c), 4.4(d), and 4.4(e) show the distribution of the total number of activated V0C cells for 0N0N+0NXN+XN0N+XNXN, 0N0N, 0NXN, XN0N, and XNXN, respectively, i.e. the total number of V0C cells hit in the selected event. A truly exclusive J/ψ event should have two V0C cells at most. The distribution is thus supposed to be rapidly falling as a function of increasing amounts of tracklets.

In particular, Fig. 4.4(b), 4.4(c), 4.4(d), and 4.4(e) show these distributions for events passing both the muon track quality requirements and the exclusivity conditions (apart from the veto on higher activities of V0C cells[4]), for all dimuons and the proper subset with dimuon invariant masses lying in a restricted region around the J/ψ mass, which, for the purpose of this visual inspection only, was chosen to be $2.9 < M_{\mu\mu} < 3.3$ GeV/c^2.

It is quite interesting to observe how the V0C distributions change in behaviour quite dramatically with and without the invariant mass condition applied. Selecting the J/ψ invariant mass region, the distributions are peaked at zero activated V0C cells, and fall rapidly. This is clearly observed in Fig. 4.4(b) and 4.4(d), for the red distributions which have the invariant mass requirement, while the green distributions without mass requirement, show the same behaviour as the other distributions of the same type. In particular, Fig. 4.4(c) and 4.4(e) show almost flat distributions up to the highest possible amount of activated V0C cells, i.e. thirty two[5]. This is due to the asymmetric online veto conditions, i.e. the online trigger has a veto *only* on the V0A's side. The veto on higher V0C activities is thus applied to reject background contributions.

[4]The selection requires at most two activated cells.

[5]V0C is divided in thirty two cells.

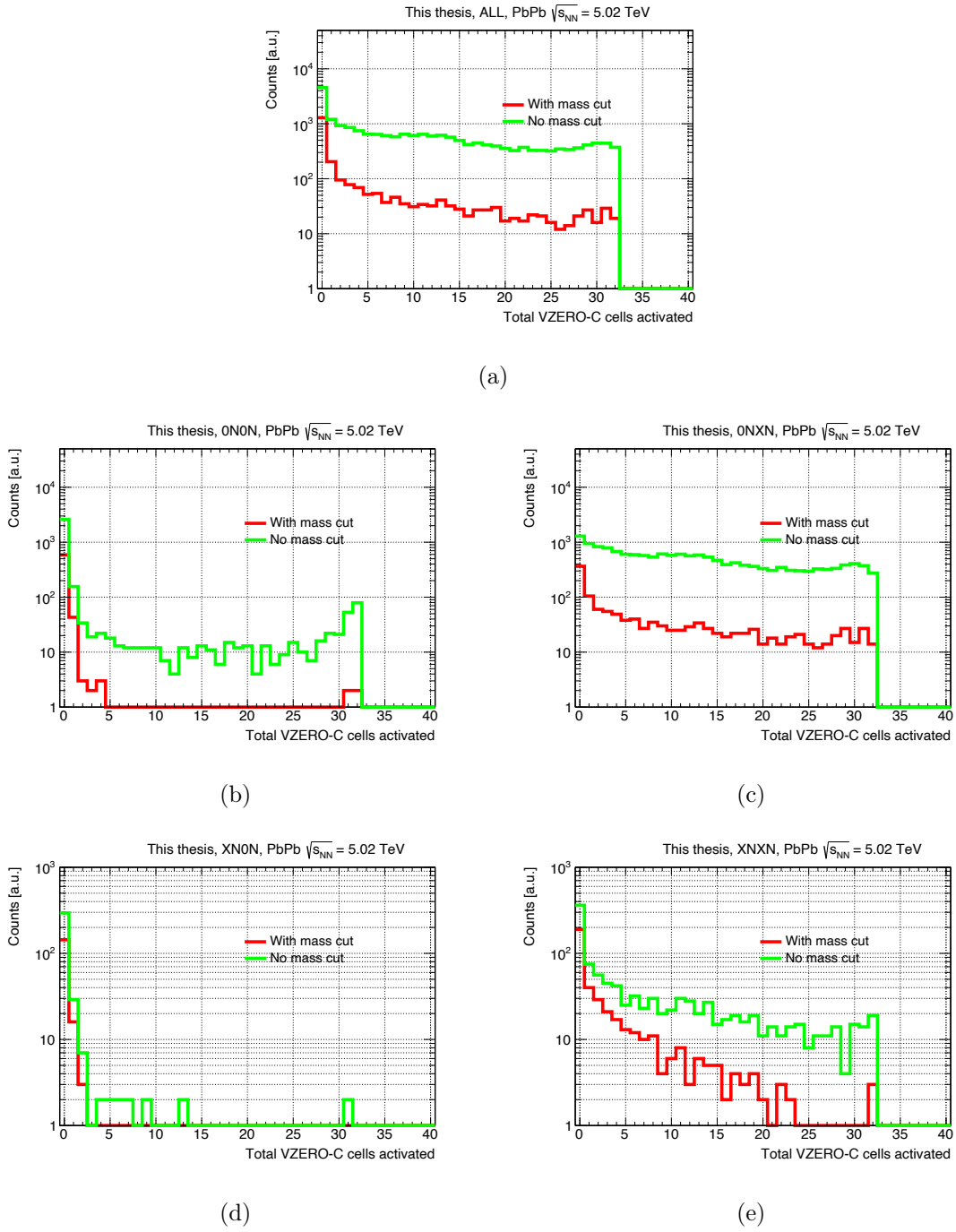


Figure 4.4: Distribution of the total number of activated V0C cells. The events have to pass both the muon quality requirements and the exclusivity conditions (apart from the veto on higher V0C cell activities). In addition, a dimuon invariant mass cut around the J/ψ peak region is required i.e. $2.9 < M_{\mu\mu} < 3.3$ GeV/c^2. Fig. 4.4(a), 4.4(b), 4.4(c), 4.4(d), and 4.4(e) show the distribution of the total number of activated V0C cells for 0N0N+0NXN+XN0N+XNXN, 0N0N, 0NXN, XN0N, and XNXN, respectively.

4.3 Fitting the invariant mass distributions

The invariant mass distributions obtained with the neutron emission classification, i.e. the invariant mass distributions for 0N0N, 0NXN, XN0N, and XNXN classes, have to be fitted to extract the raw yields needed to compute the photoproduction cross sections. As the interest lies in the low p_{T} coherent component of the J/ψ signal, the invariant mass distributions refer to those dimuons with $p_{\mathrm{T}}^{\mu\mu} < 0.25$ GeV/c. The usual ALICE UPC procedure is to describe the invariant mass distributions as a sum of two Crystal Ball functions (CB) [79] and a reasonable prescription for the background. Hence, the J/ψ and the ψ' are both described by Eq. 4.1:

$$CB(M_{\mu\mu}) = \begin{cases} A \cdot |M_{\mu\mu} - M_0|^{-n} & \text{if } M_{\mu\mu} < M_0 - \sigma \cdot \alpha, \\ \frac{1}{\sqrt{2\pi}\cdot\sigma} \cdot \exp\left[-\frac{(M_{\mu\mu}-M_0)^2}{2\sigma^2}\right] & \text{otherwise,} \end{cases} \tag{4.1}$$

where $M_{\mu\mu}$ is the invariant mass of the two muons, M_0 the mean of its Gaussian part, σ describes the width of the peak, α the number of units of width at which the distribution changes form, A the normalisation of the power-law part and n its slope. Both α and n are fixed to the values obtained by fitting the templates obtained by analysing reconstructed STARlight [27] events, in the corresponding rapidity interval, but without any classification in neutron emission classes. Unfortunately, at the moment this analysis is being carried out, and to the best of the author's knowledge, there is no generator (either in ALICE or outside of it) capable of generating events already in neutron emission classes, although there are programs known as afterburners appearing, e.g. $\mathbf{n^{O}_{O}n}$ [10], which take in the output from STARlight, and compute the probability of additional photons being exchanged. This step is theoretically quite straightforward, as the two processes - vector meson photoproduction and additional photon exchanges - happen at very different times, and can be factorised. Since there are far more J/ψ events than ψ' events, the mean of the J/ψ distributions can be left free while the mean of the ψ' distributions is fixed to the corresponding PDG value [22]. The σ for J/ψ, $\sigma_{\mathrm{J}/\psi}$, is also left free in the fit to the data

as it is sizeably larger in data than in the simulations, while in the case of the ψ', $\sigma_{\psi'}$, it is fixed as shown in Eq. 4.2:

$$\sigma_{\psi'} = \sigma_{\mathrm{J}/\psi} \cdot \frac{\sigma_{\psi',SL}}{\sigma_{\mathrm{J}/\psi,SL}} \ , \tag{4.2}$$

where $\frac{\sigma_{\psi',SL}}{\sigma_{\mathrm{J}/\psi,SL}}$ is the ratio of the widths as obtained from the fits to the corresponding STARlight templates (i.e. $\sim$1.09). The raw spectra are then fitted without any acceptance correction as they cover small invariant mass ranges, thus with negligible acceptance or efficiency variations.

The background requires a different description. At high values of invariant masses the distribution follows an exponential behaviour, as expected if it is dominated by the $\gamma\gamma \longrightarrow \mu^+\mu^-$ process, while at lower invariant masses the online trigger conditions distort the exponential trend. The background is then described by Eq. 4.3:

$$P(M_{\mu\mu}) = \begin{cases} e^{bM_{\mu\mu}}[1 + a_2(M_{\mu\mu} - M_1)^2 + \\ \qquad +a_3(M_{\mu\mu} - M_1)^3 + a_4(M_{\mu\mu} - M_1)^4] & \text{if } M_{\mu\mu} < M_1, \\ e^{bM_{\mu\mu}} & \text{otherwise,} \end{cases} \tag{4.3}$$

where M_1 is the mass where the description is changed and is fixed to the value $M_1 = 4$ GeV/c^2; $M_{\mu\mu}$ is the invariant mass of the two muons, b the slope of the exponential part, a_2, a_3, a_4 the coefficients of the polynomial part of the distribution. The polynomial fits the lower part of the mass spectrum, which is distorted by the online trigger, and hence should be reproducible in the corresponding reconstructed STARlight sample. In real data, only the coefficients of the polynomial part are fixed to the values obtained from STARlight fits, while the slope of the exponential is left free to vary but it is found to be close to the value found in the fits to the templates.

The fits to the reconstructed STARlight $\mu^+\mu^-$ invariant mass distributions are presented in Appendix C. Fig. C.1(a), C.1(b), C.1(c), and C.1(d) show the fits to the J/ψ distributions with dimuon rapidity lying in the interval $-4 < y < -2.5$, $-4 < y < -3.5$,

$-3.5 < y < -3$, and $-3 < y < -2.5$, respectively. Fig. C.2(a), C.2(b), C.2(c), and C.2(d) instead show the fits to the ψ' distributions with dimuon rapidity lying in the interval $-4 < y < -2.5$, $-4 < y < -3.5$, $-3.5 < y < -3$, and $-3 < y < -2.5$, respectively. Finally, Fig. C.3(a), C.3(b), C.3(c), and C.3(d) show the fits to the background distributions with dimuon rapidity lying in the interval $-4 < y < -2.5$, $-4 < y < -3.5$, $-3.5 < y < -3$, and $-3 < y < -2.5$, respectively.

The yield extraction for the rapidity integrated case, i.e. the dimuon rapidity $y_{\mu\mu}$ satisfying $-4 < y_{\mu\mu} < -2.5$, is shown in Fig. 4.5(a), 4.5(b), 4.5(c), 4.5(d), for 0N0N, 0NXN, XN0N, and XNXN, respectively, where the total fit is shown with a thin red line, the J/ψ distribution with a thick red line, the ψ' with a magenta line, and finally the continuum is shown with a dashed green line. It can be seen that the statistics in all classes except for 0N0N would not allow for too narrow rapidity bins, and as a consequence three equal rapidity bins have been chosen for the rapidity differential version of this analysis. The raw yields for the rapidity differential analysis in the specific 0N0N class, are shown in Fig. 4.6(a), 4.6(b), and 4.6(c). The three rapidity bins are $-4.0 < y < -3.5$, $-3.5 < y < -3.0$, and $-3.0 < y < -2.5$, respectively. The same plots for the 0NXN class are shown in Fig. 4.7(a), 4.7(b), and 4.7(c). The three rapidity bins are $-4.0 < y < -3.5$, $-3.5 < y < -3.0$, and $-3.0 < y < -2.5$, respectively. Those for the XN0N class are shown in Fig. 4.8(a), 4.8(b), and 4.8(c). The three rapidity bins are $-4.0 < y < -3.5$, $-3.5 < y < -3.0$, and $-3.0 < y < -2.5$, respectively. Finally, Fig. 4.9(a), 4.9(b), and 4.9(c) show those for the XNXN class. The three rapidity bins are $-4.0 < y < -3.5$, $-3.5 < y < -3.0$, and $-3.0 < y < -2.5$, respectively.

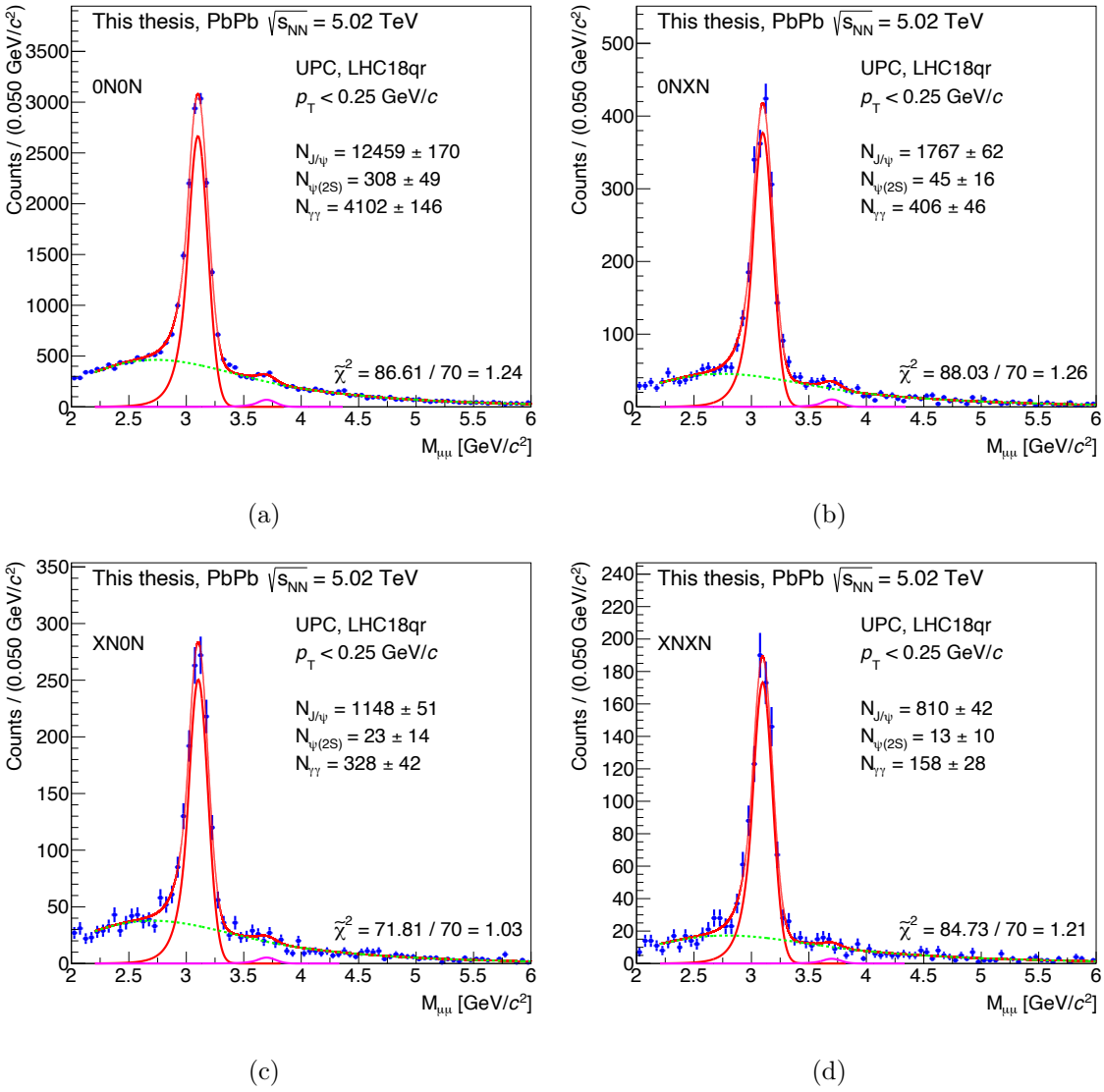


Figure 4.5: Raw yield extraction for the four neutron emission classes in the rapidity interval $-4.0 < y < -2.5$. Fig. 4.5(a), 4.5(b), 4.5(c), and 4.5(d) show the invariant mass distributions for 0N0N, 0NXN, XN0N, and XNXN, respectively.

4.4 p_{T} distributions and incoherent fractions

The p_{T} distributions for the 0N0N, 0NXN, XN0N, and XNXN classes are shown in Fig. 4.10(a), 4.10(b), 4.10(c), and 4.10(d), respectively. The distributions shown here are for dimuon rapidities $-4 < y < -2.5$. As the analysis is carried out with an open

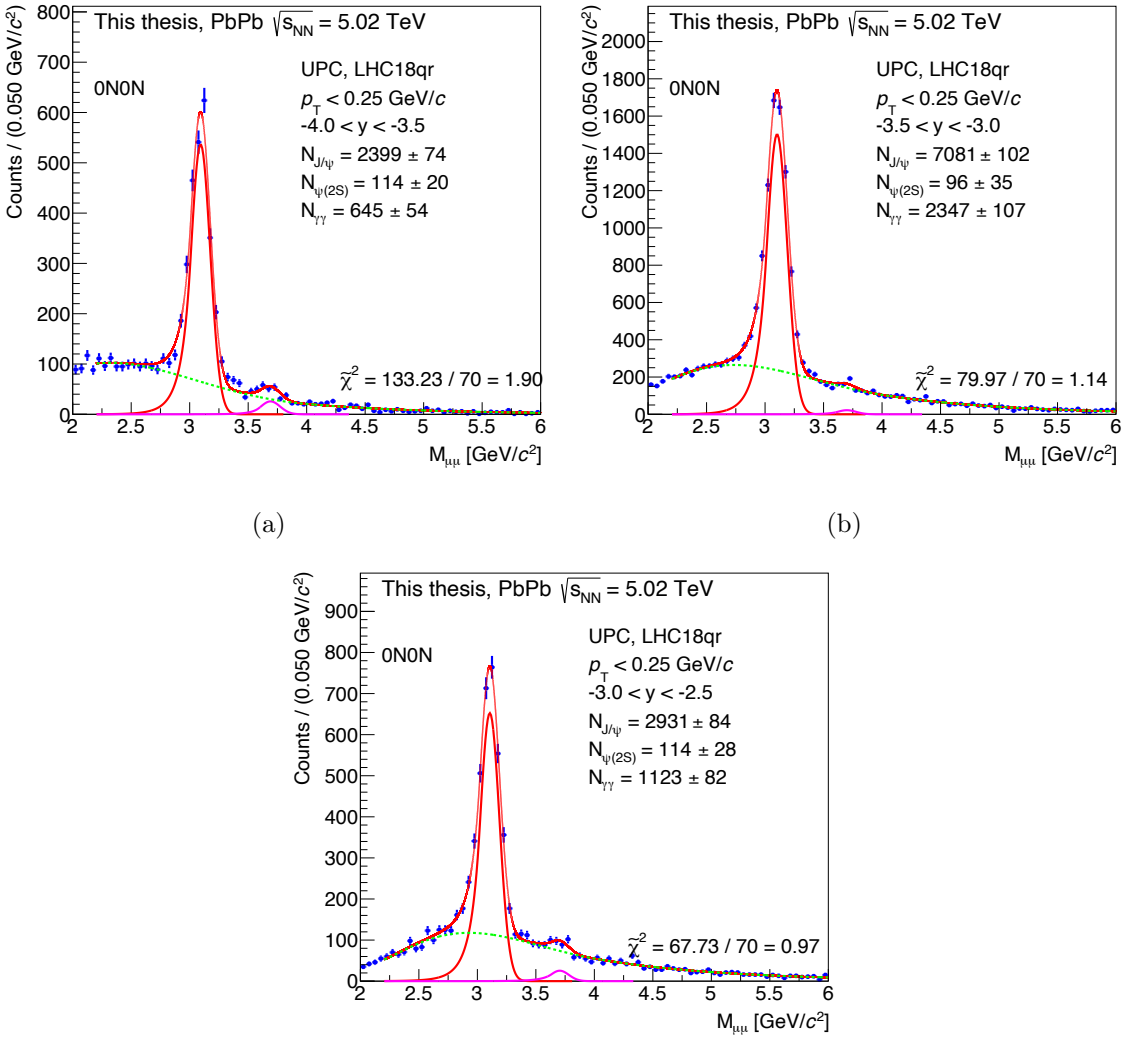


Figure 4.6: Yield extraction for the 0N0N class, in three rapidity intervals. Fig. 4.6(a), 4.6(b), and 4.6(c) show the invariant mass distributions for the rapidity intervals $-4.0 < y < -3.5$, $-3.5 < y < -3.0$, and $-3.0 < y < -2.5$, respectively.

trigger, which only requires a dimuon in the Forward Muon Spectrometer and a veto on the V0A activity[6], the plots also show the p_{T} distributions when additional offline vetoes are imposed. In particular, the plots show in red the distributions that will be fitted, without AD decision flags, in green those events that would be rejected by the ADA

[6]The typical online UPC trigger also requires vetoes on ADA and ADC activities.

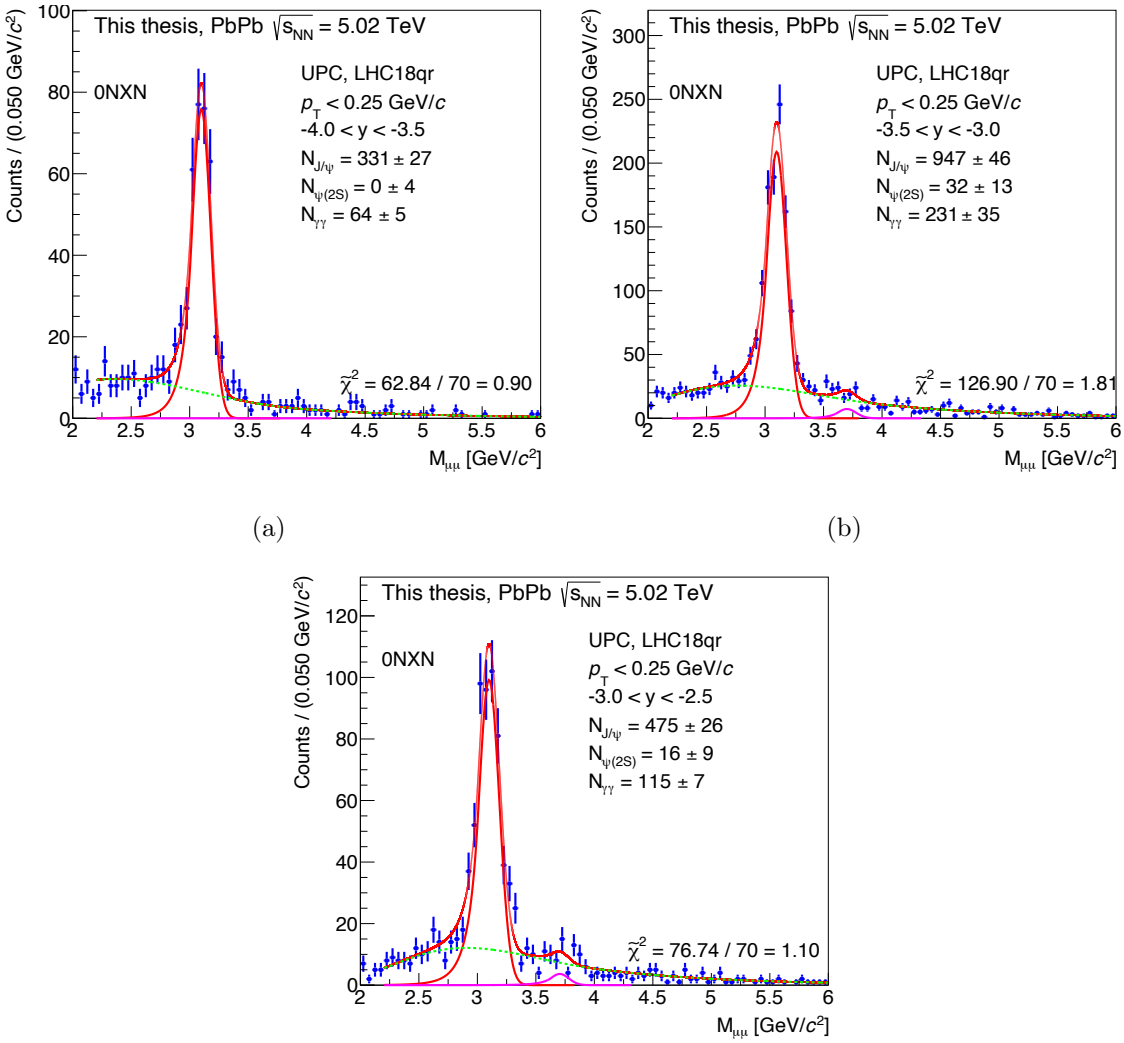


Figure 4.7: Yield extraction for the 0NXN class, in three rapidity intervals. Fig. 4.7(a), 4.7(b), and 4.7(c) show the invariant mass distributions for the rapidity intervals $-4.0 < y < -3.5$, $-3.5 < y < -3.0$, and $-3.0 < y < -2.5$, respectively.

decision flag, in blue those that would be rejected instead by the ADC decisions flags, and finally in yellow those that would be rejected by asking jointly a veto in the ADA and in the ADC. Thus, if the AD decision flags were also to have been imposed, the final distributions will be the sum of the red and yellow curves, minus the green and the blue. Writing the veto on a signal S as $\bar{S}$, the AND of two signals S and X as $S \cdot X$, the OR

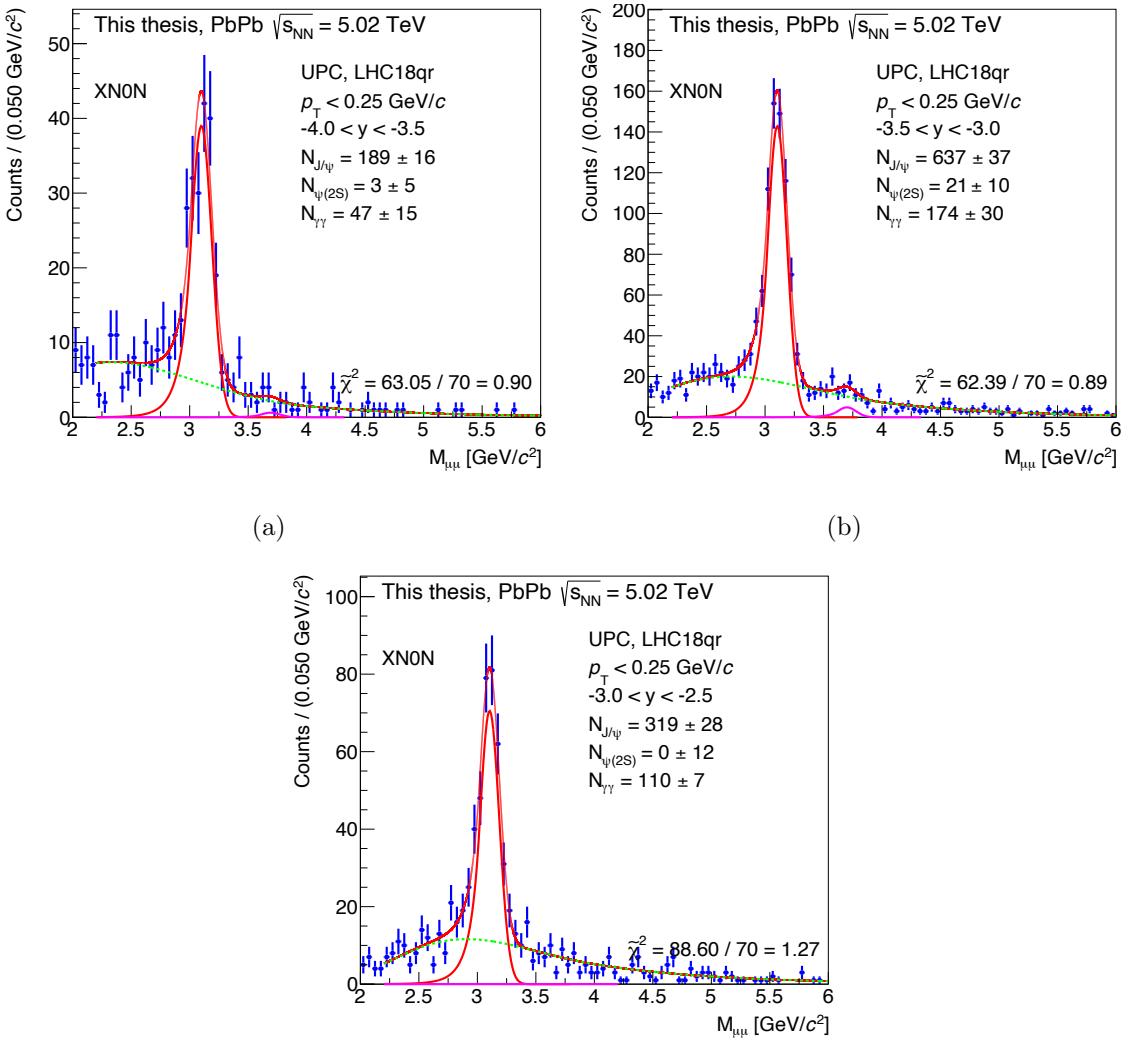


Figure 4.8: Yield extraction for the XN0N class, in three rapidity intervals. Fig. 4.8(a), 4.8(b), and 4.8(c) show the invariant mass distributions for the rapidity intervals $-4.0 < y < -3.5$, $-3.5 < y < -3.0$, and $-3.0 < y < -2.5$, respectively.

as $S \vee X$, and the set that results from the veto $\bar{S}$ as $\{\bar{S}\}$, the set resulting from a veto on AD can be written as $\{\overline{AD}\} = \{\overline{\text{ADA}} \vee \overline{\text{ADC}}\} \setminus \{\overline{\text{ADA}} \cdot \overline{\text{ADC}}\}$, where the difference between two sets A and B is expressed as $A \setminus B$. The veto in ADC, $\overline{\text{ADC}}$, would remove almost all of the events. This is all due to the asymmetric nature of the trigger. It is thus interesting to observe how the the blue curve is mostly contained in the 0NXN class, and,

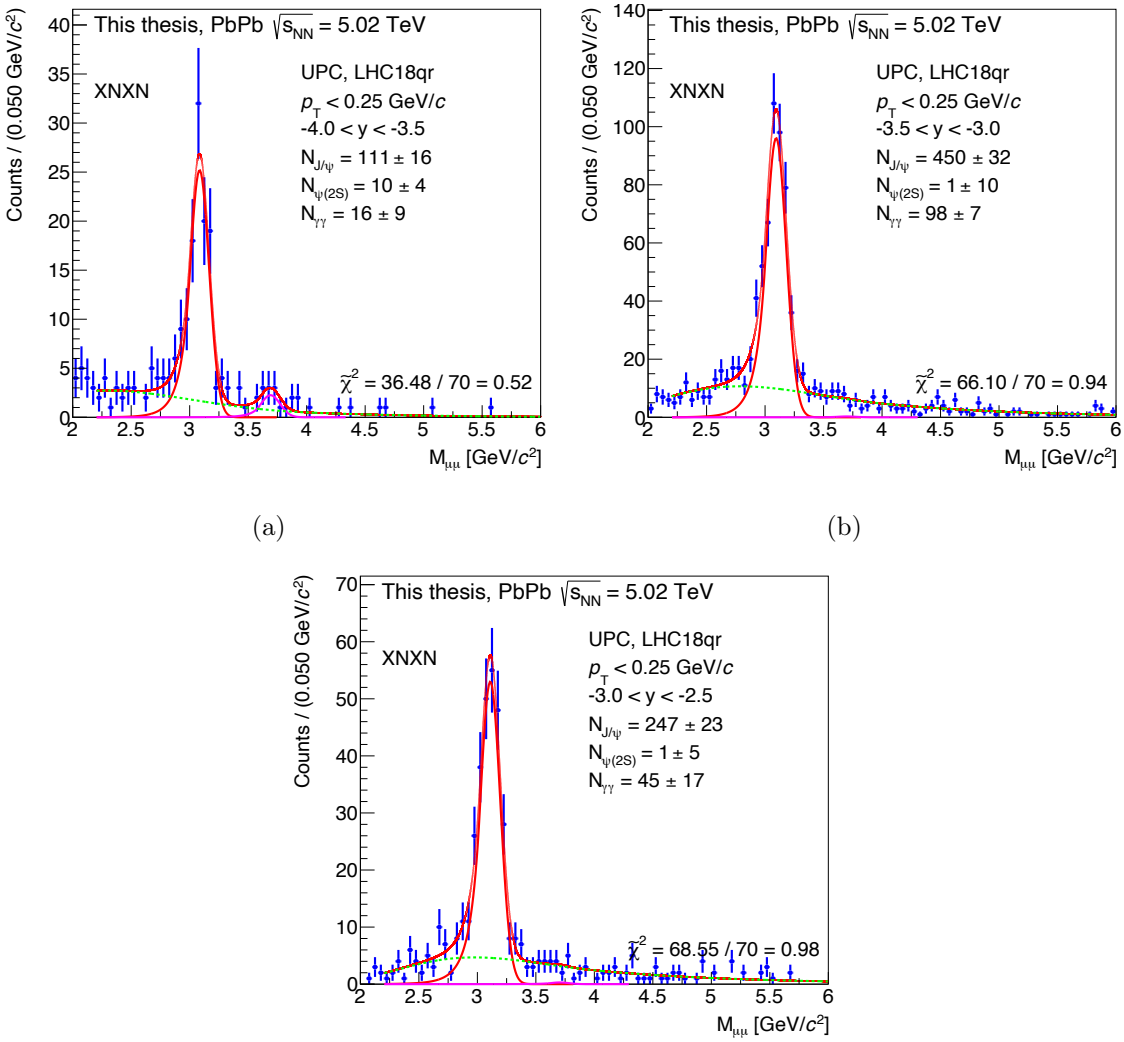


Figure 4.9: Yield extraction for the XNXN class, in three rapidity intervals. Fig. 4.9(a), 4.9(b), and 4.9(c) show the invariant mass distributions for the rapidity intervals $-4.0 < y < -3.5$, $-3.5 < y < -3.0$, and $-3.0 < y < -2.5$, respectively.

with limited statistics, in the XNXN class.

The raw yields obtained in Sec. 4.3 have to be corrected for the effective real contribution of the coherent component to the raw signal integrated in the dimuon p_{T}, $p_{\mathrm{T}}^{\mu\mu}$, range $0 < p_{\mathrm{T}}^{\mu\mu} < 0.25$ GeV/c. A correction factor, the *incoherent fraction*, f_{I}, is

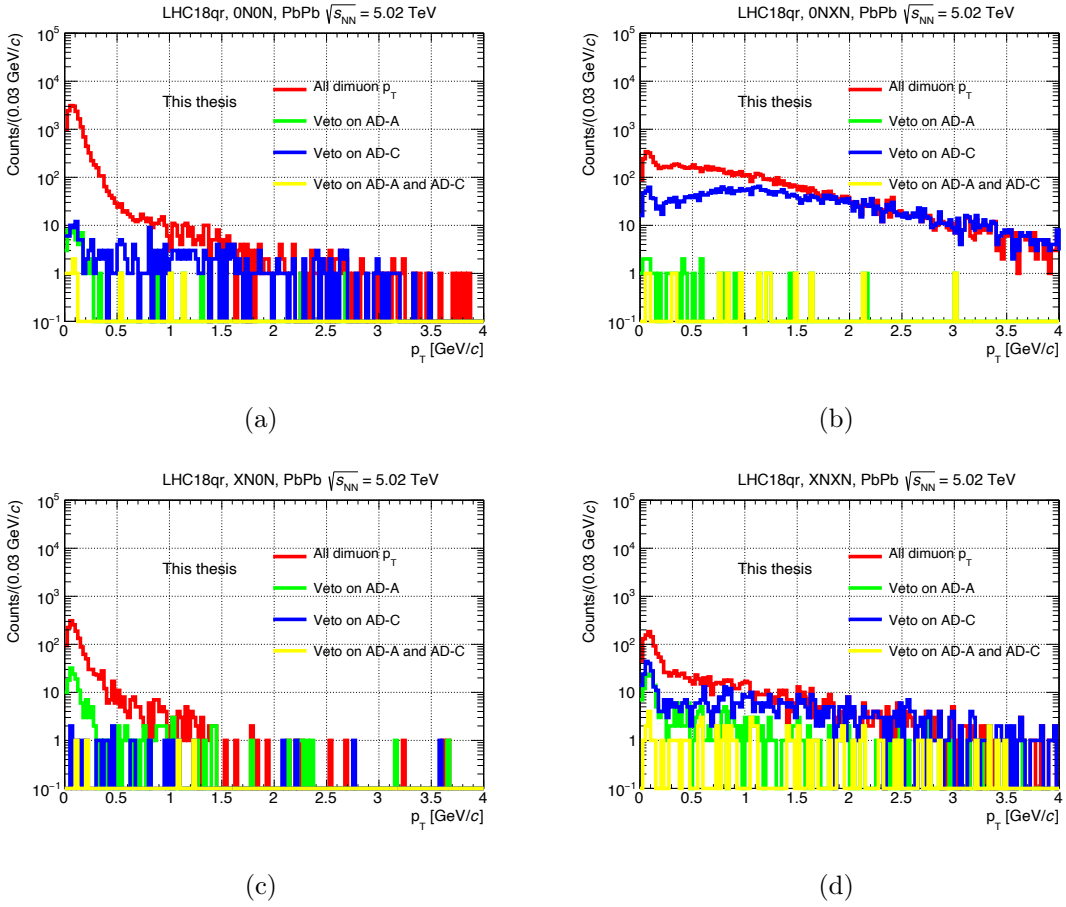


Figure 4.10: Transverse momentum distributions in the four neutron emission classes for dimuon rapidity $-4 < y < -2.5$. In red, the actual p_{T} distribution used in the analysis, in green, the proper subsets of the corresponding events which would be rejected by an offline requirement of the emptiness in ADA. In blue, the analogous distributions if ADC is requested to be empty instead. Finally, in yellow, the proper subset of all the above, namely those events that would be rejected by asking the ADA decision being not empty AND the ADC decision being not empty. Fig. 4.10(a), 4.10(b), 4.10(c), and 4.10(d) show the distributions for 0N0N, 0NXN, XN0N, and XNXN, respectively.

hence introduced to describe the contamination of the coherent signal by incoherent J/ψ photoproduction. It is defined as the ratio of incoherent to coherent J/ψ events, $f_{\mathrm{I}} = N[\text{incoh J}/\psi]/N[\text{coh J}/\psi]$, in the dimuon p_{T} range $0 < p_{\mathrm{T}}^{\mu\mu} < 0.25$ GeV/c. It is

computed by fitting the p_{T} distributions for each class and each rapidity bin. Fig. 4.11 shows a flat trend for the acceptance-cross-efficiency, $A \times \epsilon$, of the incoherent contribution of the p_{T} distributions. The raw p_{T} distributions can thus be directly fitted.

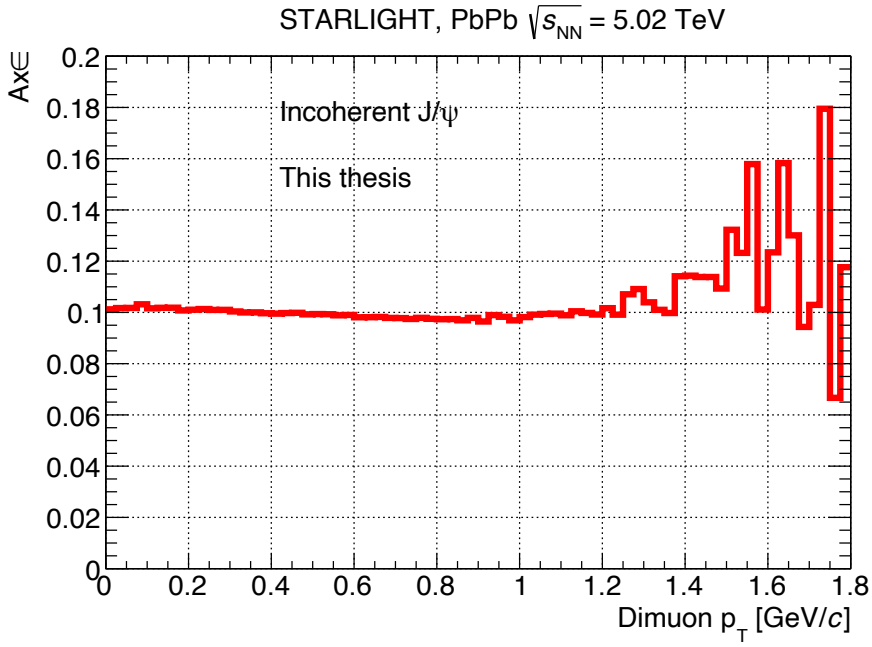


Figure 4.11: $A \times \epsilon$ for p_{T} distributions, as obtained from the corresponding incoherent J/ψ reconstructed STARlight events. The flat trend of the $A \times \epsilon$ up to high p_{T} (limited by statistics, as the generation stops at around 1.8 GeV/c), implies that the p_{T} distributions can directly be fitted without firstly applying $A \times \epsilon$ corrections.

The fit is performed using templates obtained with STARlight reconstructed events, describing coherent and incoherent J/ψ and ψ' photoproduction, coherent and incoherent ψ' feed-down, and a template to describe $\gamma\gamma \longrightarrow \mu^+\mu^-$. The higher p_{T} component, usually called *dissociative component* or incoherent photoproduction accompanied by proton dissociation, is not described by STARlight and requires a special treatment which will be explained below.

As the incoherent fraction enters as a correction to the J/ψ photoproduction cross section, it is quite reasonable for it to be computed with those events lying under the J/ψ

peak i.e. with invariant masses of the dimuon $2.85 < M_{\mu\mu} < 3.35$ GeV/c^2. The first consideration is that the coherent J/ψ p_{T} distribution and the one from $\gamma\gamma \longrightarrow \mu^+\mu^-$ have similar behaviour. So as to simultaneously reduce the correlation between these two templates and help the fit in converging, the normalisation of the latter template is fixed to the yield of the background under the J/ψ peak in the corresponding invariant mass distributions[7]. These features become more apparent with visual inspection of one such fit, e.g. Fig. 4.12(a), 4.12(b), 4.12(c), and 4.12(d), which show the p_{T}-distributions in the four neutron emission classes integrated in rapidity. The relevance of the treatment of the higher-p_{T} component, shown in Fig. 4.12 as *nucleon dissociation*, is evident looking at the XNXN and at the 0NXN especially. In the latter case, it is not negligible with respect to the signal that this analysis is targeting.

As mentioned above, STARlight does not provide a description for this process. The description is based upon the H1 model [34]:

$$\frac{dN}{dp_{\mathrm{T}}} \sim p_{\mathrm{T}} \cdot \left(1 + \frac{b}{n} \cdot p_{\mathrm{T}}^2\right)^{-n} , \tag{4.4}$$

where n is fixed to the H1 parametrisation $n = n_{\mathrm{pd}} = 3.58$. The b parameter, the *slope* of the exponential part of the dissociative component, as Eq. 4.4 can be interpreted as the expansion of an exponential, can be fixed with two different data driven procedures. This leads to two different assessments of the incoherent fraction, and, as expected from the considerations on the nucleon dissociation in 0NXN and XNXN arising from e.g. Fig. 4.12(b) and 4.12(d), a quite significant source of systematic uncertainty in this analysis. The two procedures are the following:

- **method 1**: as the ADA and ADC vetoes have not been used in this analysis[8], the b dependence of the dissociative background can be fixed by fitting the p_{T} distribution

[7] The incoherent fraction is esssentially the ratio of the sum of the two incoherent components to the coherent J/ψ. If the coherent J/ψ is strongly correlated to the $\gamma\gamma$ template the entire incoherent fraction could be wrongly assessed.

[8] Since a more open online trigger was used. The AD decision flags are an offline refinement of the

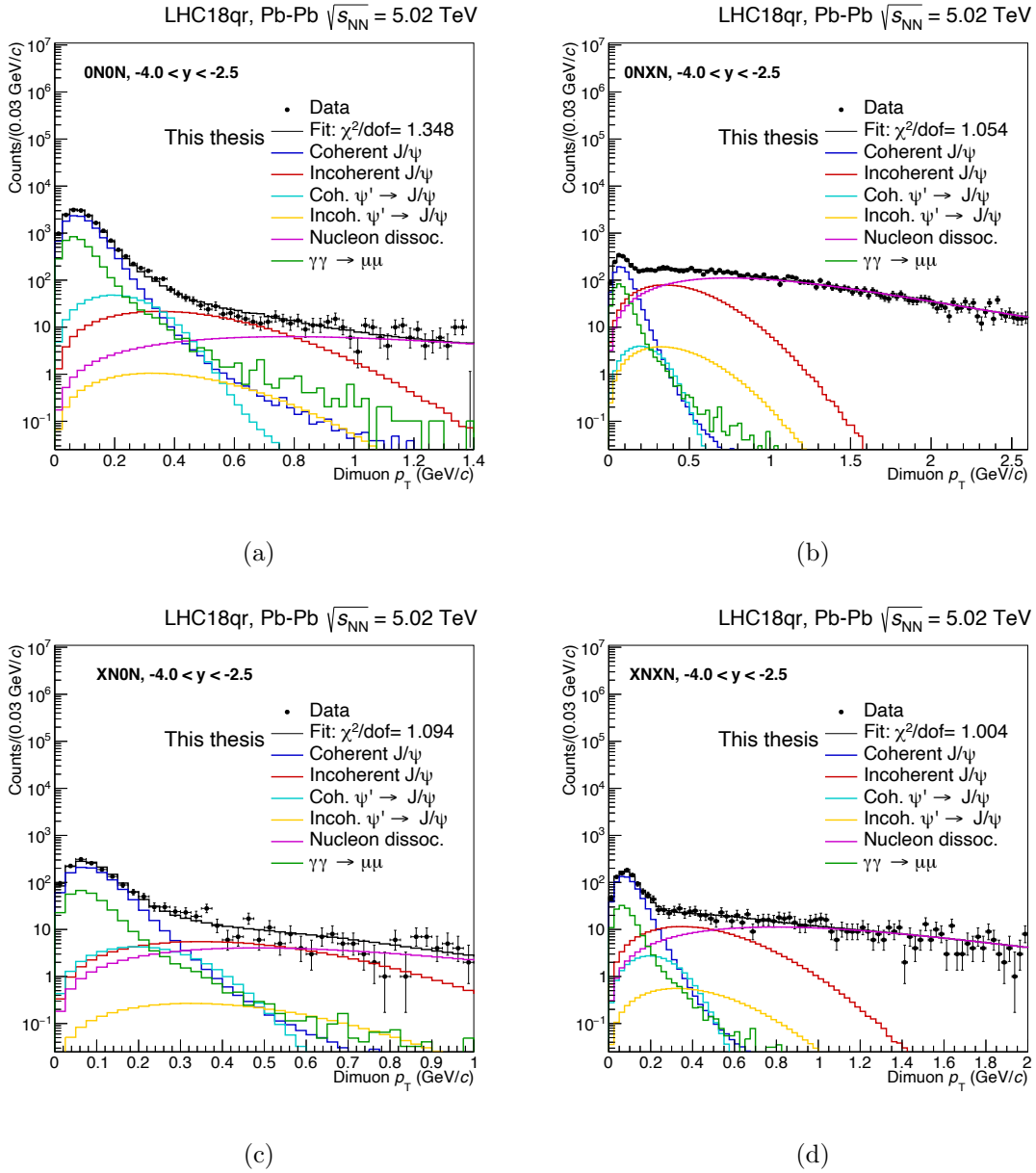


Figure 4.12: Transverse momentum distributions for the four neutron emission classes for the whole ALICE rapidity acceptance. Upper left: 0N0N. Upper right: 0NXN. Lower left: XN0N. Lower right: XNXN.

of the 0NXN class for the events that would have been otherwise removed due to the

online trigger inputs, as they are computed by averaging the AD response over 12 bunch crossings before and after the bunch crossing of interest.

vetoes[9]. As is apparent from Fig. 4.12(c), it contains most of the nucleon dissociation component while also having a limited coherent J/ψ signal. The fit is performed in the p_{T} region [0.2 , 3] GeV/c to further suppress the already limited coherent J/ψ contamination. The b parameter so obtained, is then fixed inside the p_{T} fits of each neutron emission class and each rapidity interval;

- **method 2**: another procedure is to do a first fit while leaving the b parameter free in the complete data sample i.e. all dimuons in the J/ψ mass peak region with rapidity $-4.0 < y < -2.5$, and then repeat the fit in all classes and all rapidity intervals with the b parameter fixed to the result of the first fit.

The incoherent component f_{I} can then be assessed for each class and each rapidity range with the fit procedure here outlined, as shown in Fig. 4.12(a), 4.13(a), 4.13(b), and 4.13(c) for 0N0N, Fig. 4.12(b), 4.14(a), 4.14(b), 4.14(c) for 0NXN, Fig. 4.12(c), 4.15(a), 4.15(b), 4.15(c) for XN0N, and Fig. 4.12(d), 4.16(a), 4.16(b), 4.16(c) for XNXN.

The incoherent fractions computed with the two different methods are presented in Table 4.8. The table contains the incoherent fractions for all neutron emission classes and each rapidity interval considered in this measurement. Note that the incoherent fractions appear in the denominator of the cross sections, as a correction factor of the form $(1 + f_{\mathrm{I}} + \mathrm{X})$, which is explained below. As such, the impact of the incoherent fraction is much smaller than would happen if it were a simple multiplicative factor. However, the incoherent fraction *is* a major correction for the 0NXN and XNXN classes. As the higher p_{T} contribution is quite large for these classes, it is expected that the two methods proposed for computing the incoherent fractions will lead to quite different results. This is also shown in Table 4.8. The difference between the two methods is taken as a systematic uncertainty (the main systematic uncertainty for 0NXN and XN0N, as is explained

[9]The corresponding curve is essentially the blue curve in Fig. 4.10(b), where also the negligible contribution from the ADA vetoed events was added, i.e. the green minus yellow curves.

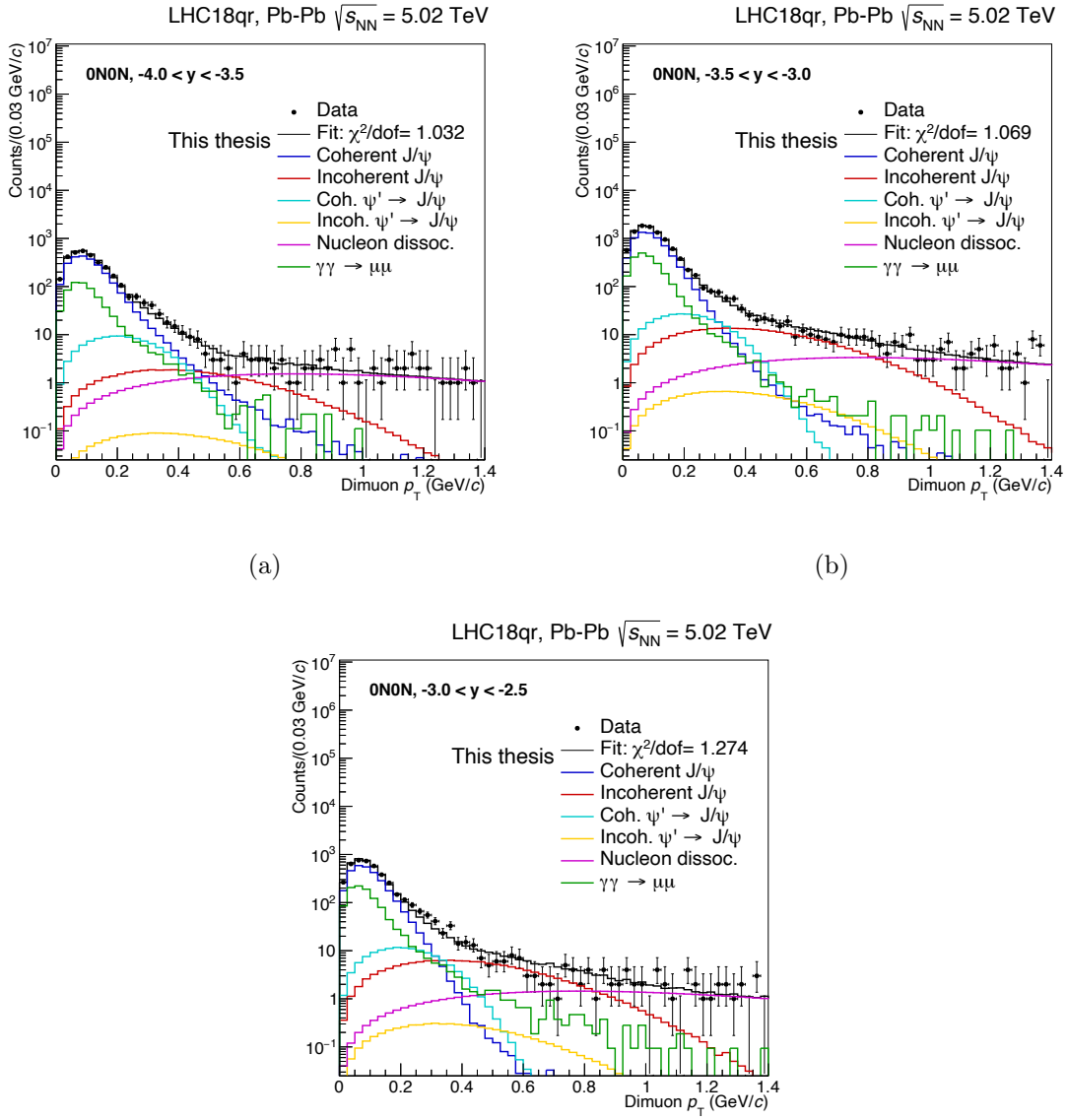


Figure 4.13: Transverse momentum distributions for the 0N0N class. Upper left: $-4.0 < y < -3.5$. Upper right: $-3.5 < y < -3.0$. Lower centre: $-3.0 < y < -2.5$.

below).

Table 4.8: Summary table with the incoherent fractions. The values are obtained with both methods in neutron emission classes as a function of rapidity. A comparison with the corresponding value of the feed-down, f_{D}, is also provided.

Class	y	f_{I} method 1	f_{I} method 2	f_{D}
0N0N	$-4 < y < -2.5$	1.20%	0.79%	5.50%
	$-4 < y < -3.5$	0.70%	0.33%	5.50%
	$-3.5 < y < -3$	1.30%	0.89%	5.50%
	$-3 < y < -2.5$	1.40%	1.02%	5.50%
0NXN	$-4 < y < -2.5$	88.30%	68.16%	5.50%
	$-4 < y < -3.5$	171.00%	121.23%	5.50%
	$-3.5 < y < -3$	91.10%	69.37%	5.50%
	$-3 < y < -2.5$	50.90%	41.83%	5.50%
XN0N	$-4 < y < -2.5$	5.20%	4.35%	5.50%
	$-4 < y < -3.5$	2.70%	2.17%	5.50%
	$-3.5 < y < -3$	4.80%	3.90%	5.50%
	$-3 < y < -2.5$	7.70%	7.09%	5.50%
XNXN	$-4 < y < -2.5$	14.50%	11.43%	5.50%
	$-4 < y < -3.5$	16.50%	14.27%	5.50%
	$-3.5 < y < -3$	15.90%	12.58%	5.50%
	$-3 < y < -2.5$	11.80%	10.21%	5.50%

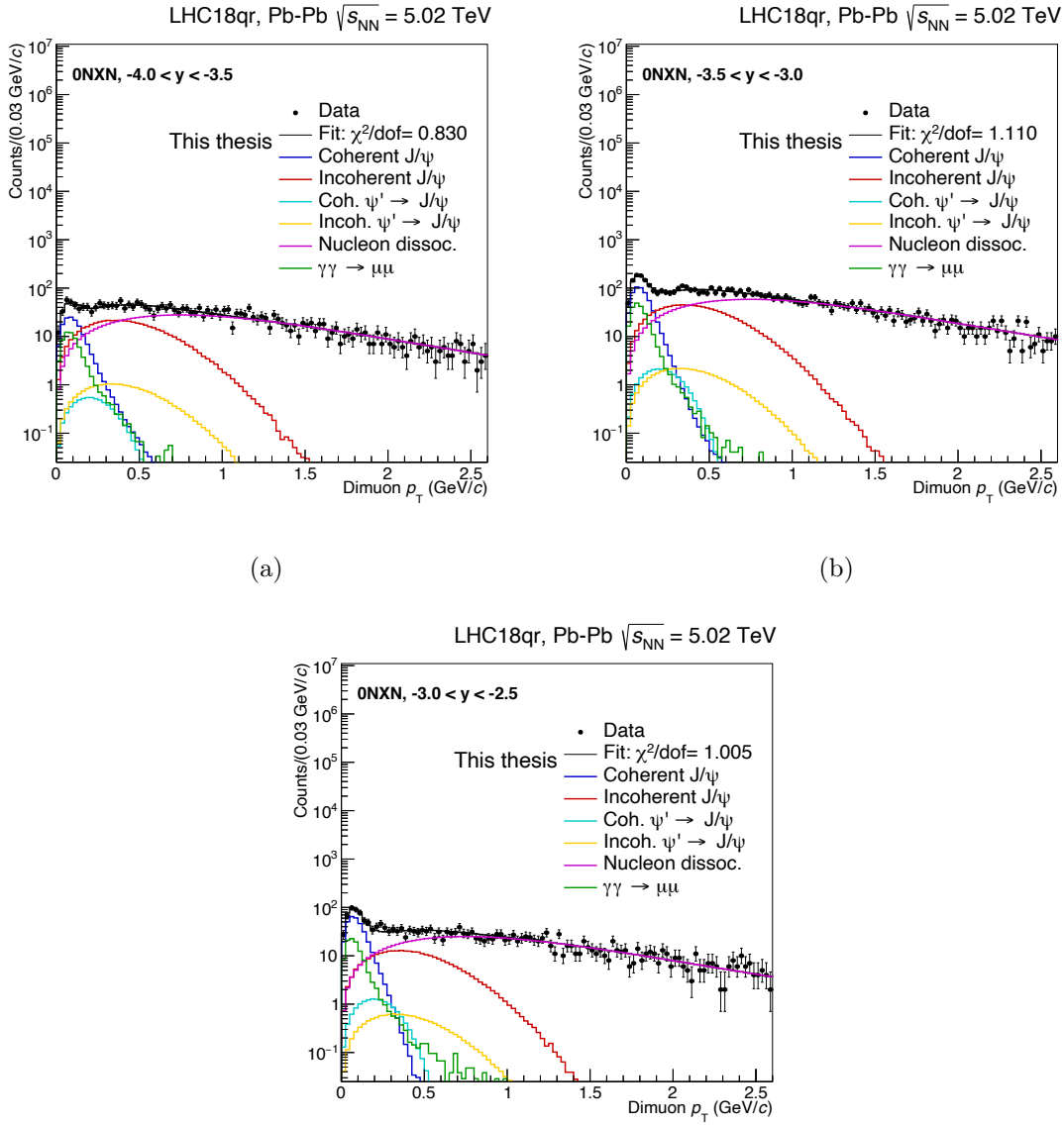


Figure 4.14: Transverse momentum distributions for the 0NXN class. Upper left: $-4.0 < y < -3.5$. Upper right: $-3.5 < y < -3.0$. Lower centre: $-3.0 < y < -2.5$.

4.5 Efficiency

The $A \times \epsilon$ acceptance-cross-efficiency values are computed by analysing reconstructed and generated coherent J/ψ STARlight events. The generated events have to pass the

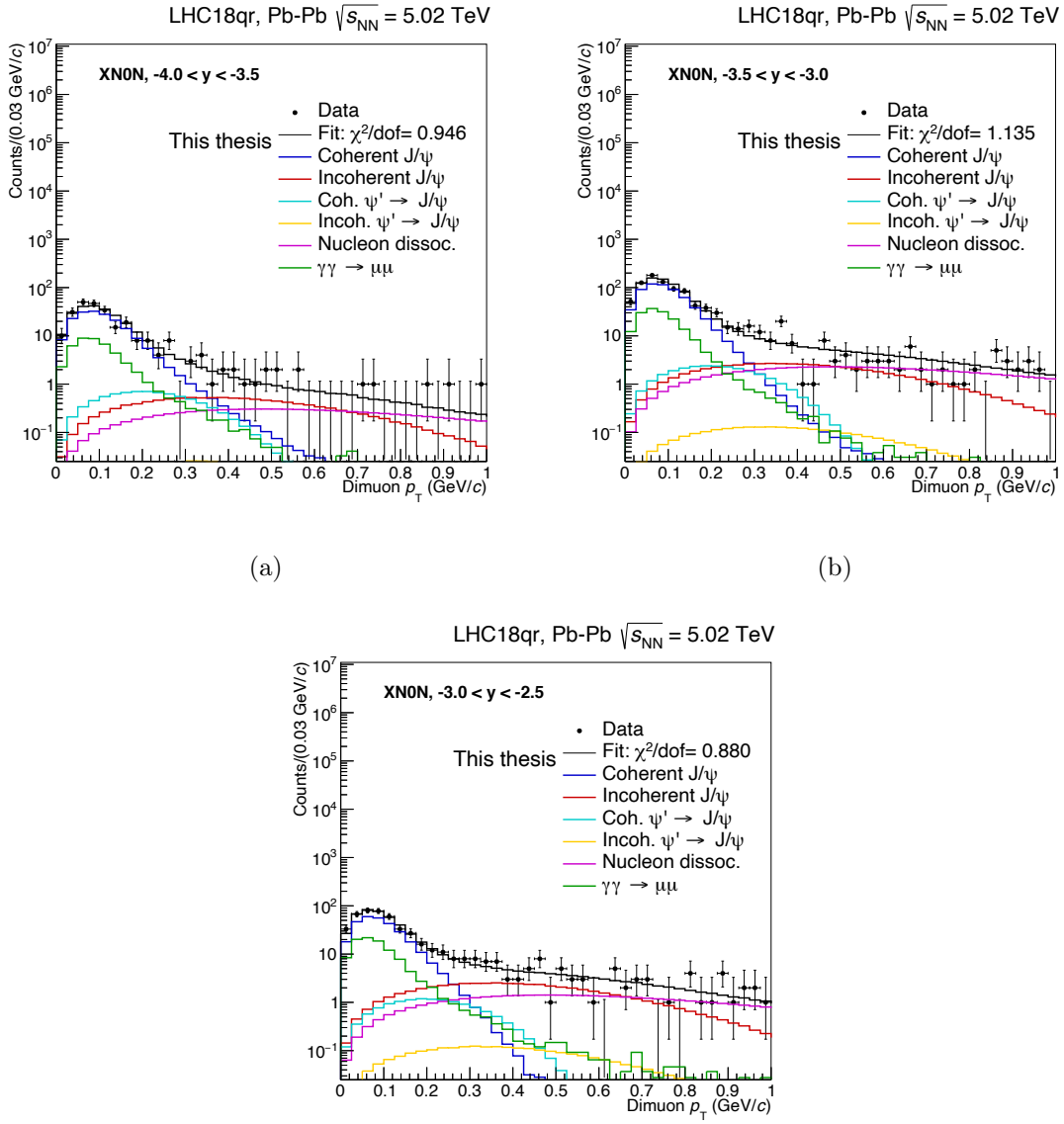


Figure 4.15: Transverse momentum distributions for the XN0N class. Upper left: $-4.0 < y < -3.5$. Upper right: $-3.5 < y < -3.0$. Lower centre: $-3.0 < y < -2.5$.

following selection:

- correct online trigger: there is no trigger class in the simulations, so the activity of the relevant detectors is checked and an online trigger is emulated by requesting no

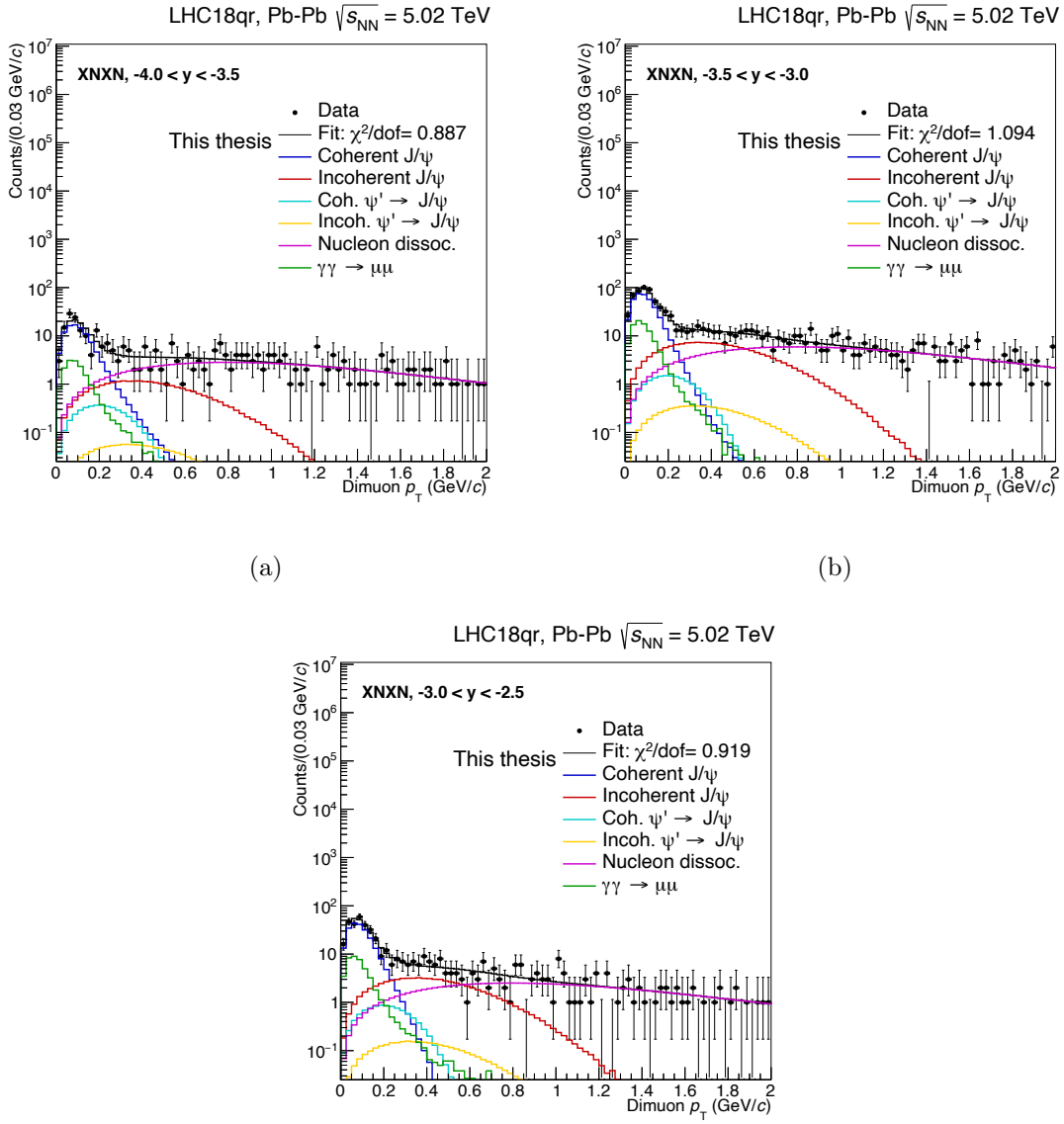


Figure 4.16: Transverse momentum distributions for the XNXN class. Upper left: $-4.0 < y < -3.5$. Upper right: $-3.5 < y < -3.0$. Lower centre: $-3.0 < y < -2.5$.

activity on the V0A;

- a dimuon in the acceptance of the forward muon spectrometer;
- the dimuon rapidity is required to be within the proper rapidity interval i.e. either

Table 4.9: $A \times \epsilon$ values for coherent J/ψ. The values are differential only in rapidity intervals. No simulation is available for neutron emission classes.

	$A \times \epsilon$
$-4 < y < -2.5$	11.8%
$-4 < y < -3.5$	9.7%
$-3.5 < y < -3$	19.5%
$-3 < y < -2.5$	7.0%

$-4 < y < -2.5$, or $-4 < y < -3.5$, $-3.5 < y < -3$, $-3 < y < -2.5$.

The reconstructed events follow the same selections as for real data. The final $A \times \epsilon$ values are then computed as the ratio of the surviving reconstructed events to the corresponding generated events in the corresponding rapidity interval, e.g. as in the following Eq. 4.5:

$$A \times \epsilon(-4 < y < -3.5) = \frac{\text{reconstructed events}(-4 < y < -3.5)}{\text{generated events}(-4 < y < -3.5)} \ . \tag{4.5}$$

The values are presented in Table 4.9.

4.6 Feed-down f_{D}

This measurement can be considered a more differential version of the recent coherent J/ψ measurement at forward rapidity by the ALICE Collaboration [5]. In the latter, the feed-down contribution due to the decay of ψ', i.e. the process $\psi' \longrightarrow \mathrm{J}/\psi + \mathrm{X}$, is computed with a mixture of data-driven and simulation-driven contributions. In fact, it is possible to measure the raw yields of J/ψ and ψ', $N[\mathrm{J}/\psi]$ and $N[\psi']$, respectively, from invariant mass distributions. They are used to compute the ratio R_N:

$$R_N = \frac{N[\psi']}{N[\mathrm{J}/\psi]} \ , \tag{4.6}$$

Table 4.10: Branching ratio values taken from the PDG. Both central values and systematic uncertainties are presented.

	BR [%]	syst.[%]
$J/\psi \to \mu\mu$	5.961	0.033
$\psi' \to \mu\mu$	0.80	0.06
$\psi' \to J/\psi + X$	61.4	0.6

which is then used to compute the quantity R, which can be considered an estimate of the coherent ψ' to J/ψ ratio:

$$R = \frac{R_N \cdot A \times \epsilon(J/\psi) \cdot BR(J/\psi \to \mu\mu)}{BR(\psi' \to \mu\mu) \cdot A \times \epsilon(\psi') - R_N \cdot A \times \epsilon(\psi' \to J/\psi) \cdot BR(\psi' \to J/\psi) \cdot BR(J/\psi \to \mu\mu)} , \tag{4.7}$$

where $A \times \epsilon(J/\psi)$ refer to the values presented in Table 4.9, $A \times \epsilon(\psi')$ to the corresponding values when coherent ψ' samples are used instead of J/ψ, and $A \times \epsilon(\psi' \to J/\psi)$ are instead the $A \times \epsilon$ values computed when the feed-down sample for $\psi' \longrightarrow J/\psi + X$ is used. The branching ratios $BR(\psi' \to J/\psi)$, $BR(J/\psi \to \mu\mu)$ and $BR(\psi' \to \mu\mu)$ are instead presented in Table 4.10. The fraction of feed-down J/ψ from the decay of ψ', f_D, is measured using the quantity R:

$$f_D = \frac{N[\text{feed-down } J/\psi]}{N[\text{coh } J/\psi]} = R \cdot \frac{A \times \epsilon(\psi' \to J/\psi)}{A \times \epsilon(J/\psi)} \cdot BR(\psi' \to J/\psi) \ . \tag{4.8}$$

The feed-down fractions f_D in [5] amount to $f_D = (5.5 \pm 1.0)\%$. In this measurement, the f_D have firstly been measured, and then found to be consistent with the values reported in [5], for all neutron emission classes and rapidity intervals. As the statistics are quite small for e.g. XNXN, the f_D is then taken as a flat $f_D = (5.5 \pm 1.0)\%$ for all neutron emission classes and all rapidity intervals.

4.7 ZDC migration

The ZDC classes obtained so far, are affected by migration effects. These result from pile up in the ZDC and from neutron detection efficiency. Let us take for example the case where an event is classified as 0N0N, so no neutron on either side. This might have been a XNXN event, with one neutron on the A side and one neutron on the C side. The neutron efficiency might have resulted in the missed detection of both neutrons, thus demoting the event to 0N0N. In another example, let us assume that the event was originally a 0N0N event. However, pile up in the C side leads to the event being promoted to a different class, so that it ends up classified as 0NXN. This section aims to provide the procedure in how to properly account for these effects. It also provides a procedure for how to account for the systematic effect due to the uncertainties on both pile up and efficiency factors.

Firstly, the following quantities will be used below: ϵ_A and ϵ_C the efficiencies on the A and C side of the neutron ZDC, respectively, p_A and p_C the corresponding pile up probabilities. The populations of each class before corrections, i.e. the *observed* number of events, are called N_i, e.g. N_{0N0N} and N_{0NXN}. The populations after corrections, i.e. the *really occurred* events, are called M_i instead, e.g. M_{0N0N} and M_{0NXN}.

The expression describing how migration affects the 0N0N class is given by Eq. 4.9:

$$\begin{aligned} N_{\text{0N0N}} = {} & M_{\text{0N0N}} \left[(1-p_A)\cdot(1-p_C)\right] + \\ & + M_{\text{0NXN}} \left[(1-\epsilon_C)\cdot(1-p_A)\cdot(1-p_C)\right] + \\ & + M_{\text{XN0N}} \left[(1-\epsilon_A)\cdot(1-p_A)\cdot(1-p_C)\right] + \\ & + M_{\text{XNXN}} \left[(1-\epsilon_A)\cdot(1-\epsilon_C)\cdot(1-p_A)\cdot(1-p_C)\right] \ . \end{aligned} \tag{4.9}$$

It is possible to analyse it bit by bit. The observed population for the 0N0N class, will be driven by the true 0N0N events if no pile up happened on A or C side, leading to the gain term $M_{\text{0N0N}}\left[(1-p_A)\cdot(1-p_C)\right]$ in Eq. 4.9. There is also a gain from the XN0N class if there is no pile up in both the A and C sides, but a neutron is missed on the A

side, leading to the gain term $M_{\mathrm{XN0N}}\left[(1-\epsilon_A)\cdot(1-p_A)\cdot(1-p_C)\right]$. This justifies the gain term $M_{\mathrm{0NXN}}\left[(1-\epsilon_C)\cdot(1-p_A)\cdot(1-p_C)\right]$ for the mirrored topology. Finally, the XNXN class will be demoted to 0N0N if there is no pile up on the A side but the neutron was missed on both sides.

The expressions for the other classes can be derived in a similar fashion, as shown in Eq. 4.10, 4.11, and 4.12.

$$\begin{aligned}
N_{\mathrm{0NXN}} = {} & M_{\mathrm{0NXN}} + \\
& + M_{\mathrm{0N0N}}\left[p_C\cdot(1-p_A)\right] - \\
& - M_{\mathrm{0NXN}}\left[(1-\epsilon_C)\cdot(1-p_A)\cdot(1-p_C)+\epsilon_C\cdot p_A+p_A+(1-\epsilon_C)\cdot p_A\cdot p_C\right] + \\
& + M_{\mathrm{XN0N}}\cdot(1-\epsilon_A)\cdot(1-p_A)p_C + \\
& + M_{\mathrm{XNXN}}\cdot(1-\epsilon_A)\cdot(1-p_A)\cdot\left[\epsilon_C+(1-\epsilon_C)\cdot p_C\right]
\end{aligned} \tag{4.10}$$

$$\begin{aligned}
N_{\mathrm{XN0N}} = {} & M_{\mathrm{XN0N}} + \\
& + M_{\mathrm{0N0N}}\left[p_A\cdot(1-p_C)\right] + \\
& + M_{\mathrm{0NXN}}\cdot(1-\epsilon_C)\cdot(1-p_C)\cdot p_A - \\
& - M_{\mathrm{XN0N}}\left[(1-\epsilon_A)\cdot(1-p_A)\cdot(1-p_C)+p_C+\epsilon_A\cdot p_C+(1-\epsilon_A)\cdot p_A\cdot p_C\right] + \\
& + M_{\mathrm{XNXN}}\cdot(1-\epsilon_C)\cdot(1-p_C)\cdot\left[\epsilon_A+(1-\epsilon_A)\cdot p_A\right]
\end{aligned} \tag{4.11}$$

$$\begin{aligned}
N_{\mathrm{XNXN}} = {} & M_{\mathrm{XNXN}} + \\
& + M_{\mathrm{0N0N}}\left[p_C\cdot p_A\right] - \\
& + M_{\mathrm{0NXN}}\cdot\left[\epsilon_C\cdot p_A+(1-\epsilon_C)\cdot p_A\cdot p_C\right] + \\
& + M_{\mathrm{XN0N}}\cdot\left[\epsilon_A\cdot p_C+(1-\epsilon_A)\cdot p_A\cdot p_C\right] - \\
& - M_{\mathrm{XNXN}}\cdot\left[(1-\epsilon_A)\cdot(1-p_A)\cdot(\epsilon_C+(1-\epsilon_C)\cdot p_C)+\right. \\
& \left.+(1-\epsilon_C)\cdot(1-p_C)\cdot(\epsilon_A+(1-\epsilon_A)\cdot p_A)+(1-\epsilon_A)\cdot(1-\epsilon_C)\cdot(1-p_A)\cdot(1-p_C)\right]
\end{aligned} \tag{4.12}$$

It is quite convenient to group Eq. 4.9, 4.10, 4.11, and 4.12 together and write them in matrix form as shown in Eq. 4.13, where the matrix **C** represents the ZDC migration matrix. The notation can also quite readily be applied to the rapidity differential analysis.

$$\begin{bmatrix} N_{\mathrm{0N0N}} \\ N_{\mathrm{0NXN}} \\ N_{\mathrm{XN0N}} \\ N_{\mathrm{XNXN}} \end{bmatrix} = \mathbf{C} \cdot \begin{bmatrix} M_{\mathrm{0N0N}} \\ M_{\mathrm{0NXN}} \\ M_{\mathrm{XN0N}} \\ M_{\mathrm{XNXN}} \end{bmatrix} . \tag{4.13}$$

The *really occurred events* can then be found by inverting the ZDC migration matrix as shown in Eq. 4.14.

$$\begin{bmatrix} M_{\mathrm{0N0N}} \\ M_{\mathrm{0NXN}} \\ M_{\mathrm{XN0N}} \\ M_{\mathrm{XNXN}} \end{bmatrix} = \mathbf{C}^{-1} \cdot \begin{bmatrix} N_{\mathrm{0N0N}} \\ N_{\mathrm{0NXN}} \\ N_{\mathrm{XN0N}} \\ N_{\mathrm{XNXN}} \end{bmatrix} . \tag{4.14}$$

A quite easy extreme case, which can be considered to validate the procedure, is when the pile up is negligible, and the ZDC is fully efficient in detecting neutrons. Then both the matrix **C** and its inverse $\mathbf{C}^{-1}$ are diagonal matrices (quite evidently $\mathbf{C} = \mathbb{1}$). As it turns out, the pile up probability is quite small and the ZDC performance is extremely good, as can be seen in Table 4.11. Finally, Table 4.12 shows the correction matrix after inversion. These are the values needed to correct the observed raw yields.

Table 4.11: Pile up probabilities and neutron ZDC detection efficiencies. The values are obtained with a separate study internal to the ALICE Collaboration.

$\mathbf{p_A}$	2.37%±0.05%
$\mathbf{p_C}$	2.38%±0.06%
$\epsilon_{\mathbf{A}}$	92% ± 4.0%
$\epsilon_{\mathbf{C}}$	90% ± 6.0%

Table 4.12: ZDC migration correction matrix after inversion. These values are directly applied to compute the corrected cross sections.

	$\mathbf{M}_{0N0N}$	$\mathbf{M}_{0NXN}$	$\mathbf{M}_{XN0N}$	$\mathbf{M}_{XNXN}$
$\mathbf{N}_{0N0N}$	1.054	-0.114	-0.08931	0.009662
$\mathbf{N}_{0NXN}$	-0.0278	1.14	0.002356	-0.09662
$\mathbf{N}_{XN0N}$	-0.0271	0.002932	1.116	-0.1208
$\mathbf{N}_{XNXN}$	0.0007148	-0.02932	-0.02944	1.208

4.7.1 Propagation of the pile up and efficiency uncertainties

As shown in Table 4.11, both the pile up probabilities and the neutron detection efficiencies have an uncertainty. This has to be propagated back to the *really occurred* events. The procedure used in this analysis follows the principles of variational techniques. Taking Eq. 4.14, the systematic uncertainty due to pile up and efficiency are taken, separately, as the maximum deviation from the central value (of the *really occurred events*) due to either an upward or downward variation of pile up and efficiency i.e. by operating in separate instances the substitution shown in the following Eq. 4.15:

$$\begin{bmatrix} \epsilon \\ \mathrm{p} \end{bmatrix} \longrightarrow \begin{bmatrix} \epsilon \\ \mathrm{p} \end{bmatrix} \pm \begin{bmatrix} \Delta\epsilon \\ \Delta\mathrm{p} \end{bmatrix} . \tag{4.15}$$

Table 4.13 shows the systematic effect due to the pile up and neutron detection efficiency.

4.8 Luminosity

Luminosity has been computed specifically for this data set, see Fig. 4.17. The integrated luminosity for the 2018 data set was estimated from the counts of a reference trigger, N^{ref}, which is based on a multiplicity selection in V0. Its visible cross section, σ^{vis}, is

Table 4.13: Systematic effect due to the variation of one sigma of pile up and neutron detection efficiency. The numbers shown represent half the discrepancy between the effects of an upward and a downward variation of one sigma of the corresponding parameters.

	y = [-4, -2.5]		**y = [-4, -3.5]**		**y = [-3.5, -3]**		**y = [-3, -2.5]**	
	p (%)	ϵ (%)	**p (%)**	ϵ (%)	**p (%)**	ϵ (%)	**p (%)**	ϵ (%)
0N0N	0.12	0.71	0.12	0.52	0.12	0.68	0.12	0.96
0NXN	−1.2	−0.30	−2.46	1.81	−1.39	0.20	−0.74	−1.44
XN0N	−0.68	2.56	−0.82	1.33	−0.70	2.49	−0.56	3.37
XNXN	−0.11	−11.10	−0.11	−11.13	−0.11	−11.11	−0.12	−11.09

computed with estimates of the inelastic Pb–Pb cross section [5, 80, 81]. The recorded luminosity $\mathcal{L}_{\rm rec}$ is then measured as the ratio:

$$\mathcal{L}_{\rm rec} = \frac{N^{\rm ref}}{\sigma^{\rm vis}} \cdot \frac{\mu}{1 - e^{-\mu}} \cdot R_{\rm LF} \ , \tag{4.16}$$

where μ is the average number of collisions for bunch crossings and it is computed as $\mu = -\ln(1 - N^{\rm ref}/N^{\rm bc})$, with $N^{\rm bc}$ the total number of beam-beam bunch crossings, whereas $R_{\rm LF}$ is the trigger lifetime, and is the fraction of UPC triggers which were accepted by the trigger electronics.

The analysed integrated luminosity, $\mathcal{L}$, is then measured as $\mathcal{L} = \mathcal{L}_{\rm rec} \cdot N^{\rm ref}_{\rm sample}/N^{\rm ref}$, since the number of triggers of the sample $N^{\rm ref}_{\rm sample}$ is lower than $N^{\rm ref}$ which were fired, due to losses in data reconstruction. The analysed integrated luminosity finally amounts to $\mathcal{L} = 533\ \mu{\rm b}^{-1} \pm 5\%$ [5].

4.9 Correction for events lost due to V0A veto

A more open online trigger was used for the measurement of coherent J/ψ photoproduction in neutron emission classes. Contrarily to the typical UPC trigger classes used in ALICE,

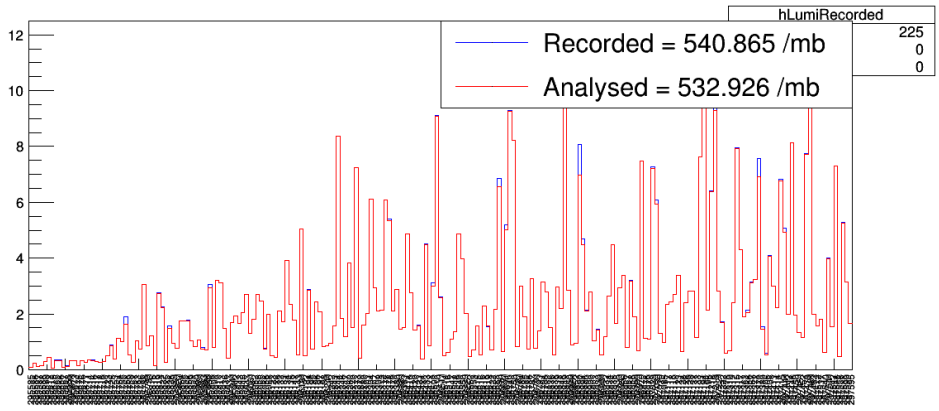


Figure 4.17: Luminosity of the sample used for the neutron emission measurement.

it requires a dimuon in the Forward Muon Spectrometer and a veto on the signal of the V0A[10]. The V0A veto is also enforced at offline level by requiring V0A to be empty.

Two processes can lead to loss of events due to V0A:

- charged particle production due to a collision of a different pair of ions in the same bunch crossing, i.e. pile-up;

- charged particle production due to the same ion pair that was involved in the production of the vector meson, e.g. (but not only) pion photoproduction from additional photon exchanges.

The correction factors have to be computed only for the XN0N and XNXN classes, where there is particle production on the A side, and an event with neutrons may thus be vetoed.

The correction factors F, where F is treated independently for the XN0N and XNXN classes, are obtained as the ratio of the number of J/ψ truly observed to those which

[10]Other trigger classes also require vetoes on ADA and ADC.

really occurred in the detector, as in the following Eq. 4.17:

$$F = \frac{N_{\mathrm{J}/\psi(\mathrm{seen})}}{N_{\mathrm{J}/\psi(\mathrm{true})}} = \\ = \frac{N_{\mathrm{J}/\psi \text{ and !V0A}} + N^{\mathrm{PU}}_{\mathrm{J}/\psi \text{ and !V0A}}}{\frac{N_{\mathrm{J}/\psi \text{ and V0A}} - N^{\mathrm{PU}}_{\mathrm{J}/\psi \text{ and V0A}}}{1-\varepsilon_{V0A}} + N_{\mathrm{J}/\psi \text{ and !V0A}} + N^{\mathrm{PU}}_{\mathrm{J}/\psi \text{ and !V0A}}} \ . \tag{4.17}$$

The reasoning is as follows: the number of seen J/ψ events, $N_{\mathrm{J}/\psi(\mathrm{seen})}$, is due to the sum of the J/ψ events which satisfied the V0A veto, $N_{\mathrm{J}/\psi \text{ and !V0A}}$, and the J/$\psi$ events due to pile-up which also satisfied the V0A veto, $N^{\mathrm{PU}}_{\mathrm{J}/\psi \text{ and !V0A}}$. The number of truly occurred J/ψ events, $N_{\mathrm{J}/\psi(\mathrm{true})}$, is the sum of $N_{\mathrm{J}/\psi(\mathrm{seen})}$ and the events from same ion pair production which were vetoed by V0A. This last contribution, which can be called $N_{\mathrm{J}/\psi(\mathrm{samepair})}$ is obtained as follows:

$$N_{\mathrm{J}/\psi(\mathrm{samepair})} = \frac{N_{\mathrm{J}/\psi \text{ and V0A}} - N^{\mathrm{PU}}_{\mathrm{J}/\psi \text{ and V0A}}}{1 - \varepsilon_{V0A}} \ . \tag{4.18}$$

Essentially, $N_{\mathrm{J}/\psi(\mathrm{samepair})}$ is obtained as the number of J/ψ events which were vetoed by V0A, but were not due to pile-up, divided by $1 - \varepsilon_{V0A}$, where ε_{V0A} is the probability of having a signal in the V0A in an otherwise empty detector.

The values obtained are:

$$F_{\mathrm{XN0N}} = 0.88 \pm 0.01 \ ; \\ F_{\mathrm{XNXN}} = 0.84 \pm 0.05 \ . \tag{4.19}$$

4.10 Cross sections

Coherent J/ψ production cross sections for each neutron emission class i, are hence obtained using Eq. 4.20 as a function of rapidity:

$$\frac{d\sigma^{\mathrm{coh}}_i}{dy} = \frac{M_i(\mathrm{J}/\psi) \cdot (1/F_i)}{(1 + f_{\mathrm{I}} + f_{\mathrm{D}}) \cdot \epsilon_{\mathrm{VETO}} \cdot A \times \epsilon(\mathrm{J}/\psi) \cdot \mathrm{BR}(\mathrm{J}/\psi \longrightarrow \mu\mu) \cdot \mathcal{L} \cdot \Delta y} \ , \tag{4.20}$$

where M_i are the yields corrected for ZDC migration effects (the *true* yields without pileup and neutron efficiency deficiencies) shown in Eq. 4.14, F_i are the V0A corrections

Table 4.14: Summary table with coherent J/ψ photoproduction cross sections in neutron emission classes as a function of rapidity. Statistical and systematic uncertainty are also shown.

Class	y	$N[\mathrm{J}/\psi]$	$A \times \epsilon(\mathrm{J}/\psi)$	$\frac{d\sigma}{dy}$ [mb]	stat. [mb]	sys.(%)
0N0N	$-4 < y < -2.5$	12 459	11.8%	2.2390	0.0307	8.44%
	$-4 < y < -3.5$	2 399	9.7%	1.5860	0.0489	8.43%
	$-3.5 < y < -3$	7 081	19.4%	2.3150	0.0333	8.43%
	$-3 < y < -2.5$	2 931	6.9%	2.6570	0.0760	8.46%
0NXN	$-4 < y < -2.5$	1 767	11.8%	0.1184	0.0041	18.15%
	$-4 < y < -3.5$	331	9.7%	0.0430	0.0035	33.29%
	$-3.5 < y < -3$	947	19.4%	0.1092	0.0053	19.10%
	$-3 < y < -2.5$	475	6.9%	0.2302	0.0126	11.67%
XN0N	$-4 < y < -2.5$	1 148	11.8%	0.1667	0.0074	8.84%
	$-4 < y < -3.5$	189	9.7%	0.0993	0.0078	8.57%
	$-3.5 < y < -3$	637	19.4%	0.1681	0.0098	8.85%
	$-3 < y < -2.5$	319	6.9%	0.2359	0.0208	9.17%
XNXN	$-4 < y < -2.5$	810	11.8%	0.1695	0.0088	14.22%
	$-4 < y < -3.5$	111	9.7%	0.0830	0.0119	14.12%
	$-3.5 < y < -3$	450	19.4%	0.1693	0.0120	14.27%
	$-3 < y < -2.5$	247	6.9%	0.2681	0.0249	14.01%

in Eq. 4.19, $\epsilon_{\mathrm{VETO}} = 1 - \varepsilon_{V0A}$ is the average veto efficiency, and the branching ratio $\mathrm{BR}(\mathrm{J}/\psi \longrightarrow \mu\mu) = (5.961 \pm 0.033)\%$.

Table 4.14 shows a summary of coherent J/ψ photoproduction cross sections for each neutron emission class as a function of rapidity, along with statistical and total systematic uncertainties. Fig. 4.18(a) shows the cross sections as a function of rapidity for all classes, while Fig. 4.18(b), 4.18(c), 4.18(d) and 4.18(e) show the cross sections for the 0N0N, 0NXN, XN0N, XNXN classes, respectively. All plots show the measurement at forward rapidity along with the corresponding midrapidity points. The midrapidity analysis is done by analysing the 0NXN and XN0N classes jointly. The relevant cross sections are then divided by a factor two for the sake of plotting. The cross sections for the 0N0N class are much larger than what is measured for the other classes, so the corresponding points are scaled. The measured cross sections are plotted against the LTA predictions [18]. The agreement with the predictions is quite good, owing to large uncertainties both for data and predictions.

4.11 Systematics

A few of the systematic uncertainties contributing to the overall systematic uncertanty are taken from [5], namely *luminosity normalisation*, *branching ratio*, *tracking*, *trigger*, *matching*, *feed-down fraction*. Other systematic sources have been computed either with different approaches or because they affect only this neutron emission measurement i.e. *signal extraction*, *incoherent fraction*, *pile-up* and *ZDC migrations*. The systematic source for the electromagnetic correction had also to be included. The systematic sources are added in quadrature to obtain the total systematic source.

The *incoherent fraction* systematic source is obtained as the difference between the values obtained with the two different approaches explained in Sec. 4.4, and this is done for all

rapidity bins and all classes. However, the difference can be quite large in classes where the dissociative component is large i.e. 0NXN. As such, this source has to be isolated and added in quadrature based on its impact on the cross sections themselves. The incoherent fraction appears as a correction factor to the cross sections in the $1 + f_{\mathrm{D}} + f_{\mathrm{I}}$ term, so the term to be added in quadrature is $[\Delta f_{\mathrm{I}}/(1 + f_{\mathrm{D}} + f_{\mathrm{I}})]^2$.

The *pile-up* and *ZDC efficiency* effects on the corrected yields obtained with the procedure explained in Sec. 4.7, are evaluated by variating the values of p_A, p_C and ϵ_A and ϵ_C independently by the reported error, so as to have an upward and downward variation on the yields. The two systematic sources are computed independently.

Table 4.15 shows that the systematic uncertainty on the classes 0N0N, XN0N, XNXN range from 8.44% to 14.27% depending on rapidity, while 0NXN displays a wider variation, namely from 11.67% to 33.29%.

4.12 Extracting $\sigma(\gamma\mathrm{Pb})$

The photonuclear cross sections in Eq. 1.9 are expressed as a function of $W_{\gamma\mathrm{Pb}}$, the centre-of-mass energy of the γPb system:

$$W^2_{\gamma\mathrm{Pb}} = \sqrt{s_{\mathrm{NN}}} \cdot M_{\mathrm{J}/\psi} \cdot e^{\pm|y|} \ , \tag{4.21}$$

where $\pm|y|$ is the rapidity of the J/ψ in the final state. It is possible to rewrite Eq. 1.9 in matrix form as:

$$\begin{bmatrix} n_{\mathrm{0N0N}}(\gamma,+y) & n_{\mathrm{0N0N}}(\gamma,-y) \\ n_{\mathrm{0NXN}}(\gamma,+y) & n_{\mathrm{0NXN}}(\gamma,-y) \\ n_{\mathrm{XN0N}}(\gamma,+y) & n_{\mathrm{XN0N}}(\gamma,-y) \\ n_{\mathrm{XNXN}}(\gamma,+y) & n_{\mathrm{XNXN}}(\gamma,-y) \end{bmatrix} \cdot \begin{bmatrix} \sigma_{\gamma\mathrm{Pb}}(+y) \\ \sigma_{\gamma\mathrm{Pb}}(-y) \end{bmatrix} = \begin{bmatrix} \frac{d\sigma^{0N0N}_{PbPb}}{dy} \\ \frac{d\sigma^{0NXN}_{PbPb}}{dy} \\ \frac{d\sigma^{XN0N}_{PbPb}}{dy} \\ \frac{d\sigma^{XNXN}_{PbPb}}{dy} \end{bmatrix} \ , \tag{4.22}$$

Table 4.15: Systematic uncertainties for the neutron emission analysis.

Source	**Value**
Lumi. Normalisation	±5.0%
Branching ratio	±0.6%
Tracking	±3.0%
Matching	±1.0%
Signal extraction	from 0.5% to 2.0%
f_{D} fraction	±0.7%
f_{I} fraction	
0N0N	0.4%
0NXN	from 9.1% to 50.0%
XN0N	from 0.5% to 0.9%
XNXN	from 1.6% to 3.3%
|pile-up|	
0N0N	0.12%
0NXN	from 0.74% to 2.46%
XN0N	from 0.56% to 0.82%
XNXN	from 0.11% to 0.12%
|ZDC efficiencies|	
0N0N	from 0.52% to 0.96%
0NXN	from 0.20% to 1.81%
XN0N	from 1.33% to 3.37%
XNXN	from 11.09% to 11.13%
Total	
0N0N, XN0N, XNXN	from 8.44% to 14.27%
0NXN	from 11.67% to 33.29%

where the photon fluxes $n_i(\gamma, \pm y)$ can be computed by either $\mathbf{n^O_O n}$ or STARlight, and are grouped in a single matrix, $\mathbf{N}$. The solutions can then be obtained by computing the pseudoinverse of the flux matrix $\mathbf{N}$, afterwards applied to a vector containing the cross sections shown in Sec. 4.10. The photonuclear cross sections $\sigma_{\gamma\mathrm{Pb}}(\pm y)$ are shown in Fig. 4.19 as a function of $W_{\gamma\mathrm{Pb}}$. The x-coordinate of each solution is computed starting from the centre of the corresponding rapidity interval. Concerning the uncertainty on each point in Fig. 4.19, the systematic uncertainties for the measured cross sections in Sec. 4.11 are partially correlated, as in the case of e.g. the normalisation of the luminosity. In a first approximation, the uncertainties can be considered uncorrelated, since for the 0NXN and XNXN classes the total systematic uncertainties are significantly larger than for 0N0N, where the uncertainty is mostly due to the correlated part.

The uncertainties on the extracted photonuclear cross sections in Fig. 4.19, are obtained with this approximation, and the uncertainty is computed by varying the measured cross sections by $\pm 1\sigma$. The latter is the sum in quadrature of the corresponding statistical and systematic uncertainties. The cross sections at lower values of $W_{\gamma\mathrm{Pb}}$ are mostly due to the 0N0N cross sections, which have smaller uncertainties, while the influence of the other neutron emission classes is stronger at higher $W_{\gamma\mathrm{Pb}}$, leading to bigger uncertainties. The photonuclear cross sections and their uncertainties are presented in Table 4.16. The photonuclear cross sections grow fast with increasing $W_{\gamma\mathrm{Pb}}$. The solutions are then fitted with a power-law function, according to [40] and [82], of the form $N \cdot (W_{\gamma\mathrm{Pb}}/W_0)^{\delta}$, where W_0 is similarly set to 90.0 GeV, and the parameters of the fit are $N = 0.0268 \pm 0.0019$ and $\delta = 0.565 \pm 0.052$, with a $\chi^2/NDF = 21.61/(6-2) \sim 5.4$ which is due to the data point at $W_{\gamma\mathrm{Pb}} = 19.1$ GeV. The predictions from STARlight and from the Impulse Approximation are also shown. The ALICE data points agree with STARlight while agreement is not expected with the Impulse Approximation since nuclear effects are neglected.

It is also possible to compute the nuclear suppression factor for the photonuclear cross sections $\sigma_{\gamma\mathrm{Pb}}$, where the nuclear suppression factor $S_{\mathrm{Pb}}(x)$ is computed as the square root

Table 4.16: Photonuclear cross sections obtained from the analysis of the neutron emission classes, compared to the predictions for the Impulse Approximation model from STARlight in the same $W_{\gamma\mathrm{Pb}}$ interval. The suppression factors are also presented.

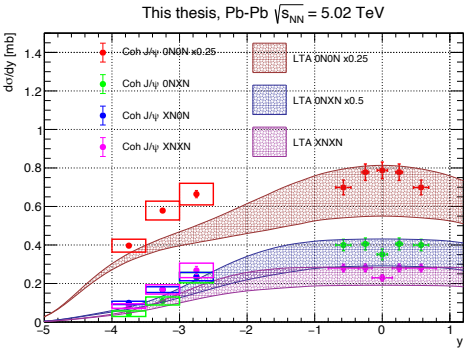
$W_{\gamma\mathrm{Pb}}$ [GeV]	$\sigma_{\gamma\mathrm{Pb}} \pm \delta\sigma_{\gamma\mathrm{Pb}}$ [mb]	$\sigma^{\mathrm{STARlight}}_{\gamma\mathrm{Pb}}$ [mb]	$\sigma^{\mathrm{IA}}_{\gamma\mathrm{Pb}}$ [mb]	$S_{\mathrm{Pb}} \pm \delta S_{\mathrm{Pb}}$ [a.u.]
19.1	0.0091 ± 0.0006	0.010	0.013	0.83 ± 0.03
24.6	0.014 ± 0.001	0.014	0.018	0.87 ± 0.04
31.5	0.0171 ± 0.0009	0.017	0.022	0.87 ± 0.02
493.4	0.057 ± 0.015	0.072	0.142	0.62 ± 0.08
633.5	0.054 ± 0.026	0.080	0.167	0.57 ± 0.14
813.5	0.05 ± 0.09	0.090	0.197	0.5 ± 0.4

of the ratio of the $\sigma_{\gamma\mathrm{Pb}}$ from data, and $\sigma^{\mathrm{IA}}_{\gamma\mathrm{Pb}}$, the photonuclear cross sections computed with the Impulse Approximation from STARlight:

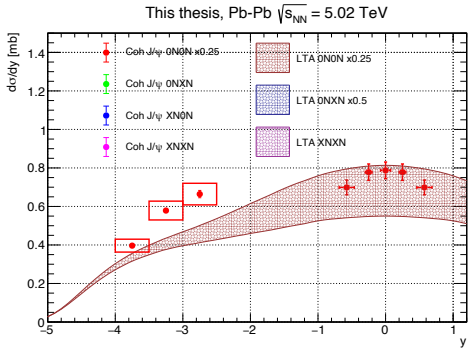
$$S_{\mathrm{Pb}}(x) = \sqrt{\frac{\sigma_{\gamma\mathrm{Pb}}}{\sigma^{\mathrm{IA}}_{\gamma\mathrm{Pb}}}} \,. \tag{4.23}$$

Fig. 4.20 shows the $S_{\mathrm{Pb}}(x)$ obtained with the solutions $\sigma_{\gamma\mathrm{Pb}}(\pm y)$. For Bjorken-$x \lesssim 10^{-2}$, the suppression factor is about 0.8, in agreement with the value reported in [5]. For the negative solutions instead, $10^{-4} \lesssim x \lesssim 10^{-5}$. The suppression factor for this x interval is about 0.6, in agreement with the reweighting shown in [9]. The photonuclear cross sections from STARlight and from the Impulse Approximation model, and the suppression factors obtained with Eq. 4.23 are reported in Table 4.16.

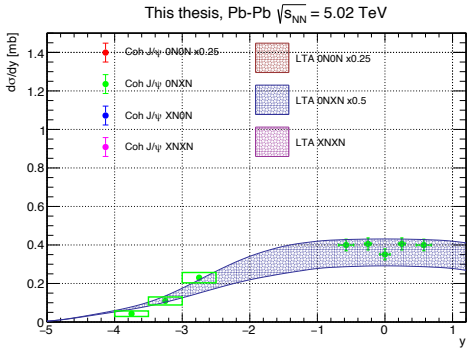
Ultimately, the usefulness of the neutron emission technique is shown, since it allows us to reach a Bjorken-x of about 10^{-5}. Disentangling the solutions to the photonuclear cross sections has become possible, using the different impact parameters, carried out in practice by selecting neutron emission classes.



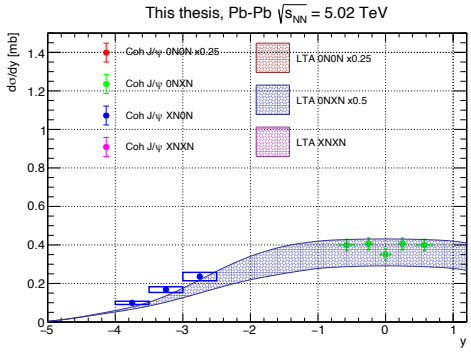
(a)



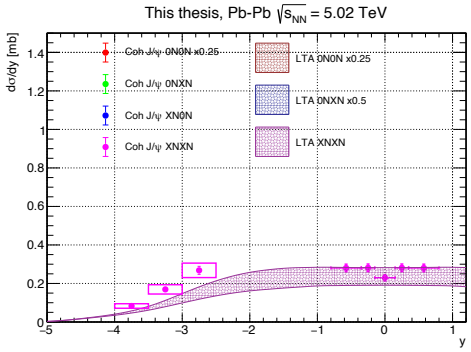
(b)



(c)



(d)



(e)

Figure 4.18: Coherent J/ψ photoproduction cross sections in neutron emission classes. Fig. 4.18(a) shows the cross sections measured at forward rapidity for all classes, along with the LTA predictions for the entire span of rapidity [18]. Fig. 4.18(b), 4.18(c), 4.18(d) and 4.18(e) show instead the 0N0N, 0NXN, XN0N, and XNXN classes, respectively. Systematic uncertainties are shown as boxes.

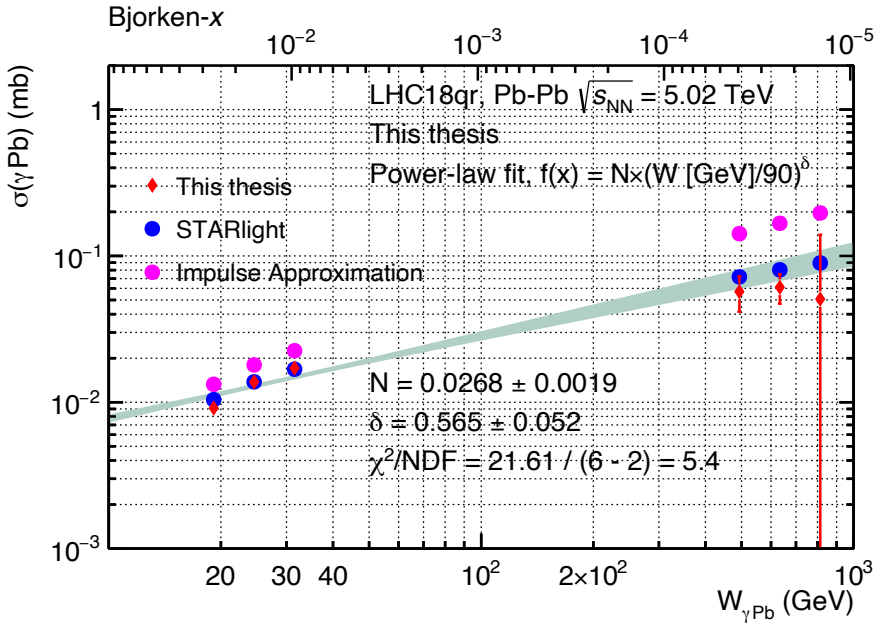


Figure 4.19: Solutions for photonuclear cross sections obtained by the simultaneous measurement of the 0N0N, 0NXN, XN0N and XNXN neutron emission classes, as reported in Sec. 4.10. The photonuclear cross sections show a growth as $W_{\gamma\mathrm{Pb}}$ increases, or, equivalently, if x decreases. The cross sections are fitted with a power-law function of the form $N \cdot (W_{\gamma\mathrm{Pb}}/W_0)^{\delta}$, and the fit parameters are also shown. The predictions from STARlight and the Impulse Approximation are also shown.

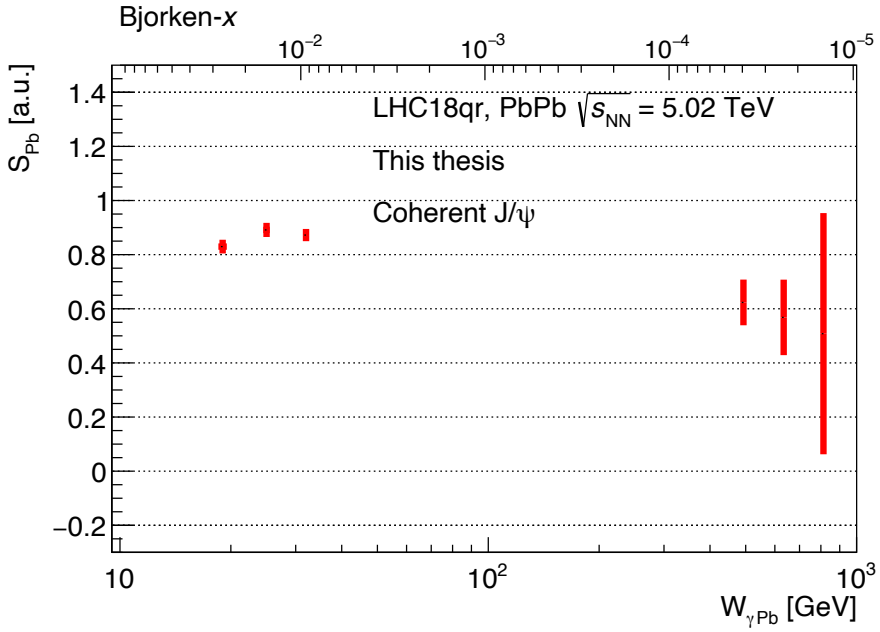


Figure 4.20: Suppression factors as a function of $W_{\gamma\mathrm{Pb}}$ and Bjorken-x for photonuclear cross sections obtained by the simultaneous measurement of the 0N0N, 0NXN, XN0N and XNXN neutron emission classes, as reported in Sec. 4.10. The measured suppression factors for $x \sim 10^{-2}$ are in agreement with the value reported in [5]. The suppression factors for $10^{-4} \lesssim x \lesssim 10^{-5}$ are in agreement with the reweighting carried out in [9].

Chapter 5

Coherent J/ψ polarisation

Coherent J/ψ polarisation is measured in Pb–Pb UPC for the first time with the data collected by the ALICE detector at forward rapidity in 2015 and 2018, with a total integrated luminosity of about 750 $\mu b^{-1} \pm 5\%$ (syst.). It follows the coherent J/ψ photoproduction measurement by ALICE with Run 2 data in Pb–Pb [5]. The analysis is carried out via the decay of the J/ψ to muon pairs in the helicity frame. The angular formalism uses the λ parameters [41], following a convention used in polarisation measurements with inclusive samples by the ALICE Collaboration [83, 84, 85, 86]. A comparison with results from previous experiments is also shown. The ALICE UPC measurements have been converted to spin-density matrix elements to aid comparison.

5.1 Physical considerations

In UPC events, the photon interacts with the Pomeron from the Pb target. The virtuality of the photon is low. If the polarisation of the produced vector meson is the same as that of the parent photon (i.e. transverse polarisation) this is known as *s-channel helicity*

conservation hypothesis (SCHC). Previous results obtained for ρ^0 from SLAC [87] and CERN SPS [88] are in agreement with SCHC. H1 [33] also reports agreement in the photoproduction regime for J/ψ with electron-proton data. The STAR Collaboration reports transverse polarisation for ρ^0 in UPC events [89]. Finally, more recently, the CLAS Collaboration reports violation of SCHC after high-statistics measurements of ρ^0, ω and ϕ [90, 91, 92]. Observation of coherent J/ψ transverse polarisation would confirm the photoproduction picture for UPC events with the ALICE detector [5].

5.2 A brief introduction to the analysis strategy

A brief introduction to the analysis strategy used for the polarisation analysis is shown in this section before providing more details in the rest of the document.

Firstly, the selected events are grouped in intervals of $\cos\theta$ and φ, since the analysis is performed with a bidimensional (2D) approach in $\cos\theta$ and φ. This will be shown better in the following. This is done for both real data and Monte Carlo samples. The latter are used to create the templates needed for the signal extraction and to create the response matrices needed for the unfolding procedure. The J/ψ yields in each $\cos\theta$ and φ interval represent the measured angular distribution. However, as discussed in more detail in Section 5.6, the φ distributions have considerable smearing, so must be unfolded in this variable.

The unfolded distributions are then fitted to measure λ_θ, λ_φ, and $\lambda_{\theta\varphi}$. This procedure is shown in Fig. 5.1.

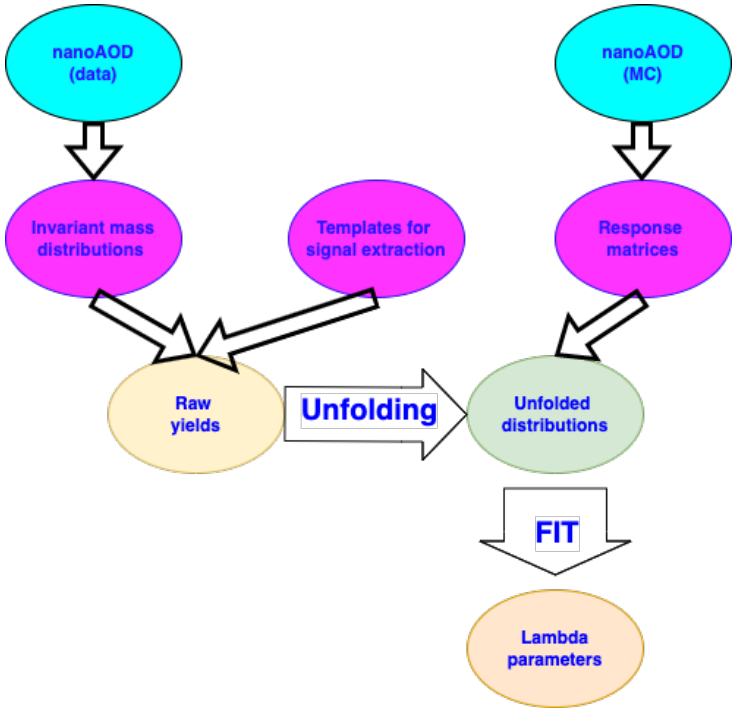


Figure 5.1: The procedure used for this measurement. Both real data and Monte Carlo simulations are analysed. The latter are used to create templates needed for the signal extraction of the former. In addition, Monte Carlo simulations are used to create the response matrices, needed to effect the unfolding of the raw distributions. Finally, the unfolded distributions are fitted to extract the λ parameters.

5.3 Polarisation formalism

The results in a polarisation analysis may be different depending on the chosen reference frame. This analysis is carried out in the *helicity* frame [41], as previously explored by the ALICE Collaboration for inclusive J/ψ [83, 84, 85, 86]. In this frame, the z-axis is taken to be the flight direction of the J/ψ in the centre-of-mass frame of the collision. The y-axis is perpendicular to the plane formed by the collision axis and the direction of the J/ψ in this frame, with the x-axis chosen to form a right-handed triplet [41]. This is shown in Fig. 1.20, where the definitions of the θ and φ angles are also presented. The former is then the angle of the positive muon in the J/ψ rest frame with respect to the z-axis, while the latter is the angle with respect to the plane formed by the beam vectors. Following the definitions for the unit vectors of the three axes $\hat{x}$, $\hat{y}$, and $\hat{z}$ presented in Eq. 1.14, $\cos\theta$ and φ are then obtained with the following definitions:

$$\begin{aligned} \cos\theta &= \frac{\hat{z}\cdot\vec{p}_{\mu}}{|\vec{p}_{\mu}|} \ , \\ \varphi &= \arctan\left(\frac{\vec{p}_{\mu}\cdot\hat{y}}{\vec{p}_{\mu}\cdot\hat{x}}\right) \ , \end{aligned} \tag{5.1}$$

where $\vec{p}_{\mu}$ is the momentum vector of the positive muon in the rest frame of the J/ψ.

The results in a polarisation measurement should, in principle, depend on the reference frame. However, this analysis is performed with forward data (beam rapidities) and low p_{T} [35]. Different definitions of the z-axis would then collapse on the one used for the helicity frame.

The angular distributions obtained with these definitions, have then to be unfolded and corrected for acceptance and efficiency ($A\times\epsilon$). The description is provided by the following Eq. 5.2 [42]:

$$W(\cos\theta,\varphi) \propto \frac{1}{3+\lambda_{\theta}}\cdot\left[1+\lambda_{\theta}\cdot\cos^2\theta+\lambda_{\varphi}\cdot\sin^2\theta\cdot\cos 2\varphi+\lambda_{\theta\varphi}\cdot\sin 2\theta\cdot\cos\varphi\right], \tag{5.2}$$

where the role of $\lambda_{\theta\varphi}$ is to measure the interference between transversely and longitudinally polarised amplitudes.

The extracted triplet of lambda parameters can then be compared to three extreme scenarios of particular interest:

- $(\lambda_\theta, \lambda_\varphi, \lambda_{\theta\varphi}) = (0, 0, 0) \longrightarrow$ isotropic decay of the J/ψ to the muon pair [83];
- $(\lambda_\theta, \lambda_\varphi, \lambda_{\theta\varphi}) = (-1, 0, 0) \longrightarrow$ longitudinal polarisation;
- $(\lambda_\theta, \lambda_\varphi, \lambda_{\theta\varphi}) = (1, 0, 0) \longrightarrow$ transverse polarisation.

5.4 Event and track selections

The selection of ultraperipheral events focuses on the exclusivity of the process. A single dimuon should be created in each event. ALICE's main analysis framework, AliPhysics, provides the user with a series of convenient tools to perform UPC analyses, especially at forward rapidity.

Firstly, the data for the polarisation analysis were collected during the 2015 and the 2018 Pb–Pb data taking period, corresponding to the totality of Pb–Pb data taken by the ALICE detector during Run 2, with an integrated luminosity $\mathcal{L}$ of $\mathcal{L} \sim 750\ \mu\text{b}^{-1}$ [5]. The online trigger is given by trigger inputs that reflect the behaviour of a typical UPC event at forward rapidity, hence a dimuon in the Forward Muon Spectrometer and exclusivity guaranteed by a VZERO-A veto together with a combination of AD-A and AD-C online vetoes.

Additional vetoes and selections are imposed offline to better ensure exclusivity and adherence to the topology of the expected process. They can be listed as the following:

- empty ADA decision[1];

[1] ALICE provides a refined approach to the online triggers at offline level. The online decision can be

- empty ADC decision;
- empty V0A decision[2];
- V0C decision can be either empty or in beam-beam timing[3];
- a maximum of two V0C cells may be crossed in the same event[4];
- each of the muon tracks have to be within the angular coverage of the hadronic absorber i.e. 17.5 cm $< R_{\text{absorber}} <$ 89.5 cm, where R_{absorber} is the radial coordinate of the impact of each track on the front face of the absorber;
- an additional momentum criterion, the $p \times DCA$ requirement, is also applied;
- each of the two muons of the dimuon candidate has to be within the pseudorapidity acceptance of the Forward Muon Spectrometer i.e. the pseudorapidity of each muon η_μ has to be $-4.0 < \eta_\mu < -2.5$;
- the dimuon candidate has to be within the rapidity range $-4.0 < y < -2.5$.

5.5 Fitting the invariant mass distributions

The crux of the analysis is to obtain the invariant mass distributions of the dimuons in the needed $\cos\theta$ and φ intervals, as already briefly mentioned in Sec. 5.2. Such distributions

reinforced offline thanks to the offline decision for both the AD and the VZERO detectors. The decision is made by averaging the readout response of the detectors in sixteen total *bunch crossings*, BCs. The four possible outcomes are: *empty*, *beam-beam timing*, *beam-gas timing*, and *ghost*. Obviously, when interested in exclusivity, an empty decision has to be required.

[2]ADA, ADC, and V0A are all vetoes required at online trigger level.

[3]Either none, one or two of the muons can cross the V0C if a dimuon has been produced in the event.

[4]V0C and the Forward Muon Spectrometer have slightly different pseudorapidity acceptances. It is then possible that either no, one, or two of the muons may cross V0C.

have to be fitted to extract only the J/ψ contribution, and in doing so, obtaining the raw distributions with already subtracted background.

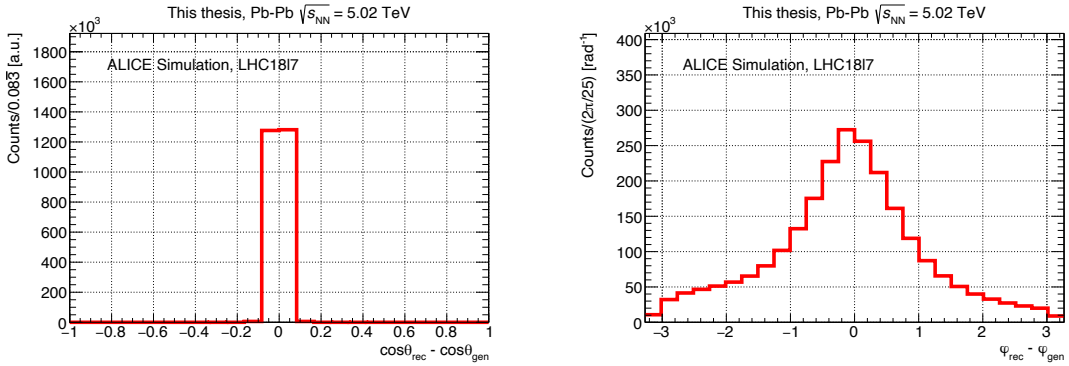
The interest lies again in the low p_{T} coherent component of the J/ψ signal i.e. the invariant mass distributions of those dimuons with $p_{\mathrm{T}}^{\mu\mu} < 0.25$ GeV/c. The fit procedure follows closely the procedure presented in Sec. 4.3. The J/ψ and the ψ' invariant mass distributions are both described by the Crystal Ball functions shown in Eq. 4.1, with the same parameters fixed to the corresponding parameters obtained by fitting the reconstructed STARlight samples after the same selections and angular intervals have been applied. The description of the background is similarly provided by Eq. 4.3.

5.6 Resolution in $\cos\theta$ and φ

The resolution in $\cos\theta$ is shown in Fig. 5.2(a), where the difference between the reconstructed and generated $\cos\theta$ is plotted as obtained from STARlight Monte Carlo simulated events. The resolution in φ is shown in Fig. 5.2(b). Fig. 5.2(b) shows that φ will require an unfolding procedure, regardless of the choice of the binning for the distributions.

5.7 Raw yields

The final choice of the binning is driven by a balance in terms of population (due to a limited acceptance in $\cos\theta$, as shown in Fig. 5.3) in each interval of $\cos\theta$ and φ, and the resolution in φ. Taking into account the respective resolutions, 24 homogeneous bins are chosen for $\cos\theta$ in the interval $[-1, 1]$, and 6 homogeneous bins are chosen for φ in $[0, 2\pi]$ instead, which satisfies the requirements imposed by the Nyquist sampling theorem [93, 94] for the $\cos 2\varphi$ term in Eq. 5.4.



(a) (b)

Figure 5.2: Resolutions in $\cos\theta$ and φ. The resolution in $\cos\theta$ is quite good. The resolution in φ necessitates unfolding to properly resolve a potential structure in the distribution.

The signal extraction is carried out using the procedure outlined in Sec. 5.5. The results are shown in Fig. 5.4(a) and 5.4(b) for the helicity frame, where the latter shows the former in a three dimensional view. Most events are focused in the region $|\cos\theta| < 0.3$, as expected from the trend shown in Fig. 5.3.

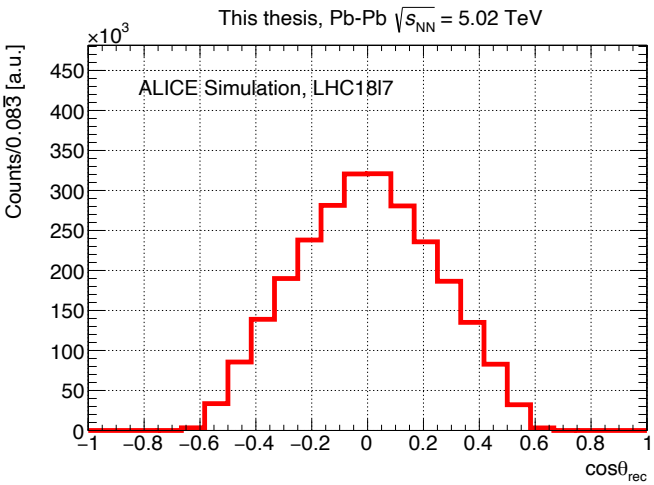
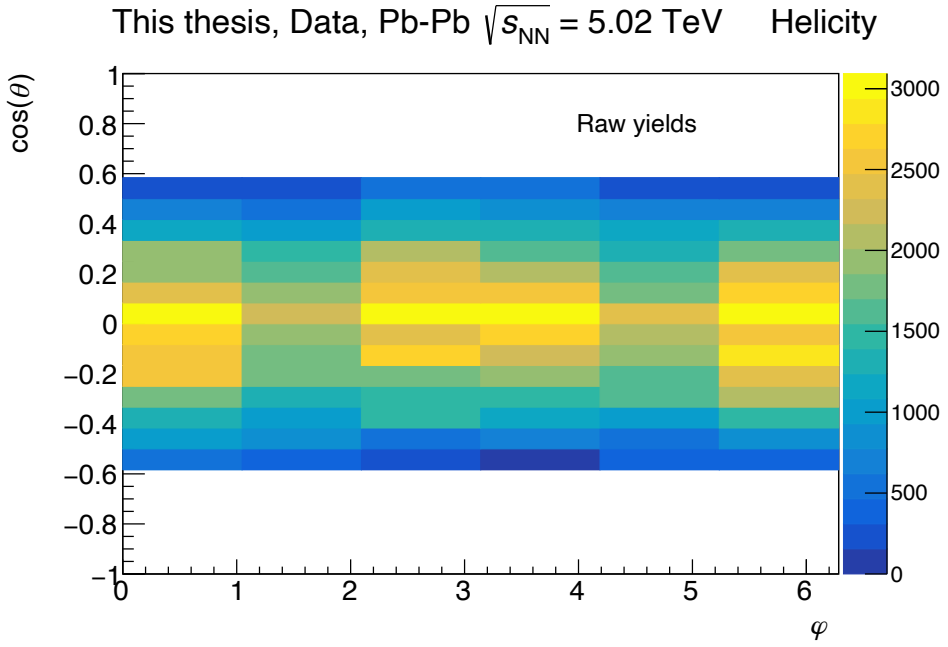
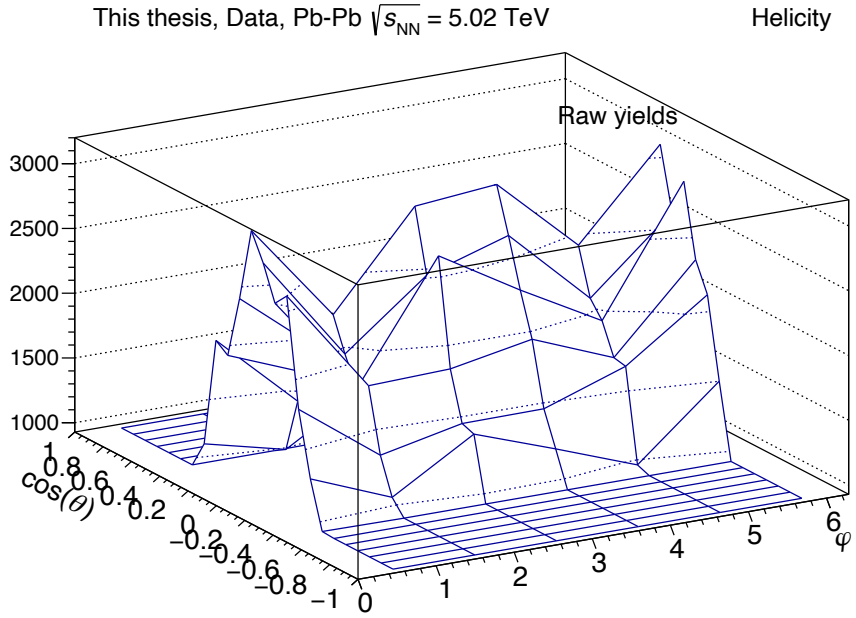


Figure 5.3: Distribution of reconstructed $\cos\theta$, obtained from STARlight Monte Carlo events. The distribution shows a range of accessible $\cos\theta$ up to $|\cos\theta| < 0.6$.



(a)



(b)

Figure 5.4: Raw yield distribution in the helicity frame for coherent J/ψ polarisation. The events are focused in the region $|\cos\theta| < 0.3$.

5.8 Unfolding procedure

Unfolding is required in φ only. As the binning in $\cos\theta$ is quite large relative to its resolution, migrations in $\cos\theta$ are negligible, and the unfolding procedure is implemented as follows:

- response matrices in φ are computed for each $\cos\theta$ interval;
- the unfolding is then performed monodimensionally, requiring a response matrix for each $\cos\theta$ interval within the acceptance;
- the correction for $\cos\theta$ comes then from the definition of the $A \times \epsilon$ used to generate the response matrix;
- the following criterion is applied to stop the iterative procedure: the average correlation coefficient $\langle\rho_i\rangle = \frac{1}{6}\sum_{i=1}^{6}\sqrt{1 - \frac{1}{V_{ii}\cdot V_{ii}^{-1}}}$ is computed as a function of the number of iterations, where V_{ii} and V_{ii}^{-1} are the diagonal terms of the covariance matrix and its inverse. The iterative procedure is then stopped when a minimum is found in the scan [95] since this minimises the correlation among data points.

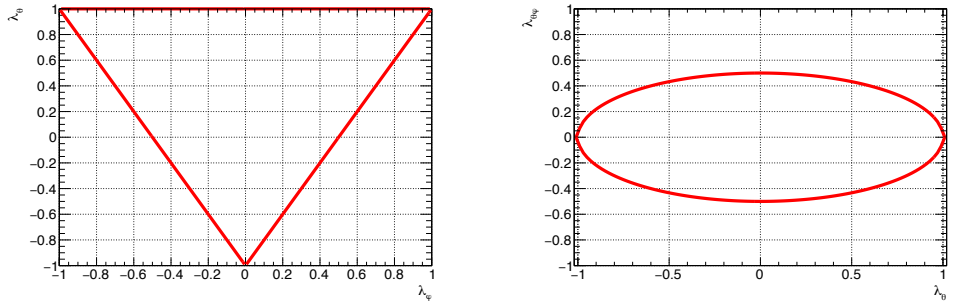
The unfolding is performed with the `RooUnfold` package [96], using a Bayesian iterative procedure [97]. The validity of the procedure is tested by checking for closure using STARlight Monte Carlo samples.

5.8.1 Fitting the corrected distributions

The physical region for the three parameters λ_θ, λ_φ, and $\lambda_{\theta\varphi}$, is limited by the following conditions shown in Eq. 5.3 [98]:

$$\begin{aligned} |\lambda_\varphi| &\leq 1 \ , \\ -1 + 2|\lambda_\varphi| \leq \lambda_\theta &\leq 1 \ , \\ |\lambda_{\theta\varphi}| &\leq \frac{1}{2} \cdot \sqrt{1 - 2\lambda_\varphi + 2\lambda_\varphi\lambda_\theta - \lambda_\theta^2} \ . \end{aligned} \tag{5.3}$$

The allowed regions for λ_θ against λ_φ, and for $\lambda_{\theta\varphi}$ against λ_θ, with the choice of λ_φ set to $\lambda_\varphi = 0$, are shown in Fig. 5.5(a) and 5.5(b), respectively. The fit to the angular



(a) (b)

Figure 5.5: Physically allowed regions for λ_θ, λ_φ, $\lambda_{\theta\varphi}$. Fig. 5.5(a) shows the allowed region for λ_θ against λ_φ. Fig. 5.5(b) shows the allowed region for $\lambda_{\theta\varphi}$ against λ_θ, with the choice of λ_φ set to $\lambda_\varphi = 0$.

distributions is effected by means of `TMinuit` [99, 100]. This allows the users to create a function of their choosing, and perform a χ^2 minimisation. It is also possible to manually apply non-rectangular limits on the lambda parameters, which would otherwise be difficult to implement. This could be carried out by means of penalty functions [99] inside the function which will be minimised. Operationally speaking, this means that the function

would assume large values whenever it tries to explore an unphysical region[5].

The description as a function of $\cos\theta$ and φ is provided by Eq. 5.2, where the normalisation and multiplicative factors are absorbed in N_0:

$$W(\cos\theta,\varphi) = \frac{N_0}{3+\lambda_\theta}\cdot\left[1+\lambda_\theta\cdot\cos^2\theta+\lambda_\varphi\cdot\sin^2\theta\cdot\cos 2\varphi+\lambda_{\theta\varphi}\cdot\sin 2\theta\cdot\cos\varphi\right] \quad . \tag{5.4}$$

The fit is then performed using integral values, owing to the coarse binning in φ[6]. This means that the data points are minimised against the integral of Eq. 5.4 in the $\cos\theta$ and φ intervals corresponding to the bin that is being considered.

Eq. 5.4 produces large correlations between N_0 and λ_θ, due to the presence of the factor $3+\lambda_\theta$ at the denominator. It is then possible to renormalise the fit function in such a way that it is possible to compare the results of the fit with the sum of the unfolded data points in a restricted $\cos\theta$ range, taken to be in this case $[-0.5, 0.58\bar{3}]$. Details of the integration are provided in Appendix D.

For a usable $\cos\theta$ interval -0.5 to $0.58\bar{3}$, the following fit function is used:

$$W(\cos\theta,\varphi) = \frac{3}{2\pi}\cdot\frac{I}{3.25+0.323495\cdot\lambda_\theta}\cdot\left[1+\lambda_\theta\cos^2\theta+\lambda_\varphi\sin^2\theta\cos 2\varphi+\lambda_{\theta\varphi}\sin 2\theta\cos\varphi\right] \quad , \tag{5.5}$$

where I is the normalisation once the range $-0.5 < \cos\theta < 0.58\bar{3}$ is applied, as shown in Appendix D.

5.9 Closure tests

Several checks are performed to test closure. Firstly, the convergence of the iterative unfolding procedure is tested on Monte Carlo simulations by effecting unfolding on each

[5]This procedure is required only if the minimum of the χ^2 minimisation falls in an unphysical region, and it has not ultimately been applied.

[6]This choice was driven by the acceptance of the detector and the resolution in φ.

$\cos\theta$ interval, with the same binning in φ described in Sec. 5.7. This is evaluated in two equivalent ways:

- generated–level Monte Carlo distributions are compared to unfolded reconstructed–level Monte Carlo distributions;
- refolded unfolded reconstructed–level Monte Carlo distributions are directly compared to reconstructed–level Monte Carlo distributions. This effectively means applying the unfolding procedure to reconstructed–level distributions, and applying the response matrix to the results of the unfolding[7]. This is also investigated as a function of the number of iterations in the iterative procedure.

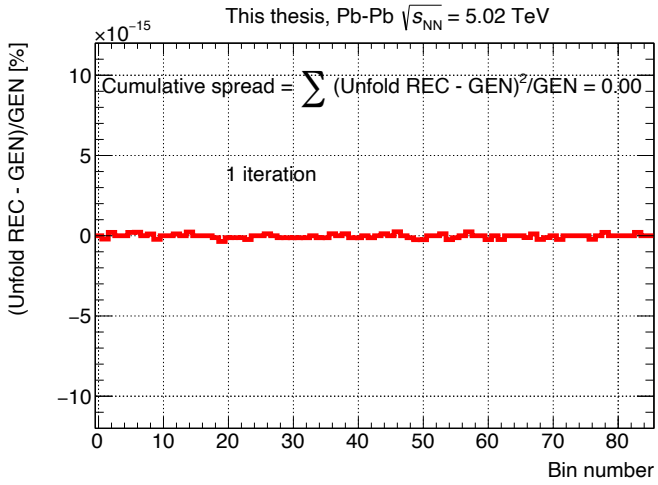
These two possible ways to test for closure are equivalent to each other, but the test of the refolded distributions can also be performed on real data to test for convergence.

5.9.1 Closure for the λ parameters

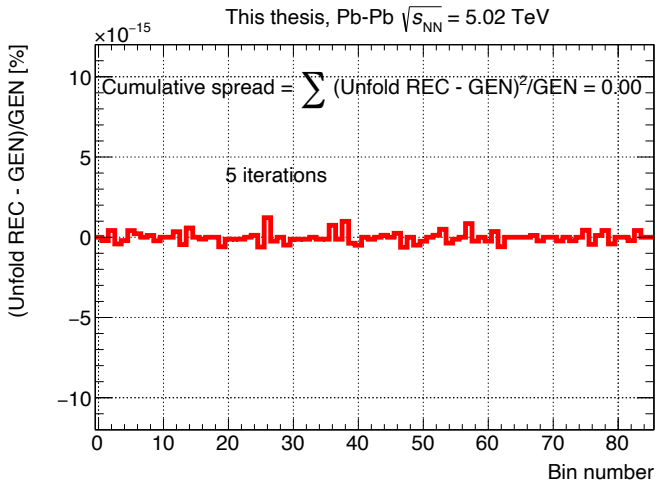
It is then possible to assess the overall quality of the unfolding procedure by measuring the relative difference between the generated–level Monte Carlo distribution and the unfolded reconstructed–level Monte Carlo distribution. This is shown in Fig. 5.6(a) and 5.6(b), where the relative difference is consistent with zero everywhere, after one and five iterations of the unfolding procedure, respectively. The distributions show the difference for each data point of the bidimensional distribution, measured as the ratio $(u_i - g_i)/g_i$, where the u_i are the unfolded reconstructed–level data points, and the g_i are the generated–level data points, for every data point i. The agreement is at the level of 10^{-15} per data point. This is due to using the same sample for the generation of the response matrices, and

[7] In the ideal case when the unfolded distributions have perfect agreement with the generated distributions, e.g. in the case of convergence, if the operation of the unfolding is denoted with U, and the response matrix is denoted by R, $R \circ U = \mathbb{1}$ holds.

for generating the reconstructed–level data tables. It is similarly possible to assess if clo-



(a)

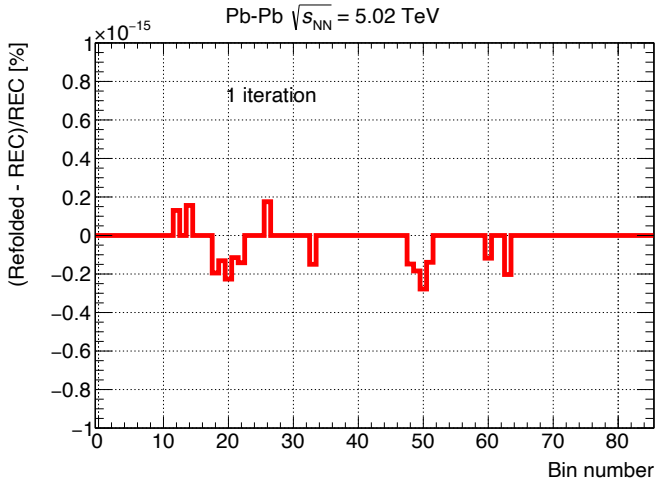


(b)

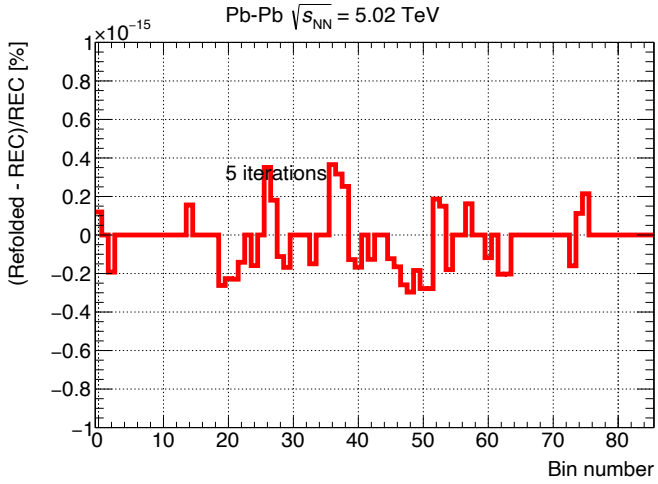
Figure 5.6: Fig. 5.6(a) shows the relative difference of the unfolded reconstructed–level and the generated–level STARlight events after one iteration of the unfolding procedure. Fig. 5.6(b) shows the same distribution after five iterations instead. The agreement is at the level of 10^{-15} for both distributions, since the same sample is used to generate both the response matrices, and the reconstructed–level distributions.

sure is reached by using the distribution of the refolded unfolded data points. Fig. 5.7(a)

and 5.7(b) show the discrepancy between the refolded distributions and the underlying reconstructed–level distributions. Both the refolded test, and the agreement of unfolded to generated–level distributions, point towards closure. The unfolded reconstructed–level



(a)



(b)

Figure 5.7: Fig. 5.7(a) shows the relative difference of the refolded unfolded and reconstructed–level STARlight events after one iteration of the unfolding procedure. Fig. 5.7(b) shows the same distribution after five iterations instead. The same sample is used to generate both the response matrices, and the reconstructed–level distributions.

distribution is compared to the generated level distribution in $\cos\theta$ and φ. This is shown in Fig. 5.8(a) and Fig. 5.8(b) for the unfolded and the generated distributions, respectively.

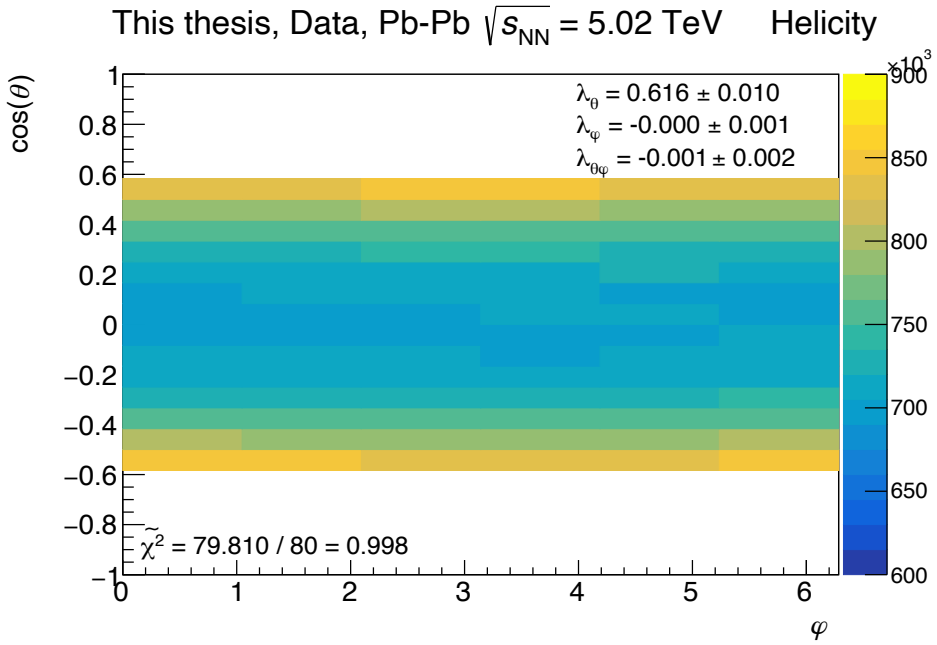
The fit to the generated–level Monte Carlo data yields, which also follows the procedure discussed in Sec. 5.8.1, yields the following λ parameters:

$$\lambda_\theta = 0.607 \pm 0.005 \ ,$$
$$\lambda_\varphi = 0.000 \pm 0.001 \ ,$$
$$\lambda_{\theta\varphi} = -0.001 \pm 0.001 \ ,$$

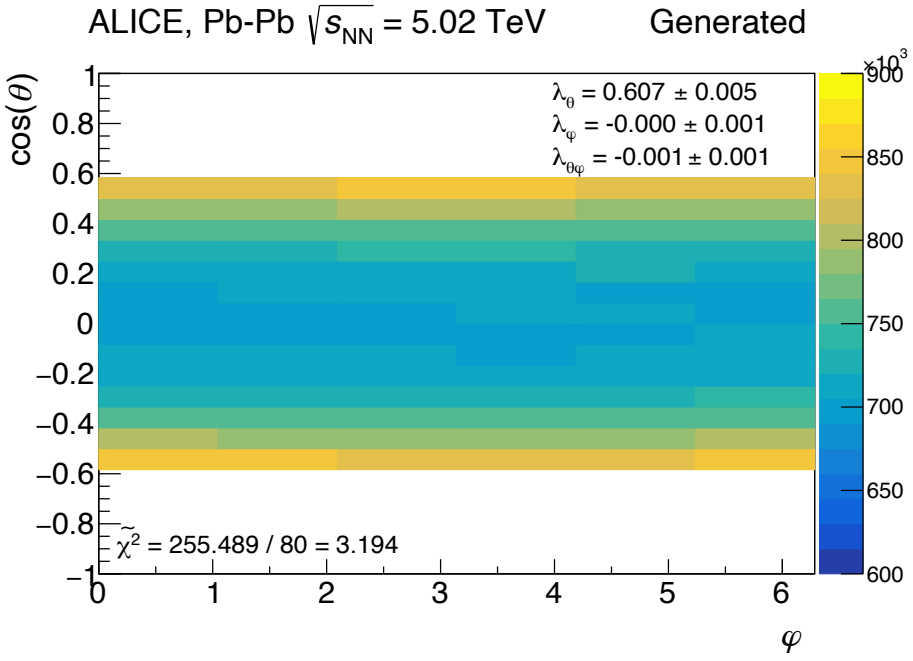
while the fit to the unfolded reconstructed–level distribution, obtained after five iterations of the unfolding procedure, shown in Fig. 5.8(a), produces:

$$\lambda_\theta = 0.616 \pm 0.010 \ ,$$
$$\lambda_\varphi = 0.000 \pm 0.001 \ ,$$
$$\lambda_{\theta\varphi} = -0.001 \pm 0.002 \ .$$

In conclusion, the unfolding procedure and the fit procedures can be considered robust, and applicable to real data.



(a)



(b)

Figure 5.8: Fig. 5.8(a) shows the unfolded reconstructed–level distribution in intervals of $\cos\theta$ and φ after five iterations of bayesian unfolding. Fig. 5.8(b) shows instead the generated–level distribution.

5.9.2 Modulations in λ_φ

The unfolding procedure explained in Sec. 5.8, is capable of coping with the poor resolution in φ of the detector. Unfortunately, no Monte Carlo generator inside of AliROOT, ALICE's dedicated analysis framework, is able to generate modulations in φ. A modulation in φ is characterised by non-null values of λ_φ when the corresponding distribution is fitted according to Eq. 5.4. The following recipe is then used to obtain a sample with modulations from the purely transverse STARlight sample:

- choose a triplet of $(\lambda_\theta, \lambda_\varphi, \lambda_{\theta\varphi})$ as an input to Eq. 5.4;
- a bidimensional histogram is created;
- the histogram is filled in a certain interval of $\cos\theta$ and φ, until its content reaches the corresponding maximum value given by Eq. 5.4 with chosen modulation;
- the reconstructed level is automatically produced since the accepted events are a subset of the full STARlight simulation.

This procedure has to be carried out since it is not known *a priori* how the reconstruction would affect generated events[8]. Afterwards, the response matrix from the trasversely polarised STARlight sample is applied, and the iterative unfolding procedure is applied.

First of all, since the procedure explained in this section is an approximation[9], it is important to test its quality. Fig. 5.9(a) and 5.9(b) show the generated–level distribution obtained by imposing this selection criterion, with a fine binning of 24 bins in $\cos\theta$ and 24 bins in φ. The modulation in φ is quite prominent. The same distribution is then fitted with the procedure explained in Sec. 5.8.1. The fit returns $\lambda_\varphi = 0.9816 \pm 0.0004$. The approximation is then considered quite good, and the fit is repeated with the same binning

[8] No generator in AliROOT is able to produce a modulation in φ.

[9] A continuous function is approximated with a bidimensional histogram.

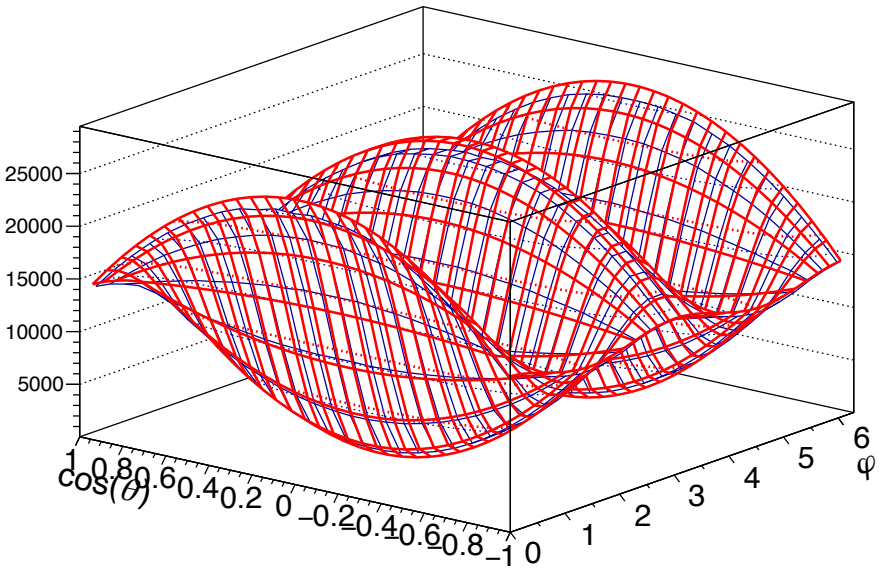
as for data, i.e. with 24 bins in $\cos\theta$ and 6 bins in φ, with an acceptance $|\cos\theta| < 0.58\bar{3}$. The distribution with this last binning is shown in Fig. 5.10. The fit returns $\lambda_\varphi = 0.9806 \pm 0.0005$. The results are then consistent when using the fine binning and the same binning as real data with the same acceptance in $\cos\theta$. The unfolding procedure is repeated over the reconstructed–level distributions obtained with this procedure.

The average correlation coefficient is plotted as a function of the number of iterations for these modulated data in φ in Fig. 5.11. A minimum is found at around fifteen iterations, which is then taken as the stopping point for this iterative procedure. Fig. 5.11 refers to the $\cos\theta$ interval $0.1\bar{6} < \cos\theta < 0.25$, which is reported as slice fourteen inside the measurement, but the same trend is found in all slices in $\cos\theta$. The relation between slices and respective $\cos\theta$ intervals is reported in Appendix E.

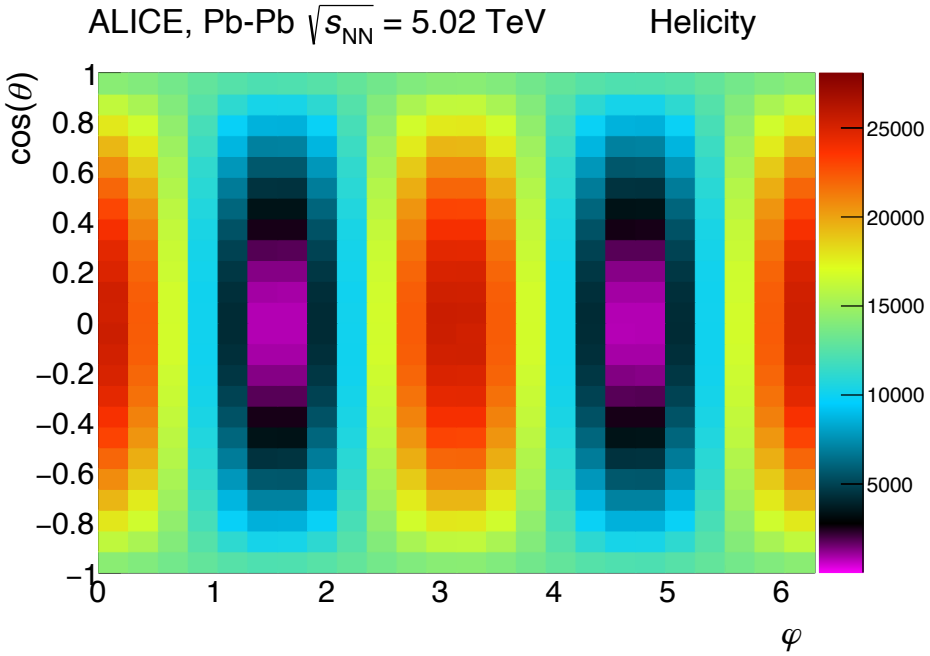
It is then possible to assess the quality of the unfolding by plotting the relative difference between the refolded unfolded distribution and the reconstructed one. This is carried out with the transverse polarisation response matrix from STARlight, which is stopped after fifteen iterations as shown in, e.g., Fig. 5.11, and by reweighting the STARlight response matrix with the input generated–level distribution, which shows a minimum in the average correlation coefficient after 25 iterations instead, in all slices. Fig. 5.12(a) and 5.12(b) show the relative difference using the transverse response matrix and the reweighted response matrix, respectively. It is evident how the quality of the refolded (and hence, of the unfolded) distribution is better when the response matrix is closer to the generated–level distribution, than in the case when the response matrix features a completely different polarisation hypothesis, as is the case for the original STARlight response matrix.

The resulting unfolded distribution in $\cos\theta$ and φ is presented in Fig. 5.13 for 25 iterations, with the reweighted STARlight response matrix. The unfolding procedure succeeds in returning large modulations in φ if the underlying distribution displays the same feature.

The fit procedure is carried out in all $\cos\theta$ slices and the fit returns $\lambda_\varphi = 0.999 \pm 0.002$, with a discrepancy of 1.8% with respect to the generated–level distribution with the same binning.



(a)



(b)

Figure 5.9: Fig. 5.9(a) shows the generated–level distribution in intervals of $\cos\theta$ and φ, with the input of $(\lambda_\theta, \lambda_\varphi, \lambda_{\theta\varphi}) = (0, 1, 0)$. Fig. 5.9(b) shows the same generated–level distribution, but in a bidimensional view.

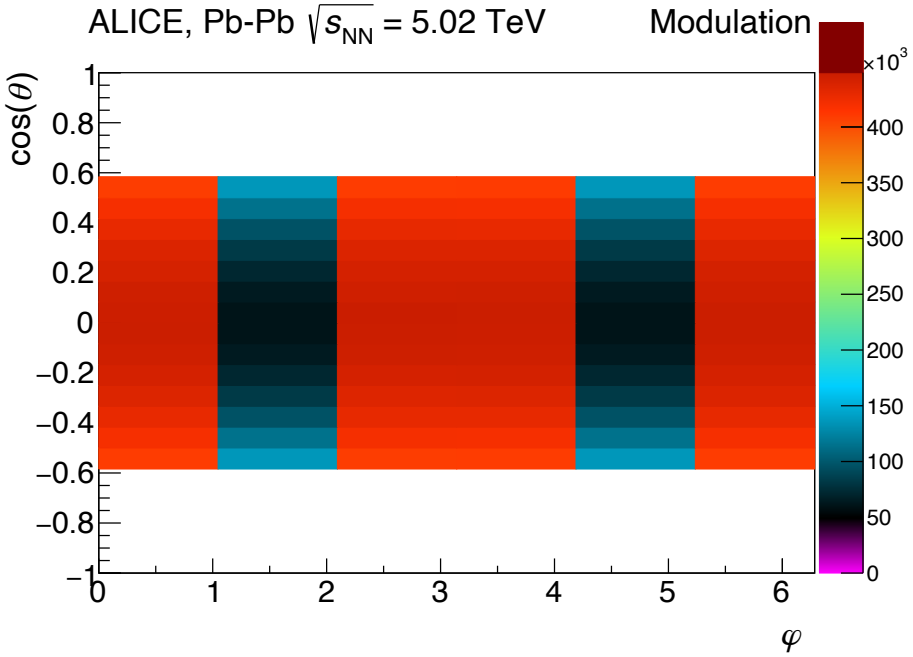


Figure 5.10: The same generated–level distribution as shown in Fig. 5.9(b), but with same binning applied to real data.

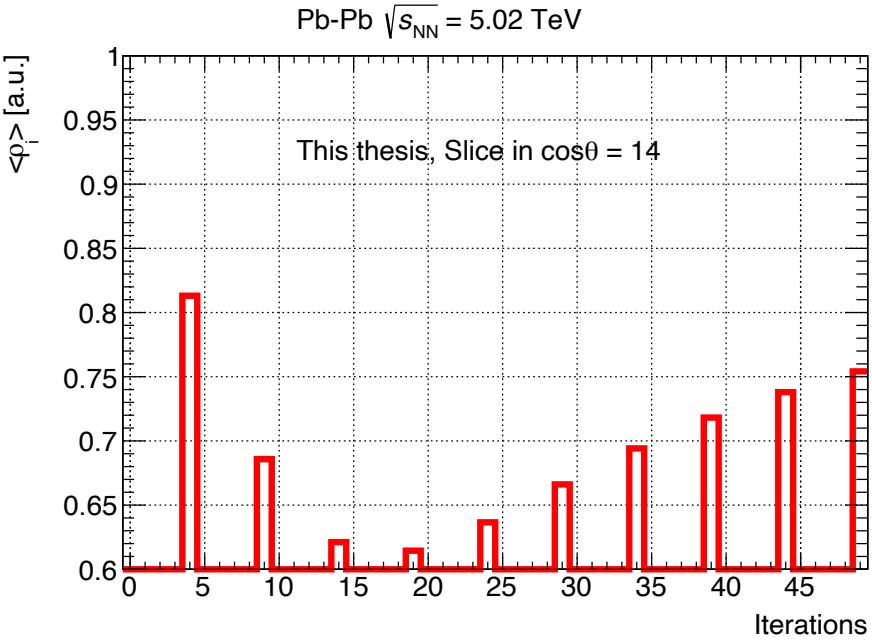
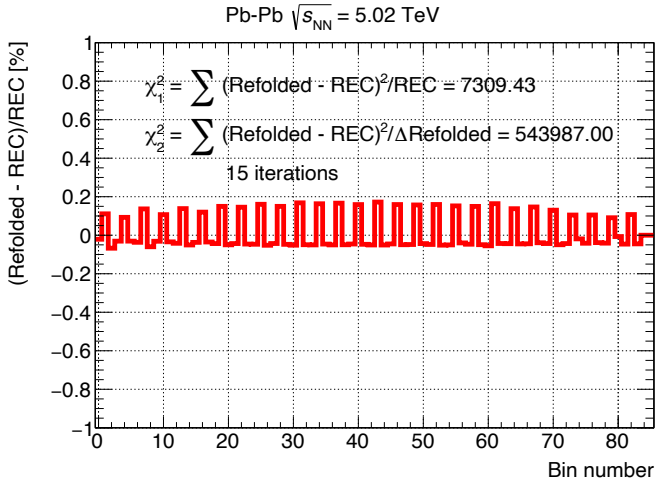
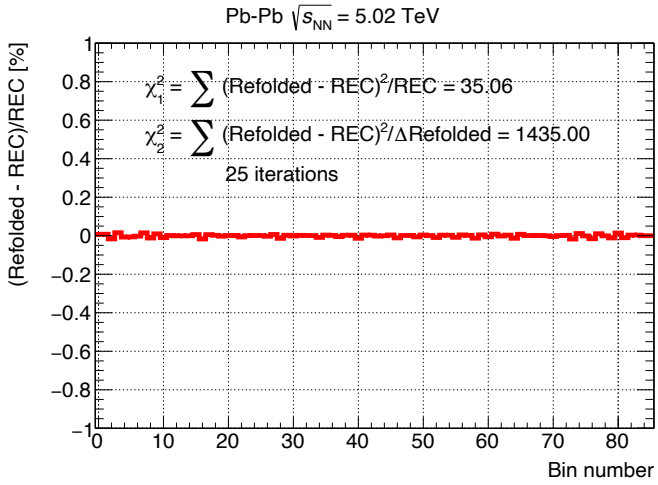


Figure 5.11: Scan of the average correlation coefficient as a function of the number of iterations when a modulation in φ is provided as input data matrix. A minimum is found at around fifteen iterations.



(a)



(b)

Figure 5.12: Fig. 5.12(a) and 5.12(b) show the relative difference of the refolded distributions to the reconstructed–level distributions, for all bins, with increasing bin numbers, with STARlight and reweighted STARlight matrices, respectively.

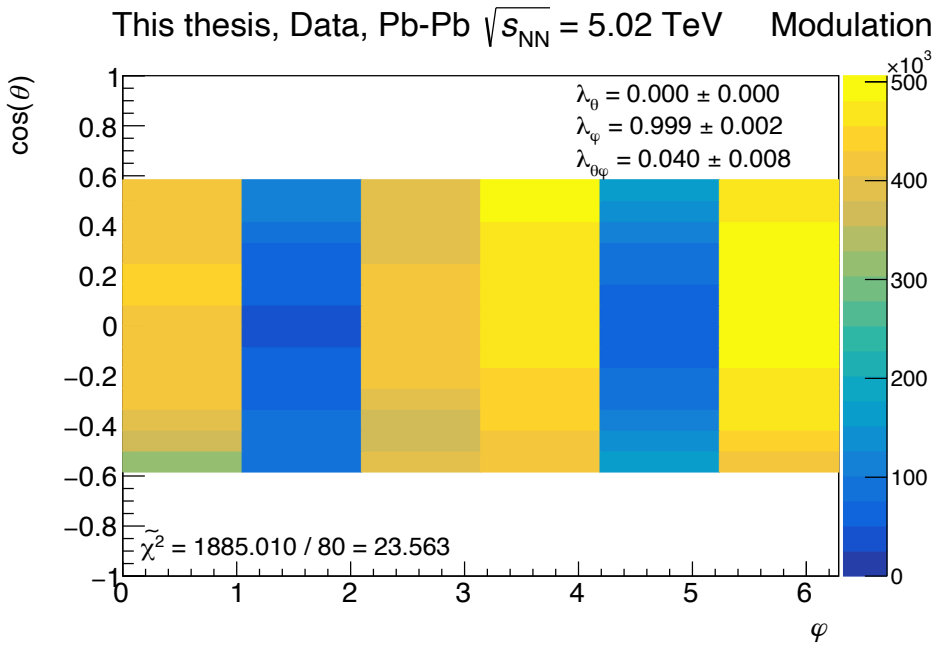


Figure 5.13: Unfolded reconstructed–level distribution with generated $\lambda_\varphi = 1$, with the same binning as real data. Large modulations are also returned by the unfolding procedure.

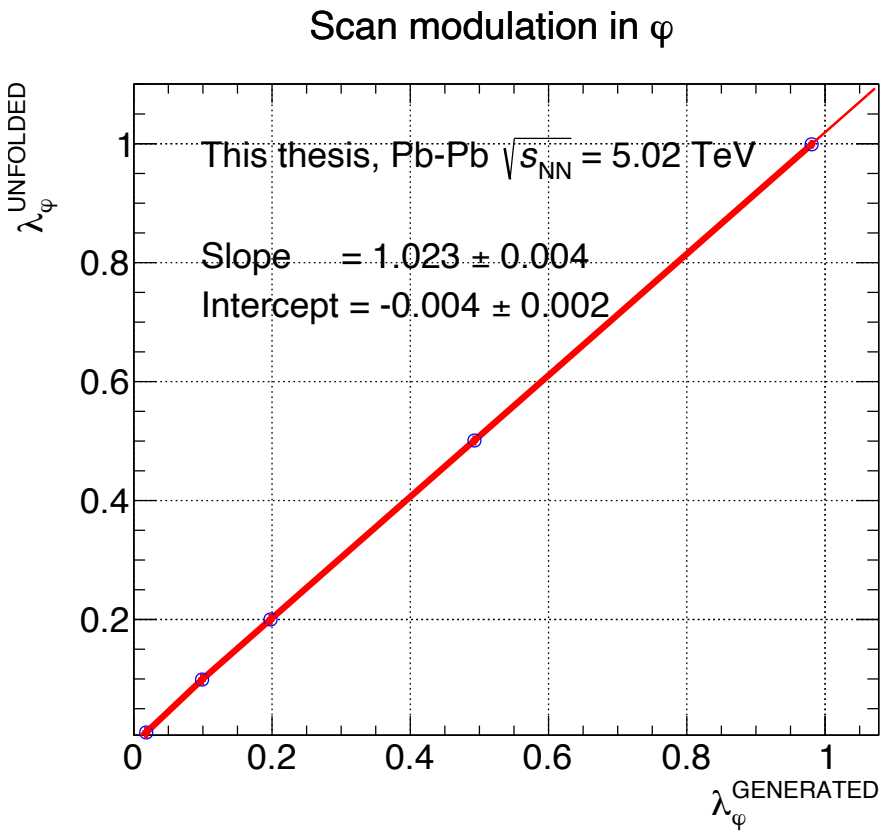


Figure 5.14: Fit to the scan in possible modulations in φ. This unfolding technique recovers consistently the input modulation.

5.9.3 Scan as a function of λ_φ

It is now possible to perform a scan of the results obtained as a function of the input λ_φ for the modulation in φ. This is shown in Fig. 5.14, where the unfolded λ_φ, $\lambda_\varphi^{\mathrm{UNFOLDED}}$, is plotted against the input λ_φ at the generated level, $\lambda_\varphi^{\mathrm{GENERATED}}$. The data points are then fitted with a straight line. The slope is close to 1, and the intercept is consistent with 0. More emphasis is given to smaller λ_φ, since a fully transverse polarisation is expected not to feature modulations in φ for real data.

It is thus shown that this analysis strategy using unfolding succeeds in recovering the input modulation in φ.

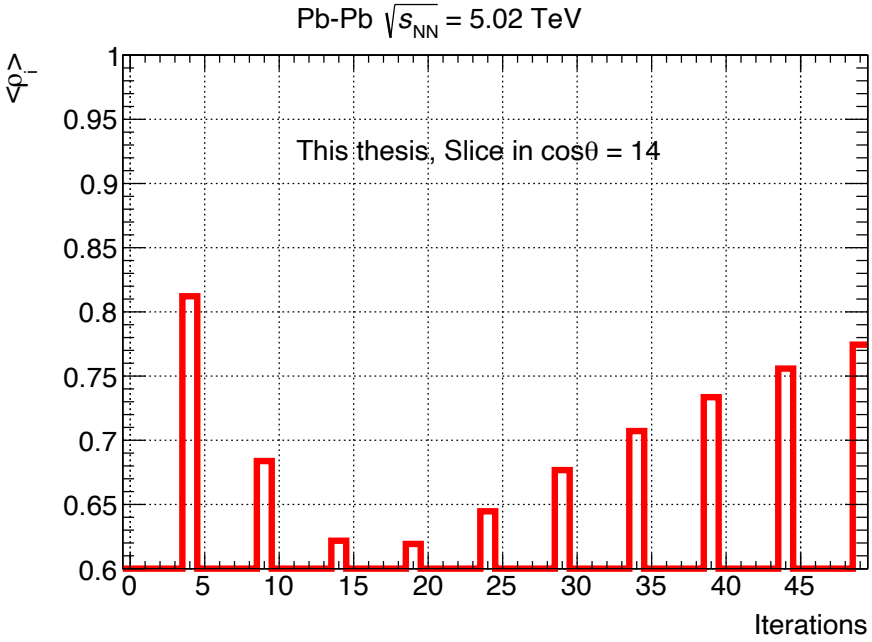


Figure 5.15: Scan of the average correlation coefficient as a function of the number of iterations when the yields from real ALICE data are used as input data matrix. A minimum is found at around fifteen iterations.

5.10 Results in the helicity frame for ALICE data

Similarly to what is seen in Sec. 5.9.2, the scan of the average correlation coefficient in the case of real ALICE data, i.e. the yields extracted from the fits to the invariant mass distributions, shows a dip at around fifteen iterations in all slices in $\cos\theta$. This is shown in Fig. 5.15. The unfolding is carried out with the STARlight response matrix. The relative difference of the refolded to the reconstructed distribution, i.e. the relative difference of the refolded to the raw yields, is shown in Fig. 5.16(a). The discrepancy is better than 20% in all bins from number 6 to 83, which correspond to the $\cos\theta$ interval $-0.5 < \cos\theta < 0.58\bar{3}$. A single bin, number 3, which corresponds to $-0.58\bar{3} < \cos\theta < -0.5$ and $3.142 < \varphi < 4.189$, shows a discrepancy above 80%. This interval is however sparsely populated. The fit to the invariant mass distributions returns a number of J/ψ, $N_{\mathrm{J}/\psi}$, equal to $N_{\mathrm{J}/\psi} = 18 \pm 5$. Hence, the large discrepancy arises from the fact that even a tiny

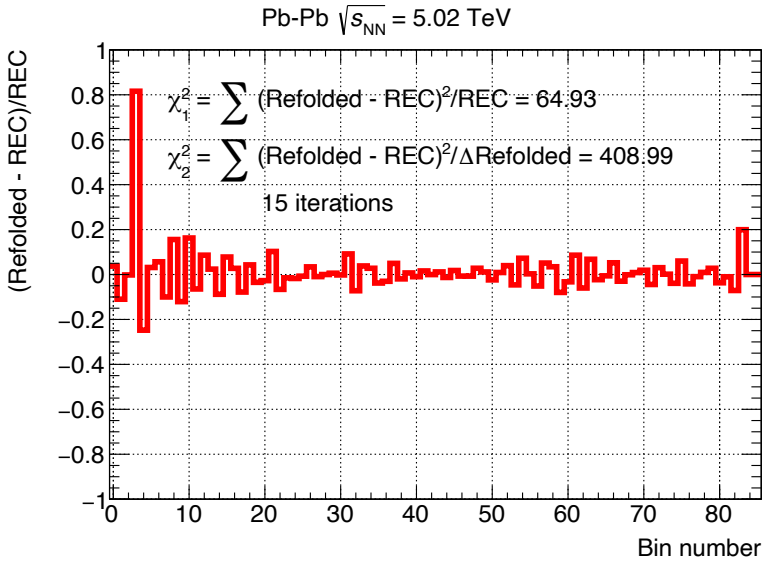
migration of events to this interval causes a sharp (positive) increase in the ratio to the reconstructed distribution. Since the unfolding is done separately for slices in $\cos\theta$, this particular slice i.e. $-0.58\bar{3} < \cos\theta < -0.5$, is not fitted. The fit is thus performed over the full range in φ, and in $-0.5 < \cos\theta < 0.58\bar{3}$, as shown in Fig. 5.16(b). The results are as follows:

$$\lambda_\theta = 0.746 \pm 0.246 \ ,$$
$$\lambda_\varphi = 0.026 \pm 0.027 \ ,$$
$$\lambda_{\theta\varphi} = 0.221 \pm 0.054 \ .$$

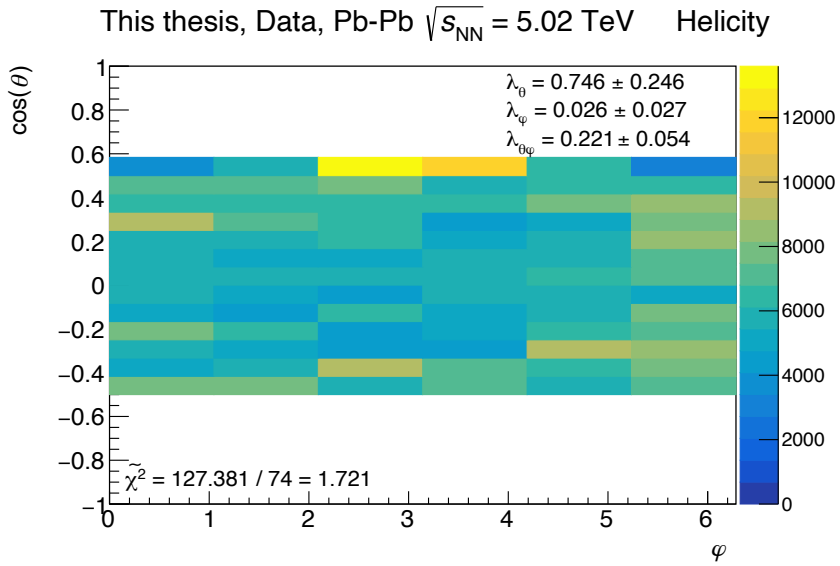
The $\chi^2/NDF = 127.381/74 = 1.721$, where the degrees of freedom are computed as $NDF = 6 \cdot 13 - 4 = 74$, where thirteen slices in $\cos\theta$ are fitted, each with six bins in φ, and the number of free parameters is four. The normalisation from the fit is $I = 80382 \pm 1407$, which can be compared to the sum of the unfolded data points in $-0.5 < \cos\theta < 0.58\bar{3}$, I_0, which is $I_0 = 76329 \pm 11913$.

5.10.1 Correlations between the angular parameters

Minuit has quite a few tools available to the end user to inspect the status of the convergence of the fit, and the stability of the results. One of these, `gMinuit->Contour()`, automatically produces the one, two, three (and so on) sigma contour plots, to visually inspect the correlations between the chosen parameters. These are shown in Fig. 5.17. Table 5.1 shows the correlation coefficients among the parameters of the fit. The three λ parameters are mildly correlated.



(a)



(b)

Figure 5.16: Fig. 5.16(a) shows the relative difference of the refolded to reconstructed–level distribution in the case of real ALICE data. Fig. 5.16(b) shows instead the fit to the unfolded distribution, along with the results.

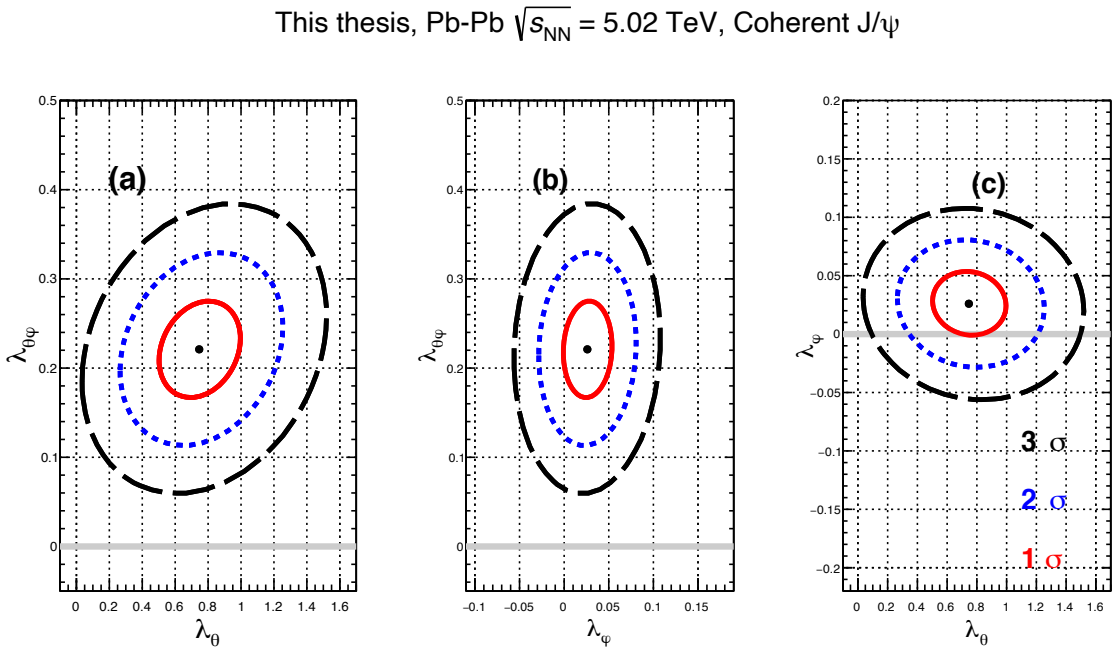


Figure 5.17: The correlations of the three lambda parameters are shown as one, two and three sigma contours in red, blue, and black, respectively, along with the central value shown as a black dot.

5.11 Systematic uncertainties

Coherent J/ψ photoproduction has already been extensively studied at the LHC, and especially in ALICE. Therefore, the sources of systematic uncertainty are well known. However, a measurement of angular distributions is affected by different systematic sources than, e.g. the measurement of the photoproduction cross sections. In addition, a few systematic uncertainties have also to be treated with a different procedure compared to a cross section measurement. This is because of a lack of statistics and/or because they are, potentially, a more prominent systematic source for an angular distribution, as will be explained in the following.

Table 5.1: Correlation coefficients among the fit parameters for real data. The correlations between the λ parameters and the normalisation from the fit, I, are also given.

	λ_θ	λ_φ	$\lambda_{\theta\varphi}$	I
λ_θ	1	-0.079	0.232	0.499
λ_φ		1	0.067	0.059
$\lambda_{\theta\varphi}$			1	0.189
I				1

5.11.1 Variations to the $\cos\theta$ interval while fitting

This particular measurement is inherently binned, as it is necessary to extract the J/ψ yields from the invariant mass distributions in intervals of $\cos\theta$ and φ. As such, the $\cos\theta$ interval covers $[-0.58\bar{3}, 0.58\bar{3}]$ continuously, owing to the reach in acceptance. The variable φ is studied in the full interval $[0, 2\pi]$ instead. As it turns out, φ displays quite flat distributions (to the extent that, *a posteriori*, the corresponding λ_φ is consistent with zero). As such, it is only needed to vary the interval over which the $\cos\theta$ distribution is fitted. This in turn, also affects λ_φ and $\lambda_{\theta\varphi}$, since the fit is performed on bidimensional distributions, and not on 1D projections.

The interval over which $\cos\theta$ is fitted is then varied to simultaneously understand also the robustness of the fit procedure over such changes. Recalling that the $\cos\theta$ binwidth is $0.08\bar{3}$, the fit is varied from the standard $[-0.5, 0.58\bar{3}]$ to $[-0.58\bar{3}, 0.58\bar{3}]$ and $[-0.5, 0.5]$, thus recovering the slice in $\cos\theta$ which was not considered for the evaluation of the central values. The systematic uncertainties on the λ parameters are taken to be half the maximum discrepancies for the computed values. The results are shown in Table 5.2.

5.11.2 Signal Extraction

The raw yields have also been extracted using a different description for the J/ψ peak. The J/ψ line shape was changed to a double-sided Crystal Ball function. The raw yields are then unfolded, and the fit procedure from Sec. 5.8.1 is applied again. Half of the deviation from the central values, obtained with the standard signal extraction (single-sided Crystal Ball), is then taken as the corresponding systematic uncertainty. The results are again shown in Table 5.2.

5.11.3 Unfolding

The central values are obtained by stopping the iterative procedure at *fifteen* iterations. The fits are then performed again with fourteen and sixteen iterations instead. Half of the maximum discrepancy is again taken as the systematic uncertainty. The results are again shown in Table 5.2.

5.11.4 Response matrices

The raw yields are corrected by unfolding with response matrices. These are computed starting from Monte Carlo data. As such, it is then likely that the original input distributions, i.e. the angular distributions which are a direct output of the Monte Carlo model, are going to be a major source of systematic uncertainty in an angular distribution measurement. STARlight is a model which only considers purely transverse polarised vector mesons [27], with no possibility to modify the input shape. This is shown in Fig. 5.18, which is an extract from `starlight/src/gammaavm.cpp`, where the decay in the rest frame of the J/ψ is modelled with a proportionality $1 + \cos^2\theta$, characteristic of a transversely polarised vector meson. This input shape is what is used to compute the central

```
case starlightConstants::MUON:
case starlightConstants::ELECTRON:
        //VM->ee/mumu
        dndtheta = sin(theta)*(1.+(cos(theta)*cos(theta)));
        break;
```

Figure 5.18: Detail taken from `starlight/src/gammaavm.cpp`. It is shown how STARlight models the decay in the helicity frame of the J/ψ. The J/ψ is purely transverse.

value of the lambda parameters. To circumvent this apparent limitation of the model, and to be able to compute the related systematic uncertainty, it is then possible to take a STARlight event and reweight it inside `RooUnfold`, while building the response matrices themselves. The weight is taken to be the inverse of Eq. 5.5, where the λ parameters are this time set as the central values obtained from the analysis of real ALICE data. The convergence test is again performed to understand how many iterations are required before stopping the iterative procedure, and a minimum is found for all slices again at around fifteen iterations. Half of the maximum discrepancy with respect to the central values is taken to be the relevant systematic uncertainty. The results are shown in Table 5.2.

5.11.5 Trigger and tracking

In inclusive J/ψ studies, the ALICE Collaboration studies the trigger and tracking efficiency by plotting the ratio of the number of muons passing the high p_{T} cut at 4.2 GeV/c to those passing the low p_{T} cut at 1 GeV/c [83, 85, 86]. With the low p_{T} involved in coherent J/ψ photoproduction, this procedure is unsuitable for an angular distribution analysis. Instead, a procedure more directly related to angular distributions can be used in these circumstances.

As the online low p_{T} cut on each muon is of 1 GeV/c, it is then possible to vary the software cut on the p_{T} of each muon, from 0.85 GeV/c to 1.15 GeV/c, both in real data

and in Monte Carlo simulations. The trigger chambers are at half efficiency at $p_{\mathrm{T}} = 1$ GeV/c. As the coherent J/ψ is characterized by very low p_{T}, it is then possible to lose one of the two muons from the decay of the J/ψ, thus losing the event altogether. The corresponding unfolded distributions are then fitted to measure the respective λ_θ, λ_φ and $\lambda_{\theta\varphi}$. Half the maximum discrepancy is taken as the corresponding systematic uncertainty.

The results are shown in Fig. 5.19(a), 5.19(b), and 5.19(c). The actual numbers are then given in Table 5.2.

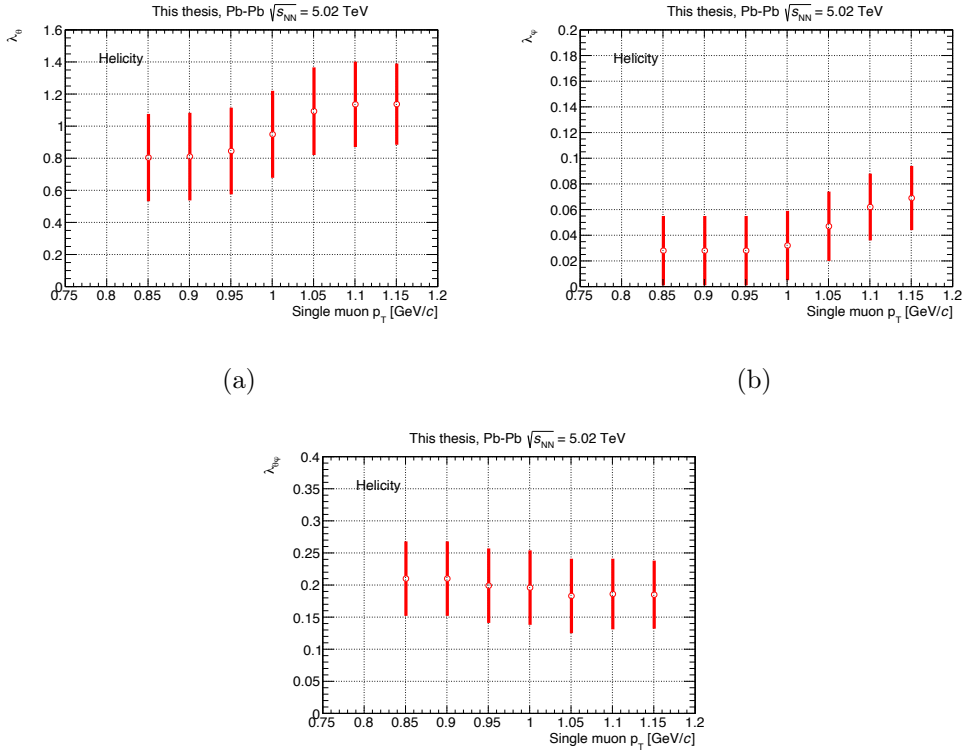


Figure 5.19: Trigger systematic uncertainties for λ_θ, λ_φ and $\lambda_{\theta\varphi}$ in Fig. 5.19(a), 5.19(b) and 5.19(c), respectively.

Table 5.2: Table summarising the absolute systematic uncertainties for the measurement of coherent J/ψ polarisation. The main systematic uncertainties considered are due to variations on the fitted $\cos\theta$ interval, the impact of different descriptions of the J/ψ line shape, the unfolding, the input Monte Carlo shape used for the response matrices, and the trigger effects on the single muons comprising the J/ψ.

Systematics	λ_θ	λ_φ	$\lambda_{\theta\varphi}$
$\cos\theta$ **range**	0.142	0.002	0.056
signal extraction	0.026	0.002	0.008
unfolding	0.019	0.004	0.004
response matrix	0.009	0.008	0.004
single muon p_{T} **threshold**	0.196	0.022	0.019
TOTAL	0.244	0.023	0.060

5.12 Final results

Table 5.2 reports the systematic uncertainties, while the final results of the measurement of coherent J/ψ polarisation are shown in Table 5.3. The measured value of $\lambda_{\theta\varphi}$ is not compatible with 0 within three sigmas. More studies are currently ongoing to assess whether there is an additional systematic source which would justify such a discrepancy.

Table 5.3: Final results for the measurement of coherent J/ψ polarisation in the helicity frame.

λ_θ	λ_φ	$\lambda_{\theta\varphi}$
$0.746 \pm 0.246 \pm 0.244$	$0.026 \pm 0.027 \pm 0.023$	$0.221 \pm 0.054 \pm 0.060$

5.12.1 Comparison with past results

While this is the first measurement of J/ψ polarisation in UPC events, J/ψ polarisation has previously been measured by the H1 Collaboration in the photoproduction [33] regime. The ZEUS Collaboration [101, 102] has also measured J/ψ polarisation at somewhat higher Q^2, i.e. $2 < Q^2 < 5$ GeV ^{2}. However, these past results have been produced with another polarisation formalism, the Schilling matrices [103], and thus the ALICE results need to be translated to directly compare with the previously published results.

It is then necessary to derive formulae to relate the two formalisms, i.e. from lambda parameters to spin-density matrix elements $r^{ik}_{\lambda\lambda'}$ [103]. This requires the use of Eq. 5.6 [42] and Eq. 5.7, which refer to distributions in the total solid angle in full phase space:

$$\begin{aligned} W(\cos\theta) &\propto \frac{1}{3+\lambda_\theta} \cdot (1 + \lambda_\theta \cdot \cos^2\theta) \ , \\ W(\varphi) &\propto 1 + \frac{2\lambda_{\theta\varphi}}{3+\lambda_\theta} \cdot \cos 2\varphi \ , \end{aligned} \tag{5.6}$$

$$\begin{aligned} W(\cos\theta) &\propto 1 + r^{04}_{00} + (1 - 3r^{04}_{00}) \cdot \cos^2\theta \ , \\ W(\varphi) &\propto 1 + r^{04}_{1,-1} \cdot \cos 2\varphi \ . \end{aligned} \tag{5.7}$$

It is possible to operate by direct comparison, and obtain Eq. 5.8:

$$\begin{aligned} r^{04}_{00} &= \frac{1-\lambda_\theta}{3+\lambda_\theta} \\ r^{04}_{1,-1} &= \frac{\lambda_\varphi}{2} \cdot (1 + r^{04}_{00}) \ . \end{aligned} \tag{5.8}$$

Error propagation is then needed to convert ALICE uncertainties on this measurement to uncertainties on the spin-density matrix elements. This yields the following Eq. 5.9 and 5.10:

$$\begin{aligned} \Delta r^{04}_{00} &= \frac{\partial}{\partial\lambda_\theta}\left(\frac{1-\lambda_\theta}{3+\lambda_\theta}\right) \cdot \Delta\lambda_\theta = \\ &= \frac{4}{(3+\lambda_\theta)^2} \cdot \Delta\lambda_\theta \ , \end{aligned} \tag{5.9}$$

$$\frac{\Delta r^{04}_{1,-1}}{r^{04}_{1,-1}} = \sqrt{\left[\frac{\Delta\lambda_\phi}{\lambda_\phi}\right]^2 + \left[\frac{\Delta r^{04}_{00}}{1+r^{04}_{00}}\right]^2} \ , \tag{5.10}$$

which are the formulae needed to translate the statistical and systematic uncertainties on r_{00}^{04} and $r_{1,-1}^{04}$, respectively.

ALICE results can now be compared with those from H1 [33] and ZEUS [101], as shown in Fig. 5.20. H1 points refer to a data sample in the photoproduction regime, with very low values of Q^2 i.e. $Q^2 \sim 0.05$ GeV ^{2}, while ZEUS data correspond to somewhat higher values of Q^2 i.e. $2 < Q^2 < 5$ GeV ^{2}. It is thus expected that the agreement should, in principle, be better between ALICE and H1, rather than ALICE and ZEUS, as is the case.

5.13 Conclusions

The measurement of coherent J/ψ polarisation in Pb–Pb UPC events has been performed with ALICE UPC Run 2 data. On the basis of the s-channel helicity conservation hypothesis, the vector meson should retain the polarisation of the originating quasi-real photon. This means that the vector meson should display transverse polarisation, unless a different production mechanism is at work in the process. ALICE data show that the J/ψ is transversely polarised. The results presented in this thesis are in good agreement with the results already presented for J/ψ photoproduction with electron-proton data by the H1 Collaboration, when the formalism is converted to spin-density matrix elements. Together with the previously published ρ^0 results in UPC by the STAR Collaboration, see Sec. 1.1.5, this confirms a photoproduction origin for both vector mesons.

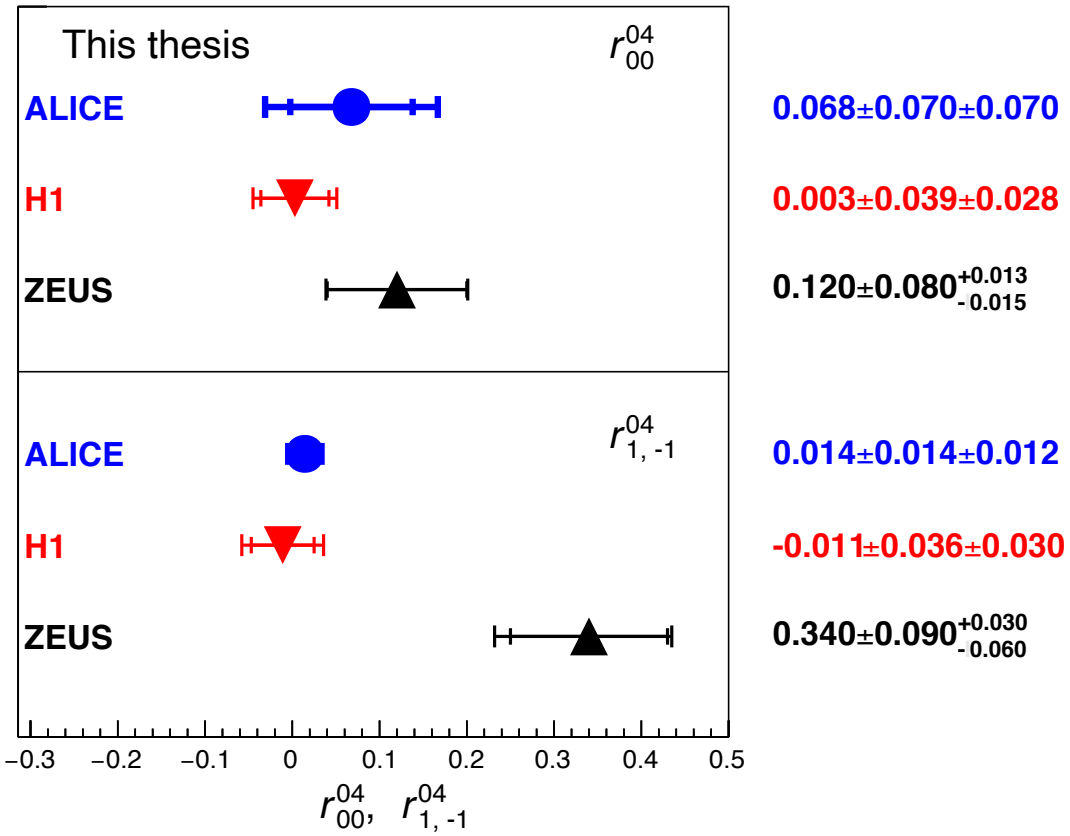


Figure 5.20: ALICE results for coherent J/ψ polarisation are shown translated to spin-density matrix elements. This allows for the direct comparison with the results achieved by H1 and ZEUS collaborations. ALICE results display better agreement with the measurement performed by H1, as expected considering that both are probing the photoproduction regime.

Conclusions

Vector meson photoproduction has been extensively studied at HERA using proton targets. The ALICE Collaboration has been involved in measurements of vector meson photoproduction with nuclear targets since Run 1. However, the available measurements did not provide a way to explore nuclear gluon pdfs at Bjorken-x lower than 10^{-3}. The measurements presented in this document, i.e. the measurement of coherent J/ψ photoproduction in neutron emission classes, presents itself as a viable technique to extract a low x contribution down to $x \sim 10^{-5}$. Nuclear shadowing can thus be explored to the same range of Bjorken-x. However, the systematic uncertainties involved are not negligible for two of the four possible neutron emission classes. This is also accompanied with a lack of statistics for e.g. the XNXN class. The theoretical models also have considerable uncertainties.

The current measurement of coherent J/ψ photoproduction in neutron emission classes provides a robust and consistent picture both at forward and midrapidity. In particular, 0NXN and XN0N cross sections agree well within current uncertainties. This is also in support of the factorisation principle, i.e. the factorisation of the main photoproduction process from the additional photon exchanges. The suppression factors obtained for $x \sim 10^{-2}$ are in agreement with the values reported by ALICE in [5] for the non-differential measurement, while the suppression factors at $10^{-4} \lesssim x \lesssim 10^{-5}$ are in agreement with the reweighting carried out in [9].

The first measurement of coherent J/ψ polarisation, in Pb–Pb UPC at $\sqrt{s_{\mathrm{NN}}} = 5.02$ TeV, is also presented. As the photon in the initial state is quasi-real, the vector meson may be expected to also be transversely polarised, thus retaining the polarisation of the original photon. This was already observed with proton targets at HERA, but it is the first time that this measurement has been performed in UPC with nuclear targets. The results confirm the picture of transverse polarisation for the vector meson. In addition, the results are provided in two different formalisms, to better compare the ALICE results with other systems e.g. inclusive samples, and with previous photoproduction measurements i.e. H1, and ZEUS.

Appendix A

Relating rapidity of the vector meson to the Bjorken-x

The rapidity of the vector meson produced in the final state of an ultraperipheral event, can be related to the Bjorken-x of the gluons being probed by the photon in the initial state.

For convenience's sake, Fig. 1.14(a) is proposed again as Fig. A.1.

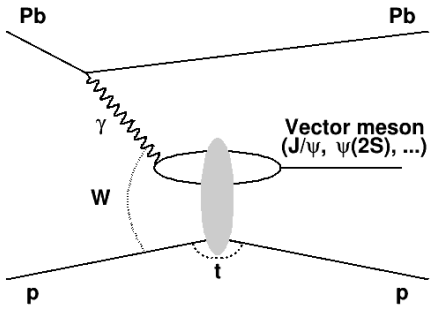


Figure A.1: Possible vector meson photoproduction topology. The photon from the emitter interacts with a Pomeron from the target. A vector meson is produced in the final state.

In the centre-of-mass frame, assuming negligible p_{T} for incoming ions or protons, it is

possible to write as follows:

$$\begin{aligned} \mathrm{p}_\gamma^\mu &= (x_1 \cdot \mathrm{p}, 0, 0, x_1 \cdot \mathrm{p}) \\ \mathrm{p}_{\mathbb{P}}^\mu &= (x_2 \cdot \mathrm{p}, 0, 0, -x_2 \cdot \mathrm{p}) \ , \end{aligned} \tag{A.1}$$

where p_γ^μ and $\mathrm{p}_{\mathbb{P}}^\mu$ are the momenta of the photon in the initial state and of the Pomeron from the target, respectively. Each carries a fraction of the momenta of the corresponding hadron, x_1 and x_2, respectively.

The invariant mass of the final state i.e. the invariant mass of the vector meson, M_{VM}, reads as in the following Eq. A.2:

$$\begin{aligned} M_{\mathrm{VM}}^2 &= [(x_1 + x_2) \cdot \mathrm{p}]^2 - [(x_1 - x_2) \cdot \mathrm{p}]^2 = \\ &= \mathrm{p}^2 \cdot (x_1^2 + x_2^2 + 2 \cdot x_1 \cdot x_2 - x_1^2 - x_2^2 + 2 \cdot x_1 \cdot x_2) = \\ &= 4 \cdot x_1 \cdot x_2 \cdot \mathrm{p}^2 = x_1 \cdot x_2 \cdot s \ , \end{aligned} \tag{A.2}$$

where s is the centre-of-mass energy of the initial state, squared.

Considering now the definition of rapidity, y, shown in the following Eq. A.3:

$$y = \frac{1}{2} \cdot \ln \frac{E + \mathrm{p}_z}{E - \mathrm{p}_z} \ , \tag{A.3}$$

it is then possible to specialise it for the case of the vector meson in the final state, as shown in the following Eq. A.4:

$$\begin{aligned} y_{\mathrm{VM}} &= \frac{1}{2} \cdot \ln \frac{(x_1 + x_2 + x_1 - x_2) \cdot \mathrm{p}}{(x_1 + x_2 - x_1 + x_2) \cdot \mathrm{p}} \\ &= \frac{1}{2} \cdot \ln \frac{x_1}{x_2} \ , \end{aligned} \tag{A.4}$$

where y_{VM} is the rapidity of the vector meson in the final state. Thus, Eq. A.5 holds:

$$e^{2 \cdot y_{\mathrm{VM}}} = \frac{x_1}{x_2} \ . \tag{A.5}$$

Using Eq. A.2 and Eq. A.5, we obtain Eq. A.6:

$$\begin{aligned} e^{2 \cdot y_{\mathrm{VM}}} \cdot \frac{M_{\mathrm{VM}}^2}{s} &= x_1^2 \\ e^{2 \cdot -y_{\mathrm{VM}}} \cdot \frac{M_{\mathrm{VM}}^2}{s} &= x_2^2 \ . \end{aligned} \tag{A.6}$$

From which Eq. A.7:

$$\begin{aligned} x_1 &= e^{y_{\mathrm{VM}}} \cdot \frac{M_{\mathrm{VM}}}{\sqrt{s}} \\ x_2 &= e^{-y_{\mathrm{VM}}} \cdot \frac{M_{\mathrm{VM}}}{\sqrt{s}} \ . \end{aligned} \tag{A.7}$$

Appendix B

Meaning of the bits assigned to the SSM

The meaning of the bits assigned to the SSM is the following:

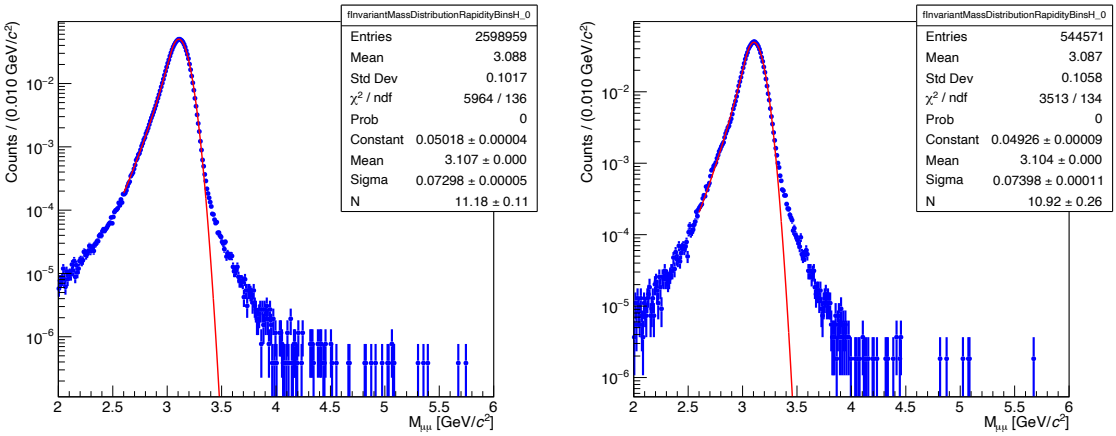
- **bit 127:** SSM flag;
- **bits 126 to 115:** BC ID bits 11 to 0;
- **bits 114 to 83:** ORBIT ID bits 31 to 0;
- **bits 82 to 51:** Trigger Types bits 31 to 0;
- **bit 50:** calibration signal;
- **bit 49:** L1 signal;
- **bit 48:** L0/LM signal;
- **bit 47:** TTC-FMC card ready;
- **bits 46 to 43:** miscellaneous decoding errors;

- **bit 42:** channel A;
- **bit 41:** strobe of a broadcast message;
- **bits 40 and 39:** bits 6 and 7 of a broadcast message;
- **bits 38 to 35:** bits 2 to 5 of a broadcast message;
- **bit 34:** event counter reset from a broadcast message;
- **bit 33:** bunch counter reset from a broadcast message;
- **bit 32:** strobe of an individually addressed message;
- **bits 31 to 18:** address bits of an individually addressed message;
- **bit 17:** strobe of an individually addressed message;
- **bits 16 to 9:** subaddress field of an individually addressed message;
- **bits 8 to 1:** data field of an individually addressed message;
- **bit 1:** clock at 40 MHz assigned to the TTCit.

Appendix C

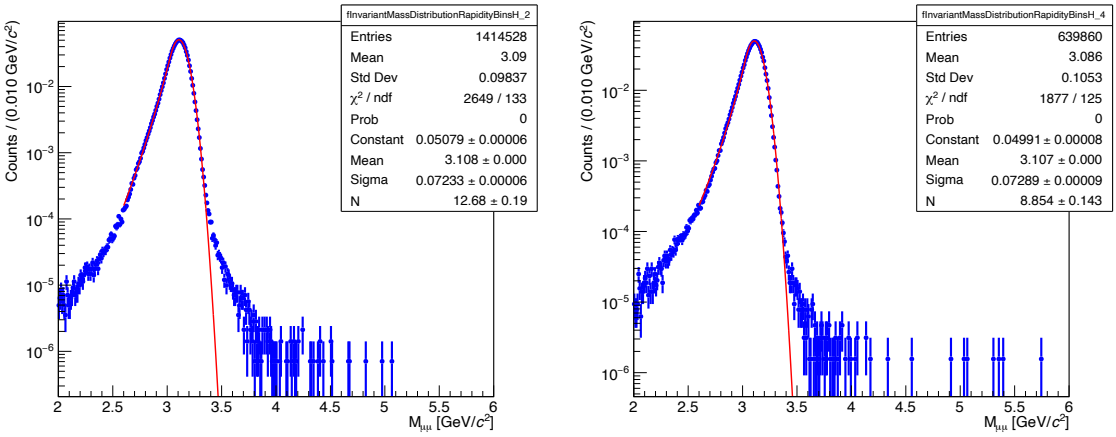
Fits to reconstructed STARlight distributions for the neutron emission analysis

In the case of the neutron emission analysis, only twelve reconstructed distributions have to be fitted to ultimately extract the yields from the real data. This is because the analysis is only differential in neutron emission classes and rapidity intervals. As no generator at the moment can create templates for neutron emission classes, this leaves reconstructed distributions differential only in dimuon rapidity. Hence, only four distributions per process have to be fitted, and thus twelve in total, i.e. coherent J/ψ, coherent ψ', and background. The fits shown in this section are all loglikelihood binned fits, with fitting range in the following dimuon invariant mass intervals: $M_{\mu\mu} \in [2.6, 4]$ GeV/c^2 for the J/ψ, $M_{\mu\mu} \in [2, 15]$ GeV/c^2 for the ψ', $M_{\mu\mu} \in [1.8, 8]$ GeV/c^2 for the $\gamma\gamma$ background.



(a)

(b)



(c)

(d)

Figure C.1: Fit to reconstructed STARlight distributions for J/ψ. Fig. C.1(a), C.1(b), C.1(c), and C.1(d) show the fits to the J/ψ distributions with dimuon rapidity lying in the interval $-4 < y < -2.5$, $-4 < y < -3.5$, $-3.5 < y < -3$, and $-3 < y < -2.5$, respectively.

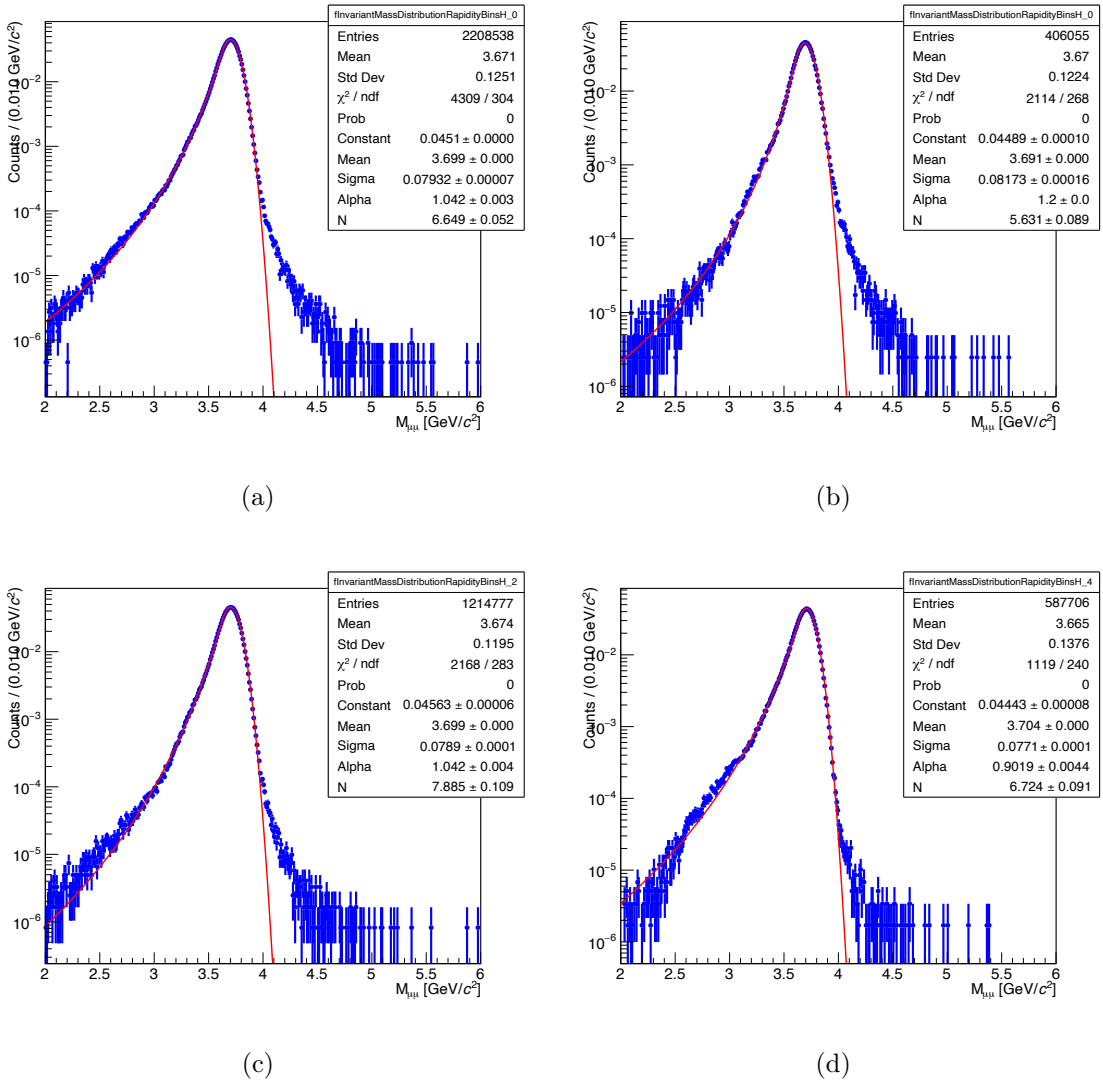


Figure C.2: Fit to reconstructed STARlight distributions for ψ'. Fig. C.2(a), C.2(b), C.2(c), and C.2(d) instead show the fits to the ψ' distributions with dimuon rapidity lying in the interval $-4 < y < -2.5$, $-4 < y < -3.5$, $-3.5 < y < -3$, and $-3 < y < -2.5$, respectively.

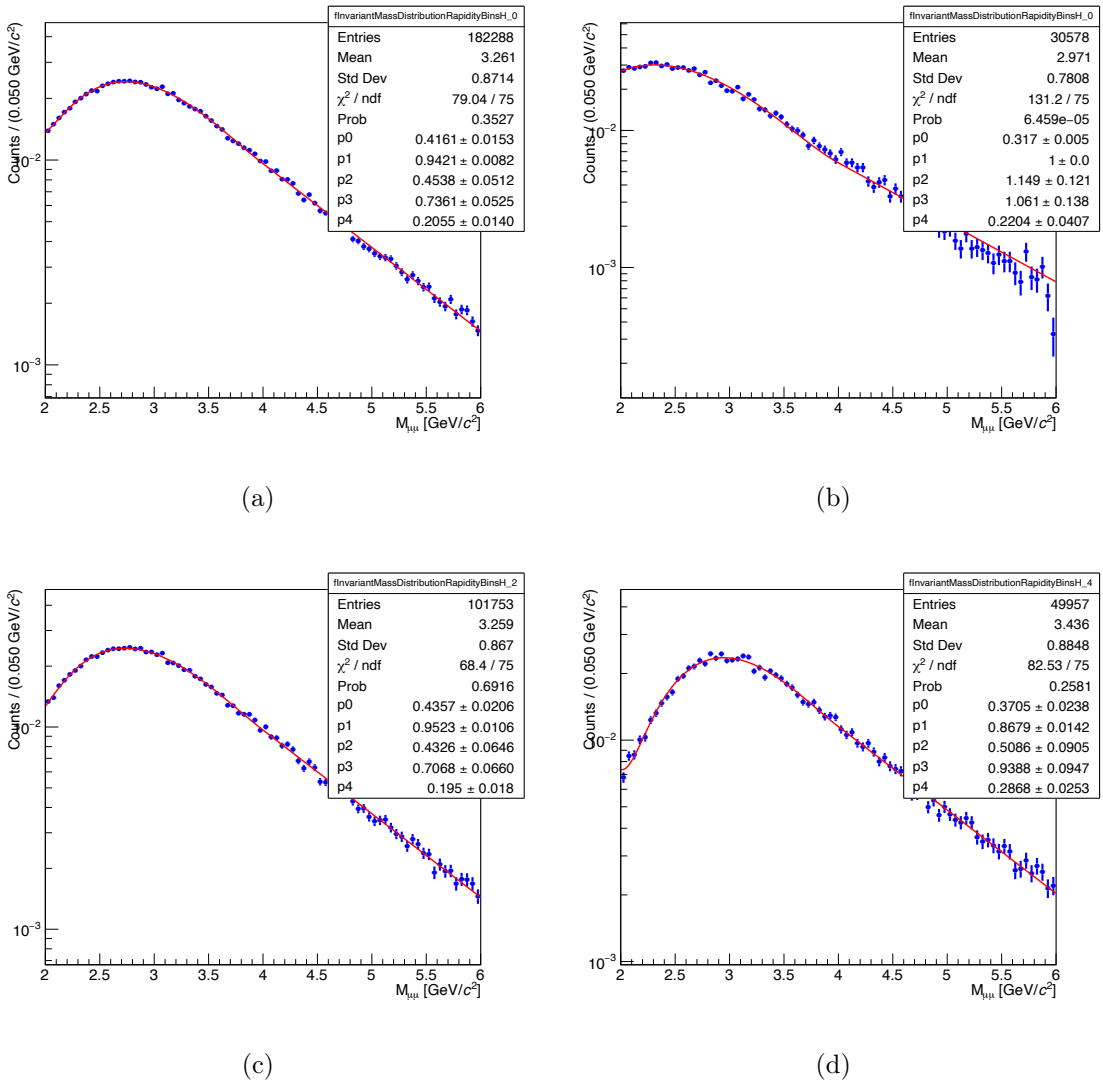


Figure C.3: Fit to reconstructed STARlight distributions for the $\gamma\gamma$ background. Finally, Fig. C.3(a), C.3(b), C.3(c), and C.3(d) show the fits to the background distributions with dimuon rapidity lying in the interval $-4 < y < -2.5$, $-4 < y < -3.5$, $-3.5 < y < -3$, and $-3 < y < -2.5$, respectively.

Appendix D

Renormalising the fit function for the polarisation measurement

Eq. 5.4 is integrated over the full acceptance in φ, i.e. $[0, 2\pi]$. It is possible to relate the normalisation of the fit function to the sum of the unfolded data points directly, by renormalising the fit function. This is carried out by firstly computing the integral in the solid angle:

$$\begin{aligned} A &= \int_a^b d\cos\theta \int_0^{2\pi} d\varphi \, W(\cos\theta, \varphi) = \\ &= \int_a^b d\cos\theta \left[1 + \lambda_\theta \cdot \cos^2\theta + \lambda_\varphi \cdot \sin^2\theta \cdot \frac{\sin 2\varphi}{2} + \lambda_{\theta\varphi} \cdot \sin 2\theta \cdot \sin\varphi\right]_0^{2\pi} = \\ &= 2\pi \cdot \left[(b-a) + \frac{1}{3} \cdot (b^3 - a^3)\lambda_\theta\right] \, , \end{aligned} \tag{D.1}$$

and by renormalising A to 1, it is possible to obtain:

$$\begin{aligned} A' &= S \cdot \int_a^b d\cos\theta \int_0^{2\pi} d\varphi \, W(\cos\theta, \varphi) = \\ &= \frac{3}{2\pi \cdot [3 \cdot (b-a) + (b^3 - a^3)\lambda_\theta]} \cdot \int_a^b d\cos\theta \int_0^{2\pi} d\varphi \, W(\cos\theta, \varphi) \, . \end{aligned} \tag{D.2}$$

There are two special cases of particular interest for the polarisation measurement reported in this thesis:

- $\mathbf{a = b = 1}$: $S = \frac{3}{4\pi} \cdot \frac{1}{3+\lambda_\theta}$;
- $\mathbf{a = -0.5,\ b = 0.58\bar{3}}$: $S = \frac{3}{2\pi} \cdot \frac{I}{3.25+0.323495 \cdot \lambda_\theta}$.

Eq. 5.4 can then be rewritten as:

$$W(\cos\theta, \varphi) = \frac{3}{2\pi} \cdot \frac{I}{3.25 + 0.323495 \cdot \lambda_\theta} \cdot \left[1 + \lambda_\theta \cos^2\theta + \lambda_\varphi \sin^2\theta \cos 2\varphi + \lambda_{\theta\varphi} \sin 2\theta \cos\varphi\right] , \tag{D.3}$$

where I then refers to the number of events in the selected $\cos\theta$ range $-0.5 < \cos\theta < 0.58\bar{3}$. Defining as I_0 the sum of the unfolded data points u_i which lie in the $\cos\theta$ range $[-0.5, 0.58\bar{3}]$, $I_0 = \sum_{\cos\theta=-0.5}^{0.58\bar{3}} u_i$, it is then possible to compare I from the results of the fit with I_0.

Appendix E

Conversion slice number to $\cos\theta$ interval for the coherent J/ψ polarisation measurement

The acceptance in $\cos\theta$ is divided in twentyfour $\cos\theta$ interval, which are then assigned a number to properly identify the results within the framework. The following conventions are then used:

- **Slice 0:** $-1 < \cos\theta < -0.91\bar{6}$;
- **Slice 1:** $-0.91\bar{6} < \cos\theta < -0.8\bar{3}$;
- **Slice 2:** $-0.8\bar{3} < \cos\theta < -0.75$;
- **Slice 3:** $-0.75 < \cos\theta < -0.\bar{6}$;
- **Slice 4:** $-0.\bar{6} < \cos\theta < -0.58\bar{3}$;
- **Slice 5:** $-0.58\bar{3} < \cos\theta < -0.5$;

- **Slice 6:** $-0.5 < \cos\theta < -0.41\bar{6}$;
- **Slice 7:** $-0.41\bar{6} < \cos\theta < -0.\bar{3}$;
- **Slice 8:** $-0.\bar{3} < \cos\theta < -0.25$;
- **Slice 9:** $-0.25 < \cos\theta < -0.1\bar{6}$;
- **Slice 10:** $-0.1\bar{6} < \cos\theta < -0.08\bar{3}$;
- **Slice 11:** $-0.08\bar{3} < \cos\theta < 0$;
- **Slice 12:** $0 < \cos\theta < 0.08\bar{3}$;
- **Slice 13:** $0.08\bar{3} < \cos\theta < 0.1\bar{6}$;
- **Slice 14:** $0.1\bar{6} < \cos\theta < 0.25$;
- **Slice 15:** $0.25 < \cos\theta < 0.\bar{3}$;
- **Slice 16:** $0.\bar{3} < \cos\theta < 0.41\bar{6}$;
- **Slice 17:** $0.41\bar{6} < \cos\theta < 0.5$;
- **Slice 18:** $0.5 < \cos\theta < 0.58\bar{3}$;
- **Slice 19:** $0.58\bar{3} < \cos\theta < 0.\bar{6}$;
- **Slice 20:** $0.\bar{6} < \cos\theta < 0.75$;
- **Slice 21:** $0.75 < \cos\theta < 0.8\bar{3}$;
- **Slice 22:** $0.8\bar{3} < \cos\theta < 0.91\bar{6}$;
- **Slice 23:** $0.91\bar{6} < \cos\theta < 1$.

References

[1] **ALICE** Collaboration, B. Abelev *et al.*, "Coherent J/ψ photoproduction in ultra-peripheral Pb–Pb collisions at $\sqrt{s_{\rm NN}} = 2.76$ TeV", *Phys. Lett.* **B718** (2013) 1273–1283, arXiv:1209.3715 [nucl-ex].

[2] **ALICE** Collaboration, E. Abbas *et al.*, "Charmonium and e^+e^- pair photoproduction at mid-rapidity in ultra-peripheral Pb–Pb collisions at $\sqrt{s_{\rm NN}} = 2.76$ TeV", *Eur. Phys. J.* **C73** no. 11, (2013) 2617, arXiv:1305.1467 [nucl-ex].

[3] **ALICE** Collaboration, J. Adam *et al.*, "Coherent ψ(2S) photo-production in ultra-peripheral Pb–Pb collisions at $\sqrt{s_{\rm NN}} = 2.76$ TeV", *Phys. Lett.* **B751** (2015) 358–370, arXiv:1508.05076 [nucl-ex].

[4] **ALICE** Collaboration, J. Adam *et al.*, "Coherent ρ^0 photoproduction in ultra-peripheral Pb–Pb collisions at $\sqrt{s_{\rm NN}} = 2.76$ TeV", *JHEP* **09** (2015) 095, arXiv:1503.09177 [nucl-ex].

[5] **ALICE** Collaboration, S. Acharya *et al.*, "Coherent J/ψ photoproduction at forward rapidity in ultra-peripheral Pb–Pb collisions at $\sqrt{s_{\rm NN}} = 5.02$ TeV", *Phys. Lett. B* **798** (2019) 134926, arXiv:1904.06272 [nucl-ex].

[6] **LHCb** Collaboration, A. Bursche, "Study of coherent J/ψ production in lead-lead collisions at $\sqrt{s_{\rm NN}} = 5$ TeV with the LHCb experiment", *Nucl. Phys. A* **982** (2019) 247–250.

[7] **LHCb** Collaboration, G. Graziani, "Results on heavy ion physics at LHCb", *J. Phys. Conf. Ser.* **1271** no. 1, (2019) 012008, arXiv:1904.04130 [hep-ex].

[8] **LHCb** Collaboration, R. Aaij *et al.*, "Study of coherent J/ψ production in lead-lead collisions at $\sqrt{s_{NN}} = 5$ TeV", arXiv:2107.03223 [hep-ex].

[9] V. Guzey, E. Kryshen, M. Strikman, and M. Zhalov, "Nuclear suppression from coherent J/ψ photoproduction at the Large Hadron Collider", *Phys. Lett. B* **816** (2021) 136202, arXiv:2008.10891 [hep-ph].

[10] M. Broz, J. G. Contreras, and J. D. Tapia Takaki, "A generator of forward neutrons for ultra-peripheral collisions: $\mathbf{n}^{\mathbf{O}}_{\mathbf{O}}\mathbf{n}$", *Comput. Phys. Commun.* **253** (2020) 107181, arXiv:1908.08263 [nucl-th].

[11] **ALICE** Collaboration, S. Acharya *et al.*, "Coherent photoproduction of ρ^0 vector mesons in ultra-peripheral Pb–Pb collisions at $\sqrt{s_{\rm NN}} = 5.02$ TeV", *JHEP* **06** (2020) 035, arXiv:2002.10897 [nucl-ex].

[12] **ALICE** Collaboration, J. Adam *et al.*, "Measurement of an excess in the yield of J/ψ at very low $p_{\rm T}$ in Pb–Pb collisions at $\sqrt{s_{\rm NN}} = 2.76$ TeV", *Phys. Rev. Lett.* **116** no. 22, (2016) 222301, arXiv:1509.08802 [nucl-ex].

[13] **ALICE** Collaboration, O. Bugnon, "Coherent J/ψ photoproduction in peripheral heavy-ion collisions", *EPL* **129** no. 4, (2020) 42001.

[14] **ALICE** Collaboration, S. Acharya *et al.*, "Energy dependence of exclusive J/ψ photoproduction off protons in ultra-peripheral p-Pb collisions at $\sqrt{s_{\rm NN}} = 5.02$ TeV", arXiv:1809.03235 [nucl-ex].

[15] CERN, "The four main LHC experiments." Jun, 1999. https://cds.cern.ch/record/40525.

[16] ALICE, "The ALICE Forward Muon Spectrometer.". https://twiki.cern.ch/twiki/bin/viewauth/ALICE/MuonTracking.

[17] J. Kvapil *et al.*, "ALICE Central Trigger System for LHC Run 3", *EPJ Web Conf.* **251** (2021) 04022, arXiv:2106.08353 [physics.ins-det].

[18] V. Guzey, E. Kryshen, and M. Zhalov, "Coherent photoproduction of vector mesons in ultraperipheral heavy ion collisions: Update for run 2 at the CERN Large Hadron Collider", *Phys. Rev. C* **93** no. 5, (2016) 055206, arXiv:1602.01456 [nucl-th].

[19] **ALICE** Collaboration, S. Ragoni, "Recent results for forward J/ψ production in Pb–Pb Ultra-Peripheral Collisions at $\sqrt{s_{\rm NN}}$ = 5.02 TeV with the ALICE detector", in *27th International Nuclear Physics Conference*. 9, 2019. arXiv:1909.12212 [hep-ex].

[20] **ALICE** Collaboration, S. Ragoni, "UPC: a powerful tool for J/ψ photoproduction analysis in ALICE", *PoS* **LHCP2020** (2021) 255, arXiv:2009.11724 [hep-ex].

[21] **ALICE, LHCb** Collaboration, S. Ragoni, "New measurements on diffractive vector mesons", in *9th Large Hadron Collider Physics Conference*. 9, 2021. arXiv:2109.03066 [hep-ex].

[22] **Particle Data Group** Collaboration, M. Tanabashi *et al.*, "Review of Particle Physics", *Phys. Rev.* **D98** no. 3, (2018) 030001.

[23] **STAR** Collaboration, G. Agakishiev *et al.*, "ρ^0 Photoproduction in Au–Au Collisions at $\sqrt{s_{NN}} = 62.4$ GeV with STAR", *Phys. Rev. C* **85** (2012) 014910, arXiv:1107.4630 [nucl-ex].

[24] **STAR** Collaboration, C. Adler *et al.*, "Coherent ρ^0 production in ultraperipheral heavy ion collisions", *Phys. Rev. Lett.* **89** (2002) 272302, arXiv:nucl-ex/0206004.

[25] **STAR** Collaboration, B. I. Abelev *et al.*, "ρ^0 photoproduction in ultraperipheral relativistic heavy ion collisions at $\sqrt{s_{NN}} = 200$ GeV", *Phys. Rev. C* **77** (2008) 034910, arXiv:0712.3320 [nucl-ex].

[26] **ALICE** Collaboration, S. Acharya *et al.*, "Coherent J/ψ and ψ' photoproduction at midrapidity in ultra-peripheral Pb–Pb collisions at $\sqrt{s_{\rm NN}} = 5.02$ TeV", arXiv:2101.04577 [nucl-ex].

[27] S. R. Klein, J. Nystrand, J. Seger, Y. Gorbunov, and J. Butterworth, "STARlight: A Monte Carlo simulation program for ultra-peripheral collisions of relativistic ions", *Comput. Phys. Commun.* **212** (2017) 258–268, arXiv:1607.03838 [hep-ph].

[28] L. Frankfurt, V. Guzey, and M. Strikman, "Leading Twist Nuclear Shadowing Phenomena in Hard Processes with Nuclei", *Phys. Rept.* **512** (2012) 255–393, arXiv:1106.2091 [hep-ph].

[29] V. Guzey, M. Strikman, and M. Zhalov, "Disentangling coherent and incoherent quasielastic J/ψ photoproduction on nuclei by neutron tagging in ultraperipheral ion collisions at the LHC", *Eur. Phys. J. C* **74** no. 7, (2014) 2942, arXiv:1312.6486 [hep-ph].

[30] J. G. Contreras, "Gluon shadowing at small x from coherent J/ψ photoproduction data at energies available at the CERN Large Hadron Collider", *Phys. Rev. C* **96** no. 1, (2017) 015203, arXiv:1610.03350 [nucl-ex].

[31] **STAR** Collaboration, J. Adam *et al.*, "Observation of excess J/ψ yield at very low transverse momenta in Au+Au collisions at $\sqrt{s_{\rm NN}} = 200$ GeV and U+U collisions

at $\sqrt{s_{\rm NN}} = 193$ GeV", *Phys. Rev. Lett.* **123** no. 13, (2019) 132302, arXiv:1904.11658 [hep-ex].

[32] **LHCb** Collaboration, R. Aaij *et al.*, "Study of J/ψ photo-production in lead-lead peripheral collisions at $\sqrt{s_{\rm NN}} = 5$ TeV", arXiv:2108.02681 [hep-ex].

[33] **H1** Collaboration, A. Aktas *et al.*, "Elastic J/ψ production at HERA", *Eur. Phys. J. C* **46** (2006) 585–603, arXiv:hep-ex/0510016.

[34] **H1** Collaboration, C. Alexa *et al.*, "Elastic and Proton-Dissociative Photoproduction of J/ψ Mesons at HERA", *Eur. Phys. J.* **C73** no. 6, (2013) 2466, arXiv:1304.5162 [hep-ex].

[35] J. G. Contreras and J. D. Tapia Takaki, "Ultra-peripheral heavy-ion collisions at the LHC", *Int. J. Mod. Phys.* **A30** (2015) 1542012.

[36] **LHCb** Collaboration, R. Aaij *et al.*, "Exclusive J/ψ and ψ(2S) production in pp collisions at $\sqrt{s} = 7$ TeV", *J. Phys. G* **40** (2013) 045001, arXiv:1301.7084 [hep-ex].

[37] **LHCb** Collaboration, R. Aaij *et al.*, "Updated measurements of exclusive J/ψ and ψ(2S) production cross-sections in pp collisions at $\sqrt{s} = 7$ TeV", *J. Phys. G* **41** (2014) 055002, arXiv:1401.3288 [hep-ex].

[38] **LHCb** Collaboration, R. Aaij *et al.*, "Central exclusive production of J/ψ and $\psi(2S)$ mesons in pp collisions at $\sqrt{s} = 13$ TeV", *JHEP* **10** (2018) 167, arXiv:1806.04079 [hep-ex].

[39] **ALICE** Collaboration, B. Abelev *et al.*, "Exclusive J/ψ photoproduction off protons in ultra-peripheral p-Pb collisions at $\sqrt{s_{\rm NN}} = 5.02$ TeV", *Phys. Rev. Lett.* **113** no. 23, (2014) 232504, arXiv:1406.7819 [nucl-ex].

[40] **ALICE** Collaboration, S. Acharya *et al.*, "Energy dependence of exclusive J/ψ photoproduction off protons in ultra-peripheral p–Pb collisions at $\sqrt{s_{\rm NN}}$ = 5.02 TeV", *Eur. Phys. J. C* **79** no. 5, (2019) 402, arXiv:1809.03235 [nucl-ex].

[41] P. Faccioli, C. Lourenço, and J. Seixas, "A New approach to quarkonium polarization studies", *Phys. Rev.* **D81** (2010) 111502, arXiv:1005.2855 [hep-ph].

[42] P. Faccioli, C. Lourenço, J. Seixas, and H. K. Wöhri, "Towards the experimental clarification of quarkonium polarization", *Eur. Phys. J. C* **69** (2010) 657–673, arXiv:1006.2738 [hep-ph].

[43] L. Bianchi, J/ψ *polarization in pp collisions at* $\sqrt{s}$ = 7 *TeV with the ALICE muon spectrometer at the LHC*. PhD thesis, Mar, 2012. https://cds.cern.ch/record/1440848. Presented 06 Mar 2012.

[44] L. Micheletti, *Quarkonium polarization in Pb–Pb collisions with the ALICE experiment at the LHC*. PhD thesis, Dec, 2020. https://cds.cern.ch/record/2753445. Presented 08 Feb 2021.

[45] R. Bailey and P. Collier, "Standard Filling Schemes for Various LHC Operation Modes",. https://cds.cern.ch/record/691782/files/project-note-323.pdf.

[46] L. M. Outreach, "Beam.". https://lhc-machine-outreach.web.cern.ch/beam.htm.

[47] J. M. Jowett and M. Schaumann, "Overview of Heavy Ions in LHC Run 2", in *9th LHC Operations Evian Workshop*, pp. 15–25. 2019.

[48] **ALICE** Collaboration, C. W. Fabjan *et al.*, "ALICE: Physics performance report, volume II", *J. Phys. G* **32** (2006) 1295–2040.

[49] **ALICE** Collaboration, G. Dellacasa *et al.*, "ALICE technical design report of the inner tracking system (ITS)", CERN CDS:http://cds.cern.ch/record/391175.

[50] **ALICE** Collaboration, M. Keil, "Upgrade of the ALICE Inner Tracking System", *JINST* **10** no. 03, (2015) C03012.

[51] **ALICE** Collaboration, F. Meddi, "The ALICE silicon pixel detector (SPD)", *Nucl. Instrum. Meth. A* **465** (2000) 40–45.

[52] J. Alme *et al.*, "The ALICE TPC, a large 3-dimensional tracking device with fast readout for ultra-high multiplicity events", *Nucl. Instrum. Meth. A* **622** (2010) 316–367, arXiv:1001.1950 [physics.ins-det].

[53] **ALICE** Collaboration, S. Acharya *et al.*, "The ALICE Transition Radiation Detector: construction, operation, and performance", *Nucl. Instrum. Meth. A* **881** (2018) 88–127, arXiv:1709.02743 [physics.ins-det].

[54] **ALICE** Collaboration, G. Dellacasa *et al.*, "ALICE technical design report of the time-of-flight system (TOF)", CERN CDS:http://cds.cern.ch/record/430132?ln=en.

[55] **ALICE** Collaboration, F. Carnesecchi, "Performance of the ALICE Time-Of-Flight detector at the LHC", *JINST* **14** no. 06, (2019) C06023, arXiv:1806.03825 [physics.ins-det].

[56] **ALICE** Collaboration, N. Jacazio, "PID performance of the ALICE-TOF detector at Run 2", *PoS* **LHCP2018** (2018) 232, arXiv:1809.00574 [physics.ins-det].

[57] **ALICE** Collaboration, "ALICE technical design report of the dimuon forward spectrometer", CERN CDS:http://cds.cern.ch/record/401974.

[58] Z. Conesa del Valle, *Performance of the ALICE muon spectrometer. Weak boson production and measurement in heavy-ion collisions at LHC*. PhD thesis, Dec, 2007. https://inis.iaea.org/collection/NCLCollectionStore/_Public/39/107/39107530.pdf. Presented 17 Dec 2007.

[59] **ALICE Muon Spectrometer** Collaboration, C. Finck, "The muon spectrometer of the ALICE", *J. Phys. Conf. Ser.* **50** (2006) 397–401.

[60] **ALICE** Collaboration, G. Martinez, "The Muon spectrometer of the ALICE experiment", *Nucl. Phys. A* **749** (2005) 313–319, arXiv:hep-ex/0410061.

[61] D. Stocco, *Development of the ALICE Muon Spectrometer: Preparation for data taking and heavy flavor measurement.* PhD thesis, Turin U., 2008.

[62] M. K. Boudjemline, *Etude des chambres de trajectographie CPC du spectromètre dimuon d'ALICE.* PhD thesis, Nantes U., 2004. https://inspirehep.net/literature/887343.

[63] **ALICE** Collaboration, E. Abbas *et al.*, "Performance of the ALICE VZERO system", *JINST* **8** (2013) P10016, arXiv:1306.3130 [nucl-ex].

[64] **ALICE** Collaboration, A. Villatoro Tello, "AD, the ALICE diffractive detector", *AIP Conf. Proc.* **1819** no. 1, (2017) 040020.

[65] M. Broz *et al.*, "Performance of ALICE AD modules in the CERN PS test beam", *JINST* **16** no. 01, (2021) P01017, arXiv:2006.14982 [physics.ins-det].

[66] **ALICE** Collaboration, M. M. Aggarwal *et al.*, "Characteristics of Photon Multiplicity Detector Modules in the ALICE Experiment,", *DAE Symp. Nucl. Phys.* **55** (2010) 696–697.

[67] M. Krivda, "The ALICE trigger electronics", in *Topical Workshop on Electronics for Particle Physics*, p. 9. 9, 2007.

[68] S. Baron *et al.*, "Timing, Trigger and Control (TTC) Systems for the LHC.". https://ttc.web.cern.ch.

[69] **ALICE** Collaboration, F. Carena *et al.*, "The ALICE data acquisition system", *Nucl. Instrum. Meth. A* **741** (2014) 130–162.

[70] M. Krivda *et al.*, "ALICE trigger system for LHC Run 3", *PoS* **TWEPP2018** (2019) 119.

[71] ALICE, "TTCit for LHC Run 2.". https://home.saske.sk/~kralik/TTCit/fI.php.

[72] J. Christiansen, A. Marchioro, and P. Moreira, "TTCrx, an ASIC for timing, trigger and control distribution in LHC experiments." 1996. https://inspirehep.net/literature/432448.

[73] J. Christiansen, A. Marchioro, and P. Moreira, "TTCrx, an ASIC for timing, trigger and control distribution in LHC experiments." 10, 2004. http://ttc.web.cern.ch/TTCrx_manual3.9.pdf.

[74] P. Vichoudis, E. van der Bij, and J. Gonzáles, "Optical Clock and Data Recovery FMC.". https://ohwr.org/project/optical-cdr-fmc.

[75] **Texas** Instruments, "ADN2814 User's Guide." C, Rev. https://www.analog.com/media/en/technical-documentation/data-sheets/ADN2814.pdf.

[76] **Texas** Instruments, "SN65LVDS250 User's Guide." 10, 2004. https://www.ti.com/lit/ds/symlink/sn65lvds250.pdf?ts=1621600755235&ref_url=https%253A%252F%252Fwww.google.com%252F.

[77] M. Tkáčik, J. Jadlovský, S. Jadlovska, L. Koska, A. Jadlovska, and M. Donadoni, "Fred—flexible framework for frontend electronics control in alice experiment at cern", *Processes* **8** (05, 2020) 565.

[78] **Texas** Instruments, "What's an LFSR." 12, 1996. https://www.ti.com/lit/an/scta036a/scta036a.pdf2F.

[79] J. E. Gaiser, *Charmonium Spectroscopy From Radiative Decays of the* J/ψ *and* ψ'. PhD thesis, SLAC, 1982. http://inspirehep.net/record/183554/files/slac-r-255.pdf.

[80] R. Lavicka, *Ultra-Peripheral Collisions at ALICE, Looking inside lead ions*. PhD thesis, May, 2021. https://cds.cern.ch/record/2778893. Presented 13 Jul 2021.

[81] **ALICE** Collaboration, "ALICE luminosity determination for Pb−Pb collisions at $\sqrt{s_{\rm NN}} = 5.02$ TeV", arXiv:2204.10148 [nucl-ex].

[82] **H1** Collaboration, F. D. Aaron *et al.*, "Measurement of the Inclusive ep Scattering Cross Section at Low Q^2 and x at HERA", *Eur. Phys. J. C* **63** (2009) 625–678, arXiv:0904.0929 [hep-ex].

[83] **ALICE** Collaboration, K. Aamodt *et al.*, "Rapidity and transverse momentum dependence of inclusive J/ψ production in pp collisions at $\sqrt{s} = 7$ TeV", *Phys. Lett.* **B704** (2011) 442–455, arXiv:1105.0380 [hep-ex]. [Erratum: Phys. Lett.B718,692(2012)].

[84] **ALICE** Collaboration, B. Abelev *et al.*, "J/ψ polarization in pp collisions at $\sqrt{s} = 7$ TeV", *Phys. Rev. Lett.* **108** (2012) 082001, arXiv:1111.1630 [hep-ex].

[85] **ALICE** Collaboration, S. Acharya *et al.*, "Measurement of the inclusive J/ψ polarization at forward rapidity in pp collisions at $\sqrt{s} = 8$ TeV", *Eur. Phys. J. C* **78** no. 7, (2018) 562, arXiv:1805.04374 [hep-ex].

[86] **ALICE** Collaboration, S. Acharya *et al.*, "First measurement of quarkonium polarization in nuclear collisions at the LHC", *Phys. Lett. B* **815** (2021) 136146, arXiv:2005.11128 [nucl-ex].

[87] J. Ballam *et al.*, "Vector Meson Production by Polarized Photons at 2.8 GeV, 4.7 GeV, and 9.3 GeV", *Phys. Rev. D* **7** (1973) 3150.

[88] **OMEGA Photon** Collaboration, R. J. Apsimon *et al.*, "Comparison of photon and hadron induced production of ρ^0 mesons in the energy range of 65 GeV to 175 GeV", *Z. Phys. C* **53** (1992) 581–594.

[89] **STAR** Collaboration, B. I. Abelev *et al.*, "ρ^0 photoproduction in ultraperipheral relativistic heavy ion collisions at $\sqrt{s_{\rm NN}}$ = 200 GeV", *Phys. Rev. C* **77** (2008) 034910, arXiv:0712.3320 [nucl-ex].

[90] **CLAS** Collaboration, S. A. Morrow *et al.*, "Exclusive ρ^0 electroproduction on the proton at CLAS", *Eur. Phys. J. A* **39** (2009) 5–31, arXiv:0807.3834 [hep-ex].

[91] **CLAS** Collaboration, B. Vernarsky, "First measurements of the ρ^3 spin density matrix elements in $\gamma p \to p\omega$ using CLAS at JLAB", *Int. J. Mod. Phys. Conf. Ser.* **26** (2014) 1460063.

[92] **CLAS** Collaboration, B. Dey *et al.*, "Data analysis techniques, differential cross sections, and spin density matrix elements for the reaction $\gamma p \to \phi p$", *Phys. Rev. C* **89** no. 5, (2014) 055208, arXiv:1403.2110 [nucl-ex]. [Addendum: Phys.Rev.C 90, 019901 (2014)].

[93] H. Nyquist, "Certain topics in telegraph transmission theory", *Transactions of the American Institute of Electrical Engineers* **47** no. 2, (1928) 617–644.

[94] E. T. Whittaker, "Xviii.—on the functions which are represented by the expansions of the interpolation-theory", *Proceedings of the Royal Society of Edinburgh* **35** (1915) 181–194.

[95] S. Schmitt, "Data Unfolding Methods in High Energy Physics", *EPJ Web Conf.* **137** (2017) 11008, arXiv:1611.01927 [physics.data-an].

[96] T. Adye, "Unfolding algorithms and tests using RooUnfold", in *PHYSTAT 2011*, pp. 313–318. CERN, Geneva, 2011. arXiv:1105.1160 [physics.data-an].

[97] G. D'Agostini, "A Multidimensional unfolding method based on Bayes' theorem", *Nucl. Instrum. Meth. A* **362** (1995) 487–498.

[98] J. C. Martens, J. P. Ralston, and J. D. Tapia Takaki, "Quantum tomography for collider physics: Illustrations with lepton pair production", *Eur. Phys. J. C* **78** no. 1, (2018) 5, arXiv:1707.01638 [hep-ph].

[99] F. James and M. Winkler, "MINUIT User's Guide." 6, 2004. https://inspirehep.net/files/c92c2ba4dac7c0a665cce687fb19b29c.

[100] F. Rademakers and R. B. et al., "ROOT - An Object-Oriented Data Analysis Framework. root-project/root: v6.10/04." Aug., 2017. https://doi.org/10.5281/zenodo.848819.

[101] **ZEUS** Collaboration, S. Chekanov *et al.*, "Exclusive electroproduction of J/ψ mesons at HERA", *Nucl. Phys. B* **695** (2004) 3–37, arXiv:hep-ex/0404008.

[102] **ZEUS** Collaboration, J. Breitweg *et al.*, "Exclusive electroproduction of ρ^0 and J/ψ mesons at HERA", *Eur. Phys. J. C* **6** (1999) 603–627, arXiv:hep-ex/9808020.

[103] K. Schilling and G. Wolf, "How to analyze vector meson production in inelastic lepton scattering", *Nucl. Phys. B* **61** (1973) 381–413.